creative commons
COMMONS DEED

저작자표시-비영리-변경금지 2.0 대한민국

이용자는 아래의 조건을 따르는 경우에 한하여 자유롭게

- 이 저작물을 복제, 배포, 전송, 전시, 공연 및 방송할 수 있습니다.

다음과 같은 조건을 따라야 합니다:

저작자표시. 귀하는 원저작자를 표시하여야 합니다.

비영리. 귀하는 이 저작물을 영리 목적으로 이용할 수 없습니다.

변경금지. 귀하는 이 저작물을 개작, 변형 또는 가공할 수 없습니다.

- 귀하는, 이 저작물의 재이용이나 배포의 경우, 이 저작물에 적용된 이용허락조건을 명확하게 나타내어야 합니다.
- 저작권자로부터 별도의 허가를 받으면 이러한 조건들은 적용되지 않습니다.

저작권법에 따른 이용자의 권리는 위의 내용에 의하여 영향을 받지 않습니다.

이것은 이용허락규약(Legal Code)을 이해하기 쉽게 요약한 것입니다.

Disclaimer

dCollection

[UCI]I804:48009-200000503690

Doctor of Philosophy

ADVANCED CONTROL STRATEGIES FOR n-DOF SERIAL HYDRAULIC ROBOTIC MANIPULATOR IN INDUSTRIAL APPLICATIONS

The Graduate School

of the University of Ulsan

Department of Mechanical Engineering

HOAI VU ANH TRUONG

ADVANCED CONTROL STRATEGIES FOR n-DOF SERIAL HYDRAULIC ROBOTIC MANIPULATOR IN INDUSTRIAL APPLICATIONS

Supervisor: Professor KYOUNG KWAN AHN

A Dissertation

Submitted to
the Graduate School of the University of Ulsan
In Partial Fulfillment of the Requirement
for the Degree of

DOCTOR OF PHILOSOPHY
(Mechanical and Automotive Engineering)

by

HOAI VU ANH TRUONG

Department of Mechanical Engineering

University of Ulsan, Korea

June 2021

ADVANCED CONTROL STRATEGIES FOR n-DOF SERIAL HYDRAULIC ROBOTIC MANIPULATOR IN INDUSTRIAL APPLICATIONS

This certifies that the dissertation of

TRUONG HOAI VU ANH is approved by

Committee Chair: Prof. BYOUNG RYOUNG LEE

Committee member: Prof. KYOUNG KWAN AHN

Committee member: Prof. CHEOL KEUN HA

Committee member Prof. HEE JUN KANG

Committee member Dr. MAOLIN JIN

Department of Mechanical and Automotive Engineering

University of Ulsan, Korea

June 2021

Acknowledgement

During the time in which this research was undertaken, I have had the best opportunity to work with excellent people. The thesis would not have been finished without their encouragement and kindly help.

First and foremost, I would like to express my deep gratitude and appreciation to my advisor, Prof. Kyoung Kwan, Ahn, for the continuous support of my Ph.D. study and related research, for his motivation, patience, immense knowledge, and during my study in the University of Ulsan. His guidance and f helped me in all the time of research and writing of this thesis. I could not have imagined having a better advisor and mentor for my Ph.D. study. Forever, respect for him exists in my mind.

Besides my advisor, I would like to thank Prof. Byung Ryong, Lee, Prof. Cheol Keun, Ha, Prof. Hee Jun, Kang, and Dr. Maolin, Jin, for their insightful comments and encouragement, but also for the hard questions which incented me to enhance my research from various perspectives.

I would also like to thank to my friends in Korea and in Vietnam, all members of FPMI Lab. for their encouragement, discussion, and friendship during my research.

I would like to extend my sincere thanks to Prof. Duy Anh, Nguyen and Prof. Tri Cong, Phung, who infused me fundamentally academic knowledge, inspiration, as well as orientation for my research pathway in Korea.

Finally, I am grateful to my love family with the most fantastic members. Their love and encouragement have become the infinite power for me to face difficulties during the time I study abroad.

Ulsan, Korea, June 2021

Hoai-Vu-Anh Truong

Contents

Acknowledgement ..... *I*

Contents ..... *II*

List of figures ..... *VII*

List of tables ..... *XI*

Abbreviations ..... *XII*

Abstract ..... *XIII*

CHAPTER 1 Introduction *1*

1.1 Overview 1

1.2 Research objectives 4

1.3 Limitations 5

1.4 Dissertation outline 6

CHAPTER 2 Mathematical preliminaries. *8*

2.1 Introduction 8

2.2 Mathematic 8

2.2.1 Vector and matrices analysis 8

2.2.2 Vectors and matrices differential calculus 9

2.2.3 Vector and matrix norms 10

2.2.3.1 Vector norms 10

2.2.3.2 Matrix norms 11

2.2.3.3 Eigen value of square matrix 11

2.2.4 Inequalities 11

2.2.4.1 Young's inequality 11

2.2.4.2 Rayleigh inequality 12

2.2.4.3 Lipschitz functions 12

2.3 Lyapunov stability theory 12
2.3.1 Stability concepts for autonomous systems 12
2.3.2 Stability concepts for non-autonomous systems 13
2.3.3 Lyapunov stability theorems 14
2.3.4 Lyapunov stability using Barbalat's lemma 15
CHAPTER 3 Dynamics of n-DOF Serial Hydraulic Manipulator Including Actuator Dynamics 16
3.1 Introduction 16
3.2 Problem formulation of n-DOF serial manipulator system 16
3.2.1 Mechanical structure of n-DOF serial hydraulic manipulator 16
3.2.2 Dynamics of n-DOF serial hydraulic manipulator 17
3.3 Problem formulation Electro-hydraulic system 18
3.3.1 Importance of the electro-hydraulic system 18
3.3.2 Electro-hydraulic system dynamics modeling 20
3.4 Comprehensive dynamics of the n-DOF serial hydraulic manipulator system 21
3.5 Adaptive backstepping sliding mode control for n-DOF serial hydraulic manipulator 23
3.6 Remained problems and discussion 28
CHAPTER 4 Verification of n-DOF Serial Hydraulic Manipulator in Free Motion 29
4.1 Introduction 29
4.2 Structure of the 3-DOF Serial hydraulic manipulator 29
4.3 Adaptive fuzzy backstepping sliding mode control with disturbance observer 29
4.3.1 Generalized momentum observer for force disturbance 30
4.3.1.1 Model-based disturbance observer 31
4.3.1.2 Disturbance estimator-based generalized momentum observer technique 32
4.3.1.3 General momentum and observer matrix gain design 33
4.3.2 Adaptive backstepping sliding mode control with GMO 37

4.3.3 Adaptive Fuzzy BSMC with GMO 38

4.3.4 Controller gains initialization 41

4.3.4.1 Neural network sliding mode control 41

4.3.4.2 The Constraint of the Updating Law 45

4.4 Numerical simulations 45

4.4.1 Case study 1 49

4.4.2 Case study 2 53

4.4.3 Case study 3 57

4.5 Experiments 63

4.5.1 Experimental test bench setup 63

4.5.2 Experimental Results 63

4.5.2.1 Case study 1 64

4.5.2.2 Case study 2 64

4.5.2.3 Case study 3 65

4.6 Discussions 71

Chapter 5 Fault estimation and Fault-tolerant Control for n-DOF serial Hydraulic Manipulator in Constrained Motion *72*

5.1 Introduction 72

5.2 System modeling and Problem formulation 73

5.2.1 Structure of the impedance control 73

5.2.2 System modeling with sensor faults 75

5.3 A novel robust fault estimation based extended state observer 76

5.4 Development of adaptive fuzzy backstepping sliding mode control based on fault-tolerant control-based 81

5.5 Numerical simulation 83

5.5.1 Setup scenario 83

5.5.2 Simulation results 85

5.5.2.1 Case study 1: Occurrence of encoder sensor faults in free motion 85

5.5.2.2 Case study 2: Occurrence of force sensor fault in constrained motion 87

5.6 Conclusion 91

CHAPTER 6 Control strategy for Safety Operation with Contact-loss for n-DOF serial Hydraulic Manipulator in Constrained Motion *92*

6.1 Introduction 92

6.2 Modified position-based impedance control with virtual energy tank 93

6.2.1 Contact-loss consideration-based virtual energy tank and passivity control 93

6.2.2 Modification of trajectory 96

6.3 Force sensorless-based extended state observer (ESO) 97

6.4 Whole system stability analysis 100

6.5 Numerical simulation results 101

6.5.1 Scenario for verification and setting parameters 101

6.5.2 Simulated results 102

6.5.2.1 Case study 1 103

6.5.2.2 Case study 2 105

6.5.2.3 Case study 3 107

6.6 Conclusion 109

Chapter 7 Conclusion and future work *111*

7.1 Conclusions 111

7.2 Future works and developments 113

Appendixes *114*

Appendix A 114

A.1 3-DOF hydraulic manipulator dynamics 114

A.2 Forward kinetic and Jacobian matrix 115

Appendix B 115

Published papers and patents *116*

References *119*

List of figures

Figure 2-1 Concept of stability illustrations: curve 1 - asymptotically stable, curve 2 - marginally stable, curve 3 – unstable [69]. 13

Figure 3-1 Structure of n-serial hydraulic manipulator 16

Figure 3-2 Closed-chain structure of the {i^{th}} joint 17

Figure 3-3 Working principle of electro-hydraulic system. 19

Figure 3-4 three-land-four-way servo valve (a) real 4/3 servo valve, and (b) servo valve schematic. . 21

Figure 4-1 Structure of the 3-DOF serial hydraulic manipulator. 30

Figure 4-2 Link frame of the 3-DOF serial hydraulic manipulator. 30

Figure 4-3 Architecture of the GMO for nonlinear systems. 32

Figure 4-4 Proposed adaptive Fuzzy BSMC with GMO and NN initialization. 39

Figure 4-5 Membership function of the error and the rate of error. 40

Figure 4-6 Membership function of the tuned factor $\boldsymbol{\alpha}_1^f$: (**a**) $\boldsymbol{\alpha}_{11}^f$, (**b**) $\boldsymbol{\alpha}_{12}^f$, (**c**) $\boldsymbol{\alpha}_{13}^f$ 40

Figure 4-7 The motion of the state trajectory of the sliding mode control in which the two stages and the two terms affecting the convergence rate of the state error are considered. The sub-figure shows the correlation between the robust term K and α with the slope of the sliding surface λ 42

Figure 4-8 Architecture of the proposed neural network based sliding mode control. 43

Figure 4-9 The payload variation profile. 46

Figure 4-10 AFBSMC with feedforward disturbance compensator 47

Figure 4-11 Membership function of the load torque variation: (a) $d_{\tau_{load},1}$ on joint 1, (b) $d_{\tau_{load},2}$ on joint 2, (c) $d_{\tau_{load},3}$ on joint 3 48

Figure 4-12 Membership function of the tuned scaling gains: (a) K_{m1}, (b) K_{m2}, (c) K_{m3}. 49

Figure 4-13 The tracking performance of the: (a) first joint; (b) second joint; (c) third joint. 50

Figure 4-14 The tracking error of the: (a) first joint, (b) second joint, and (c) third joint. 51

Figure 4-15 The load torque estimated of the: (a) first joint, (b) second joint, and (c) third joint. 52

Figure 4-16 The control signal acting on the: (a) first joint, (b) second joint, and (c) third joint. 53

Figure 4-17 The tracking performance of the: (a) first joint; (b) second joint; (c) third joint. 54

Figure 4-18 The tracking error of: (a) The first joint, (b) the second joint, and (c) the third joint. 55

Figure 4-19 The load torque estimated of the: (a) first joint, (b) second joint, and (c) third joint. 56

Figure 4-20 The control signal acting on the: (a) first joint, (b) second joint, and (c) third joint. 57

Figure 4-21 The tracking performance of the: (a) first joint; (b) second joint; (c) third joint. 58

Figure 4-22 The tracking error of the: (a) first joint, (b) second joint, and (c) third joint. 59

Figure 4-23 The tracking performance in: (a) X direction, (b) Y direction, and (c) Z direction. 60

Figure 4-24 Response of the manipulator in 3D space. 60

Figure 4-25 The load torque estimated on (a) first joint, (b) second joint, and (c) third joint. 61

Figure 4-26 The control signal acting on the: (a) first joint, (b) second joint, and (c) third joint. 62

Figure 4-27 Setup test bend for experiments. 64

Figure 4-28 Case study 1: The tracking performance, in case of sinusoidal signal without load, of the: (a) first joint; (b) second joint; (c) third joint. 65

Figure 4-29 Case study 1: The tracking error, in case of sinusoidal signal without load, of the: (a) first joint; (b) second joint; (c) third joint. 66

Figure 4-30 Case study 2: Tracking performance, in case of sinusoidal signal with load, of the: (a) first joint; (b) second joint; (c) third joint. 67

Figure 4-31 Case study 2: Tracking error, in case of sinusoidal signal with load, of the: (a) first joint; (b) second joint; (c) third joint. 68

Figure 4-32 Case study 3: Tracking performance, in the case of step response, of the: (a) first joint; (b) second joint; (c) third joint. 69

Figure 4-33 Case study 3: Tracking error, in the case of step response, of the: (a) first joint; (b) second joint; (c) third joint. 70

Figure 5-1 Structure of the position-based impedance control with sensor faults. 74

Figure 5-2 Illustration of physical interaction between the end-effector with environment. 75

Figure 5-3 Proposed AFBSMC-based FTC with sensor faults. 81

Figure 5-4 3-DOF serial hydraulic manipulator: (a) Structure with link frame, and (b) working environment framework. 84

Figure 5-5 Position tracking performance and estimation without FTC under the presence of fault signals: (a) 2nd joint with measured joint angle feedback, (b) 3rd joint with measured joint angle feedback. 86

Figure 5-6 Real faults and faults estimation using robust observer. 86

Figure 5-7 Position tracking performance under the FTC with ESO: (a) 2nd joint with the estimated joint angle feedback, (b) 3rd joint with the estimated joint angle feedback. 87

Figure 5-8 Force tracking performance and estimation results without FTC in the presence of sensor fault. 89

Figure 5-9 Force tracking performance under the FTC with ESO (i.e. estimated interactive force is feedback to the main controller)..... 89

Figure 5-10 Signal fault estimation results: (a) magnitude of faulty signal, and (b) estimation error. . 90

Figure 5-11 End-effector behavior under the presence of force sensor fault in constrained motion. ... 90

Figure 6-1 3D design of the 6-DOF serial hydraulic KIRO robot. 93

Figure 6-2 Schematic representation of the 6-DOF serial hydraulic KIRO robot..... 93

Figure 6-3 Schematic diagram of the impedance control with virtual energy tank and passivity control for contact lost consideration. 94

Figure 6-4 Strategy of fading function for smoothing trajectory. 97

Figure 6-5 Impedance control-based energy tank with force observer for contact-loss problem. 98

Figure 6-6 Scenario for algorithm of contact-loss validation..... 102

Figure 6-7 Position tracking of the end-effector in X-direction..... 103

Figure 6-8 Position tracking of the end-effector in Y-direction..... 103

Figure 6-9 Position tracking of the end-effector in X-direction..... 104

Figure 6-10 Response of the switched parameter β when contact-loss happens..... 104

Figure 6-11 Force tracking performance subjected to contact-loss situation. 105

Figure 6-12 Estimation error between the actual and the estimated interactive forces. 105

Figure 6-13 Response of the end-effector in X-direction under different force control gains. 106

Figure 6-14 Response of the energy variable under different force control gains. 106

Figure 6-15 Response of the end-effector in X-direction in case of friction under different force control gains. 108

Figure 6-16 Response of the energy variable in case of friction under different force control gains. 108

Figure 6-17 State of the switching parameter β under different force control gains. 108

List of tables

Table 4-1. Rules table of the fuzzy logic system. 40

Table 4-2. The mechanical parameters used for simulations. 46

Table 4-3. The hydraulic parameters used for simulations 46

Table 4-4 Rules table of the fuzzy logic system. 49

Table 5-1. Mechanical parameters. 84

Table 5-2. Hydraulic parameters. 84

Table 6-1. Parameters of the hydraulic specification. 101

Table 6-2. Parameters of hydraulic actuators. 101

Table 6-3. Parameters of the contact-loss impedance control. 102

Table B-1 The link parameters of the 6-DOF KIRO robot. 115

Abbreviations

ABSMC	Adaptive backstepping sliding mode control
AFBSMC	Adaptive fuzzy backstepping sliding mode control
BSMC	Backstepping sliding mode control
DOAFBSMC	Disturbance observer adaptive fuzzy backstepping sliding mode control
EHS	Electro-hydraulic system
ESO	Extended state observer
FBSMC	Fuzzy backstepping sliding mode control
FFDOAFSMC	Feedforward disturbance observer adaptive fuzzy backstepping sliding mode control
FLC	Fuzzy logic control
GMO	Generalized momentum observer
IC-CL	Impedance control with contact-loss
n-DOF	n-Degree-of-freedom
PB-IC	Position-based impedance control
SMC	Sliding mode control

Abstract

This thesis presents advanced control strategies so as to address existing problems of an n-DOF serial hydraulic manipulator, subjected to matched and mismatched disturbances and faults identification for industrial applications. Due to the high power-to-weight ratio, the electro-hydraulic actuator and electro-hydraulic system (EHS) are reasonably employed to drive the manipulator link frame and enhance system performance. However, the EHS is a highly nonlinear system that cannot be neglected like electric actuators when developing control strategies. Besides, the influence of mismatched uncertainties from external impacts and matched uncertainty available existing in the EHS challenges the control development. Therefore, in order to address those problems, the proposed control scheme based on the adaptive backstepping sliding mode control (ABSMC) is designed to achieve the system stability and robustness against the perturbations. Based on the ABSMC technique, disturbance estimator is also involved to estimate and compensate for the matched/mismatched disturbances and observe unmeasured variables. Besides, intelligent techniques are also used to satisfy the different working operations. Both comparative simulations and experiment between the proposed control scheme and other conventional algorithms are verified on a 3-DOF serial hydraulic manipulator, subjected to the payload variations in free motion, to evaluate the effectiveness of the proposed methodology.

Subsequently, based on the obtained results, sensor fault and safety operation are then considered as the main objectives to develop the control strategy for the n-DOF serial hydraulic manipulator in constrained frameworks. During this process, position-based impedance control (PB-IC) is preferred as the key point to achieve the force regulation and system stability under the influence of the sensor fault. This fault type is generated from the additive unknown faulty signals, which may be a constant offset or time-variant variable, to the sensors. Due to not obvious effect caused by the sensor faults, the system behavior is the same as the fault free condition; however, the controller executes erroneous control action on the actuator. Therefore, a robust fault estimation based on extended state observer (ESO) is proposed to estimate the faulty signals to achieve the desired actuation. With the estimated signals, the active fault-tolerant control (FTC) based on the ABSMC technique is constructed. Furthermore, the behavior of the manipulator may be unstable or exhibit unexpected motion in a case of sudden contact-loss or environment step-change. Therefore, a modified PB-IC based on virtual energy tank and passivity control concepts is deployed to decouple the force control action when sudden contact-loss happens.

The closed-loop system stability is theoretically proven by Lyapunov theorem. Additionally, comparative simulations are given to verify the effectiveness of the proposed algorithm.

CHAPTER 1
Introduction

1.1 Overview

Nowadays, the manipulators have been essential in industrial application point of view to assist human in specific fields such as assembling, polishing, welding in heavy industries, construction, exploration, medical field, and other relevant robotic areas. The control of the manipulator, in general, is still a challenge due to its high nonlinearity, coupling dynamic reaction, and model parametric uncertainties [1]. Conventionally, the actuator dynamics is excluded from the robotic system to simplify the control design procedure. However, according to [2], the actuator dynamics generates remarkable influences on system stability [2,3], as well as dominates the robot dynamics characteristics [4]. Therefore, the actuator dynamics should be included in control development [3–6]. Electric actuators (EAs), widely deployed in industrial applications point of view, are utilized as primary force/torque generators due to owning properties such as excellent accuracy and controllability but suffer from the possibility of sparking [6]. However, this type of actuator is not suitable for heavy industrial application, such as construction machineries, cranes, rescue robotic manipulators, due to restriction of size-to-power workability. Pneumatic actuators (PAs) are another potential candidate to replace the electric actuators because of its advantage of quick response, high power-to-weight, and power-to-volume ratios [7,8]. However, friction, compressed air, and material elasticity structure are the main drawbacks that restrict system performance and should be dedicatedly analyzed [9,10]. On the contrary, electro-hydraulic systems (EHSs) can remain a small size even when driving large and heavy loads due to their high-power-to-weight ratio, high stiffness compared with those of the EAs and PAs [11,12]. Although the EHSs can enhance its workability of loading, control algorithm development for the EHSs is complicated and still a big challenge due to their characteristics such as nonlinear, coupled reaction, and parametric uncertainties.

The Backstepping technique (BSP), in recent years, has gained a vast attention due to its property of step-by-step recursive design for nonlinear feedback control. This process, in principle, is suitable for addressing nonlinear system dynamics, and matched and mismatched uncertainties [13]; thereby, achieving the stabilization and tracking performance. However, assumptions of slow-varying or constant uncertainties, which cannot be practically achieved, are required for designing adaptive laws. As a result, the BSP cannot guarantee the asymptotic convergence of tracking performance in the presence of matched and mismatched uncertainties, measurement noise or signals constraint [14]. Additionally,

classical BSP control executes derivatives of virtual stabilized control signals as requirement at each design step that results in increasing higher system-order. Meanwhile, the Sliding Mode Control (SMC) is known as fast response and strong robustness against perturbations such as matched and mismatched uncertainties, disturbances or noise. Using SMC is an effective way to reduce the high-order system to lower-order system. Therefore, the backstepping sliding mode control (BSMC) that reserves the advantages of both SMC and BSP control is appropriate methodology for high-order nonlinear systems like hydraulic manipulators or construction machineries where the actuator dynamics is included [15].

Although the BSMC algorithm can deal with system dynamics and uncertainties; nevertheless, this technique is only sensitive to mismatched uncertainties such as external disturbances or external interaction regarding sliding surface dynamics [16]. In terms of mismatched uncertainties, the sliding mode robust gains should be designed as large enough to cover the upper bound of mismatched uncertainties to guarantee the robustness. Thereby, chattering phenomenon may be executed since the fundamental idea of the robust gains is using discontinuous term to force the system's error state variables toward the sliding manifold [17]. In order to reduce chattering effect, the robust control gains value should be lowered, and the effect of the mismatched uncertainties should be eliminated. Disturbance estimator methodology is realized as a powerful tool to cancel out influences of the mismatched uncertainties through feedforward methodology [18,19]. The mismatched uncertainties exist in various forms such as external disturbances, external force interaction, or payload variation. Wonhee Kim et al. [20] proposed a disturbance observer (DO) in the form of a two-order high-pass filter to estimate the disturbances consisting of external load torque and constant friction. In [21,22], a nonlinear robust controller based on the DO was applied to improve the control accuracy of EHSs in which the DO was considered as a good compensation method to eliminate the effect of external disturbance and model uncertainties. In [23–26], the authors constructed a method based on extended state observers (ESOs) to estimate uncertain nonlinearities, parametric uncertainties, and external disturbances. The ESO-based control schemes are usually applied not only to give the system states but also estimate the uncertain terms and unknown disturbances by using extended states. In [24], the matched and unmatched disturbances of the hydraulic actuator were estimated by linear ESOs and then compensated by the proposed controller to reduce the effects of undesired disturbances. These results revealed that the estimation error converges to zero by increasing the observer bandwidth. In [23,25], the ESOs-based backstepping control algorithm was proposed to handle the load disturbance and mechanical dynamics uncertainties. In [26], the author combined the DO and ESO to simultaneously address the influence of matched and mismatched uncertainties of the EHS. The effect of uncertainties

is minimized depending on the accuracy of the estimation process. Practically, the estimated error between the unknown real and estimated uncertainties is always existing. Therefore, this error should be resolved by some adaptive laws, or intelligent technique to enhance system qualification.

Although the tracking performance could be achieved, all automatically controlled systems may be inevitably subjected to faults caused by system element, actuator or sensor in practice. The actuator and sensor faults are more popular due to the coupled association with the control algorithms design. As the highly coupled nonlinear characteristics, the actuator fault causes obvious effects on the system dynamics; therefore, they can be easily detected through monitoring abnormal system performances. Following the literature of actuator fault detection and isolation and estimation, such fault can be considered as matched or mismatched disturbances and observed by using observers such as ESO [26–28], DO [15], [29–31], uncertainty and disturbance estimator (UDE) [32,33], time-delayed estimation (TDE) [34–36], super-twisting algorithm [37], Kalman estimators [38], unknown input observer [39, 40], etc. Then, Fault-tolerant control (FTC) that combines these observers compensation with advanced control algorithms such as active disturbance rejection control (ADRC) [41,42], adaptive algorithms [43–45], or passive FTC with high robust gains can be employed to address the influence of the actuator fault. Meanwhile, the sensor fault is generated from unknown constant or time-variant offset added to the measured signal and does not cause obvious influences. Due to the additive measurements, the system behavior is the same as the fault-free condition, but the measured feedback signal cannot present the true value of the system states. However, wrong feedback signal results in an unsuitable execution in terms of physical interactions; thus, being able to cause severe problems such as system performance deterioration and instability, loss of information fidelity unless promptly addressing [46]. Therefore, the main objective of the sensor fault detection is to critically achieve a fast and reliable sensor fault detection and estimation. Various methodologies for this topic were proposed. Nguyen et al. [47,48] employed a nonlinear UIO to detect the sensor fault on the mini motion package EHS. Nahian et al. [49] used an extended Kalman-Bucy unknown input observer to detect the sensor fault and estimate the system state and developed an FTC for the EHS. Brambilla et al [50] and Capisani et al [51] conducted a bank of observers based on the SMO for sensor fault detection and isolation on serial manipulators. Pang et al. constructed an active FTC with the SMO to address the influence of sensor fault on automobile active suspension systems. Paviglianiti et al. [52] proposed a robust fault detection based on traditional Luenberger observer to detect and isolate the sensor faults on multi-output system. Various approaches can be referred from [53–55]. The UIO and SMO are usually employed for fault detection and isolation; however, the complicated calculation using LMI, and requirement of coordinate

transformation increase the difficulty for high-order nonlinear systems. The sensor faults, in another aspect, can be considered as extended states of the controlled system. Therefore, this motivates us to propose a simple robust fault detection methodology based on ESO to achieve fast and reliable estimation of the signal residual fault for designing an active FTC.

The currently growing attractiveness in field of industrial applications such as polishing, welding, wiping, assembling, etc. reasonably results in requirements of workability in constrained framework. Following the literature of robotic manipulators in the relevant fields, many scholars proposed methods to improve system performance and reliability such as using force estimation [56–58], adaptive laws or intelligent techniques [59–61] in terms of force tracking performance, or estimation of environment characteristics [62], force dynamics observers [63–65], and impedance behaviors [66,67] for enhancing system reliability. Generally, hybrid position/force control, impedance, and/or admittance controls which are directly involved in force regulation are frequently applied to deal with problems of physical interactions. Despite achieving good outcomes, safety operation of the manipulator in cases of sudden contact-loss due to moving out the constrained framework, step-change of environment, accidentally unloading or payload drop is rarely mentioned. Stability, robustness, and especially safety are mandatory requirements when the robot is in interacting with the environment.

1.2 Research objectives

Motivated by the aforementioned problems, the main objectives of this dissertation are to provide dedicated dynamics analysis and control strategy of n-degree-of-freedom (n-DOF) serial hydraulic manipulator including actuator dynamics for realistic industrial applications point of view.

The proposed methodology design process and its effectiveness are apparently discussed for specific tasks in free motion and constrained framework. At first, the characteristics of the highly nonlinear system with coupled parameters are specified by mathematical equations. Regarding the mathematical model, a control strategy is developed based on sliding mode controller and the backstepping technique with disturbance estimator and adaptive laws to cancel out effect of matched and mismatched, system parametric uncertainties, as well as model error. They help to improve the effectiveness and robustness of system performance against perturbations. Then, a modified impedance control based on passivity and virtual energy tank concept is developed to solve a problem of sudden contact-loss in constrained framework. The system stability is theoretically proven by Lyapunov approach. In order to demonstrate the effectiveness, and robustness of the advanced methodology,

simulations and experiments have been conducted on three DOF and six DOF serial hydraulic manipulators subject to free motion and constrained framework, respectively.

In detail, the motivations of this dissertation have come from:

(1) Requirement of understanding and solving existing problems of highly nonlinear system under the presence of external disturbance and uncertainties. The investigated system includes manipulator dynamics and hydraulic actuator dynamics. In the hydraulic dynamics, valve-controlled EHS dynamics for rotary actuators and cylinder actuators are presented with parametric uncertainties and leakages. The manipulator dynamics is expressed with modeling error, unknown friction, and external disturbances.

(2) Estimating and compensating both mismatched and matched uncertainties in the hydraulic manipulator to achieve high system performance. For these purposes, disturbance estimators based on generalized momentum observer, and extended state observer are employed and compared to estimate external force interaction. With this outcome, the advanced control based on backstepping sliding mode control technique integrated with fuzzy logic control is designed to exhibit high tracking requirement. Besides, initial control parameters are also determined by using neural network.

(3) Requirement of addressing sensor fault problem. This fault type, generated from constant or time-variant offset added to the measured signal, does not cause obvious effects on the system behavior. In this case, the system behavior is the same as the fault-free condition, but the measured feedback signal cannot present the true value of the system states. Therefore, a robust fault estimation should be designed to obtain the actual system behavior with high accuracy and robustness.

(4) Practical applications in term of robot-environment interaction. In this scenario, the modified impedance control based on a virtual energy tank and concept of passivity control is developed to not only achieve force tracking control in constrained framework, but also keep the manipulator from damage in a case of sudden contact-loss due to moving out of working surface. Besides, A modified trajectory algorithm is developed to achieve smooth transient movement after contact-loss happens.

(5) Requirement of the robustness of the adaptive algorithm and system stability.

1.3 Limitations

In this study, the advanced methodology with disturbance estimator are examined on n-DOF serial hydraulic manipulator under the presence of modeling error, unknown friction, matched and mismatched uncertainties. The verifications are implemented in both simulations and experiments subject to free motion and constrained framework. However, some limitations of the dissertation are still existing as follows:

- The proposed control methodology is constructed based on assumption that most system dynamics such as link frame, hydraulic circuit specification, components and actuators parameters are all supposed to be well-known. Indeed, those parameters should be identified since exact model parameters are not available for investigation.
- The disturbance estimator integrated with control strategy is constructed to estimate and compensate effects of uncertainties that are assumed to be unknown but bounded, and their estimated errors (between the real and estimated variables) are also assumed to be bounded for choosing the robust control gains.
- The dynamics of drivers and electric component is derived as simplified linear function.
- Since the main concern of this dissertation is applicability of the proposed control strategy for real implementation, the advanced control structure is very simple based on basic sliding mode control and backstepping technique with disturbance estimator and fuzzy logic control.
- All the researches are conducted in specified scenarios.
- The robust fault estimation algorithm and the modified impedance control for contact-loss scenario are only verified by simulations.

1.4 Dissertation outline

The research outline of this dissertation is arranged as follows:

Chapter 1 introduces motivations, research objectives, limitations and outline of this dissertation.

Chapter 2 presents some mathematic notions and Lyapunov stability theories.

Chapter 3 derives an adaptive backstepping sliding mode control algorithm for n-DOF serial hydraulic manipulator including actuator dynamics. The system modeling including actuator dynamics is dedicatedly derived and the backstepping sliding mode control algorithm for the MIMO system is designed. Besides, adaptive laws are explained to deal with system parametric uncertainties. The overall system stability is theoretically proven by using Lyapunov approach.

Chapter 4 verifies an adaptive fuzzy backstepping sliding mode control for a 3-DOF serial hydraulic manipulator including actuator dynamics with generalized momentum observer subjects to external payload variation in free motion. The proposed control is also developed based on backstepping background. The generalized momentum observer is utilized to estimate the payload through its influence on each joint torque. Moreover, the fuzzy logic control is designed to compensate the estimated error.

Chapter 5 introduces the impedance control and involves in addressing the problem of matched and mismatched and sensor faults in which the measured variables are offset by unknown faulty signals

during constrained motion. In order to achieve the system stability and for safe operation, the robust fault estimation based on Extended state observer is proposed to estimate both measured, actual, and faulty signals. Then the fault-tolerant control is constructed based on the estimated parameters. The stability of the closed-loop system is theoretically proven by Lyapunov theorem. Several case studies are given to verify the workability of the proposed control scheme.

Chapter 6 concerns impedance control for a 6-DOF serial hydraulic manipulator subjects to contact-loss consideration in constrained motion. The contact-loss situation is addressed by a modified impedance control methodology based on virtual energy tank and passivity control scheme. Shock due to contact-loss is also mentioned with fading technique. Moreover, extended state observer is also employed to estimate environment force interaction.

In Chapter 7, discussions of the proposed methodology for industrial application point of view are provided for future development.

CHAPTER 2
Mathematical preliminaries

2.1 Introduction

In this chapter, mathematic notions are presented for control methodology design in the latter chapters. They can be realized in most mathematics books [68]. Additionally, preliminaries of control theories are also described as the background for the theoretical development later.

2.2 Mathematic

2.2.1 Vector and matrices analysis

Consider matrix $\mathbf{P} \in R^{m\times n}$, with $p_{ij(i=1,...,m)(j=1,...,n)}$ is an element in i^{th} row, j^{th} column of the matrix **P**. A transpose matrix of **P** is determined by interchanging the rows and columns of the matrix **P** and denoted as $\mathbf{P}^T \in R^{n\times m}$. The transpose operation has some properties as

Property 2-1:

- $\left(\mathbf{P}^T\right)^T = \mathbf{P}$
- $\left(\alpha\mathbf{P}\right)^T = \alpha\mathbf{P}^T$
- $\left(\mathbf{P}+\mathbf{Q}\right)^T = \mathbf{P}^T + \mathbf{Q}^T$, with $\mathbf{Q} \in R^{m\times n}$ and α is a scalar.
- $\left(\mathbf{PQ}\right)^T = \mathbf{Q}^T\mathbf{P}^T$
- $\mathbf{P}^T\mathbf{P}$ is a square matrix
- If all element of the matrix **P** is real, then the matrix $\mathbf{P}^T\mathbf{P}$ is a semi-positive definite

Property 2-2: Consider a square matrix $\mathbf{P} \in R^{n\times n}$, then:

- **P** is a symmetric matrix if $\mathbf{P}^T = \mathbf{P}$
- **P** is a skew matrix if $\mathbf{P}^T = -\mathbf{P}$
- $\mathbf{P}+\mathbf{P}^T$ is a symmetric matrix
- $\mathbf{P}-\mathbf{P}^T$ is a skew matrix
- **P** is a diagonal matrix if $p_{ij} = 0, \forall i \neq j$. In this case, the matrix **P** can be presented as $\mathbf{P} = diag\left(p_{11} \quad p_{22} \quad ... \quad p_{ii} \quad ... \quad p_{nn}\right)$
- **P** is an identity matrix (unit matrix) if $p_{ii} = 1, \forall i \in [1, n]$
- **P** is a null matrix if $p_{ij} = 0, \forall i, j$
- $\det\left(\mathbf{P}^T\right) = \det\left(\mathbf{P}\right)$

The square matrix $\mathbf{P} \in R^{n\times n}$ is non-singular (or invertible) if and only if $\exists \mathbf{Q} \in R^{n\times n}$ such that $\mathbf{PQ} = \mathbf{QP} = \mathbf{I}_n$, where $\mathbf{I}_n$ is an n-by-n identity matrix. In this result, **Q** is defined as an inverse of **P**, and is presented as $\mathbf{Q} = \mathbf{P}^{-1}$. The non-singular square matrix P has the following properties:

Property 2-3:

- $\det\left(\mathbf{P}^T\right) = \det\left(\mathbf{P}\right) \neq 0$
- $\left(\mathbf{P}^{-1}\right)^{-1} = \mathbf{P}$
- $\left(\mathbf{P}^T\right)^{-1} = \left(\mathbf{P}^{-1}\right)^T$
- $\left(\alpha\mathbf{P}\right)^{-1} = \frac{1}{\alpha}\mathbf{P}^{-1}, \forall \alpha \in R, \alpha \neq 0$
- $\left(\mathbf{PQ}\right)^{-1} = \mathbf{Q}^{-1}\mathbf{P}^{-1}$, with $\mathbf{Q} \in R^{n\times n}$ is non-singular square matrix

Property 2-4: Consider a square matrix $\mathbf{P} \in R^{n\times n}$, and a vector $\mathbf{x} \in R^n$. The matrix **P** is

- positive definite if $\forall \mathbf{x} \neq 0, \mathbf{x}^T\mathbf{P}\mathbf{x} > 0$
- semi-positive definite if $\forall \mathbf{x} \neq 0, \mathbf{x}^T\mathbf{P}\mathbf{x} \geq 0$
- negative definite if $\forall \mathbf{x} \neq 0, \mathbf{x}^T\mathbf{P}\mathbf{x} < 0$.
- semi-negative definite if $\forall \mathbf{x} \neq 0, \mathbf{x}^T\mathbf{P}\mathbf{x} \leq 0$

2.2.2 Vectors and matrices differential calculus

Consider a vector $\mathbf{x} \in R^n$ and a differentiable function $f\left(x\right): R^n \to R$. The gradient vector is obtained as

$$\nabla f = \frac{\partial}{\partial x} f\left(x\right) = \left(\frac{\partial f}{\partial x_1} \quad \frac{\partial f}{\partial x_2} \quad \ldots \quad \frac{\partial f}{\partial x_i} \quad \ldots \quad \frac{\partial f}{\partial x_n} \right)^T \in R^n \tag{2.1}$$

Then, the Hessian matrix is obtained if f is twice differentiable as

$$\mathbf{H}f = \frac{\partial^2}{\partial x^2} f\left(x\right) = \begin{pmatrix} \frac{\partial^2 f}{\partial x_1^2} & \frac{\partial^2 f}{\partial x_1 \partial x_2} & \cdots & \frac{\partial^2 f}{\partial x_1 \partial x_i} & \cdots & \frac{\partial^2 f}{\partial x_1 \partial x_n} \\ \frac{\partial^2 f}{\partial x_2 \partial x_1} & \frac{\partial^2 f}{\partial x_2^2} & \cdots & \frac{\partial^2 f}{\partial x_2 \partial x_i} & \cdots & \frac{\partial^2 f}{\partial x_2 \partial x_n} \\ \vdots & \vdots & \ddots & \vdots & \vdots & \vdots \\ \frac{\partial^2 f}{\partial x_i \partial x_1} & \frac{\partial^2 f}{\partial x_i \partial x_2} & & \frac{\partial^2 f}{\partial x_i^2} & & \frac{\partial^2 f}{\partial x_i \partial x_n} \\ \vdots & \vdots & & \vdots & \ddots & \vdots \\ \frac{\partial^2 f}{\partial x_n \partial x_1} & \frac{\partial^2 f}{\partial x_n \partial x_2} & \cdots & \frac{\partial^2 f}{\partial x_n \partial x_i} & \cdots & \frac{\partial^2 f}{\partial x_n^2} \end{pmatrix} \in R^{n\times n} \tag{2.2}$$

Consider matrix $\mathbf{P} \in R^{m\times n}$, with element $p_{ij}, q_{ij}\left(i = 1,\ldots,m\right)\left(j = 1,\ldots,n\right)$ is a function of $x \in R$, then:

$$\frac{d}{dx}\mathbf{P}(x)=\begin{pmatrix} \frac{dp_{11}}{dx} & \frac{dp_{12}}{dx} & \cdots & \frac{dp_{1j}}{dx} & \cdots & \frac{dp_{1n}}{dx} \\ \frac{dp_{21}}{dx} & \frac{dp_{22}}{dx} & \cdots & \frac{dp_{2j}}{dx} & \cdots & \frac{dp_{2n}}{dx} \\ \vdots & \vdots & \ddots & \vdots & \vdots & \vdots \\ \frac{dp_{i1}}{dx} & \frac{dp_{i1}}{dx} & & \frac{dp_{ij}}{dx} & & \frac{dp_{in}}{dx} \\ \vdots & \vdots & & \vdots & \ddots & \vdots \\ \frac{dp_{m1}}{dx} & \frac{dp_{m2}}{dx} & \cdots & \frac{dp_{mj}}{dx} & \cdots & \frac{dp_{mn}}{dx} \end{pmatrix} \in R^{m\times n} \tag{2.3}$$

Consider matrix **P**, **Q**, with elements p_{ij}, q_{ij} are a function of $x \in R$, then:

$$\frac{d}{dx}(\mathbf{P}+\mathbf{Q})=\frac{d\mathbf{P}}{dx}+\frac{d\mathbf{Q}}{dx}, \forall \mathbf{P},\mathbf{Q}\in R^{m\times n} \tag{2.4}$$

$$\frac{d}{dx}(\mathbf{PQ})=\frac{d\mathbf{P}}{dx}\mathbf{Q}+\mathbf{P}\frac{d\mathbf{Q}}{dx},\ \forall \mathbf{P}\in R^{m\times n},\mathbf{Q}\in R^{n\times m} \tag{2.5}$$

$$\frac{d}{dx}(\mathbf{PQ})=\frac{d\mathbf{P}}{dx}\mathbf{Q}+\mathbf{P}\frac{d\mathbf{Q}}{dx},\ \forall \mathbf{P}\in R^{m\times n},\mathbf{Q}\in R^{n\times m} \tag{2.6}$$

$$\begin{aligned}\frac{d}{dt}(\mathbf{x}^T\mathbf{P}\mathbf{x})&=\frac{d\mathbf{x}^T}{dt}\mathbf{P}\mathbf{x}+\mathbf{x}^T\frac{d\mathbf{P}}{dt}\mathbf{x}+\mathbf{x}^T\mathbf{P}\frac{d\mathbf{x}}{dt}\\ &=2\frac{d\mathbf{x}^T}{dt}\mathbf{P}\mathbf{x}+\mathbf{x}^T\frac{d\mathbf{P}}{dt}\mathbf{x}, \forall \mathbf{P}\in R^{n\times n},\mathbf{x}\in R^n, t\in R\end{aligned} \tag{2.7}$$

$$\frac{d}{d\mathbf{x}}(\mathbf{x}^T\mathbf{P}\mathbf{x})=2\mathbf{P}\mathbf{x}, \forall \mathbf{P}\in R^{n\times n},\mathbf{x}\in R^n, \text{ } \mathbf{P} \text{ is independent on } \mathbf{x} \tag{2.8}$$

2.2.3 Vector and matrix norms

2.2.3.1 Vector norms

Consider a vector $\mathbf{x}\in R^n$, then the vector norm induced by the *p*-norm is defined as

$$\|\mathbf{x}\|_p=\left(\sum_{i=1}^{n}|x_i|^p\right)^{\frac{1}{p}} \text{ with } 1\le p\le\infty \tag{2.9}$$

Particularly, the norm of vector $\mathbf{x}\in R^n$ is:

$$\begin{aligned}&\|\mathbf{x}\|_p=\|\mathbf{x}\|_1=\sum_{i=1}^{n}|x_i| \text{ when } p=1 \text{ } (l_1 \text{ norm on } R^n)\\ &\|\mathbf{x}\|_p=\|\mathbf{x}\|_2=\sqrt{\sum_{i=1}^{n}|x_i|^2} \text{ when } p=2 \text{ } (l_2 \text{ norm on } R^n)\\ &\|\mathbf{x}\|_p=\|\mathbf{x}\|_\infty=\max(|x_i|), \text{ with } 1\le i\le\infty, \text{ when } p=\infty \text{ } (l_\infty \text{ norm on } R^n)\end{aligned} \tag{2.10}$$

l_2 norm on R^n can be called as Euclidean norm. All norms are equivalent (here is two norms $\|\mathbf{x}\|_{p1}$ and $\|\mathbf{x}\|_{p2}$ for instance) if $\exists m,n>0$ such that $m\|\mathbf{x}\|_{p1} \le \|\mathbf{x}\|_{p2} \le n\|\mathbf{x}\|_{p1}$ with $\mathbf{x} \in R^n$.

2.2.3.2 Matrix norms

Consider a square matrix $\mathbf{P} \in R^{m\times n}$, then the matrix norm induced by the p-norm of vector $\mathbf{x} \in R^n$ is defined as

$$\|\mathbf{P}\|_p = \sup_{\mathbf{x}\neq 0} \frac{\|\mathbf{P}\mathbf{x}\|_p}{\|\mathbf{x}\|_p} = \sup_{\|\mathbf{x}\|_p=1} \|\mathbf{P}\mathbf{x}\|_p, \text{ with } 1 \le p \le \infty \tag{2.11}$$

Particularly, when p = 1, 2, ∞, norm of matrix M is calculated as

$$\begin{cases} \|\mathbf{P}\|_1 = \max\limits_{1\le j\le n} \sum\limits_{i=1}^{n} |a_{ij}| \\ \|\mathbf{P}\|_2 = \sqrt{\lambda_{\max}\left(\mathbf{P}^T\mathbf{P}\right)} \\ \|\mathbf{P}\|_\infty = \max\limits_{1\le i\le n} \sum\limits_{i=1}^{n} |a_{ij}| \end{cases} \tag{2.12}$$

2.2.3.3 Eigen value of square matrix

Consider a square matrix $\mathbf{P} \in R^{m\times n}$ is a linear transformation of a vector $\mathbf{x} \in R^n$. A scalar λ is called the eigenvalue of $\mathbf{P}$ if $\mathbf{P}\mathbf{x} = \lambda\mathbf{x}$, or equivalent to $\det(\mathbf{P} - \lambda\mathbf{I}_n) = 0$. λ is presented as $\lambda(\mathbf{P})$. In the set of eigenvalues, maximum eigenvalue of the matrix $\mathbf{P}$ is denoted as $\lambda_{\max}(\mathbf{P})$, and minimum eigenvalue of the matrix $\mathbf{P}$ is denoted by $\lambda_{\min}(\mathbf{P})$.

2.2.4 Inequalities

2.2.4.1 Young's inequality

Let f be a real-valued, continuous, and strictly increasing function on $[0,c]$ with c > 0. If $f(0) = 0$, $a \in [0,c]$ and $b \in [0, f(c)]$, then:

$$\int_o^u f(x)\,dx + \int_o^b f^{-1}(x)\,dx \ge ab \tag{2.13}$$

Taking the particular function $f(x) = x^{p-1}$ gives the symmetric form:

$$\frac{a^p}{p} + \frac{b^q}{q} \ge ab \tag{2.14}$$

where $a,b>0$, $p,q>1$, and $\frac{1}{p}+\frac{1}{q}=1$.

Equality holds if and only if $b = f(a) \Leftrightarrow a^p = b^q$.

2.2.4.2 Rayleigh inequality

Consider a square matrix $\mathbf{P} \in R^{m \times n}$ and non-zero vector $\mathbf{x} \in R^n$, then:

$$\lambda_{\min} \|\mathbf{x}\|^2 \leq \mathbf{x}^T \mathbf{P} \mathbf{x} \leq \lambda_{\max} \|\mathbf{x}\|^2 \tag{2.15}$$

where $\lambda_{\min}$, $\lambda_{\max}$ are the lower bound and upper bound eigenvalues of the matrix **P**.

2.2.4.3 Lipschitz functions

Definition 2-1 [29]: A function *f* holds a Lipschitz condition on Ω with Lipschitz constant κ if:

$$\left\| f(t, x_1) - f(t, x_2) \right\|^2 \leq \kappa \|x_1 - x_2\|, \forall (t, x_1), (t, x_2) \in \Omega \tag{2.16}$$

Theorem 2.1 [29]: If $f(t, x)$ is piecewise continuous in t and satisfied a Lipschitz condition on a compact set containing $x(t_0)$, then there exists some $\delta > 0$ such that the initial value problem

$$\dot{x} = f(t, x), \text{ with } x(t_0) = x_0 \tag{2.17}$$

has a unique solution on $[t_0, t_0 + \delta]$.

2.3 Lyapunov stability theory

The Lyapunov stability approach has been widely employed in the design and analysis of the control systems. In order to guarantee closed-loop stability and boundedness of internal signals, all controllers proposed in this dissertation will be based on the careful mathematical proof through the Lyapunov or Lyapunov-like theories. In this section, we introduce the stability concept, based on Lyapunov stability theorems, for autonomous and non-autonomous systems and review the invariant set theorem to simplify the proof for asymptotical stability of autonomous systems. Additionally, a Lyapunov-like approach summarized in Barbalat's lemma will also be described [69].

2.3.1 Stability concepts for autonomous systems

Essentially, stability (also called stability in the sense of Lyapunov, or Lyapunov stability) means that the system trajectory can be kept arbitrarily close to the origin by starting sufficiently close to it. Then, the following explicit definitions are worthy for later use:

Definition 2-2: *An equilibrium state* $x = 0$ *is said to be stable if* $\forall R > 0, \exists r > 0$, *such that if* $\|x(0)\| < r$, *then* $\|x(t)\| < R, \forall t > 0, x(t) \in B_R$. *Otherwise, the equilibrium point is unstable*.

Definition 2-3: *An equilibrium state* $x = 0$ *is asymptotically stable if it is stable, and* if $\exists r > 0$ *such that* $\|x(0)\| < r \Rightarrow \lim x(t) \rightarrow 0$ as $t \rightarrow \infty$. *Asymptotic stability means that the equilibrium is stable, and that in addition, states started close to* 0 *actually converge to* 0 *as time t goes to infinity*.

Definition 2-4: *An equilibrium state* $x = 0$ *is exponentially stable if there exist two strictly positive numbers* $\alpha, \lambda > 0$ *such that* $\|x(t)\| \leq \alpha \|x(t_0)\| e^{-\lambda t}$, $\forall t \geq 0$, *in some ball* B_r *around the origin*.

Definition 2-5: *If asymptotic* (*or exponential*) *stability holds for any initial states, the equilibrium point is said to be asymptotically* (*or exponentially*) *stable in the large*. *It is also called globally asymptotically* (*or exponentially*) *stable*.

It is also noteworthy to point out that, since the autonomous systems behavior is independent of the initial time, all the stability properties of an autonomous system are uniform.

More formally, the definition states that the origin is stable, if, given that we do not want the state trajectory $x(f)$ to get out of a ball of arbitrarily specified radius B_r, a value $r(R)$ can be found such that starting the state from within the ball B_r at time 0 guarantees that the state will stay within the ball B_r thereafter as shown in Figure 2-1.

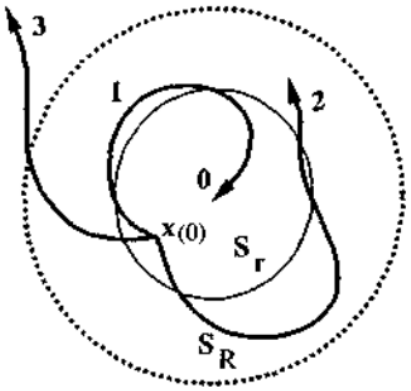

Figure 2-1 Concept of stability illustrations: curve 1 - asymptotically stable, curve 2 - marginally stable, curve 3 – unstable [69].

2.3.2 Stability concepts for non-autonomous systems

Non-autonomous systems are presented in the form:

$$\dot{x} = f(x,t) \tag{2.18}$$

where equilibrium state x^* is defined as

$$f(x^*,t) = 0, \forall t \geq t_0 \tag{2.19}$$

The concepts of stability for non-autonomous systems are quite similar to those of autonomous systems. However, due to the dependence of non-autonomous system behavior on initial time t_0, the definitions of these stability concepts include t_0 explicitly.

Definition 2-6: *The equilibrium state is* <u>*stable*</u> *at* t_0 if $\forall R \geq 0, \exists r(R,t_0) > 0$ *such that* $\|x(t_0)\| < r \Rightarrow \|x(t)\| < R, \forall t \geq t_0$. *Otherwise the equilibrium point is unstable*.

Definition 2-7: *The equilibrium state is locally uniformly stable if the scalar r in* ***Definition*** 2-6 *can be chosen independently of* t_0 , i.e., $\forall R>0, \exists r(R)>0$ *such that* $\|x(t_0)\|<r \Rightarrow \|x(t)\|<R, \forall t \geq t_0$.

Definition 2-8: *The equilibrium state is asymptotically stable at time* t_0 *if it is stable and* $\exists r(t_0)>0$ *such that* $\|x(t_0)\|<r(t_0) \Rightarrow \|x(t)\| \to 0$ as $t \to \infty$.

Definition 2-9: *The equilibrium state at the origin is locally uniformly asymptotically stable if it is uniformly stable, and* $\exists B_{R0}$, *whose radius is independent of* t_0 , *then* $\forall R_1, R_2>0$ satisfying $0<R_2<R_1 \leq R_0$, $\exists T(R_1,R_2)>0$ such that $\forall t_0>0, \|x(t_0)\|<R_1 \Rightarrow \|x(t)\|<R_2, \forall t \geq t_0+T(R_1,R_2)$.

Definition 2-10: *The equilibrium state is exponentially stable if* $\exists \alpha, \lambda>0$, *such that for sufficiently small* $x(t_0)$, $\|x(t)\| \leq \alpha \|x(t_0)\| e^{-\lambda(t-t_0)}, \forall t \geq t_0$.

Definition 2-11: *The equilibrium state is globally asymptotically stable if* $\forall x(t_0), \lim x(t_0) \to 0$, as $t \to \infty$.

2.3.3 Lyapunov stability theorems

Consider a continuous function α: $R^+ \to R^+$. the function α is said to be of class *K* (or to belong to class *K*), if:

$$\begin{gathered} \alpha(0) = 0 \\ \alpha(k) > 0,\ \forall k > 0 \\ \alpha \text{ is non-decreasing, i.e., } \alpha(k_1) \leq \alpha(k_2), \forall k_1 \leq k_2 \end{gathered} \tag{2.20}$$

A continuous function $V(x,t)$: $R^n \times R^+ \to R$ is:

- Locally (or globally) positive definite if, and only if, $\exists\, \alpha \in$ K such that $V(0,t) = 0$ and $V(x,t) \geq \alpha(\|x(t)\|), \forall t \geq 0 \cap \forall x \in B_{R0}$ (or the whole state space).
- Locally (or globally) decrescent if and only if $\exists\, \beta \in$ K such that $V(0,t) = 0$ and $V(x,t) \leq \beta(\|x(t)\|), \forall t \geq 0 \cap \forall x \in B_{R0}$ (or the whole state space).
- Radially unbounded $\lim V(x,t) \to \infty$ uniformly in time as $x \to \infty$.

Consider an autonomous system with equilibrium point. In a neighborhood of the equilibrium point, consider a scalar continuous function $V(x,t)$ with continuous first order derivatives and a class-K function α. The origin equilibrium point is

- Lyapunov stable if there exists a positive definite function $V(x,t)$ with a non-positive derivative, i.e., $V(x,t) \geq \alpha \|x(t)\|, \forall x \neq 0$ and $\dot{V}(x,t) \leq 0$.
- uniformly stable if: $\alpha \|x(t)\| \leq V(x,t) \leq \beta \|x(t)\|, \forall x \neq 0$ and $\dot{V}(x,t) \leq 0$

- uniformly asymptotic stable if there exists a positive definite and decrescent function $V(x,t)$ with a negative definite derivative, i.e., $\alpha\|x(t)\| \le V(x,t) \le \beta\|x(t)\|, \forall x \ne 0$ and $\dot{V}(x,t) < 0$
- globally uniformly asymptotically stable if: $\alpha\|x(t)\| \le V(x,t) \le \beta\|x(t)\|, \forall x \ne 0$, $\dot{V}(x,t) < 0$, and $\lim V(x,t) \to \infty$ uniformly in time as $x \to \infty$
- exponentially stable if, and only if, there exists a function $V(x, t)$ and strictly positive constants $\alpha_1, \alpha_2, \alpha_3, \alpha_4$ such that $\forall t \ge 0 \cap \forall x \in B_{R0}$, $\alpha_1\|x(t)\|^2 \le V(x,t) \le \alpha_2\|x(t)\|^2$, $\dot{V}(x,t) \le -\alpha_3\|x(t)\|^2$, $\left\|\frac{\partial V}{\partial x}\right\| \le \alpha_4\|x(t)\|$.

2.3.4 Lyapunov stability using Barbalat's lemma

The Barbalat's lemma states that if the differentiable function $f(t)$ has a finite limit as $t \to \infty$, and if $\dot{f}(t)$ is uniformly continuous, then $\dot{f}(t) \to 0$ as $t \to \infty$. Given the simple sufficient condition for uniform continuity mentioned earlier, an immediate and practical corollary of Barbalat's lemma can be stated as follows: if the differentiable function $f(t)$ has a finite limit as $t \to \infty$, and $\ddot{f}(t)$ exists and is bounded, then $\dot{f}(t) \to 0$ as $t \to \infty$. In the Lyapunov stability, Barbalat's lemma can be applied in the fashion similar to La Salle's theorem.

CHAPTER 3
Dynamics of n-DOF Serial Hydraulic Manipulator Including Actuator Dynamics

3.1 Introduction

In this chapter, the dynamics of an n-degree-of-freedom (n-DOF) serial hydraulic manipulator including the actuator dynamics is analyzed for the adaptive backstepping sliding mode control (ABSMC) design subjects to matched and mismatched uncertainties. The first aim of this analysis comes from the fact that the actuator dynamics in traditional manipulator (conventionally using electric actuator) is usually excluded from the manipulator modeling to simplify the system dynamics and control design procedure. However, influences of uncertainties and nonlinear parameters availably existing inside the actuator may generate malfunctions and then execute unexpected motions and system stability unless consideration. This can be obviously observed when running hydraulic systems where the actuator dynamics is treated as important part to achieve more efficiency of system tracking performance. Then, in order to deal with the parametric uncertainties that exist in the actuator dynamic and guarantee the stability of the system, the ABSMC that takes advantage of the sliding mode control in strong robustness against perturbation and reducing the order system [70–72], and backstepping technique in recursive algorithm to solve the problem of the system stabilization and tracking performance [73–76] is dedicated designed with adaptive laws to lower influence of the actuator parametric uncertainties.

3.2 Problem formulation of n-DOF serial manipulator system

3.2.1 Mechanical structure of n-DOF serial hydraulic manipulator

An n-DOF serial hydraulic manipulator is structured as depicted in **Figure 3-1**.

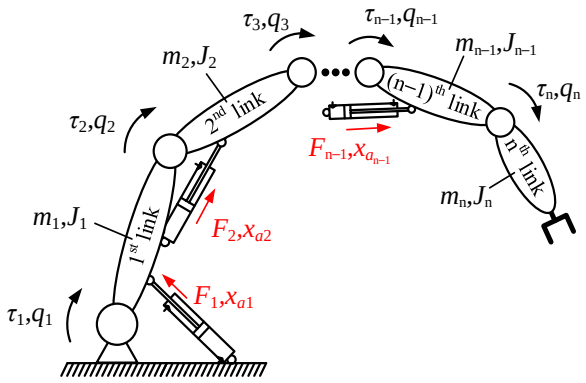

Figure 3-1 Structure of n-serial hydraulic manipulator

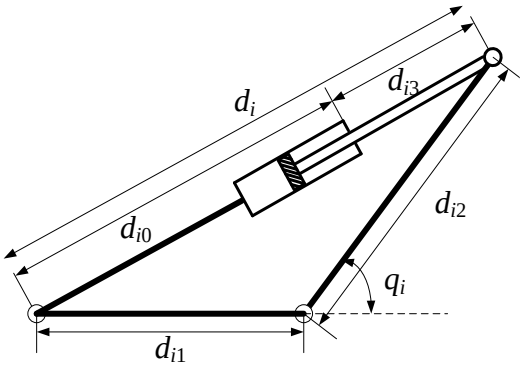

Figure 3-2 Closed-chain structure of the {i^{th}} joint.

The n-DOF serial hydraulic manipulator is structured by n-revolute joints. Regarding mechanical design for specific tasks, each joint is driven by either hydraulic rotary actuator or cylinder. In a case of using cylinder, force induced from cylinder is converted to torque through closed-chain; thereby, rotational motion of the joint is generated from movement of the cylinder as described in **Figure 3-2**.

The relationship motion between actuator space and joint space can be derived by [15]:

$$d_3 = d_0 - \sqrt{d_1^{\,2} + d_2^{\,2} - 2d_1 d_2 \cos(\pi - q_3)} \tag{3.1}$$

where d_0 is an initial length in case of maximum retracting, the positive direction in the actuator space is chosen such that extracting the piston. d_3 denotes length of the link under motion of the cylinder, d_1 and d_2 are fixed length of the hinge joints.

To obtain the correlational velocity between the actuator and the joint motion, taking derivative the Equation (3.1) yields:

$$\dot{d}_3 = \frac{\partial d_3}{\partial q_3}\dot{q}_3 = \frac{d_1 d_2 \sin(\pi - q_3)}{\sqrt{d_1^{\,2} + d_2^{\,2} - 2d_1 d_2 \cos(\pi - q_3)}}\dot{q}_3 \tag{3.2}$$

Let $J_{ai} = \dfrac{d_1 d_2 \sin(\pi - q_i)}{\sqrt{d_1^{\,2} + d_2^{\,2} - 2d_1 d_2 \cos(\pi - q_i)}}$, then Equation (3.2) is rewritten as

$$\dot{d}_3 = J_{a3}(q_3)\dot{q}_3 \tag{3.3}$$

where $J_{ai}(q_i)$ is Jacobian matrix of the {i^{th}} joint.

Thus, torque acting on this joint can be derived as

$$\tau_3 = J_{a3}^T(q_3)F_3 \tag{3.4}$$

3.2.2 Dynamics of n-DOF serial hydraulic manipulator

The manipulator dynamics is presented by:

$$\mathbf{M}(\mathbf{q})\ddot{\mathbf{q}} + \mathbf{C}(\mathbf{q},\dot{\mathbf{q}})\dot{\mathbf{q}} + \mathbf{G}(\mathbf{q}) + \boldsymbol{\Delta} + \mathbf{J}^T(\mathbf{q})\mathbf{F}_{ext} = \boldsymbol{\tau} \tag{3.5}$$

where $\mathbf{q},\dot{\mathbf{q}},\ddot{\mathbf{q}} \in R^n$ are position, angular velocity and angular acceleration vectors of each joint, respectively; $\mathbf{M}(\mathbf{q}) \in R^{n\times n}$ is the symmetric and positive definite matrix of nominal inertia; $\mathbf{C}(\mathbf{q},\dot{\mathbf{q}}) \in R^{n\times n}$ denotes the nominal Coriolis and Centrifugal term matrix; $\mathbf{G}(\mathbf{q}) \in R^n$ is the nominal gravity term; $\mathbf{\Delta} \in R^n$ denotes lumped parametric uncertainties, disturbances, and model error; $\mathbf{F}_{ext} \in R^n$ represents for external load induced from environment interaction in the end-effector; $\boldsymbol{\tau} \in R^n$ is the torque vectors acting on joints; $\mathbf{J}(\mathbf{q}) \in R^{n\times n}$ is the Jacobian matrix to transfer from Cartesian to manipulator joint-space as

$$\begin{aligned} \mathbf{x} &= f(\mathbf{q}) \\ \dot{\mathbf{x}} &= \frac{\partial f(\mathbf{q})}{\partial \mathbf{q}} = \mathbf{J}(\mathbf{q})\dot{\mathbf{q}} \end{aligned} \tag{3.6}$$

Property 3-1: $\dot{\mathbf{M}}(\mathbf{q}) - 2\mathbf{C}(\dot{\mathbf{q}},\dot{\mathbf{q}})$ *is a skew matrix that satisfies the condition* $\mathbf{X}^T\left(\dot{\mathbf{M}}(\mathbf{q}) - 2\mathbf{C}(\dot{\mathbf{q}},\dot{\mathbf{q}})\right)\mathbf{X} = 0$ *for any non-zero vector* $\mathbf{X} \in R^n$.

Property 3-2: *The inertia matrix* $\mathbf{M}(\mathbf{q}) \in R^{n\times n}$ *is a symmetric and positive definite matrix and is bounded as* $m_l \|\mathbf{X}\|^2 \le \mathbf{X}^T\mathbf{M}(\mathbf{q})\mathbf{X} \le m^u \|\mathbf{X}\|^2$, *in which* m_l *and* m^u *are lower and upper bound positive constants, respectively*.

Movements of each link are driven by an electro-hydraulic actuator. Due to its complicated characteristics, the actuator dynamics should be derived and included in the whole system dynamics. Define $\mathbf{x}_a = \begin{pmatrix} x_{a1} & x_{a2} & \dots & x_{a(n-1)} & x_{an} \end{pmatrix}^T \in R^n$ is a vector of actuator positions in the actuator-space. The actuator position can be relevant calculated from manipulator joint-space as

$$\begin{cases} \mathbf{x}_a = f_a(\mathbf{q}) \\ \dot{\mathbf{x}}_a = \mathbf{J}_a(\mathbf{q})\dot{\mathbf{q}} \end{cases} \tag{3.7}$$

where $\mathbf{J}_a$ is obtained from solving relationship between the actuator space and joint space as described in Equations (3.2) and (3.3). It is noteworthy that in case of rotary actuator, the joint space and actuator space is same if ignoring differences due to mechanical designs. In this case, the Jacobian element is one.

3.3 Problem formulation Electro-hydraulic system

3.3.1 Importance of the electro-hydraulic system

Electro-hydraulic systems (EHS) are considered as a good choice to replace the electric actuators and pneumatic actuators and are increasingly used in industries because of their high power to weight ratio and high stiffness [11,12]. Nevertheless, the EHS are complicated and still a big challenge because of their characteristics such as nonlinear and matched and mismatched parametric uncertainties.

Therefore, this sub-section aims at expressing mathematical formulation of the EHS for the development of control methodology based on BSMC to achieve high tracking performance subjects to matched and mismatched uncertainties. The dynamics of the EHS is derived based on fluid power theory in which all components and influences of factors such as frictions, external and internal leakages (i.e. matched uncertainties), external impacts (i.e. mismatched uncertainties) are taken into consideration.

The common circuit of the EHS consists of a hydraulic pump, filter, a safe relieve valve, a servo-valve, an actuator (rotary type or cylinder), and connecting-pipes as shown in **Figure 3-3**. This structure is concerned as valve-controlled electro-hydraulic system.

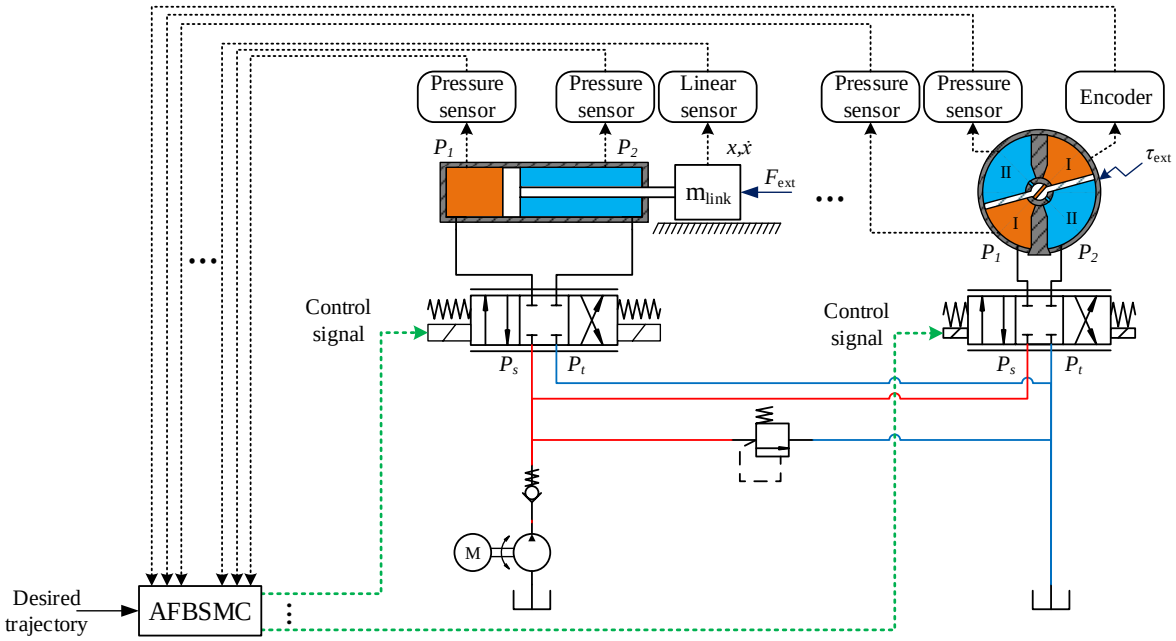

Figure 3-3 Working principle of electro-hydraulic system.

The operation of the hydraulic pump, normally driven by another electric motor, generates the pressurized hydraulic flow that drives the hydraulic actuator. The actuator behaviors (velocity, directional movement, environment interaction, etc.) are regulated through controlling the proportional servo-valve. The filter is to remove impurities of the fluid. The relieve valve is equipped to constrain the circuit pressure at a maximum level as safety operation. The fluid pressure supplied from the oil tank to the EHS is considered as P_s, and the fluid returning to the oil tank is denoted as P_t.

The hydraulic actuator can be classified as cylinder and rotary type. The rotary actuator generates rotational movement whereas the cylinder actuator generates translational movement. The dynamics of each type of hydraulic actuator should be dedicatedly presented for designing control algorithm.

3.3.2 Electro-hydraulic system dynamics modeling

Without losing the generality, let consider one element of the total robotic system. Then, the action torque on each joint actuator is expressed by [15]:

$$\tau_i = \begin{cases} A_{ri}(P_{ai1} - P_{ai2}) & (\text{for rotary actuator}) \\ J_{ai}^T(q)\left(A_{ai1}P_{ai1} - A_{ai2}P_{ai2}\right) & (\text{for cylinder}) \end{cases} \tag{3.8}$$

where A_{ri}, A_{ai1} and A_{ai2} are volumetric areas of rotary actuator and areas of piston head part and rod part of cylinders, respectively. P_{ai1} and P_{ai2} (i=1,2,…,n) are pressures of two chambers of each actuator.

These pressures are expressed as

$$\dot{P}_{ai1} = \frac{\beta}{V_{i1_0} + A_{ai1}x_{ai}}\left[\quad Q_{ai1} - A_{ai1}\frac{\partial x_{ai}}{\partial q_i}\dot{q}_i - C_{leak_i}\left(P_{ai1} - P_{ai2}\right)\right] \tag{3.9}$$

$$\dot{P}_{ai2} = \frac{\beta}{V_{i2_0} - A_{ai2}x_{ai}}\left[-Q_{ai2} + A_{ai2}\frac{\partial x_{ai}}{\partial q_i}\dot{q}_i + C_{leak_i}\left(P_{ai1} - P_{ai2}\right)\right] \tag{3.10}$$

where β is the effective bulk modulus, $V_{ij_0(j=1,2)}$ are initial volumes of the two chambers, $C_{leak,i}$ is internal leakage coefficient, and $Q_{aij}\left(t\right)_{(j=1,2)}$ represent for two flows in to and out of the two chambers.

Assumption 3-1: *Only internal leakage of the actuator is considered in this paper*. *The external leakage, and other parametric uncertainties or model errors are ignored*. *Moreover, the leakage is supposed to be proportional to load pressure as expressed in Equations* (3.9) *and* (3.10).

These flows are expressed as [77]

$$Q_{ai1} = C_d\omega x_{svi}\left(s(x_{svi})\sqrt{\frac{2}{\rho}\left(P_s - P_{ai1}\right)} + s(-x_{svi})\sqrt{\frac{2}{\rho}\left(P_{ai1} - P_t\right)}\right) \tag{3.11}$$

$$Q_{ai2} = C_d\omega x_{svi}\left(s(x_{svi})\sqrt{\frac{2}{\rho}\left(P_{ai2} - P_t\right)} + s(-x_{svi})\sqrt{\frac{2}{\rho}\left(P_s - P_{ai2}\right)}\right) \tag{3.12}$$

where C_d is the discharge coefficient, ω is the valve orifice area gradient, ρ is the density of oil, and x_{svi} is the spool motion of the i^{th} valve. $s\left(x_{svi}\right)=1$ if $x_{svi}>0$ and $s\left(x_{svi}\right)=0$ when $x_{svi}<0$ is a function to determine direction of the spool valve for obtaining flow rate through a proportional valve.

The hydraulic power supply is calculated from pressure supply and pressurized flow rate as

$$P_{power} = \frac{P_s Q}{\eta_v \eta_m} \tag{3.13}$$

where Q is pump flow rate; η_v and η_m are volumetric and mechanical efficiencies, respectively.

The proportional valves, well-known as servo-valves, have one major concept in common: usually the output variable, i.e., spool valve position (directional valves), pressure (pressure valve), or flow (flow valves), is proportional to the input signal. The input signal can be manual, mechanical, pneumatic or electrical. Modern servo and proportional valve system often use a low-power electrical analogue or digital signal. The fundamental principle of operation of proportional valves is based on the use of a proportional solenoid, which moves the valve spool to the desired position, as shown in **Figure 3-4**. The servo-valves are high-sophisticated control valves, usually applied in closed-loop control arrangements, they must have very accurate metering dimensions, and thus often involve high installation and purchasing costs.

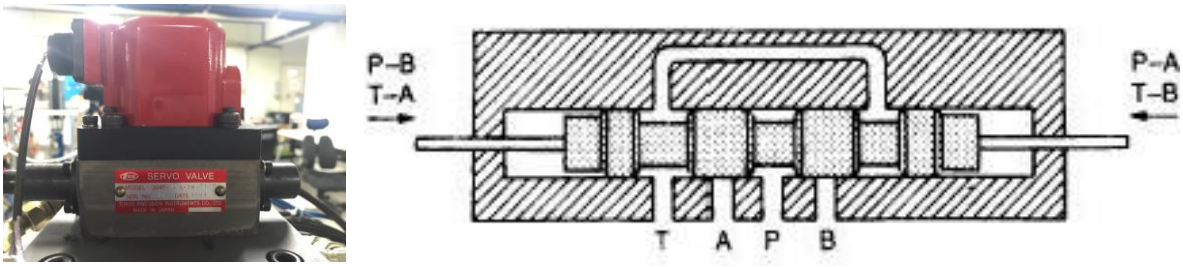

Figure 3-4 three-land-four-way servo valve (a) real 4/3 servo valve, and (b) servo valve schematic.

The dynamic behavior of the valves can be approximated by a second-order model as follows:

$$\ddot{x}_{sv} + 2\omega_{sv}\zeta_{sv}\dot{x}_{sv} + \omega_{sv}^2 x_{sv} + f_{sv} sign\left(\dot{x}_{sv}\right) + K_v u \tag{3.14}$$

where $x_{sv}, \dot{x}_{sv}, \ddot{x}_{sv}$ are spool valve position, velocity, and acceleration, respectively; u is voltage input signal; K_v is the valve gain; ω_{sv} is the valve natural frequency; ζ_{sv} is damping coefficient; and the parameter f_{sv} considers the valve hysteresis and response sensitivity.

The motions of the valve are constrained by:

$$\begin{cases} \left|x_{sv}\right| \le x_{sv,\max} \\ \left|\dot{x}_{sv}\right| \le \dot{x}_{sv,\max} \\ \left|\ddot{x}_{sv}\right| \le \ddot{x}_{sv,\max} \end{cases} \tag{3.15}$$

Remark 3-1: *Ignored the time-delay phenomenon in valve dynamics and its uncertainties, the spool displacement of the proportional valve can be simplified as a linear function of applied input voltage u* as $x_{sv} = K_v u$.

3.4 Comprehensive dynamics of the n-DOF serial hydraulic manipulator system

To conveniently derive the backstepping sliding mode algorithm, the dynamics of the manipulator including actuators is rewritten from Equation (3.5) and from Equations (3.9)–(3.12) as

$$\begin{cases} \dot{\mathbf{x}}_1 = \mathbf{x}_2 \\ \dot{\mathbf{x}}_2 = \mathbf{M}^{-1}(\mathbf{x}_1)\left(-\mathbf{C}(\mathbf{x}_1,\mathbf{x}_2)\mathbf{x}_2 - \mathbf{G}(\mathbf{x}_1) - \boldsymbol{\Delta} - \mathbf{J}^T\mathbf{F}_{ext} + \mathbf{J}_a^T\mathbf{x}_3\right) \\ \dot{\mathbf{x}}_3 = \mathbf{f}(\mathbf{x}_1,\mathbf{x}_2) + \mathbf{g}\mathbf{u} - \boldsymbol{\Psi}\mathbf{C}_{leak} \end{cases} \tag{3.16}$$

where $\mathbf{x} = \begin{pmatrix}\mathbf{x_1} & \mathbf{x_2} & \mathbf{x_3}\end{pmatrix}^T = \begin{pmatrix}\mathbf{q}^T & \dot{\mathbf{q}}^T & \left(\mathbf{A_{a1}P_{a1}} - \mathbf{A_{a2}P_{a2}}\right)\end{pmatrix}^T \in R^{3n}$ is a new state vector; $\mathbf{x}_1 = \begin{pmatrix}x_{11} & x_{12} & \ldots & x_{1i} & \ldots & x_{1n}\end{pmatrix}^T \in R^n$ is a vector of measurable joint angle (x_{1i} denotes the joint angle of joint i^{th}); $\mathbf{x}_2 = \begin{pmatrix}x_{21} & x_{22} & \ldots & x_{2i} & \ldots & x_{2n}\end{pmatrix}^T \in R^n$ is a vector of joint velocity (x_{2i} is the velocity of joint i^{th}); $\mathbf{A}_{a1} = diag\begin{pmatrix}A_{a11} & A_{a21} & \ldots & A_{ai1} & \ldots & A_{an1}\end{pmatrix} \in R^{n\times n}$; $\mathbf{A}_{a2} = diag\begin{pmatrix}A_{a12} & A_{a22} & \ldots & A_{ai2} & \ldots & A_{an2}\end{pmatrix} \in R^{n\times n}$; $\mathbf{P}_{a1} = \begin{pmatrix}P_{a11} & P_{a21} & \ldots & P_{ai1} & \ldots & P_{an1}\end{pmatrix}^T \in R^n$; $\mathbf{P}_{a2} = \begin{pmatrix}P_{a12} & P_{a22} & \ldots & P_{ai2} & \ldots & P_{an2}\end{pmatrix}^T \in R^n$; and $\mathbf{f}(\mathbf{x}_1,\mathbf{x}_2)$, $\mathbf{g}$, $\boldsymbol{\Psi}$, $\mathbf{C}_{leak}$ are defined as the following:

$$\mathbf{f}(\mathbf{x}_1,\mathbf{x}_2) \triangleq \begin{pmatrix} f_1(x_{11},x_{21}) & f_2(x_{12},x_{22}) & \ldots & f_i(x_{1i},x_{2i}) & \ldots & f_n(x_{1n},x_{2n})\end{pmatrix}^T \tag{3.17}$$

$$f_i(x_{1i},x_{2i}) = \left(-A_{ai1}\frac{\partial x_{ai}}{\partial q_i}\dot{q}_i\psi_{1i} - A_{ai2}\frac{\partial x_{ai}}{\partial q_i}\dot{q}_i\psi_{2i}\right) \tag{3.18}$$

$$\psi_{1i} = \frac{\beta A_{ai1}}{V_{i1_0} + A_{ai1}x_{ai}}, \psi_{2i} = \frac{\beta A_{ai2}}{V_{i2_0} + A_{ai2}(L_{ai} - x_{ai})} \tag{3.19}$$

$$\mathbf{g} \triangleq diag\begin{pmatrix}g_1 & g_2 & \ldots & g_i & \ldots & g_n\end{pmatrix} \tag{3.20}$$

$$\begin{aligned} g_i = {} & \psi_{1i}\left(s(x_{svi})\sqrt{\frac{2}{\rho}(P_s - P_{ai1})} + s(-x_{svi})\sqrt{\frac{2}{\rho}(P_{ai1} - P_t)}\right)C_d\omega K_{vi} \\ & + \psi_{2i}\left(s(x_{svi})\sqrt{\frac{2}{\rho}(P_{ai2} - P_t)} + s(-x_{svi})\sqrt{\frac{2}{\rho}(P_s - P_{ai2})}\right)C_d\omega K_{vi} \end{aligned} \tag{3.21}$$

$$\boldsymbol{\Psi} \triangleq diag\begin{pmatrix}\Psi_1 & \Psi_2 & \ldots & \Psi_i & \ldots & \Psi_n\end{pmatrix} \tag{3.22}$$

$$\Psi_i = \left((P_{ai1} - P_{ai2})\psi_{1i} + (P_{ai1} - P_{ai2})\psi_{2i}\right) \tag{3.23}$$

$$\mathbf{C}_{leak} \triangleq \begin{pmatrix}C_{leak,1} & C_{leak,2} & \ldots & C_{leak,i} & \ldots & C_{leak,n}\end{pmatrix}^T \tag{3.24}$$

To facilitate the control design, the following assumptions are presented:

Assumption 3-2: *The lumped mismatched uncertainties is supposed to vary slowly relative to the system dynamics, i.e.,* $\dot{\Delta} \approx 0$.

Assumption 3-3: *The lumped uncertainties is unknown but bounded by* $\|\Delta\| \le \bar{\Delta}$; *thus, its estimated error is bounded by pre-determined upper bound, i.e.,* $\left\|\tilde{\boldsymbol{\Delta}}\right\| = \left\|\boldsymbol{\Delta} - \hat{\boldsymbol{\Delta}}\right\| \le \bar{\delta}_{mismatched}$.

Assumption 3-4: *The internal leakage coefficient is supposed to vary slowly relative to the system dynamics, i.e.,* $\dot{C}_{leak,i} \approx 0$.

Assumption 3-5: *The internal leakage coefficient is unknown but bounded by* $\left|C_{leak,i}\right| \le \bar{C}_{leak,i}$. *Thus, the internal leakage is bounded by* $\left\|\mathbf{Q}_{leak}\right\| \le \bar{Q}_{leak}$. *Therefore, their estimated error are bounded by pre-determined upper bound, i.e.,* $\left\|\tilde{Q}_{leak}\right\| = \left\|\hat{Q}_{leak} - Q_{leak}\right\| \le \bar{\delta}_{matched}$.

3.5 Adaptive backstepping sliding mode control for n-DOF serial hydraulic manipulator

Regarding the system dynamics derived in the previous sub-section, the backstepping sliding mode control for an n-DOF system is designed. First, define state error as $\mathbf{e}_1 = \mathbf{x}_1 - \mathbf{x}_{1d} \in R^n$, and $\mathbf{e}_2 = \mathbf{x}_2 - \mathbf{x}_{2d} \in R^n$ where $\mathbf{x}_{1d}, \mathbf{x}_{2d} \in R^n$ are the vector of desired joint angles and angular velocities, respectively.

Step 1: the sliding surface and its derivative are designed as

$$\begin{cases} \mathbf{s}_1 = \mathbf{e}_2 + \boldsymbol{\lambda}_1 \mathbf{e}_1 \in R^n \\ \dot{\mathbf{s}}_1 = \dot{\mathbf{e}}_2 + \boldsymbol{\lambda}_1 \mathbf{e}_2 \in R^n \end{cases} \tag{3.25}$$

with $\boldsymbol{\lambda}_1 = diag\left(\lambda_{11} \quad \lambda_{12} \quad ... \quad \lambda_{1i} \quad ... \quad \lambda_{1n}\right) \in R^{n\times n}$ is the positive definite matrix.

A new equivalent variable is introduced as

$$\begin{cases} \mathbf{x}_{2s} = \mathbf{x}_2 - \mathbf{s}_1 = \mathbf{x}_{2d} - \boldsymbol{\lambda}_1 \mathbf{e}_1 \in R^n \\ \dot{\mathbf{x}}_{2s} = \dot{\mathbf{x}}_2 - \mathbf{s}_1 = \dot{\mathbf{x}}_{2d} - \boldsymbol{\lambda}_1 \mathbf{e}_2 \in R^n \end{cases} \tag{3.26}$$

Define $\hat{\boldsymbol{\Delta}}$ is an estimation of mismatched lumped uncertainties, and $\tilde{\boldsymbol{\Delta}} = \boldsymbol{\Delta} - \hat{\boldsymbol{\Delta}}$ is an estimated error between the actual and estimated lumped uncertainties. The estimation of the lumped uncertainties satisfies:

$$\dot{\hat{\boldsymbol{\Delta}}} = -\mathbf{s}_1 \tag{3.27}$$

Choose a Lyapunov candidate V_1 as

$$V_1 = \frac{1}{2}\mathbf{s}_1^T \mathbf{M} \mathbf{s}_1 + \frac{1}{2}\tilde{\boldsymbol{\Delta}}^T \tilde{\boldsymbol{\Delta}} \tag{3.28}$$

Taking derivative the Lyapunov candidate V_1, with Property 4-1 and substituting Equations (3.25) and (3.26) yields:

$$\dot{V}_1 = \mathbf{s}_1^T \left(\mathbf{x}_3 - \left(\tilde{\boldsymbol{\Delta}} + \hat{\boldsymbol{\Delta}}\right) - \mathbf{M}\left(\mathbf{x}_1\right)\dot{\mathbf{x}}_{2s} - \mathbf{C}(\mathbf{x}_1, \mathbf{x}_2)\mathbf{x}_{2s} - \mathbf{G}(\mathbf{x}_1) - \mathbf{J}\left(\mathbf{x}_1\right)^T \mathbf{F}_{ext}\right) + \dot{\tilde{\boldsymbol{\Delta}}}^T \tilde{\boldsymbol{\Delta}} \tag{3.29}$$

Define an error between an actual virtual torque $\mathbf{x}_3$ and desired torque $\mathbf{x}_{3d}$ as $\mathbf{e}_3 = \mathbf{x}_3 - \mathbf{x}_{3d} \in R^n$. Then the desired torque is designed as

$$\mathbf{x}_{3d} = \mathbf{M}\left(\mathbf{y}_1\right)\dot{\mathbf{x}}_{2s} + \mathbf{C}(\mathbf{x}_1, \mathbf{x}_2)\mathbf{x}_{2s} + \mathbf{G}(\mathbf{x}_1) + \mathbf{J}\left(\mathbf{x}_1\right)^T \mathbf{F}_{ext} + \hat{\boldsymbol{\Delta}} - \mathbf{K}_1 \mathbf{s}_1 - \boldsymbol{\eta}_1 \tanh\left(\frac{\mathbf{s}_1}{\sigma_s}\right) \tag{3.30}$$

where $\mathbf{K}_1 = diag\left(K_{11} \;\; K_{12} \;\; ... \;\; K_{1i} \;\; ... \;\; K_{1n}\right)$ and $\boldsymbol{\eta}_1 = diag\left(\eta_{11} \;\; \eta_{12} \;\; ... \;\; \eta_{1i} \;\; ... \;\; \eta_{1n}\right)$ are n-by-n positive definite matrices. The term $-\mathbf{K}_1\mathbf{s}_1$ is added to enhance the convergence rate when $\mathbf{s}_1$ is large; $\tanh\left(\frac{\mathbf{s}_1}{\sigma_s}\right) = \left(\tanh\left(\frac{s_{11}}{\sigma_s}\right) \;\; \tanh\left(\frac{s_{12}}{\sigma_s}\right) \;\; ... \;\; \tanh\left(\frac{s_{1n}}{\sigma_s}\right)\right)^T \in R^n$ with s_{1i} is the sliding surface of joint i^{th} and σ_s is an arbitrarily small value.

Remark 3-2: *The term* $-\boldsymbol{\eta}_1 \tanh\left(\mathbf{s}_1/\sigma_s\right)$ *is employed instead of using signum function, i.e.,* $-\boldsymbol{\eta}_1 sign\left(\mathbf{s}_1\right)$ *because this discontinuous function is un-differentiable. Therefore, to closely achieve the robustness, small value of gain* σ_s *is chosen.*

Substituting Equation (3.30) into Equation (3.29) yields:

$$\dot{V}_1 = \mathbf{s}_1^T\left(\mathbf{J}_a^T\mathbf{e}_3 - \mathbf{K}_1\mathbf{s}_1 - \boldsymbol{\eta}_1 \tanh\left(\frac{\mathbf{s}_1}{\sigma_s}\right) - \tilde{\boldsymbol{\Delta}}\right) + \dot{\tilde{\boldsymbol{\Delta}}}^T\tilde{\boldsymbol{\Delta}} \tag{3.31}$$

Substituting the adaptive law in Equation (3.27) yields:

$$\dot{V}_1 \le \mathbf{s}_1^T\left(\mathbf{J}_a^T\mathbf{e}_3 - \mathbf{K}_1\mathbf{s}_1 - \boldsymbol{\eta}_1 \tanh\left(\frac{\mathbf{s}_1}{\sigma_s}\right) + \bar{\delta}_{mismatched}\right) \tag{3.32}$$

Remark 3-3: *The aim of using the adaptive law in Equation* (3.27) *is to cancel out influences of the lumped uncertainties to force the model as same as an ideal model. In practical simulation, to enhance the convergence rate of estimation, this equation is modified as*

$$\dot{\hat{\boldsymbol{\Delta}}} = -\mathbf{K}_{s1}\mathbf{s}_1 - \boldsymbol{\eta}_{s1} sign\left(\mathbf{s}_1\right) \tag{3.33}$$

where $\mathbf{K}_{s1}, \boldsymbol{\eta}_{s1} \in R^{n\times n}$ *are diagonal positive definite matrices of learning rate to increase the convergence rate of the estimated lumped uncertainties.*

Remark 3-4: *Regarding Assumption* 3-3, *the lumped uncertainties* $\boldsymbol{\Delta}$ *is unknown but bounded and its estimated error is also bounded by* $\left\|\tilde{\boldsymbol{\Delta}}\right\| = \left\|\boldsymbol{\Delta} - \hat{\boldsymbol{\Delta}}\right\| \le \bar{\delta}_{mismatched}$ *, then the term,* $\boldsymbol{\eta}_1$ *is chosen to be greater than the upper bound of the estimated error, i.e.,* $\eta_{1i} \ge \bar{\delta}_{mismatched,i}$ *. This means the controller gains are much smaller instead of designing with large value enough to cover the upper bound of uncertainties in the conventional design.*

From Equation (3.32), the derivative of the Lyapunov function V_1 is semi-negative if the error $\mathbf{e}_3$ converges to zero. Therefore, this error should be compensated so as to keep the torque error as small as possible.

Step 2: Define the sliding surface as

$$\mathbf{s}_2 = \mathbf{e}_3 + \boldsymbol{\lambda}_2 \int \mathbf{e}_3 \in R^n \tag{3.34}$$

where $\boldsymbol{\lambda}_2 = diag\left(\lambda_{21} \;\; \lambda_{22} \;\; ... \;\; \lambda_{2i} \;\; ... \;\; \lambda_{2n}\right) \in R^{n\times n}$ is a positive matrix definite.

This step is designed to deal with the actuator dynamics. Regarding the third equation of (3.16), the internal leakage term, $Q_{leak,i} = C_{leak,i}\left(P_{ai1} - P_{ai2}\right)$, cannot be measured; then, this term should be estimated using adaptive law. Define the $\tilde{\boldsymbol{\Delta}}_{leak} = \hat{\mathbf{Q}}_{leak} - \mathbf{Q}_{leak}$ as the estimated error between the estimated and actual internal leakage.

Taking derivative the sliding surface $\mathbf{s}_2$, one obtains:

$$\dot{\mathbf{s}}_2 = \dot{\mathbf{e}}_3 + \boldsymbol{\lambda}_2\mathbf{e}_3 = f\left(\mathbf{x}_1, \mathbf{x}_2\right) + \mathbf{g}\mathbf{u} + \boldsymbol{\psi}\mathbf{Q}_{leak} - \dot{\mathbf{x}}_{3d} + \boldsymbol{\lambda}_2\mathbf{e}_3 \tag{3.35}$$

Choosing the second Lyapunov function V_2 as

$$V_2 = V_1 + \frac{1}{2}\mathbf{s}_2^T\mathbf{s}_2 + \frac{1}{2}\tilde{\boldsymbol{\Delta}}_{leak}^T\tilde{\boldsymbol{\Delta}}_{leak} \tag{3.36}$$

Taking derivative of the Lyapunov function V_2 and substituting Equation (3.35) yields:

$$\begin{aligned}\dot{V}_2 = \mathbf{s}_1^T\left(\mathbf{J}_a^T\mathbf{e}_3 - \mathbf{K}_1\mathbf{s}_1 - \boldsymbol{\eta}_1\tanh\left(\frac{\mathbf{s}_1}{\sigma_s}\right) + \tilde{\boldsymbol{\delta}}_{mismatched}\right) \\ + \mathbf{s}_2^T\left(\mathbf{f}\left(\mathbf{x}_1, \mathbf{x}_2\right) + \mathbf{g}\mathbf{u} + \boldsymbol{\psi}\mathbf{Q}_{leak} - \dot{\mathbf{x}}_{3d} + \boldsymbol{\lambda}_2\mathbf{e}_3\right) + \tilde{\boldsymbol{\Delta}}_{leak}^T\dot{\tilde{\boldsymbol{\Delta}}}_{leak}\end{aligned} \tag{3.37}$$

To guarantee the system robustness and global stability, the control input signal **u** is designed as

$$\mathbf{u} = \mathbf{g}^{-1}\left(-\mathbf{f}\left(\mathbf{x}_1, \mathbf{x}_2\right) + \boldsymbol{\psi}\hat{\mathbf{Q}}_{leak} + \dot{\mathbf{x}}_{3d} - \mathbf{K}_2\mathbf{s}_2 - \boldsymbol{\eta}_2\tanh\left(\frac{\mathbf{s}_2}{\sigma_s}\right) - \mathbf{J}_a^T\mathbf{s}_1 - \boldsymbol{\lambda}_2\mathbf{e}_3\right) \tag{3.38}$$

where $\mathbf{K}_2 \triangleq diag\left(K_{21} \;\; K_{22} \;\; ... \;\; K_{2i} \;\; ... \;\; K_{2n}\right)$ and $\boldsymbol{\eta}_2 \triangleq diag\left(\eta_{21} \;\; \eta_{22} \;\; ... \;\; \eta_{2i} \;\; ... \;\; \eta_{2n}\right)$ are n-by-n positive definite matrices. The term $-\mathbf{K}_2\mathbf{s}_2$ is added to enhance the convergence rate when $\mathbf{s}_2$ is large. A function $\tanh\left(\frac{\mathbf{s}_i}{\sigma_s}\right) = \left(\tanh\left(\frac{s_{i1}}{\sigma_s}\right) \;\; \tanh\left(\frac{s_{i2}}{\sigma_s}\right) \;\; ... \;\; \tanh\left(\frac{s_{in}}{\sigma_s}\right)\right)^T \in R^n$ (i=1,2) in both Equations (3.30) and (3.38) are used to replace a conventional signum function to achieve chattering free.

Hence, the derivative of the Lyapunov function V_2 becomes:

$$\begin{aligned}\dot{V}_2 = -\mathbf{s}_1^T\mathbf{K}_1\mathbf{s}_1 - \mathbf{s}_1^T\left(\boldsymbol{\eta}_1\tanh\left(\frac{\mathbf{s}_1}{\sigma_s}\right) - \tilde{\mathbf{F}}_{ext}\right) - \mathbf{s}_2^T\mathbf{K}_2\mathbf{s}_2 - \mathbf{s}_2^T\boldsymbol{\eta}_2\tanh\left(\frac{\mathbf{s}_2}{\sigma_s}\right) \\ - \mathbf{s}_2^T\boldsymbol{\psi}\tilde{\boldsymbol{\Delta}}_{leak} + \tilde{\boldsymbol{\Delta}}_{leak}^T\dot{\tilde{\boldsymbol{\Delta}}}_{leak} - \mathbf{s}_1^T\mathbf{J}_a^T\boldsymbol{\lambda}_2\int\mathbf{e}_3\end{aligned} \tag{3.39}$$

To achieve system performance as an ideal model, the term $-\mathbf{s}_2^T\boldsymbol{\psi}\tilde{\boldsymbol{\Delta}}_{leak} + \tilde{\boldsymbol{\Delta}}_{leak}^T\dot{\tilde{\boldsymbol{\Delta}}}_{leak}$ should be cancelled out. Therefore, the following adaptive law is satisfied:

$$\dot{\hat{C}}_{leak,i} = \begin{cases}\eta_{leak,i}\dfrac{s_{2i}\psi_i}{\left(P_{ai1} - P_{ai2}\right)}, & \text{if } P_{ai1} \neq P_{ai2} \\ 0 & \text{otherwise}\end{cases} \tag{3.40}$$

Remark 3-5: *The adaptive law, presented in Equation* (3.40)*, is considered in the steady state, i.e., all parameters are in equilibrium points. In other words, the constant values of pressures and actual leakage coefficient are exhibited; therefore, their derivative are zero, i.e.,* $\dot{\hat{C}}_{leak,i} = \dot{P}_{ai1} = \dot{P}_{ai2} = 0$. *This assumption is to facilitate the control strategy design and verify the effectiveness of using BSMC. Indeed, applying this adaptive law is difficult to accurately estimate the matched uncertainties since these parameters are time-variant. Therefore, the use of an observer, will be presented in the later chapters, is preferable to obtain accurate estimations.*

Remark 3-6: *The aim of using the adaptive law in* Equation (3.40) *is to cancel out influences of the leakage to achieve the ideal model with no uncertainties or disturbances. In practical simulation, to enhance the convergence rate of estimation, this equation is modified as*

$$\dot{\hat{\mathbf{C}}}_{leak,i} = \boldsymbol{\eta}_{leak}\boldsymbol{\psi} diag\left(\left(\mathbf{P}_{a1} - \mathbf{P}_{a2}\right)^{-1}\right)\mathbf{s}_2 + \boldsymbol{\eta}_{leak,s}\boldsymbol{\psi} diag\left(\left(\mathbf{P}_{a1} - \mathbf{P}_{a2}\right)^{-1}\right) sign\left(\mathbf{s}_2\right) \tag{3.41}$$

where $\boldsymbol{\eta}_{leak}$ and $\boldsymbol{\eta}_{leak,s}$ are n-by-n diagonal positive definite matrices to adjust the convergence rate of the estimation; $sign\left(\mathbf{s}_2\right) = \left(sign\left(s_{21}\right) \quad sign\left(s_{22}\right) \quad ... \quad sign\left(s_{2n}\right)\right)^T \in R^n$.

Remark 3-7: *Regarding Assumption 3-5, the estimated error of the leakage coefficient is bounded by* $\left\|\tilde{\boldsymbol{\Delta}}_{leak}\right\| = \left\|\hat{\mathbf{Q}}_{leak} - \mathbf{Q}_{leak}\right\| \le \left\|\boldsymbol{\delta}_{matched}\right\|_\infty \le \bar{\delta}_{matched}$. *Then the robust matrix gain* $\boldsymbol{\eta}_2$ *is chosen to be greater than the error of estimated leakage coefficient, i.e.,* $\eta_{2i} \ge \bar{\delta}_{matched}$. *This means the controller gains are much smaller instead of designing with large value enough to cover the upper bound of uncertainties in conventional design.*

Consequently, the derivative of Lyapunov function V_2 becomes:

$$\dot{V}_2 = -\mathbf{s}_1^T\mathbf{K}_1\mathbf{s}_1 - \mathbf{s}_1^T\left(\boldsymbol{\eta}_1 \tanh\left(\frac{\mathbf{s}_1}{\sigma_s}\right) - \tilde{\mathbf{F}}_{ext}\right) - \mathbf{s}_2^T\mathbf{K}_2\mathbf{s}_2 - \mathbf{s}_2^T\boldsymbol{\eta}_2 \tanh\left(\frac{\mathbf{s}_2}{\sigma_s}\right) - \mathbf{s}_1^T\mathbf{J}_a^T\boldsymbol{\lambda}_2\int\mathbf{e}_3 \tag{3.42}$$

$$\dot{V}_2 = -S^T\boldsymbol{\Omega}S - \mathbf{s}_1^T\left(\boldsymbol{\eta}_1 \tanh\left(\frac{\mathbf{s}_1}{\sigma_s}\right) - \tilde{\mathbf{F}}_{ext}\right) - \mathbf{s}_2^T\boldsymbol{\eta}_2 \tanh\left(\frac{\mathbf{s}_2}{\sigma_s}\right) \tag{3.43}$$

where $S = \begin{pmatrix} \mathbf{s}_1 \\ \int\mathbf{e}_3 \\ \mathbf{e}_3 \end{pmatrix}$ and $\boldsymbol{\Omega} = \begin{bmatrix} \mathbf{K}_1 & \frac{1}{2}\mathbf{J}_a^T\boldsymbol{\lambda}_2 & \mathbf{0}_n \\ \frac{1}{2}\mathbf{J}_a^T\boldsymbol{\lambda}_2 & \mathbf{K}_2\boldsymbol{\lambda}_2^2 & \mathbf{K}_2\boldsymbol{\lambda}_2 \\ \mathbf{0}_n & \mathbf{K}_2\boldsymbol{\lambda}_2 & \mathbf{K}_2 \end{bmatrix}$.

Hence, in order to guarantee the system stability and robustness, the robust matrices $\mathbf{K}_1, \mathbf{K}_2$ and slope $\boldsymbol{\lambda}_2$ should be carefully designed such that the matrix $\boldsymbol{\Omega}$ is semi-positive definite; therefore, the $\dot{V}_2$ becomes semi-negative definite. In the special case, when $\boldsymbol{\lambda}_2$ is zero, the second sliding surface is simplified as a torque tracking error, i.e., $\mathbf{s}_2 = \mathbf{e}_3$. Then, $\dot{V}_2$ becomes:

$$\dot{V}_2 = -\mathbf{s}_1^T\mathbf{K}_1\mathbf{s}_1 - \mathbf{s}_1^T\left(\boldsymbol{\eta}_1 \tanh\left(\frac{\mathbf{s}_1}{\sigma_s}\right) - \tilde{\mathbf{F}}_{ext}\right) - \mathbf{s}_2^T\mathbf{K}_2\mathbf{s}_2 - \mathbf{s}_2^T\boldsymbol{\eta}_2 \tanh\left(\frac{\mathbf{s}_2}{\sigma_s}\right) \le 0 \tag{3.44}$$

as long as *Assumptions* 3-2 to 3-5 and *Remarks* 3-4 and 3-7 are hold.

Remark 3-8: *In practical system, the position of the end-effector can be calculated from angular position of each joint. These values can be directly measured by using encoders. However, angular and acceleration are not available. Conventionally, these variables are obtained from taking derivative of joint angles and thereby, measured noises are also amplified. To effectively estimate unmeasurable variables for designing the controller, a second-order exact differentiation (SOED) is utilized as*

$$\begin{cases} \dot{\boldsymbol{\upsilon}}_1 = \mathbf{f}_1 \\ \mathbf{f}_1 = -\boldsymbol{\kappa}_1 \left|\boldsymbol{\upsilon}_1 - \mathbf{q}\right|^{2/3} sign\left(\boldsymbol{\upsilon}_1 - \mathbf{q}\right) + \boldsymbol{\upsilon}_2 \\ \dot{\boldsymbol{\upsilon}}_2 = \mathbf{f}_2 \\ \mathbf{f}_2 = -\boldsymbol{\kappa}_2 \left|\boldsymbol{\upsilon}_2 - \mathbf{f}_1\right|^{1/2} sign\left(\boldsymbol{\upsilon}_2 - \mathbf{f}_1\right) + \boldsymbol{\upsilon}_3 \\ \dot{\boldsymbol{\upsilon}}_3 = -\boldsymbol{\kappa}_3 sign\left(\boldsymbol{\upsilon}_2 - \mathbf{f}_1\right) \end{cases} \tag{3.45}$$

where $\boldsymbol{\upsilon}_1, \boldsymbol{\upsilon}_2, \boldsymbol{\upsilon}_3$ *are estimated values of* $\mathbf{q}, \dot{\mathbf{q}}, \ddot{\mathbf{q}}$, respectively. *Then the estimation of* $\boldsymbol{\upsilon}_2, \boldsymbol{\upsilon}_3$ *can converge to true velocity and acceleration in finite time by choosing suitable values of observer gains* $\boldsymbol{\kappa}_1, \boldsymbol{\kappa}_2, \boldsymbol{\kappa}_3$ [29,78–80].

Remark 3-9: *It should be noted that all estimated errors of the SOED can achieve finite-time convergence no matter what a control input signal is. This implies that the SOED observer can be designed separately to the main controller and thereby, a full state is available for designing control signals.*

Remark 3-10: *Generally, increasing those observer gains* $\boldsymbol{\kappa}_1, \boldsymbol{\kappa}_2, \boldsymbol{\kappa}_3$ *results in faster convergence. However, large values of observer gain also result in more noise influence. Too large or too small values of observer gains may lead to overshoot. Therefore, the values of all observer gains* $\boldsymbol{\kappa}_1, \boldsymbol{\kappa}_2, \boldsymbol{\kappa}_3$ *should be chosen based on carefully tuning. Adaptive laws for automatically adjusting observer gains are not considered as the main scope in this scope.*

As shown in Equation (3.44), $\dot{V}_2(\mathbf{s}_1, \mathbf{s}_2)$ is a negative-definite function, i.e., $V_2(\mathbf{s}_1(t), \mathbf{s}_2(t)) \le V_2(\mathbf{s}_1(0), \mathbf{s}_2(0))$. It means that $\mathbf{s}_1$ and $\mathbf{s}_2$ are bounded. Let a function $P_{v2} = -\mathbf{s}_1^T\mathbf{K}_1\mathbf{s}_1 - \mathbf{s}_2^T\mathbf{K}_2\mathbf{s}_2 \le \dot{V}_2$ and integrate function P_{v2} with respect to time.

$$\int_0^t P_{v2}(\tau)\, d\tau \le V_2(s_1(0), s_2(0)) - V_2(s_1(t), s_2(t)) \tag{3.46}$$

Because $V_2(\mathbf{s}_1(0), \mathbf{s}_2(0))$ is a bounded function, and $V_2(\mathbf{s}_1(t), \mathbf{s}_2(t))$ is non-increasing and bounded, so:

$$\lim_{t\to\infty}\int_0^t P_{v2}(\tau)d\tau < \infty \tag{3.47}$$

Additionally, $\dot{P}_{v2}$ is also bounded, by Barbalat's lemma [13], it can be shown that $\lim_{t\to\infty}\int_0^t P_{v2}(\tau)d\tau \to 0$ and the sliding variable constants are chosen to satisfy the Hurwitz theorem. They mean that the vectors $\mathbf{s}_1(t),\mathbf{s}_2(t),\mathbf{e}_1(t),\mathbf{e}_2(t)$ will converge to zero as $t\to\infty$.

3.6 Remained problems and discussion

Although the adaptive laws are designed to reduce influences of matched and mismatched uncertainties, they cannot track exactly the actual value since their calculations are directly based on the errors of tracking performance. Besides, the external force disturbance is supposed to be measured, then it is directly feedback to the controller design. If the external force is lumped into the mismatched uncertainties, the adaptive law, essentially, can also satisfy. However, in practical, these estimated errors are minimized such that they tend to zero under the regulation of the advanced control with adaptive laws but cannot be equal to zero at all time. Moreover, since the system state tracking errors oscillates around zero, then the tracking performance of the lumped mismatched uncertainties also oscillates around their real values. This implies that the estimated state cannot be accurately estimated even when increasing large updating gains. Therefore, another method like using specific observer should be considered to exhibit more precise estimation of the external force disturbance.

CHAPTER 4
Verification of n-DOF Serial Hydraulic Manipulator in Free Motion

4.1 Introduction

In this chapter, the effectiveness of the adaptive backstepping sliding mode control (BSMC) is verified in a particular 3-Degree-of-freedom (3-DOF) serial hydraulic manipulator subjects to external payload variation. As discussed in Subsection 3.5 of the previous chapter, this chapter presents a methodology in which the ABSMC is integrated with fuzzy logic control (FLC) and generalized momentum observer (GMO) to cope with influence of the external payload variations (i.e. mismatched disturbance). Besides, the control gains of the BSMC is dedicatedly initialized based on using a neural network with back-propagation process. Due to coupled characteristics of the system, the external payload generates homologous torque disturbances that systematically affects torque command of each joint. Regarding this phenomenon, the GMO is employed to estimate the torque disturbance and subtract it from the torque command signals through feedforward control. The FLC is utilized to compensate the deviation of the actual and estimated torque disturbances. The whole closed-loop system stability and its robustness are theoretically proved by Lyapunov approach. In order to verify the effectiveness of the proposed methodology, several comparative simulations and experiments between the proposed algorithm with other conventional controllers are implemented.

4.2 Structure of the 3-DOF Serial hydraulic manipulator

The structure of the 3-DOF serial hydraulic manipulator is displayed in **Figure 4-1** [15]. This manipulator belongs to 3-RRR manipulator (three revolute joints) that is constructed with three hydraulic actuators. Two rotary actuators are utilized to drive the first and second joints whereas the third joint is driven by a cylinder through close-chained structure. The link frame of the 3-DOF serial hydraulic manipulator is shown in **Figure 4-2**.

4.3 Adaptive fuzzy backstepping sliding mode control with disturbance observer

This subsection presents the adaptive fuzzy BSMC with disturbance observer (DOAFSMC) in which the ABSMC methodology is once again designed with integration of the DO-based generalized momentum observer (GMO) and fuzzy logic control (FLC) for system tracking performance. The stability of the whole system is mathematically proved and evidenced through comparative simulations and experiments.

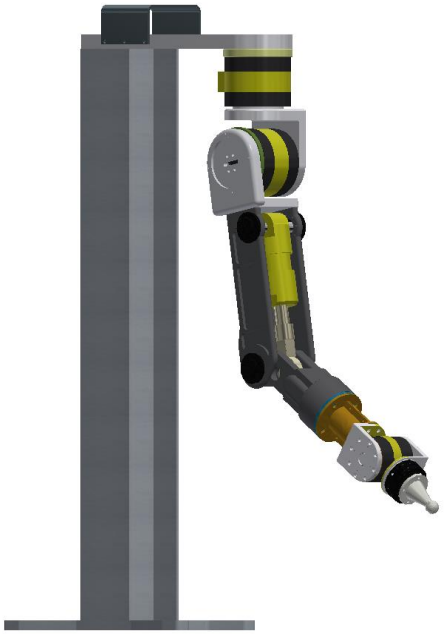

Figure 4-1 Structure of the 3-DOF serial hydraulic manipulator.

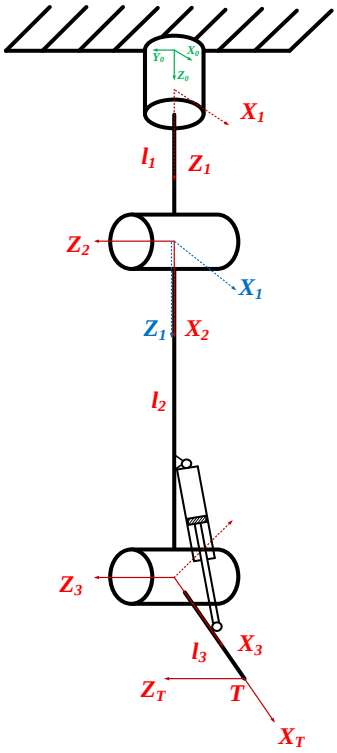

Figure 4-2 Link frame of the 3-DOF serial hydraulic manipulator.

4.3.1 Generalized momentum observer for force disturbance

The disturbance estimator-based generalized momentum observer (GMO) is normally used to estimate and eliminate the effect of external disturbance from the environment or some internal disturbance insider the system such as friction. The advantages of the disturbance observer are briefly shown in [19,31,81]. In this study, the GMO is used to observe the change of the external payload considered as an external disturbance.

4.3.1.1 Model-based disturbance observer

Practically, the manipulator behavior gets influenced by interactions from environment, or external disturbances uncertainties such as noise, external force, payload variation, or modeling error that distorts the robot orbit. These issues exist in any automatic systems; thus, dealing with these one is critical that can improve the system qualification.

According to [15], The manipulator dynamics can be generally expressed by:

$$\mathbf{M}(\mathbf{q})\ddot{\mathbf{q}} + \mathbf{C}(\mathbf{q},\dot{\mathbf{q}})\dot{\mathbf{q}} + \mathbf{G}(\mathbf{q}) + \boldsymbol{\Delta} + \mathbf{J}^T(\mathbf{q})\mathbf{F}_{ext} = \boldsymbol{\tau} \tag{4.1}$$

where $\mathbf{J}^T(\mathbf{q})\mathbf{F}_{ext}$ represents for external disturbance to be observed and eliminated for position tracking performance. From Equation (4.1), the lumped disturbance can be mathematically computed as

$$\mathbf{d} = \mathbf{M}(\mathbf{q})\ddot{\mathbf{q}} + \mathbf{D}(\mathbf{q},\dot{\mathbf{q}}) - \boldsymbol{\tau} \tag{4.2}$$

where $\mathbf{D}(\mathbf{q},\dot{\mathbf{q}}) = \mathbf{C}(\mathbf{q},\dot{\mathbf{q}})\dot{\mathbf{q}} + \mathbf{G}(\mathbf{q})$, $\mathbf{d} = \boldsymbol{\Delta} + \mathbf{J}^T(\mathbf{q})\mathbf{F}_{ext}$.

The disturbance observer for robotic manipulator is proposed as [19]. Let $\hat{\mathbf{d}}$ is a vector of estimated disturbance, then the estimated disturbance error is expressed as

$$\tilde{\mathbf{d}} = \mathbf{d} - \hat{\mathbf{d}} \tag{4.3}$$

The disturbance estimator is designed such that the estimated error dynamics

$$\dot{\tilde{\mathbf{d}}} + \mathbf{L}\tilde{\mathbf{d}} = 0 \tag{4.4}$$

zero as $t \to \infty$. Herein, $\mathbf{L} \in R^{n \times n}$ is observer matrix gain to be designed later.

Assumption 4-1: *The disturbance has slow time-varying relative to system dynamics, i.e.,* $\dot{\mathbf{d}} \approx 0$.

Assumption 4-2: *The estimated disturbance is unknown but bounded, i.e.,* $\left\|\tilde{\mathbf{d}}\right\| \le \left\|\tilde{\mathbf{d}}\right\|_\infty \le \bar{d}$ *. The upper bound* $\bar{d}$ *is theoretically supposed to be a pre-determined scalar.*

Assumption 4-3*: The derivative of an estimated disturbance is bounded, i.e.,* $\left\|\dot{\tilde{\mathbf{d}}}\right\| \le \left\|\dot{\tilde{\mathbf{d}}}\right\|_\infty \le \bar{\delta}_d$ *. The upper bound* $\bar{\delta}_d$ *is theoretically supposed to be a pre-determined scalar from the system and components characteristics.*

Then, Equation (4.4) is equivalent to

$$\dot{\hat{\mathbf{d}}} + \mathbf{L}\tilde{\mathbf{d}} = 0 \tag{4.5}$$

Finally, the adaptive laws for disturbance estimation is derived by:

$$\begin{aligned} \dot{\hat{\mathbf{d}}} &= -\mathbf{L}(\mathbf{q},\dot{\mathbf{q}})\hat{\mathbf{d}} + \mathbf{L}(\mathbf{q},\dot{\mathbf{q}})\left[\mathbf{M}(\mathbf{q})\ddot{q} + \mathbf{D}(\mathbf{q},\dot{\mathbf{q}}) - \boldsymbol{\tau}\right] \\ &= -\mathbf{L}(\mathbf{q},\dot{\mathbf{q}})\hat{\mathbf{d}} + \mathbf{L}(\mathbf{q},\dot{\mathbf{q}})\mathbf{d} \\ &= \mathbf{L}(\mathbf{q},\dot{\mathbf{q}})\tilde{\mathbf{d}} \end{aligned} \tag{4.6}$$

The idea of disturbance estimator lies on comparing the difference between the command input signal (joint torques) and system state to extract the unknown external disturbance.

4.3.1.2 Disturbance estimator-based generalized momentum observer technique

Regarding the obtained result in Equation (4.6), joint acceleration value is required for calculation. This is the main drawback of the methodology due to measured acceleration requirement. Without concerning cost, using accelerometers or relevant functional sensor is one solution for acceleration measurement; however, it cannot return exact value of real acceleration due to sensitive characteristic or effect of measurement noise. Levant's differentiator is a good robust calculator to provide high accurate estimated acceleration. Nevertheless, it is still difficult to practically achieve high accurate estimated value with second-order differentiation. Therefore, a momentum method is an alternative solution where information of acceleration is not required. The architecture of the GMO is displayed in **Figure 4-3**.

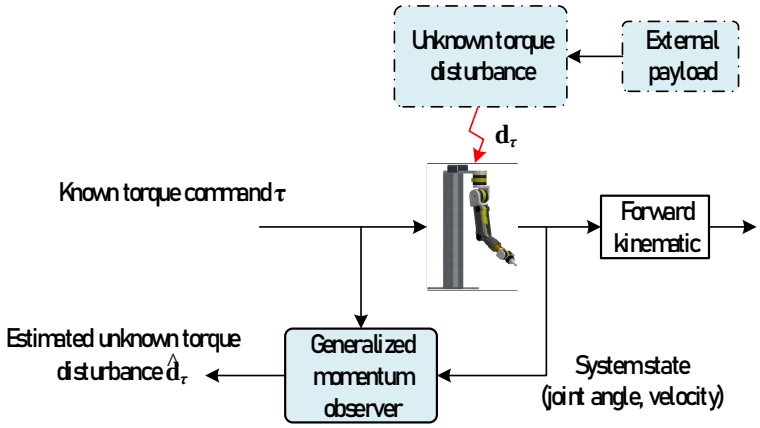

Figure 4-3 Architecture of the GMO for nonlinear systems.

First, let define auxiliary variable vector $\mathbf{z} \in R^n$ that satisfies:

$$\mathbf{z} = \hat{\mathbf{d}} - \mathbf{p}(\mathbf{q}, \dot{\mathbf{q}}) \tag{4.7}$$

where $\mathbf{p}(\mathbf{q}, \dot{\mathbf{q}}) \in R^n$ is a generalized momentum vector, defined by:

$$\frac{d}{dt}\left(\mathbf{p}(\mathbf{q}, \dot{\mathbf{q}})\right) = \mathbf{L}(\mathbf{q}, \dot{\mathbf{q}})\mathbf{M}(\mathbf{q})\ddot{\mathbf{q}} \tag{4.8}$$

where $\mathbf{L}(\mathbf{q}, \dot{\mathbf{q}}) \in R^{n \times n}$ is observer matrix gain to be determined.

Then, taking derivative Equation (4.7) yields:

$$\dot{\mathbf{z}} = \dot{\hat{\mathbf{d}}} - \frac{d}{dt}\left(\mathbf{p}(\mathbf{q}, \dot{\mathbf{q}})\right) \tag{4.9}$$

Combine with Equations (4.6), (4.8), Equation (4.9) becomes:

$$\dot{\mathbf{z}} = -\mathbf{L}(\mathbf{q},\dot{\mathbf{q}})\hat{\mathbf{d}} + \mathbf{L}(\mathbf{q},\dot{\mathbf{q}})\mathbf{d} - \mathbf{L}(\mathbf{q},\dot{\mathbf{q}})\mathbf{M}(\mathbf{q})\ddot{\mathbf{q}} \tag{4.10}$$

$$\Leftrightarrow \dot{\mathbf{z}} = -\mathbf{L}(\mathbf{q},\dot{\mathbf{q}})\hat{\mathbf{d}} + \mathbf{L}(\mathbf{q},\dot{\mathbf{q}})\left(\mathbf{M}(\mathbf{q})\ddot{\mathbf{q}} + \mathbf{D}(\mathbf{q},\dot{\mathbf{q}}) - \boldsymbol{\tau}\right) - \mathbf{L}(\mathbf{q},\dot{\mathbf{q}})\mathbf{M}(\mathbf{q})\ddot{\mathbf{q}} \tag{4.11}$$

$$\Leftrightarrow \dot{\mathbf{z}} = -\mathbf{L}(\mathbf{q},\dot{\mathbf{q}})\hat{\mathbf{d}} + \mathbf{L}(\mathbf{q},\dot{\mathbf{q}})\left(\mathbf{D}(\mathbf{q},\dot{\mathbf{q}}) - \boldsymbol{\tau}\right) \tag{4.12}$$

Substituting Equation (4.7) into Equation (4.12) yields:

$$\dot{\mathbf{z}} = -\mathbf{L}(\mathbf{q},\dot{\mathbf{q}})\left(\mathbf{z} + \mathbf{p}(\mathbf{q},\dot{\mathbf{q}})\right) + \mathbf{L}(\mathbf{q},\dot{\mathbf{q}})\left(\mathbf{D}(\mathbf{q},\dot{\mathbf{q}}) - \boldsymbol{\tau}\right) \tag{4.13}$$

Finally, one can obtain value of vector **z** by solving:

$$\Leftrightarrow \dot{\mathbf{z}} = -\mathbf{L}(\mathbf{q},\dot{\mathbf{q}})\mathbf{z} + \mathbf{L}(\mathbf{q},\dot{\mathbf{q}})\left(\mathbf{D}(\mathbf{q},\dot{\mathbf{q}}) - \boldsymbol{\tau} - \mathbf{p}(\mathbf{q},\dot{\mathbf{q}})\right) \tag{4.14}$$

Consequently, the generalized momentum disturbance observer does not need the acceleration measurement since the term $\mathbf{M}(\mathbf{q})\ddot{\mathbf{q}}$ is cancelled. The joint velocity can be obtained from Levant's differentiator in ***Remark* 3-8**, ***Chapter*** 3.

The dynamics of the disturbance tracking error is realized by:

$$\dot{\tilde{\mathbf{d}}} = \dot{\mathbf{d}} - \dot{\hat{\mathbf{d}}} = \dot{\mathbf{d}} - \dot{\mathbf{z}} - \frac{d}{dt}\left(\mathbf{p}(\mathbf{q},\dot{\mathbf{q}})\right) \tag{4.15}$$

Substituting Equation (4.14) into Equation (4.15) results in:

$$\dot{\tilde{\mathbf{d}}} = \dot{\mathbf{d}} + \mathbf{L}(\mathbf{q},\dot{\mathbf{q}})\mathbf{z} - \mathbf{L}(\mathbf{q},\dot{\mathbf{q}})\left(\mathbf{D}(\mathbf{q},\dot{\mathbf{q}}) - \boldsymbol{\tau} - \mathbf{p}(\mathbf{q},\dot{\mathbf{q}})\right) - \mathbf{L}(\mathbf{q},\dot{\mathbf{q}})\mathbf{M}(\mathbf{q})\ddot{\mathbf{q}} \tag{4.16}$$

$$\Leftrightarrow \dot{\tilde{\mathbf{d}}} = \dot{\mathbf{d}} + \mathbf{L}(\mathbf{q},\dot{\mathbf{q}})\mathbf{z} - \mathbf{L}(\mathbf{q},\dot{\mathbf{q}})\left(\mathbf{M}(\mathbf{q})\ddot{\mathbf{q}} + \mathbf{D}(\mathbf{q},\dot{\mathbf{q}}) - \boldsymbol{\tau} - \mathbf{p}(\mathbf{q},\dot{\mathbf{q}})\right) \tag{4.17}$$

$$\Leftrightarrow \dot{\tilde{\mathbf{d}}} = \dot{\mathbf{d}} - \mathbf{L}(\mathbf{q},\dot{\mathbf{q}})\left(\mathbf{d} - \mathbf{p}(\mathbf{q},\dot{\mathbf{q}}) - \mathbf{z}\right) \tag{4.18}$$

$$\Leftrightarrow \dot{\tilde{\mathbf{d}}} = \dot{\mathbf{d}} - \mathbf{L}(\mathbf{q},\dot{\mathbf{q}})\left(\mathbf{d} - \hat{\mathbf{d}}\right) \tag{4.19}$$

Finally, the estimated error dynamics is obtained as

$$\dot{\tilde{\mathbf{d}}} = \dot{\mathbf{d}} - \mathbf{L}(\mathbf{q},\dot{\mathbf{q}})\tilde{\mathbf{d}} \tag{4.20}$$

exactly the same as that one in Equation (4.4).

4.3.1.3 General momentum and observer matrix gain design

According to Mohammadi et al. [81], the observer matrix gain is calculated by:

$$\mathbf{L}(\mathbf{q},\dot{\mathbf{q}}) = \boldsymbol{\Phi}^{-1}\mathbf{M}^{-1}(\mathbf{q}) \in R^{n\times n} \tag{4.21}$$

where $\boldsymbol{\Phi}^{-1} \in R^{n\times n}$ is a constant invertible matrix.

Then, Equation (4.8) is re-expressed as

$$\frac{d}{dt}\left(\mathbf{p}(\mathbf{q},\dot{\mathbf{q}})\right) = \boldsymbol{\Phi}^{-1}\ddot{\mathbf{q}} \tag{4.22}$$

or

$$\mathbf{p}(\mathbf{q},\dot{\mathbf{q}}) = \boldsymbol{\Phi}^{-1}\dot{\mathbf{q}} \tag{4.23}$$

The matrix $\boldsymbol{\Phi} \in R^{n\times n}$ is constrained by the following conditions:

***Condition** 4-1*: $\boldsymbol{\Phi} \in R^{n\times n}$ *is a constant invertible matrix.*

***Condition** 4-2*: $\boldsymbol{\Phi} \in R^{n\times n}$ *is designed such that the inequality*

$$\boldsymbol{\Phi} + \boldsymbol{\Phi}^T - \boldsymbol{\Phi}\dot{\mathbf{M}}\boldsymbol{\Phi}^T \geq \boldsymbol{\Gamma} \tag{4.24}$$

is hold, where $\boldsymbol{\Gamma}$ *is semi-positive symmetric matrix.*

Theorem 3-1: *Consider the system dynamics subject to the external disturbance d, with the above GMO design, the disturbance can be obtained with the estimation error converging to the small neighborhood of the origin.*

Proof of theorem 3-1:

Consider the Lyapunov candidate as

$$V_d = \tilde{\mathbf{d}}^T\boldsymbol{\Phi}^T\mathbf{M}\boldsymbol{\Phi}\tilde{\mathbf{d}} \tag{4.25}$$

Taking derivative Lyapunov function V_d yields:

$$\dot{V}_d = \dot{\tilde{\mathbf{d}}}^T\boldsymbol{\Phi}^T\mathbf{M}\boldsymbol{\Phi}\tilde{\mathbf{d}} + \tilde{\mathbf{d}}^T\boldsymbol{\Phi}^T\mathbf{M}\boldsymbol{\Phi}\dot{\tilde{\mathbf{d}}} + \tilde{\mathbf{d}}^T\boldsymbol{\Phi}^T\dot{\mathbf{M}}\boldsymbol{\Phi}\tilde{\mathbf{d}} \tag{4.26}$$

Here, let consider two situations: slow-varying and fast-varying disturbance

4.3.1.3.1 Slow-varying disturbance

In this case, holding assumption 4-1, then:

$$\dot{\tilde{\mathbf{d}}} = \dot{\hat{\mathbf{d}}} = \mathbf{L}(\mathbf{q},\dot{\mathbf{q}})\tilde{\mathbf{d}} \tag{4.27}$$

Then, Equation (4.26) is derived as

$$\begin{aligned}
\dot{V}_d &= -\left(\mathbf{L}\tilde{\mathbf{d}}\right)^T\boldsymbol{\Phi}^T\mathbf{M}\boldsymbol{\Phi}\tilde{\mathbf{d}} - \tilde{\mathbf{d}}^T\boldsymbol{\Phi}^T\mathbf{M}\boldsymbol{\Phi}\left(\mathbf{L}\tilde{\mathbf{d}}\right) + \tilde{\mathbf{d}}^T\boldsymbol{\Phi}^T\dot{\mathbf{M}}\boldsymbol{\Phi}\tilde{\mathbf{d}} \\
&= -\tilde{\mathbf{d}}^T\mathbf{L}^T\boldsymbol{\Phi}^T\mathbf{M}\boldsymbol{\Phi}\tilde{\mathbf{d}} - \tilde{\mathbf{d}}^T\boldsymbol{\Phi}^T\mathbf{M}\boldsymbol{\Phi}\mathbf{L}\tilde{\mathbf{d}} + \tilde{\mathbf{d}}^T\boldsymbol{\Phi}^T\dot{\mathbf{M}}\boldsymbol{\Phi}\tilde{\mathbf{d}} \\
&= -\tilde{\mathbf{d}}^T\mathbf{M}^{-T}\boldsymbol{\Phi}^{-T}\boldsymbol{\Phi}^T\mathbf{M}\boldsymbol{\Phi}\tilde{\mathbf{d}} - \tilde{\mathbf{d}}^T\boldsymbol{\Phi}^T\mathbf{M}\boldsymbol{\Phi}\boldsymbol{\Phi}^{-1}\mathbf{M}^{-1}\tilde{\mathbf{d}} + \tilde{\mathbf{d}}^T\boldsymbol{\Phi}^T\dot{\mathbf{M}}\boldsymbol{\Phi}\tilde{\mathbf{d}} \\
&= -\tilde{\mathbf{d}}^T\boldsymbol{\Phi}\tilde{\mathbf{d}} - \tilde{\mathbf{d}}^T\boldsymbol{\Phi}^T\tilde{\mathbf{d}} + \tilde{\mathbf{d}}^T\boldsymbol{\Phi}^T\dot{\mathbf{M}}\boldsymbol{\Phi}\tilde{\mathbf{d}} \\
&= -\tilde{\mathbf{d}}^T\left(\boldsymbol{\Phi} + \boldsymbol{\Phi}^T - \boldsymbol{\Phi}^T\dot{\mathbf{M}}\boldsymbol{\Phi}\right)\tilde{\mathbf{d}} \\
&\leq -\tilde{\mathbf{d}}^T\boldsymbol{\Gamma}\tilde{\mathbf{d}} \leq 0
\end{aligned} \tag{4.28}$$

According to Equation (4.28), the derivative $\dot{V}_d$ is semi-negative definite when ***Condition* 4-2** is hold. Therefore, the estimator stability is proven. The estimated disturbance error asymptotically converges to zero as

$$\lim_{t\to\infty}\tilde{\mathbf{d}}=0,\forall\tilde{\mathbf{d}}\in R^n \tag{4.29}$$

Moreover, referring Equation (4.25) and using Rayleigh Inequality [82], the Lyapunov function of V_d is saturated by [81]:

$$\lambda_{\min}\left(\mathbf{\Phi}^T\mathbf{M}\mathbf{\Phi}\right)\left\|\mathbf{d}\right\|^2\le V_d=\tilde{\mathbf{d}}^T\mathbf{\Phi}^T\mathbf{M}\mathbf{\Phi}\tilde{\mathbf{d}}\le\lambda_{\max}\left(\mathbf{\Phi}^T\mathbf{M}\mathbf{\Phi}\right)\left\|\mathbf{d}\right\|^2 \tag{4.30}$$

It is noteworthy that the matrix $\mathbf{\Phi}^T\mathbf{M}\mathbf{\Phi}$ is positive symmetric matrix, then:

$$\lambda_{\max}\left(\mathbf{\Phi}^T\mathbf{M}\mathbf{\Phi}\right)\le\left\|\mathbf{M}\right\|\left\|\mathbf{\Phi}\right\|^2 \tag{4.31}$$

Consequently, one can obtain:

$$V_d\le\lambda_{\max}\left(\mathbf{\Phi}^T\mathbf{M}\mathbf{\Phi}\right)\left\|\mathbf{d}\right\|^2\le\left\|\mathbf{M}\right\|\left\|\mathbf{\Phi}\right\|^2\left\|\mathbf{d}\right\|^2\le m^u\left\|\mathbf{\Phi}\right\|^2\left\|\mathbf{d}\right\|^2 \tag{4.32}$$

Similarly, the following inequality is hold:

$$\tilde{\mathbf{d}}^T\mathbf{\Gamma}\tilde{\mathbf{d}}\ge\lambda_{\min}\left(\mathbf{\Gamma}\right)\left\|\mathbf{d}\right\|^2 \tag{4.33}$$

Then, using this inequality for Equation (4.28) yields:

$$\dot{V}_d\le-\tilde{\mathbf{d}}^T\mathbf{\Gamma}\tilde{\mathbf{d}}\le-\lambda_{\min}\left(\mathbf{\Gamma}\right)\left\|\tilde{\mathbf{d}}\right\|^2 \tag{4.34}$$

Combining inequalities (4.32) and Equation (4.34) yields:

$$\dot{V}_d\le-\lambda_{\min}\left(\mathbf{\Gamma}\right)\frac{1}{m^u\left\|\mathbf{\Phi}\right\|^2}V_d \tag{4.35}$$

$$\Rightarrow V_d\left(t\right)\le V_d\left(t_0\right)e^{\left(-\frac{\lambda_{\min}\left(\mathbf{\Gamma}\right)}{m^u\left\|\mathbf{\Phi}\right\|^2}\right)t} \tag{4.36}$$

Moreover, since $\lambda_{\min}\left(\mathbf{\Phi}^T\mathbf{\Phi}\right)m_l\left\|\mathbf{d}\right\|^2\le\lambda_{\min}\left(\mathbf{\Phi}^T\mathbf{M}\mathbf{\Phi}\right)\left\|\mathbf{d}\right\|^2\le V_d$, then, applying this inequality with inequality (4.36) results in:

$$\left\|\mathbf{d}\right\|^2\le\frac{1}{\lambda_{\min}\left(\mathbf{\Phi}^T\mathbf{\Phi}\right)m_l}V_d\left(t_0\right)e^{\left(-\frac{\lambda_{\min}\left(\mathbf{\Gamma}\right)}{m^u\left\|\mathbf{\Phi}\right\|^2}\right)t} \tag{4.37}$$

Consequently, the observer can achieve exponential convergence.

4.3.1.3.2 Fast-varying disturbance

In this circumstance, the derivative of Lyapunov function V_d becomes:

$$\dot{V}_d=-\tilde{\mathbf{d}}^T\left(\mathbf{\Phi}+\mathbf{\Phi}^T-\mathbf{\Phi}^T\dot{\mathbf{M}}\mathbf{\Phi}\right)\tilde{\mathbf{d}}+\dot{\mathbf{d}}^T\mathbf{\Phi}^T\mathbf{M}\mathbf{\Phi}\tilde{\mathbf{d}}+\tilde{\mathbf{d}}^T\mathbf{\Phi}^T\mathbf{M}\mathbf{\Phi}\dot{\mathbf{d}} \tag{4.38}$$

Note that since $\left\|\tilde{\mathbf{d}}\right\|\le\left\|\tilde{\mathbf{d}}\right\|_\infty\le\bar{\delta}_d$ as mentioned in ***Assumption 4-3***, and combine with results in Equations (4.31) and (4.33), then one can easily obtain:

$$\dot{V}_d\le-\lambda_{\min}\left(\mathbf{\Gamma}\right)\left\|\tilde{\mathbf{d}}\right\|^2+2\bar{\delta}_d m^u\left\|\mathbf{\Phi}\right\|^2\left\|\tilde{\mathbf{d}}\right\| \tag{4.39}$$

Here, Equation (4.39) can be rearranged as [81]

$$\dot{V}_d \le -(1-\theta)\lambda_{\min}(\boldsymbol{\Gamma})\left\|\tilde{\mathbf{d}}\right\|^2 - \theta\lambda_{\min}(\boldsymbol{\Gamma})\left\|\tilde{\mathbf{d}}\right\|^2 + 2\bar{\delta}_d m^u \left\|\boldsymbol{\Phi}\right\|^2 \left\|\tilde{\mathbf{d}}\right\| \tag{4.40}$$

With $\theta \in (0,1)$.

Then the derivative is semi-negative definite when:

$$-\theta\lambda_{\min}(\boldsymbol{\Gamma})\left\|\tilde{\mathbf{d}}\right\|^2 + 2\bar{\delta}_d m^u \left\|\boldsymbol{\Phi}\right\|^2 \left\|\tilde{\mathbf{d}}\right\| \le 0 \tag{4.41}$$

$$\left\|\tilde{\mathbf{d}}\right\|^2 \ge \frac{2\bar{\delta}_d m^u \left\|\boldsymbol{\Phi}\right\|^2}{\theta\lambda_{\min}(\boldsymbol{\Gamma})} \tag{4.42}$$

Generally, the estimated error is globally uniformly ultimate boundedness. Then, the convergence rate can be obtained as

$$\Rightarrow V_d(t) \le V_d(t_0) e^{\left(-\frac{(1-\theta)\lambda_{\min}(\boldsymbol{\Gamma})}{m^u \left\|\boldsymbol{\Phi}\right\|^2}\right)t} \tag{4.43}$$

$$\left\|\mathbf{d}\right\|^2 \le \frac{1}{\lambda_{\min}\left(\boldsymbol{\Phi}^T\boldsymbol{\Phi}\right)m_l} V_d(t_0) e^{\left(-\frac{(1-\theta)\lambda_{\min}(\boldsymbol{\Gamma})}{m^u \left\|\boldsymbol{\Phi}\right\|^2}\right)t} \tag{4.44}$$

Hence, the estimated error converges to the ball with radius $\frac{2\bar{\delta}_d m^u \left\|\boldsymbol{\Phi}\right\|^2}{\theta\lambda_{\min}(\boldsymbol{\Gamma})}$, where $\theta \in (0,1)$, with exponential rate of $\frac{(1-\theta)\lambda_{\min}(\boldsymbol{\Gamma})}{m^u \left\|\boldsymbol{\Phi}\right\|^2}$.

The remained work is designing the observer matrix gain and generalized momentum vector through matrix $\boldsymbol{\Phi}$. Generally, the Linear Matrix Inequalities formulation is employed to find out values of matrices $\boldsymbol{\Phi}$ and $\boldsymbol{\Gamma}$ simultaneously. Fortunately, for the planar manipulator, the matrix $\boldsymbol{\Phi}$ can be simply designed as

$$\boldsymbol{\Phi} = \begin{bmatrix} \phi_{d1} & 0 & \cdots & 0 \\ \phi_{d2} & \phi_{d2} & \cdots & 0 \\ \vdots & \vdots & \ddots & 0 \\ \phi_{dn} & \phi_{dn} & \cdots & \phi_{dn} \end{bmatrix} \in R^{n\times n} \tag{4.45}$$

Hence, the generalized momentum vector **p** and observer matrix gain are expressed as

$$\mathbf{p}(\mathbf{q},\dot{\mathbf{q}}) = \begin{bmatrix} \phi_{d1} & 0 & \cdots & 0 \\ \phi_{d2} & \phi_{d2} & \cdots & 0 \\ \vdots & \vdots & \ddots & 0 \\ \phi_{dn} & \phi_{dn} & \cdots & \phi_{dn} \end{bmatrix} \begin{pmatrix} \dot{\mathbf{q}}_1 \\ \dot{\mathbf{q}}_2 \\ \vdots \\ \dot{\mathbf{q}}_n \end{pmatrix} = \begin{pmatrix} \phi_{d1}\dot{\mathbf{q}}_1 \\ \phi_{d2}(\dot{\mathbf{q}}_1 + \dot{\mathbf{q}}_2) \\ \vdots \\ \phi_{dn}(\dot{\mathbf{q}}_1 + \dot{\mathbf{q}}_2 + \ldots + \dot{\mathbf{q}}_n) \end{pmatrix} \tag{4.46}$$

$$\mathbf{L}(\mathbf{q},\dot{\mathbf{q}}) = \frac{d}{dt}\mathbf{p}(\dot{\mathbf{q}},\dot{\mathbf{q}})\ddot{\mathbf{q}}^{-1}\mathbf{M}^{-1}(\mathbf{q}) = \begin{bmatrix} \phi_{d1} & 0 & \cdots & 0 \\ \phi_{d2} & \phi_{d2} & \cdots & 0 \\ \vdots & \vdots & \ddots & 0 \\ \phi_{dn} & \phi_{dn} & \cdots & \phi_{dn} \end{bmatrix} \mathbf{M}^{-1}(\mathbf{q}) \tag{4.47}$$

where ϕ_{di} is chosen depending on system dynamics and maximum joint velocity. Normally, ϕ_{di} is chosen such that:

$$\phi_{di} \geq \alpha_l \dot{q}_{n,\max} \tag{4.48}$$

where α_l is a weighting positive definite matrix depending on the length of each link; and $\dot{q}_{n,\max}$ is the maximum velocity of the end-effector.

Remark 4-1: *According to the constraints in Equation* (3.15)*, since the velocity of the spool valve is saturated by the upper bound, the velocity of each link of the n-DOF manipulator is bounded. Therefore, the maximum velocity of the end-effector is also bounded. In this work, this upper bound is supposed to be pre-determined to facilitate the control design*.

4.3.2 Adaptive backstepping sliding mode control with GMO

In this sub-section, the GMO is combined with the ABSMC designed in Section 4.5. Based on the combination between the advanced control algorithm and disturbance estimator for mismatched uncertainties (external interactions) compensation, the system stability is theoretically proven through Lyapunov theorems.

Regarding the control law obtained in Equation (3.30) and influence of external force disturbance in Equation (4.1), the virtual control signal $\mathbf{x}_{3d}$ for position tracking performance is re-written as

$$\mathbf{x}_{3d} = \mathbf{M}(\mathbf{x}_1)\dot{\mathbf{x}}_{2s} + \mathbf{C}(\mathbf{x}_1,\mathbf{x}_2)\mathbf{x}_{2s} + \mathbf{G}(\mathbf{x}_1) + \mathbf{J}^T\hat{\mathbf{F}}_{ext} + \hat{\boldsymbol{\Delta}} - \mathbf{K}_1\mathbf{s}_1 - \boldsymbol{\eta}_1 \tanh\left(\frac{\mathbf{s}_1}{\sigma_s}\right) \tag{4.49}$$

where $\hat{\mathbf{F}}_{ext}$ represents for an estimated external force disturbance obtained from the GMO.

Choose a Lyapunov candidate V_1^* as

$$V_1^* = \frac{1}{2}\mathbf{s}_1^T\mathbf{M}\mathbf{s}_1 + \frac{1}{2}\tilde{\boldsymbol{\Delta}}^T\tilde{\boldsymbol{\Delta}} + V_d \tag{4.50}$$

Taking derivative the Lyapunov candidate V_1^* with Property 4-1 and results obtained in Equations (3.29) and (4.26) yields:

$$\begin{aligned} \dot{V}_1^* = {} & \mathbf{s}_1^T\left(\mathbf{x}_3 - \left(\tilde{\boldsymbol{\Delta}} + \hat{\boldsymbol{\Delta}}\right) - \mathbf{M}(\mathbf{x}_1)\dot{\mathbf{x}}_{2s} - \mathbf{C}(\mathbf{x}_1,\mathbf{x}_2)\mathbf{x}_{2s} - \mathbf{G}(\mathbf{x}_1) - \mathbf{J}^T\mathbf{F}_{ext}\right) + \dot{\tilde{\boldsymbol{\Delta}}}^T\tilde{\boldsymbol{\Delta}} \\ & + \dot{\tilde{\mathbf{F}}}_{ext}^T\boldsymbol{\Phi}^T\mathbf{M}\boldsymbol{\Phi}\tilde{\mathbf{F}}_{ext} + \tilde{\mathbf{F}}_{ext}^T\boldsymbol{\Phi}^T\mathbf{M}\boldsymbol{\Phi}\dot{\tilde{\mathbf{F}}}_{ext} + \tilde{\mathbf{F}}_{ext}^T\boldsymbol{\Phi}^T\dot{\mathbf{M}}\boldsymbol{\Phi}\tilde{\mathbf{F}}_{ext} \end{aligned} \tag{4.51}$$

where $\tilde{\mathbf{F}}_{ext} = \mathbf{F}_{ext} - \hat{\mathbf{F}}_{ext}$.

Herein, the external force is considered as disturbance to be addressed. Then, substituting the virtual control signal in Equation (4.49) and adaptive law derived in Equation (3.27) into Equation (4.51) results in:

$$\begin{aligned}\dot{V}_1^* = \mathbf{s}_1^T\left(\mathbf{J}_a^T\mathbf{e}_3 - \mathbf{K}_1\mathbf{s}_1 - \boldsymbol{\eta}_1\tanh\left(\frac{\mathbf{s}_1}{\sigma_s}\right) + \tilde{\mathbf{F}}_{ext}\right) \\ + \dot{\tilde{\mathbf{F}}}_{ext}^T\boldsymbol{\Phi}^T\mathbf{M}\boldsymbol{\Phi}\tilde{\mathbf{F}}_{ext} + \tilde{\mathbf{F}}_{ext}^T\boldsymbol{\Phi}^T\mathbf{M}\boldsymbol{\Phi}\dot{\tilde{\mathbf{F}}}_{ext} + \tilde{\mathbf{F}}_{ext}^T\boldsymbol{\Phi}^T\dot{\mathbf{M}}\boldsymbol{\Phi}\tilde{\mathbf{F}}_{ext}\end{aligned} \tag{4.52}$$

In the case of the external force disturbance consideration, the external force is a slow-varying disturbance; therefore, applying the result obtained in Equation (4.34) yields:

$$\dot{V}_1^* \le \mathbf{s}_1^T\left(\mathbf{J}_a^T\mathbf{e}_3 - \mathbf{K}_1\mathbf{s}_1 - \boldsymbol{\eta}_1\tanh\left(\frac{\mathbf{s}_1}{\sigma_s}\right) + \tilde{\mathbf{F}}_{ext}\right) - \lambda_{\min}\left(\boldsymbol{\Gamma}\right)\left\|\tilde{\mathbf{F}}_{ext}\right\|^2 \tag{4.53}$$

Remark 4-2: *Compared to the case when the external force disturbance is not compensated, the robust term of the controller, i.e.,* $-\mathbf{K}_1\mathbf{s}_1 - \boldsymbol{\eta}_1\tanh\left(\mathbf{s}_1/\sigma_s\right)$ *should be designed such that it can cover the sum of the upper bounds of the estimation errors of the mismatched uncertainties and external force disturbance, i.e.,* $\eta_{1i} \ge \bar{\delta}_{F_{ext}} \ge \left\|\tilde{\mathbf{F}}_{ext}\right\|_\infty$.

With the external force estimated by using the GMO, the robust terms of the control law are consequently much smaller instead of choosing large values to cover the upper bound of the external force in the conventional design.

From Equation (4.53), the derivative of the Lyapunov function V_1^* is semi-negative if the error $\mathbf{e}_3$ converges to zero. Therefore, this error should be tackled as small as possible. The next step for minimizing the tracking error $\mathbf{e}_3$ is exactly same as that one presented in **Section 4.5**.

4.3.3 Adaptive Fuzzy BSMC with GMO

The external force disturbance and mismatched uncertainties can be observed and compensated; however, the estimated error still exists. The control law is designed such that the robust terms can cover the upper bound of the estimated error. However, in some cases such as time-delayed, occurrence of component or actuator faults, or abrupt interactions, the tracking error may be suddenly enlarged. Fixed robust gains, in this case, may not guarantee the fast convergence if their values are not large enough. Conversely, when the system is in normal operation, with small tracking errors, these fixed large gains may amplify the tracking errors and noise; thus, resulting in instability. Therefore, in order to optimize the controller design, the robust gains should be adapted depended on the system performance tracking error instead of using fixed values. Therefore, the fuzzy logic control is employed to flexibly adjust the robust gains to the system behavior to reduce the chattering induced from the reaching phase progress.

The overall schematic of the proposed disturbance observer AFBSMC (DOAFBSMC) methodology is illustrated in **Figure 4-4**.

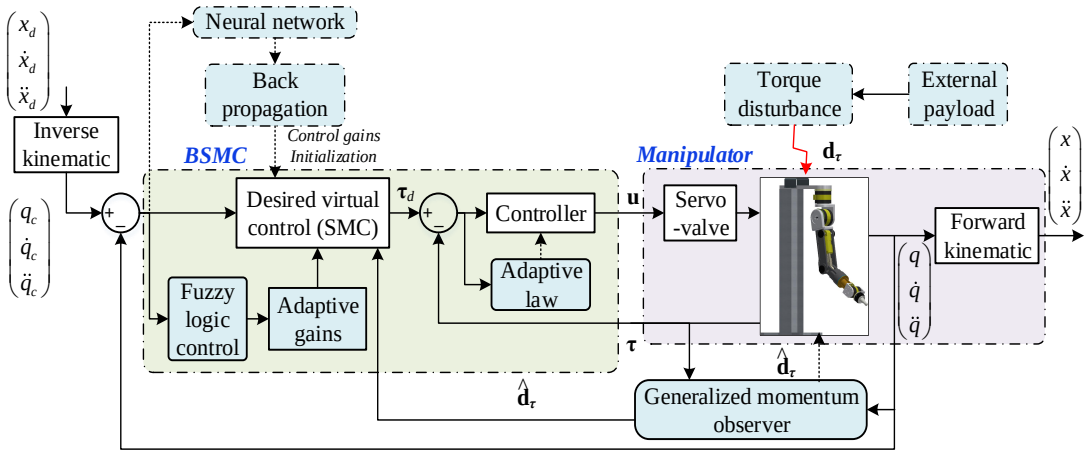

Figure 4-4 Proposed adaptive Fuzzy BSMC with GMO and NN initialization.

First, to reflect the effect of the payload, let us rewrite the Equation (4.49):

$$\mathbf{x}_{3d} = \mathbf{M}(\mathbf{x}_1)\dot{\mathbf{x}}_{2s} + \mathbf{C}(\mathbf{x}_1,\mathbf{x}_2)\mathbf{x}_{2s} + \mathbf{G}(\mathbf{x}_1) + \mathbf{J}^T\hat{\mathbf{F}}_{ext} + \hat{\boldsymbol{\Delta}} - \mathbf{K}_1^f\mathbf{s}_1 - \boldsymbol{\eta}_1^f \tanh\left(\frac{\mathbf{s}_1}{\sigma_s}\right) \tag{4.54}$$

where $\mathbf{K}_1^f$ and $\boldsymbol{\eta}_1^f$ are the matrix gains of the robust term determined from the FLC.

The linguistic fuzzy rules are defined in the following form:

$$\begin{aligned} &\text{IF } e(t) \text{ is } A_1^{i=1,2,\ldots,N} \text{ and } \dot{e}(t) \text{ is } A_2^{i=1,2,\ldots,N} \\ &\text{THEN } \boldsymbol{\alpha}_1^f \text{ is } B^{i=1,2,\ldots,N}. \end{aligned} \tag{4.55}$$

where N is the total number of rules, $\boldsymbol{\alpha}_1^f = diag\left(\alpha_{11}^f \quad \alpha_{12}^f \quad \ldots \quad \alpha_{1n}^f\right) \in R^{n\times n}$ represents for the matrix of tuned factors for the robust gains; $A_{1,2}^i$ and B^i are the linguistic variables of the fuzzy sets characterized by fuzzy membership functions.

The fuzzy control rules can be represented as the mapping of the input linguistic variables $e(t)$ and $\dot{e}(t)$ to the output linguistic variable $\boldsymbol{\alpha}_1^f$. The input linguistic variable characterized by seven membership functions (NB (Negative Big), NM (Negative Medium), NS (Negative Small), Z (Zero), PS (Positive Small), PM (Positive Medium), PB (Positive Big)) are employed for the control strategy such that the stability of the system can be guaranteed as stable. The membership functions of the two input linguistic variables $e(t)$ and $\dot{e}(t)$, and the output linguistic variable $\boldsymbol{\alpha}_1^f$ are described in **Figure 4-5** and **Figure 4-6**, (VVS (Very Very Small), VS (Very Small), S (Small), M (Medium), B (Big), VB (Very Big), VVB (Very Very Big)); the control strategy is described in **Table 4-1** [38]. In this study, triangular membership functions are considered as shown in **Figure 4-5** and **Figure 4-6**.

***Table 4-1**. Rules table of the fuzzy logic system.*

$\boldsymbol{\alpha}_1^f$		$\dot{e}(t)$						
		NB	**NM**	**NS**	**Z**	**PS**	**PM**	**PB**
$e(t)$	**NB**	M	B	VB	VVB	VB	B	M
	NM	S	M	B	VB	B	M	S
	NS	VS	S	M	B	M	S	VS
	Z	VVS	VS	S	M	S	VS	VVS
	PS	VS	S	M	B	M	S	VS
	PM	S	M	B	VB	B	M	S
	PB	M	B	VB	VVB	VB	B	M

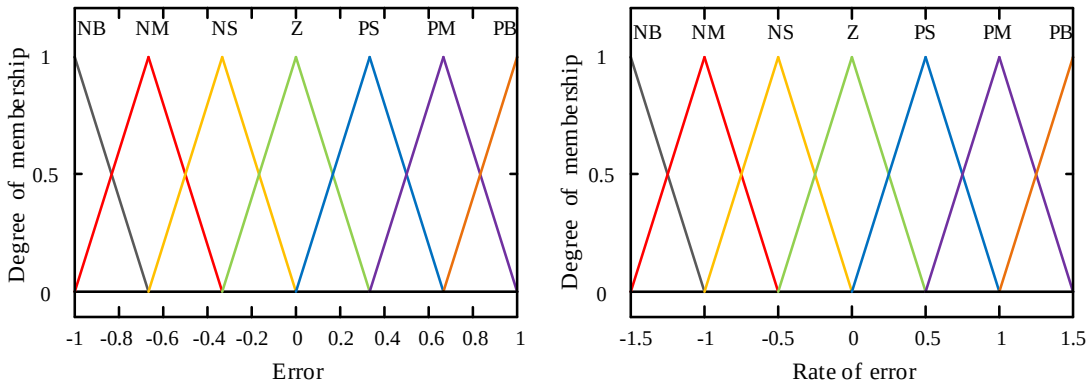

Figure 4-5 Membership function of the error and the rate of error.

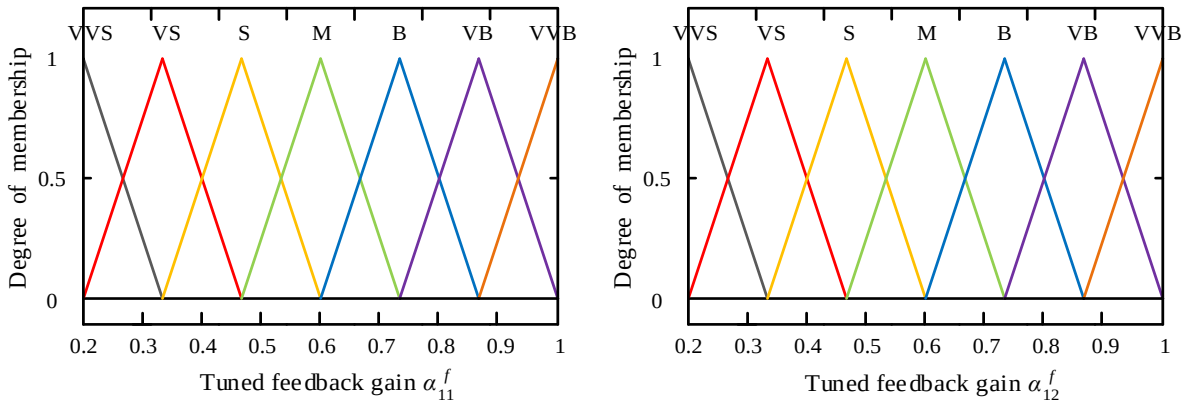

(a) **(b)**

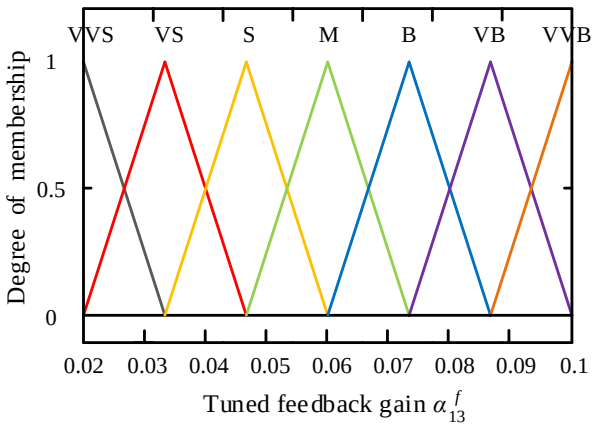

(c)

*Figure 4-6 Membership function of the tuned factor $\boldsymbol{\alpha}_1^f$: (**a**) $\boldsymbol{\alpha}_{11}^f$, (**b**) $\boldsymbol{\alpha}_{12}^f$, (**c**) $\boldsymbol{\alpha}_{13}^f$.*

Remark 4-3: *Conventionally, the gain* $\boldsymbol{\eta}_1$ *is designed such that it can cover the upper bound, and its main aim is to achieve the system robustness and fast convergence. However, regarding the fact that this gain should not be chosen too large, then the output is designed with small upper bound.*

$$\boldsymbol{\alpha}_{K_1}^f = 100\boldsymbol{\alpha}_1^f \tag{4.56}$$

Finally, the adaptive robust gains are obtained by:

$$\boldsymbol{\eta}_1^f = \left(\mathbf{I}_n + \boldsymbol{\alpha}_1^f\right)\boldsymbol{\eta}_{1,\text{int}} + \mathbf{I}_n\bar{d} \tag{4.57}$$

$$\mathbf{K}_1^f = \mathbf{K}_{1,\text{int}} + \boldsymbol{\alpha}_{K_1}^f \tag{4.58}$$

where $\boldsymbol{\eta}_{1,\text{int}} \in R^{n\times n}$ and $\mathbf{K}_{1,\text{int}} \in R^{n\times n}$ are initial robust gains in the case of ideal working operation (i.e., system operation without matched and mismatched uncertainties) that should be determined.

4.3.4 Controller gains initialization

4.3.4.1 Neural network sliding mode control

According to the portrait phase of the sliding mode control presented in Yuri et al. [83] and Wilfrid [17], the first stage is when the state trajectory is outside the sliding surface and needs to be driven towards the sliding surface. Then the second phase occurs when the state trajectory moves along towards the sliding surface. The term $-\mathbf{K}_1\mathbf{s}_1 - \boldsymbol{\eta}_1 \tanh\left(\mathbf{s}_1/\sigma_s\right)$ is to drive the state trajectory toward the sliding surface, whereas the slope $\boldsymbol{\lambda}$ of the sliding surface affects the convergence of state variables. The term $\boldsymbol{\lambda}$ and robust term $-\mathbf{K}_1\mathbf{s}_1 - \boldsymbol{\eta}_1 \tanh\left(\mathbf{s}_1/\sigma_s\right)$, in fact, depend on each other. The correlation between the two terms is depicted in **Figure 4-7**.

Despite the robustness of the sliding mode control, the tracking performance is difficult to achieve with high precision with fixed robust gains in the presence of the external payload. Some articles have reported the algorithm for gains-tuning using the neural network (NN) method. In this part, the neural network based sliding mode control is designed to adapt with the parameter variation. The NN-based SMC architecture is described in **Figure 4-8**.

As can be seen in **Figure 4-8**, instead of setting the fixed value for both the slope of the sliding surface and controller gains, in the NNSMC, the slope of the sliding surface and controller gains are considered as a weighting factor to be adjusted. Tracking error $e(t)$ and its change rate $\dot{e}(t)$ are considered as two nodal inputs of the NN. The first weights to be tuned are the gains for each $e(t)$ and $\dot{e}(t)$ that specify the slope of the sliding surface. The hidden layer is presented by using three nodes determined from the sliding surface that is an output of the input layer. Then the controller gains of the SMC are

considered as the second weights to be tuned to adapt with the system dynamics. The output of the NN is a control signal.

The input of the NN is the error and the rate of the error:

$$\varsigma_{in} = \begin{pmatrix} \mathbf{e}_1 & \dot{\mathbf{e}}_1 \end{pmatrix}^T \in R^{2n} \tag{4.59}$$

The output of the first layer is:

$$\varsigma_{out} = \boldsymbol{\lambda}_1^e \mathbf{e}_1 + \boldsymbol{\lambda}_1^{\dot{e}} \dot{\mathbf{e}}_1 = \boldsymbol{\Lambda} \varsigma_{in} \tag{4.60}$$

where $\boldsymbol{\lambda}_1^e = diag\begin{pmatrix} \lambda_{11}^e & \lambda_{12}^e & \dots & \lambda_{1n}^e \end{pmatrix} \in R^{n \times n}$, $\boldsymbol{\lambda}_1^{\dot{e}} = diag\begin{pmatrix} \lambda_{11}^{\dot{e}} & \lambda_{12}^{\dot{e}} & \dots & \lambda_{1n}^{\dot{e}} \end{pmatrix} \in R^{n \times n}$ are matrices gain corresponding to $e(t)$ and $\dot{e}(t)$, respectively; $\boldsymbol{\Lambda} = diag\begin{pmatrix} \boldsymbol{\lambda}_1^e & \boldsymbol{\lambda}_1^{\dot{e}} \end{pmatrix} \in R^{2n \times 2n}$.

Then, the sliding surface $\mathbf{s}_1$ is expressed as

$$\mathbf{s}_1 = f\left(\varsigma_{out}\right) = \boldsymbol{\lambda}_1^e \mathbf{e}_1 + \boldsymbol{\lambda}_1^{\dot{e}} \dot{\mathbf{e}}_1 = \boldsymbol{\Lambda} \varsigma_{in} \tag{4.61}$$

where $f\left(\varsigma_{out,i}\right) = \begin{pmatrix} f\left(\varsigma_{out,1}\right) & f\left(\varsigma_{out,2}\right) & \dots & f\left(\varsigma_{out,n}\right) \end{pmatrix}^T \in R^n$ is a vector of activate functions of each element $\varsigma_{out,i}$.

The input of the hidden layer is defined by:

$$\varsigma_{hid} = \begin{pmatrix} \mathbf{s}_1 & \tanh\left(\mathbf{s}_1 / \sigma_s\right) & \mathbf{b}_s \end{pmatrix}^T \in R^{3n} \tag{4.62}$$

where $\mathbf{b}_s \in R^n$ is an offset signal to compensate the control input signal.

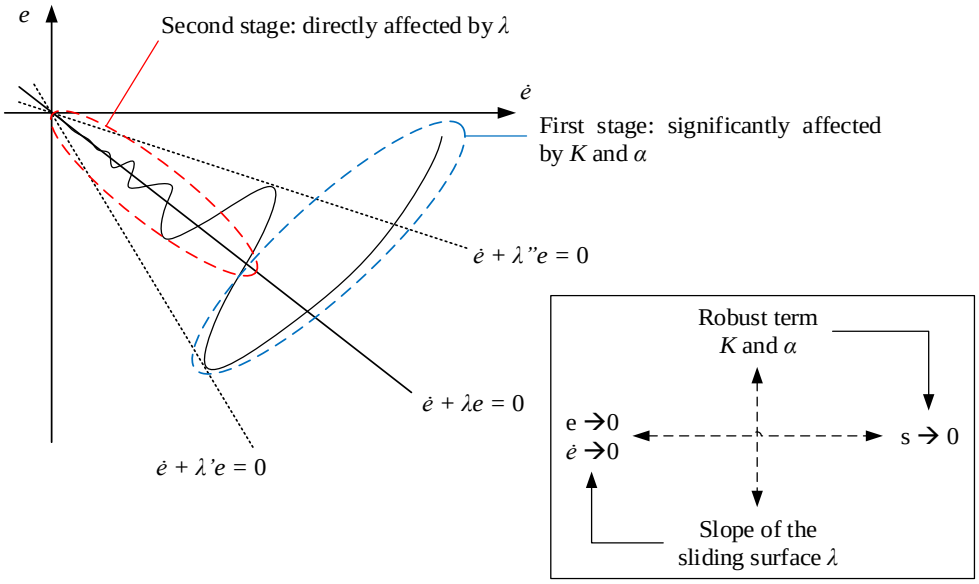

Figure 4-7 The motion of the state trajectory of the sliding mode control in which the two stages and the two terms affecting the convergence rate of the state error are considered. The sub-figure shows the correlation between the robust term K and α with the slope of the sliding surface λ.

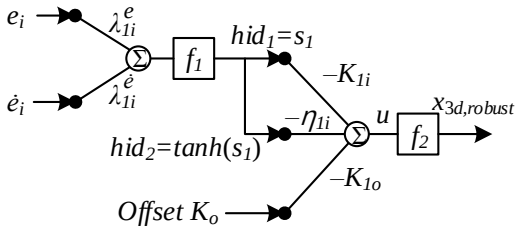

Figure 4-8 Architecture of the proposed neural network based sliding mode control.

The output of the hidden layer and the control input signal, respectively, are:

$$\mathbf{x}_{3d,robust} = \Upsilon \varsigma_{hid} = -\mathbf{K}_{1,\text{int}}\mathbf{s}_1 - \boldsymbol{\eta}_{1,\text{int}} \tanh\left(\mathbf{s}_1/\sigma_s\right) - \mathbf{b}_s \tag{4.63}$$

where $\mathbf{K}_{1,\text{int}} = diag\left(K_{11,\text{int}} \quad K_{12,\text{int}} \quad ... \quad K_{1n,\text{int}}\right)$ and $\boldsymbol{\eta}_{1,\text{int}} = diag\left(\eta_{11,\text{int}} \quad \eta_{12,\text{int}} \quad ... \quad \eta_{1n,\text{int}}\right)$ are n-by-n matrices of initial robust gains; $\Upsilon = diag\left(-\mathbf{K}_{1,\text{int}} \quad -\boldsymbol{\eta}_{1,\text{int}} \quad \mathbf{I}_n\right) \in R^{3n\times 3n}$; $\mathbf{b}_s$ is a vector of offset value.

In order to facilitate the control methodology design and simplify the calculation, the relationship between the control voltage signal **u** and torque action **τ**, considered as the output of the NN, is simplified by:

$$\boldsymbol{\tau}_{robust} = f\left(\mathbf{u}\right) = \mathbf{u} \tag{4.2}$$

The weighting matrices $\mathbf{K}_{1,\text{int}}$, $\boldsymbol{\eta}_{1,\text{int}}$ and $\boldsymbol{\Lambda}$ are automatically updated to reach optimal values such that the following cost function is minimized:

$$E(t) = \frac{1}{2}\left(\mathbf{q}_d(t) - \mathbf{q}(t)\right)^T \left(\mathbf{q}_d(t) - \mathbf{q}(t)\right) \tag{4.65}$$

Let define vectors of desired threshold $\varpi_e \in R^n$ and $\varpi_s \in R^n$. When the cost function is greater than ϖ_s, each element of the initial matrix gains Υ is updated such that the state trajectory is regulated towards the sliding surface, and when the error is greater than ϖ_e, the slope of the sliding surface $\boldsymbol{\Lambda}$ is adjusted.

Without losing the generality, let us consider one pair of elements of the input ς_{in}, i.e., $\varsigma_{in,i} = \left(e_i \quad \dot{e}_i\right)^T \in R^2$ and gains corresponding to these inputs, i.e., λ_{1i}^{e}, $\lambda_{1i}^{\dot{e}}$, $K_{1i,\text{int}}$, $\eta_{1i,\text{int}}$, and $b_{s,i}$. Based on the chain-rules, these gains are updated as the following:

$$K_{1i,\text{int}}\left(t+1\right) = K_{1i,\text{int}}\left(t\right) + l_i^K \frac{\partial E_i\left(t\right)}{\partial K_{1i,\text{int}}\left(t\right)} \tag{4.66}$$

$$\eta_{1i,\text{int}}\left(t+1\right) = \eta_{1i,\text{int}}\left(t\right) + l_i^\eta \frac{\partial E_i\left(t\right)}{\partial \eta_{1i,\text{int}}\left(t\right)} \tag{4.67}$$

$$b_{s,i}\left(t+1\right) = b_{s,i}\left(t\right) + l_i^b \frac{\partial E_i\left(t\right)}{\partial b_{s,i}\left(t\right)} \tag{4.68}$$

$$\lambda_{1i}^{e}(t+1)=\lambda_{1i}^{e}(t)+l_i^{e}\frac{\partial E_i(t)}{\partial \lambda_{1i}^{e}(t)} \tag{4.69}$$

$$\lambda_{1i}^{\dot{e}}(t+1)=\lambda_{1i}^{\dot{e}}(t)+l_i^{\dot{e}}\frac{\partial E_i(t)}{\partial \lambda_{1i}^{\dot{e}}(t)} \tag{4.70}$$

where l_i^K, l_i^h, l_i^b, l_i^e and $l_i^{\dot{e}}$ are positive constants that present the learning rates with relating to adjusted gains $K_{1i,\text{int}}$, $\eta_{1i,\text{int}}$, $b_{s,i}$, λ_{1i}^{e} and $\lambda_{1i}^{\dot{e}}$, respectively.

The change of each gain is computed using gradient descent:

$$\frac{\partial E_i(t)}{\partial K_{1i,\text{int}}(t)}=\frac{\partial E_i(t)}{\partial q_i(t)}\frac{\partial q_i(t)}{\partial \tau_i(t)}\frac{\partial \tau_i(t)}{\partial u_i(t)}\frac{\partial u_i(t)}{\partial K_{1i,\text{int}}(t)}=-e_{1i}\frac{\Delta q_i(t)}{\Delta \tau_i(i)}1(-s_{1i}) \tag{4.71}$$

$$\frac{\partial E_i(t)}{\partial \eta_{1i,\text{int}}(t)}=\frac{\partial E_i(t)}{\partial q_i(t)}\frac{\partial q_i(t)}{\partial \tau_i(t)}\frac{\partial \tau_i(t)}{\partial u_i(t)}\frac{\partial u_i(t)}{\partial \eta_{1i,\text{int}}(t)}=-e_{1i}\frac{\Delta q_i(t)}{\Delta \tau_i(t)}1\left(-\tanh\left(\frac{s_{1i}}{\sigma_s}\right)\right) \tag{4.72}$$

$$\frac{\partial E_i(t)}{\partial b_{s,i}(t)}=\frac{\partial E_i(t)}{\partial q_i(t)}\frac{\partial q_i(t)}{\partial \tau_i(t)}\frac{\partial \tau_i(t)}{\partial u_i(t)}\frac{\partial u_i(t)}{\partial b_{s,i}(t)}=-e_{1i}\frac{\Delta q_i(t)}{\Delta \tau_i(t)}1(-1) \tag{4.73}$$

After updating the controller gains, the slope of the sliding surface is then tuned due to the back-propagation process to satisfy the performance. The change of the slope is computed as

$$\begin{aligned}\frac{\partial E_i(t)}{\partial \lambda_{1i}^{e}(t)}&=\frac{\partial E_i(t)}{\partial q_{i1}(t)}\frac{\partial q_i(t)}{\partial \tau_i(t)}\frac{\partial \tau_i(t)}{\partial u_i(t)}\frac{\partial u_i(t)}{\partial s_i(t)}\frac{\partial s_i(t)}{\partial \varsigma_{out,i}(t)}\frac{\partial \varsigma_{out,i}(t)}{\partial \lambda_{1i}^{e}(t)}\\&=-e_{1i}(t)\frac{\Delta q_i(t)}{\Delta \tau_i(t)}1\left(-K_{1i,\text{int}}(t)-\eta_{1i,\text{int}}(t)\frac{\partial\left(\tanh\left(s_{1i}(t)/\sigma_s\right)\right)}{\partial s_{1i}(t)}\right)f_{i1}^{'}e_{1i}(t)\\&=-e_{1i}(t)\frac{\Delta q_i(t)}{\Delta \tau_i(t)}1\left(-K_{1i,\text{int}}(t)-\eta_{1i,\text{int}}(t)\frac{4e^{-2(s_{1i}(t)/\sigma_s)}}{\sigma_s\left(1+e^{-2(s_{1i}(t)/\sigma_s)}\right)^2}\right)1e_{1i}\end{aligned} \tag{4.74}$$

$$\begin{aligned}\frac{\partial E_i(t)}{\partial \lambda_{1i}^{\dot{e}}(t)}&=\frac{\partial E_i(t)}{\partial q_i(t)}\frac{\partial q_i(t)}{\partial \tau_i(t)}\frac{\partial \tau_i(t)}{\partial u_i(t)}\frac{\partial u_i(t)}{\partial s_{1i}(t)}\frac{\partial s_{1i}(t)}{\partial \varsigma_{out,i}(t)}\frac{\partial \varsigma_{out,i}(t)}{\partial \lambda_{1i}^{\dot{e}}(t)}\\&=-e_{1i}(t)\frac{\Delta q_i(t)}{\Delta \tau_i(t)}1\left(-K_{1i,\text{int}}(t)-\eta_{1i,\text{int}}(t)\frac{\partial\left(\tanh\left(s_{1i}(t)/\sigma_s\right)\right)}{\partial s_{1i}(t)}\right)f_{i1}^{'}\dot{e}_{1i}(t)\\&=-e_{1i}(t)\frac{\Delta q_i(t)}{\Delta \tau_i(t)}1\left(-K_{1i,\text{int}}(t)-\eta_{1i,\text{int}}(t)\frac{4e^{-2(s_{1i}(t)/\sigma_s)}}{\sigma_s\left(1+e^{-2(s_{1i}(t)/\sigma_s)}\right)^2}\right)1\dot{e}_{1i}\end{aligned} \tag{4.75}$$

Hence:

$$K_{1i,\text{int}}(t+1)=K_{1i,\text{int}}(t)+l_i^K+e_{1i}\frac{\Delta q_i(t)}{\Delta \tau_i(i)}s_{1i} \tag{4.76}$$

$$\eta_{1i,\text{int}}(t+1)=\eta_{1i,\text{int}}(t)+l_i^{\eta}+e_{1i}\frac{\Delta q_i(t)}{\Delta \tau_i(t)}\tanh\left(\frac{s_{1i}}{\sigma_s}\right) \tag{4.77}$$

$$b_{s,i}(t+1) = b_{s,i}(t) + l_i^b e_{1i} \frac{\Delta q_i(t)}{\Delta \tau_i(t)} \tag{4.78}$$

$$\lambda_{1i}^e(t+1) = \lambda_{1i}^e(t) - l_i^e e_{1i}(t) \frac{\Delta q_i(t)}{\Delta \tau_i(t)} \left(-K_{1i,\text{int}}(t) - \eta_{1i,\text{int}}(t) \frac{4e^{-2(s_{1i}(t)/\sigma_s)}}{\sigma_s \left(1+e^{-2(s_{1i}(t)/\sigma_s)}\right)^2} \right) \dot{e}_{1i} \tag{4.79}$$

$$\lambda_{1i}^{\dot{e}}(t+1) = \lambda_{1i}^{\dot{e}}(t) - l_i^{\dot{e}} e_{1i}(t) \frac{\Delta q_i(t)}{\Delta \tau_i(t)} \left(-K_{1i,\text{int}}(t) - \eta_{1i,\text{int}}(t) \frac{4e^{-2(s_{1i}(t)/\sigma_s)}}{\sigma_s \left(1+e^{-2(s_{1i}(t)/\sigma_s)}\right)^2} \right) \dot{e}_{1i} \tag{4.80}$$

4.3.4.2 The Constraint of the Updating Law

According to Equation (4.60), the sliding surface is:

$$s_{1i} = \varsigma_{out,i} = \lambda_{1i}^e e_{1i} + \lambda_{1i}^{\dot{e}} \dot{e}_{1i} \tag{4.81}$$

When the state trajectory moves towards the sliding surface:

$$s_{1i} = \lambda_{1i}^e e_{1i} + \lambda_{1i}^{\dot{e}} \dot{e}_{1i} = 0 \Rightarrow \dot{e}_{1i} = -\frac{\lambda_{1i,\text{int}}^e}{\lambda_{1i,\text{int}}^{\dot{e}}} e_{1i} = -\lambda_{1i,eqv} e_{1i} \tag{4.82}$$

where $\lambda_{1i,eqv} = \dfrac{\lambda_{1i,\text{int}}^e}{\lambda_{1i,\text{int}}^{\dot{e}}}$ is an equivalent slope of the sliding surface.

Taking derivative Equation (4.82) respects to time, we obtain:

$$\int_0^t \frac{\dot{e}_{1i}}{e_{1i}} d\imath = -\lambda_{1i,eqv} \int_0^t d\imath \rightarrow e_{1i} = e_{1i}(0) e^{-\lambda_{1i,eqv} t} \tag{4.83}$$

Hence, to reduce the convergence time, the updating law for the slope of the sliding surface is then adjusted such that the equivalent slope increases and achieves optimal value:

$$\lambda_{1i,eqv} = \frac{\lambda_{1i,\text{int}}^e}{\lambda_{1i,\text{int}}^{\dot{e}}} \rightarrow \lambda_{1i,eqv}^{opt} \tag{4.84}$$

4.4 Numerical simulations

In this part, some numerical simulations and comparison are implemented to evaluate the effectiveness of the proposed algorithm by using the MATLAB/Simulink program. The mechanical parameters and hydraulic parameters used for simulating are shown in **Table 4-2** and **Table 4-3**, respectively. In our simulations, discrete time with the fixed step is 10^{-4} s and the Runge–Kutta method is used for the approximate calculation of some differential problems. We investigate performance of the manipulator in three case studies with the same condition: the initial value of the three joints is $[0.1 \quad 0.6 \quad 0.8]^T$ (rad), and the initial velocity of the three joints are all zero; the external payload varies in the interval [5,20] kg and is shown in **Figure 4-9**; and the time for simulating is 20 s. The comparison

between sliding mode control (SMC), fuzzy sliding mode control (FSMC), and adaptive fuzzy sliding mode control (AFSMC) are utilized. The white noise is added to illustrate uncertainty parameters and verify the proposed method.

***Table 4-2**. The mechanical parameters used for simulations.*

Symbols	Quantity	Value (unit)
m_1	Mass of the first link	2 [kg]
m_2	Mass of the second link	5.1 [kg]
m_3	Mass of the third link	4.7 [kg]
L_1	Length of the second link	0.5 [m]
L_2	Length of the third link	0.2 [m]

***Table 4-3**. The hydraulic parameters used for simulations*

Symbol	Quantity	Value [unit]
P_S	Supply pressure from the tank	100 [bar]
P_t	Return pressure to the tank	1 [bar]
K_v	Gain factor of the valve dynamics	$1.2\text{x}10^{-3}$ [m/V]
ω	Servo valve area gradient	0.024 [m^2]
ρ	Oil density	800 [kg/m^3]
β	Effective Bulk modulus	$1.25\text{x}10^{9}$ [pa]
A_{11}, A_{12}	Volumetric area of rotary actuator 2	$2\text{x}10^{-4}$ [m^3/rad]
A_{21}, A_{22}	Volumetric area of rotary actuator 3	$1.2\text{x}10^{-4}$ [m^3/rad]
A_{31}	Cylinder area of piston head part	$1.53\text{x}10^{-3}$ [m^2]
A_{32}	Cylinder area of piston rod part	$1.04\text{x}10^{-3}$ [m^2]

The controller gains used for simulation are $k_{qij(i,j=1,2)} = 2.1610^{-8} m^3/\left(\sqrt{Pa}.s.V\right)$, λ = *diag* (60;60;50), $k_{qi3(i=1,2)} = 3.510^{-8} m^3/\left(\sqrt{Pa}.s.V\right)$, $\mathbf{K}_1$=*diag*(30;30;25), $\boldsymbol{\eta}_1$=*diag*(0.5;0.5;0.1), $\mathbf{K}_2$=*diag*(1000;1000;400), $\boldsymbol{\eta}_2$ = *diag*(20;20;10).

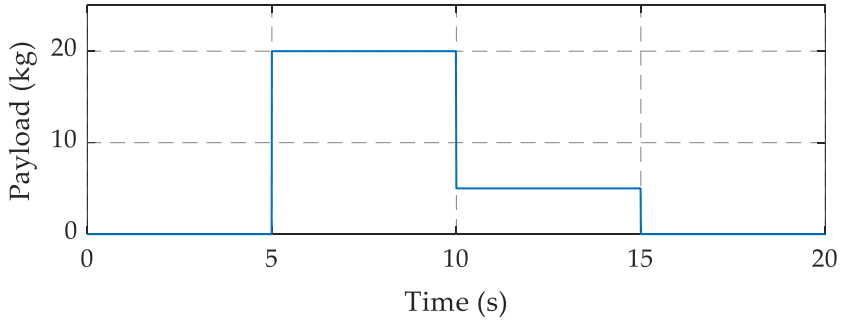

Figure 4-9 The payload variation profile.

Besides, the Proportional-Integral-Derivative control, SMC, and AFBSMC with feedforward disturbance compensator (FFDOAFBSMC) are also considered and compared with the proposed algorithm. In the FFDOAFBSMC, the estimated external force disturbance is compensated directly to the torque commanded signal, without considering the whole system stability, as shown in **Figure 4-10**. Compared with the proposed DOAFBSMC control architecture in **Figure 4-4**, there is no disturbance force feedback to the ABSMC.

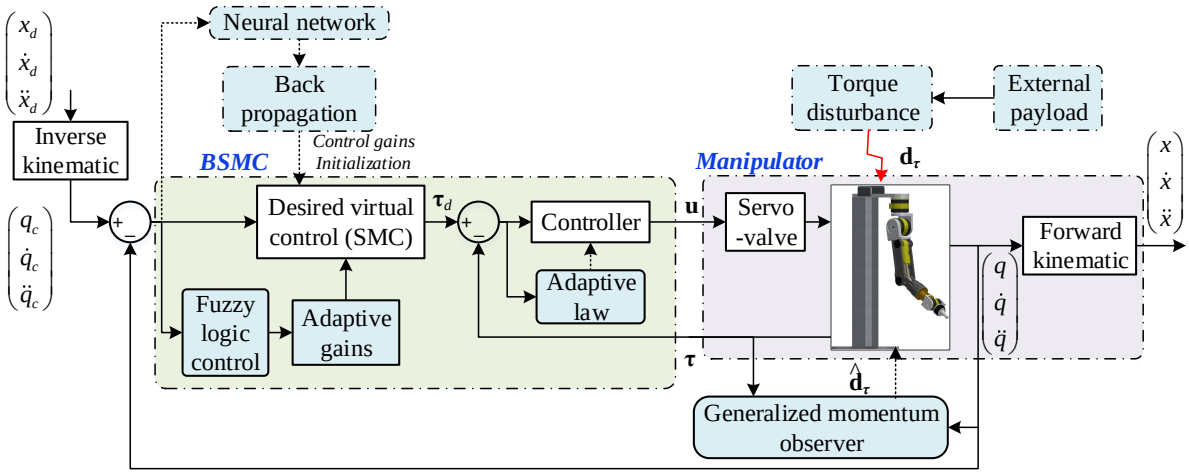

Figure 4-10 AFBSMC with feedforward disturbance compensator.

In this case, the virtual control signal of the position control is designed as

$$\mathbf{x}_{3d} = \mathbf{M}(\mathbf{x}_1)\dot{\mathbf{x}}_{2s} + \mathbf{C}(\mathbf{x}_1, \mathbf{x}_2)\mathbf{x}_{2s} + \mathbf{G}(\mathbf{x}_1) + \mathbf{J}^T\hat{\mathbf{F}}_{ext} + \hat{\boldsymbol{\Delta}} - \mathbf{K}_1^{FF}\mathbf{s}_1 - \boldsymbol{\eta}_1^{FF}\tanh\left(\frac{\mathbf{s}_1}{\sigma_s}\right) \tag{4.85}$$

$$\mathbf{K}_1^{FF} = \mathbf{K}_{1,\text{int}} + \mathbf{K}_m \tag{4.86}$$

$$\boldsymbol{\eta}_1^{FF} = \boldsymbol{\eta}_{1,\text{int}} + \boldsymbol{\eta}_m \tag{4.87}$$

where $\mathbf{K}_m$ and $\boldsymbol{\eta}_m$ are n-by-n diagonal positive definite matrices

The matrices $\mathbf{K}_m$ and $\boldsymbol{\eta}_m$ depend on the estimated disturbance, induced by the payload attached at the end-effector, and are adjusted to compensate the different between the real and actual disturbance. Since the estimated disturbance load torques are not feedback to the closed-loop control design, both $\mathbf{K}_m$ and $\boldsymbol{\eta}_m$ matrices are determined based on the fuzzy logic mechanism as follows:

$$(\mathbf{K}_m, \boldsymbol{\eta}_m) = f_{fuzzy}(m) \tag{4.88}$$

The estimated disturbance load torques obtained from using the GMO are considered as the linguistic input variables. Seven membership functions, namely NB (Negative Big), NM (Negative Medium), NS (Negative Small), Z (zero), PS (Positive Small), PM (Positive Medium), PB (Positive Big) are assigned to level the output adjusted robust term. For the output of the fuzzy system, the

adjustable scaling gain $\boldsymbol{\eta}_m$ and $\mathbf{K}_m$, specified by seven membership functions including Z (Zero), S (Small), LS (Light Small), M (medium), LB (Light Big), B (Big), VB (Very Big) is employed. Both linguistic input and output sets are signified in detail in **Figure 4-11** and **Figure 4-12**. The fuzzy rules are defined by IF-THEN rules and its laws are discussed in Table 4-4. The triangular membership functions are described in **Figure 4-11** for the change of load torque and **Figure 4-12** for the adaptive gains.

$$\text{IF } d_{\tau_{load,i}} \text{ is } A_1^{p=1,2,...,N} \text{ and } d_{\tau_{load,j}} \text{ is } A_2^{p=1,2,...,N} \text{ THEN } K_{m,i} = K_{load}^{p=1,2,...,N} \tag{4.89}$$

In the closed-loop system, the system position tracking performance is directly regulated and influenced from the estimated disturbances and adaptive robust terms, then the fuzzy logic mechanism is exploited that assigns the tracking error and its change rate as inputs. Unlikely, in the FFDOAFBSMC, the estimated disturbance load torque is not feedback to the controller designed; then, the fuzzy logic mechanism assigns their estimated values as inputs to adjust the gains of the robust term to compensate the estimated error that cannot be obtained practically.

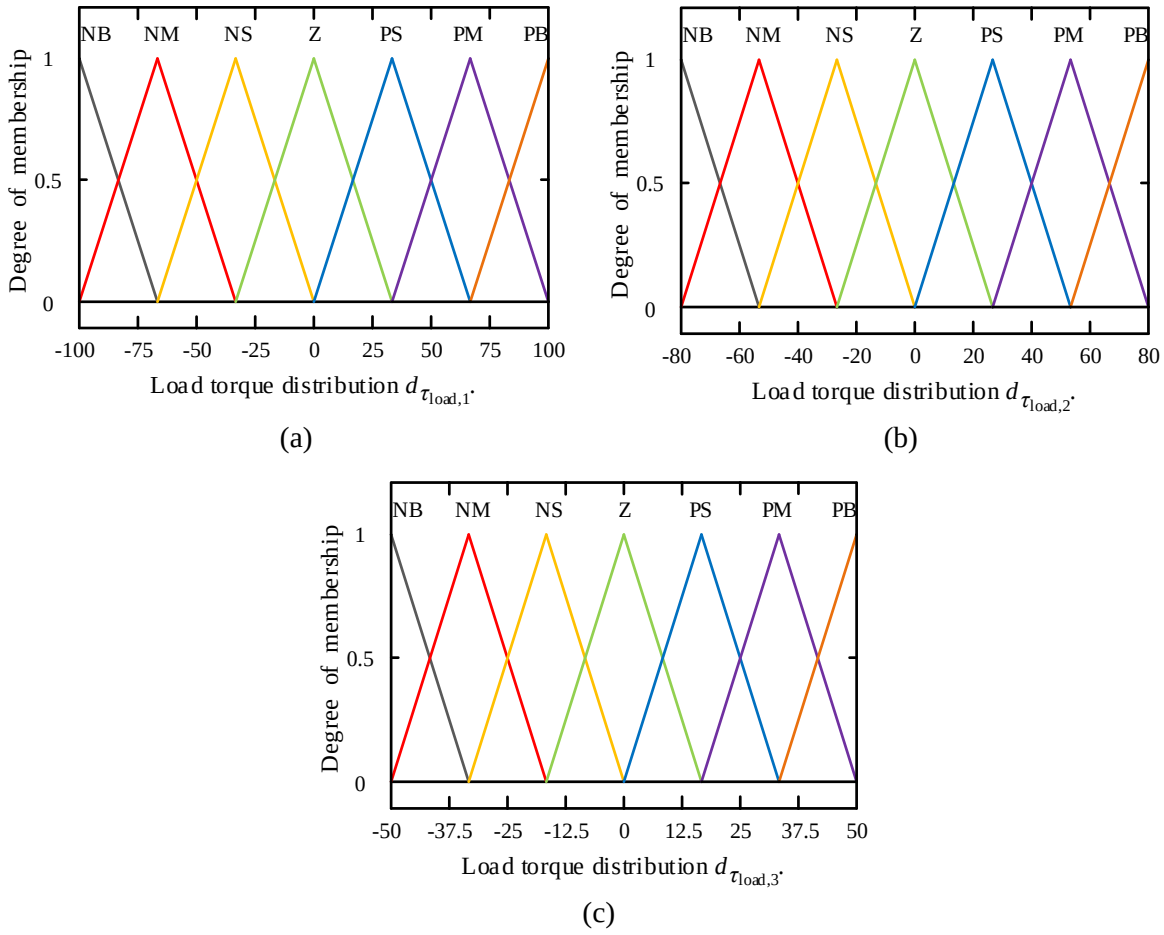

Figure 4-11 Membership function of the load torque variation: (a) $d_{\tau_{load,1}}$ on joint 1, (b) $d_{\tau_{load,2}}$ on joint 2, (c) $d_{\tau_{load,3}}$ on joint 3.

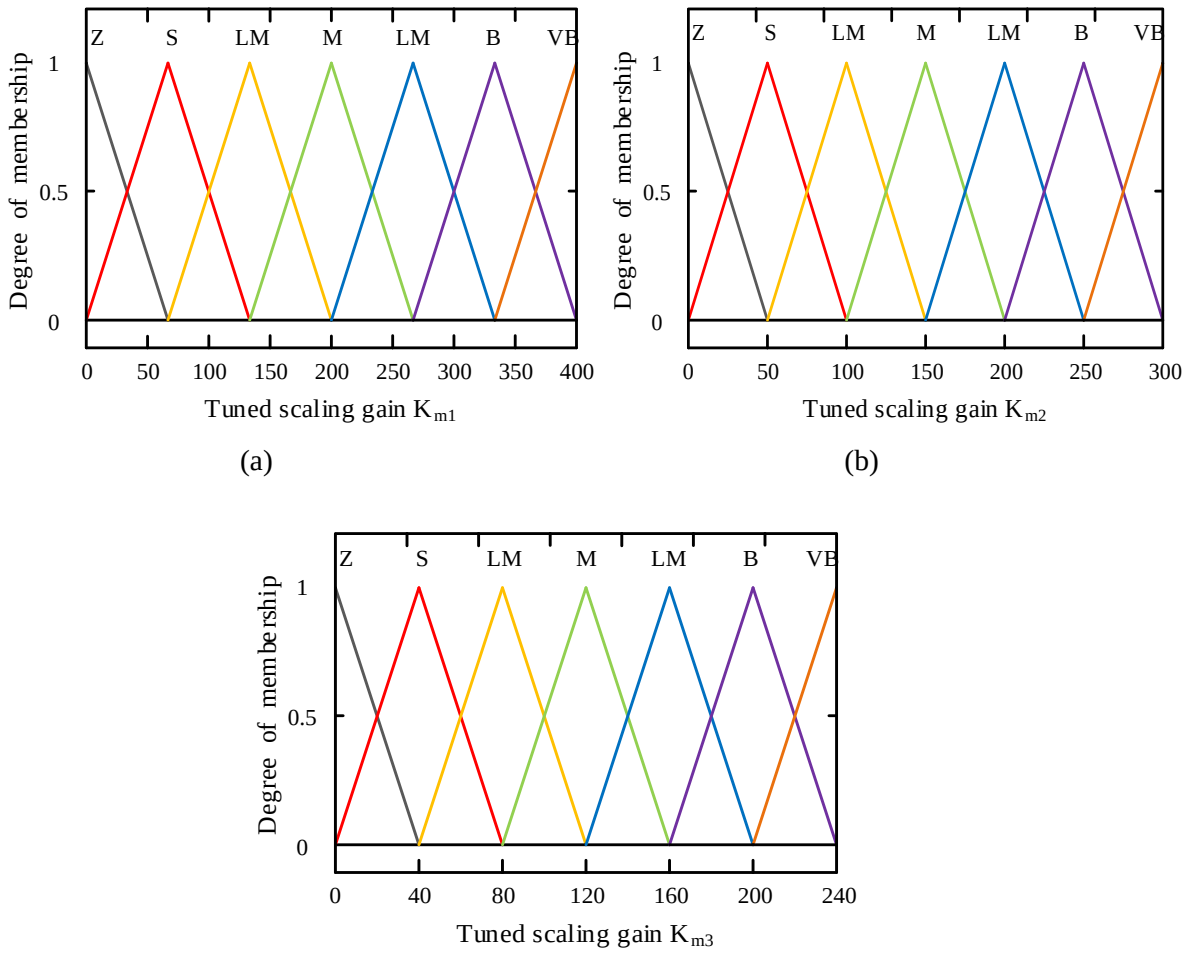

Figure 4-12 Membership function of the tuned scaling gains: (*a*) K_{m1}, (b) K_{m2}, (c) K_{m3}.

Table 4-4 Rules table of the fuzzy logic system.

K_{mi}		τ_{load_i}						
		NB	**NM**	**NS**	**Z**	**PS**	**PM**	**PB**
τ_{load_j}	**NB**	VB	B	LB	M	LB	B	VB
	NM	B	LB	M	LM	M	LB	B
	NS	LB	M	LM	S	LM	M	LB
	Z	M	LM	S	Z	S	LM	M
	PS	LB	M	LM	S	LM	M	LB
	PM	B	LB	M	LM	M	LB	B
	PB	VB	B	LB	M	LB	B	VB

4.4.1 Case study 1

The desired trajectory of the three joints is supposed to be tooth saw profile created by input shaping. The tracking performance and tracking error of the three joints are described in **Figures 4-13** and **4-14**, respectively. The role of the proposed controller is validated at the time when the external payload is applied. The error of the AFSMC is the smallest, in which the smallest overshoot is at the time the payload changed, compared with that of the FSMC and SMC. The load torques estimated by

using disturbance observer are depicted in **Figure 4-15**. And the control input signals which are constrained in the interval [–15, 15] (V) are performed in **Figure 4-16**.

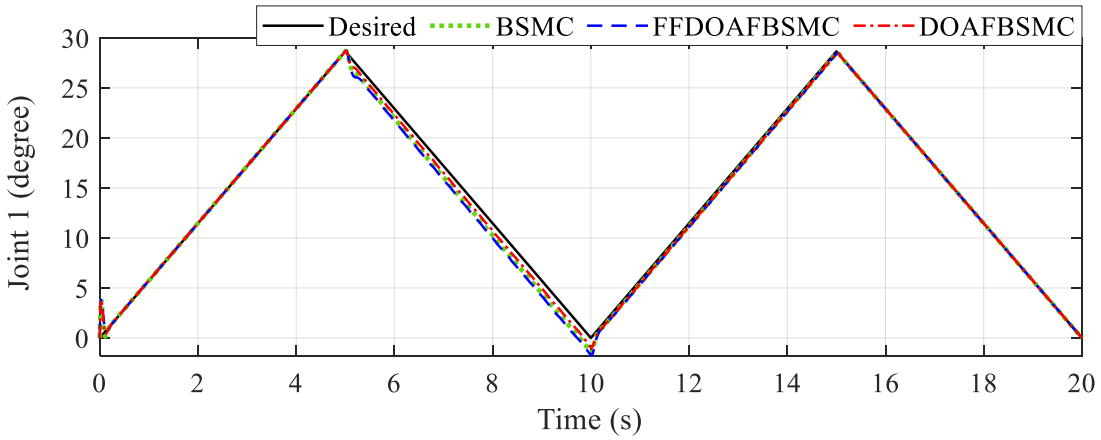

(a)

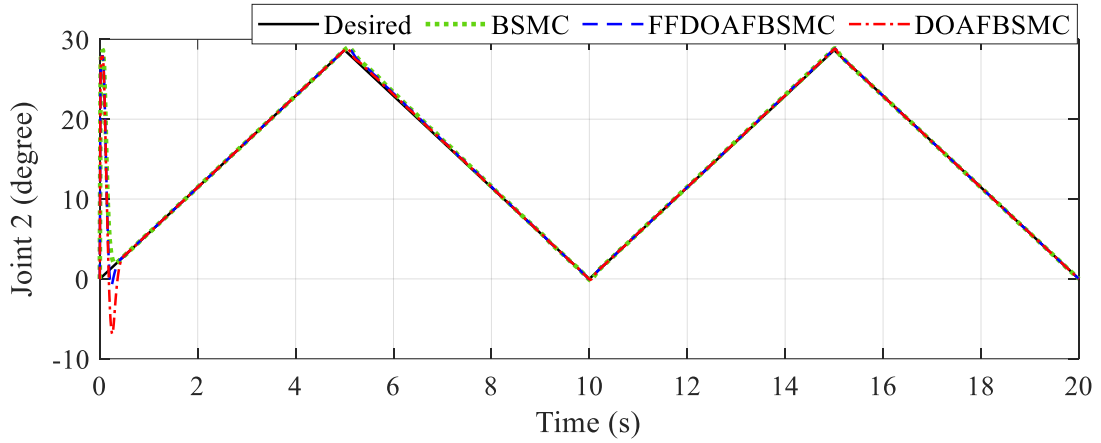

(b)

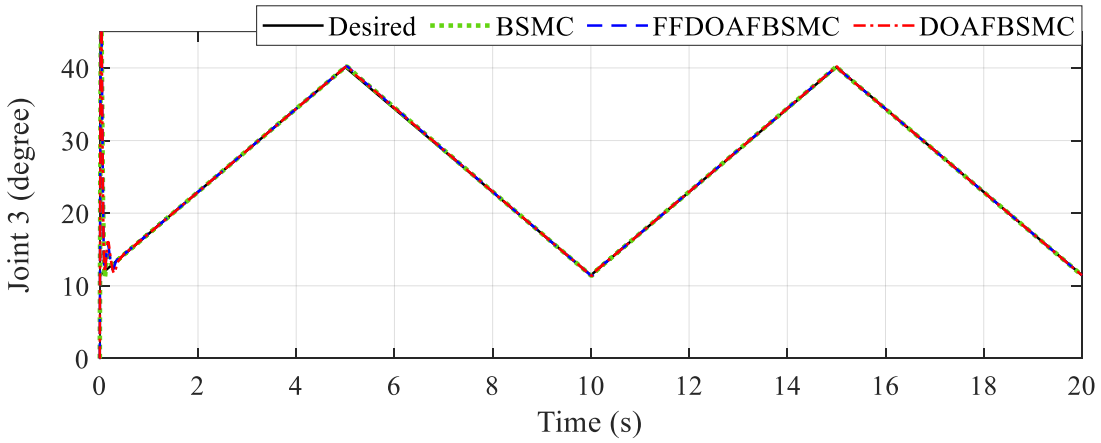

(c)

Figure 4-13 The tracking performance of the: (a) *first joint;* (b) *second joint;* (c) *third joint.*

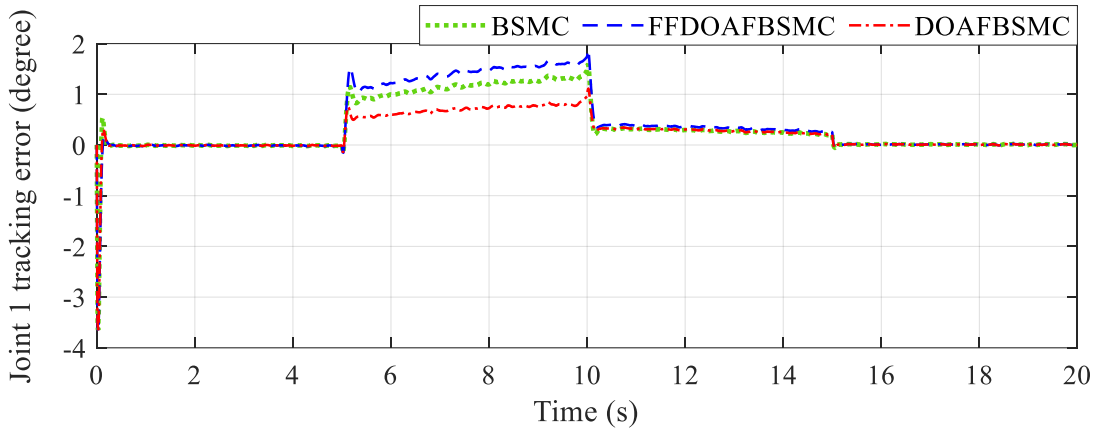

(a)

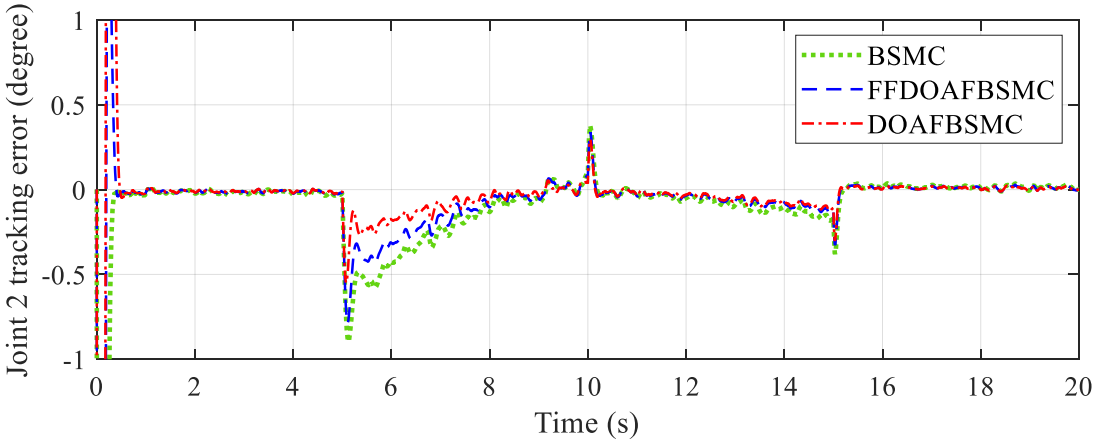

(b)

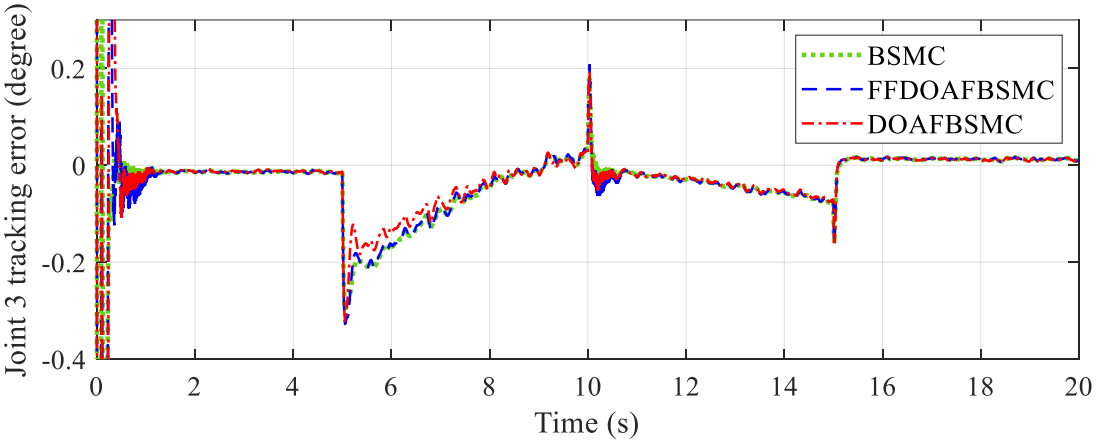

(c)

Figure 4-14 The tracking error of the: (a) *first joint,* (b) *second joint, and* (c) *third joint.*

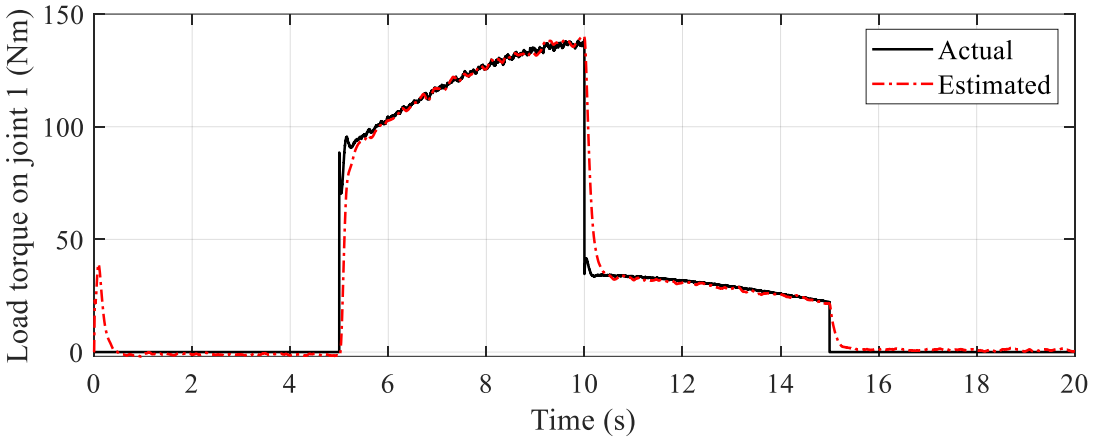

(a)

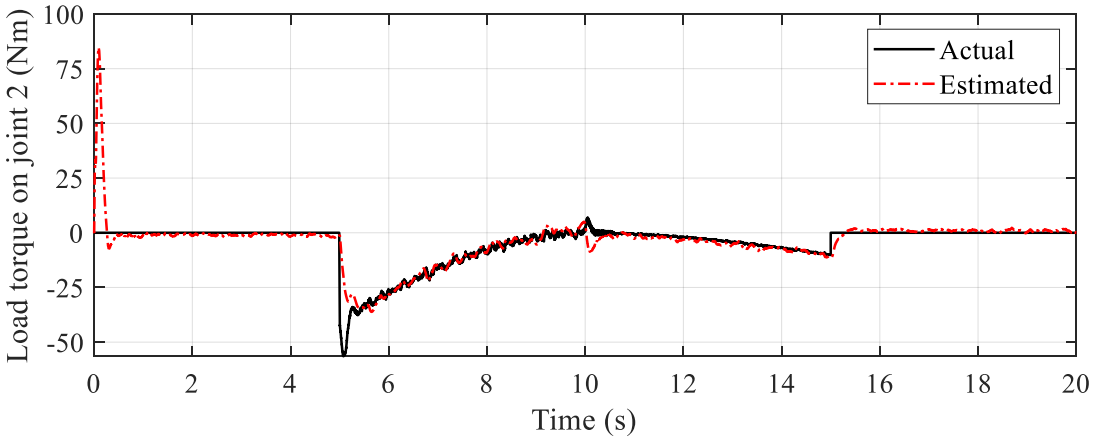

(b)

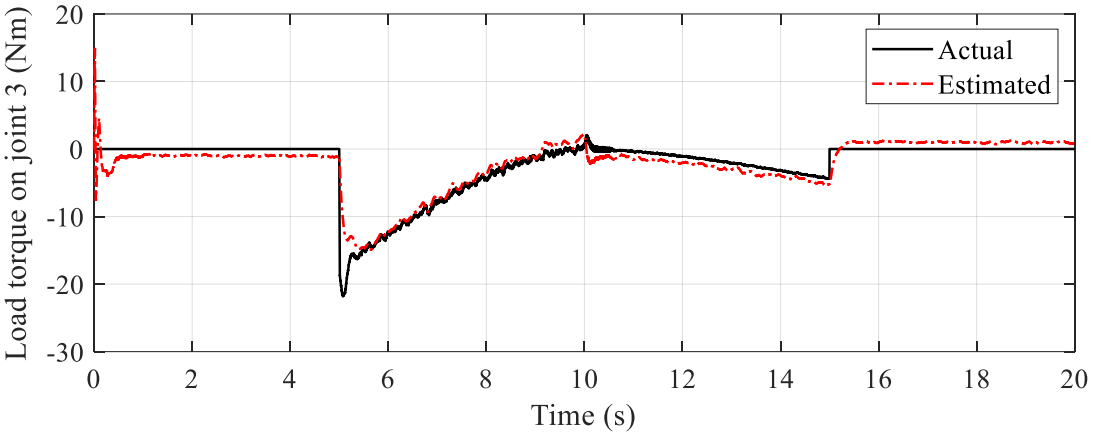

(c)

Figure 4-15 The load torque estimated of the: (a) *first joint,* (b) *second joint, and* (c) *third joint.*

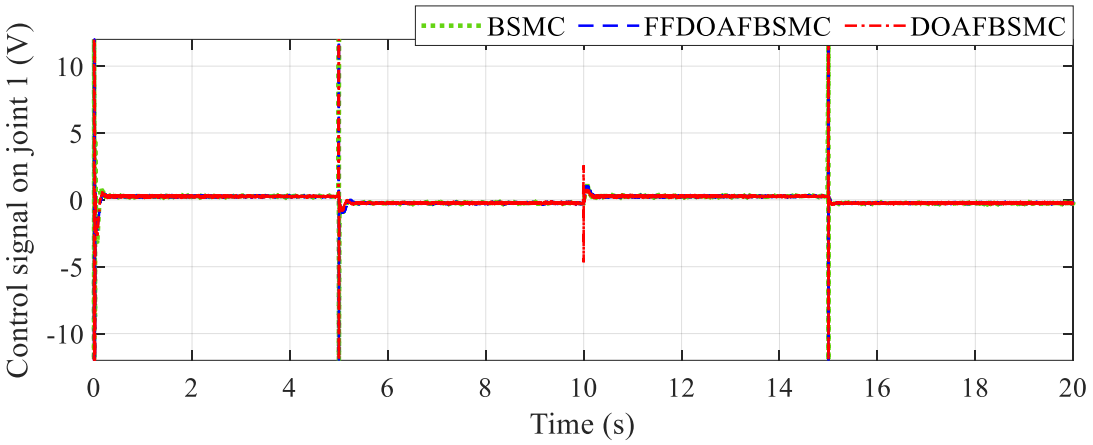

(a)

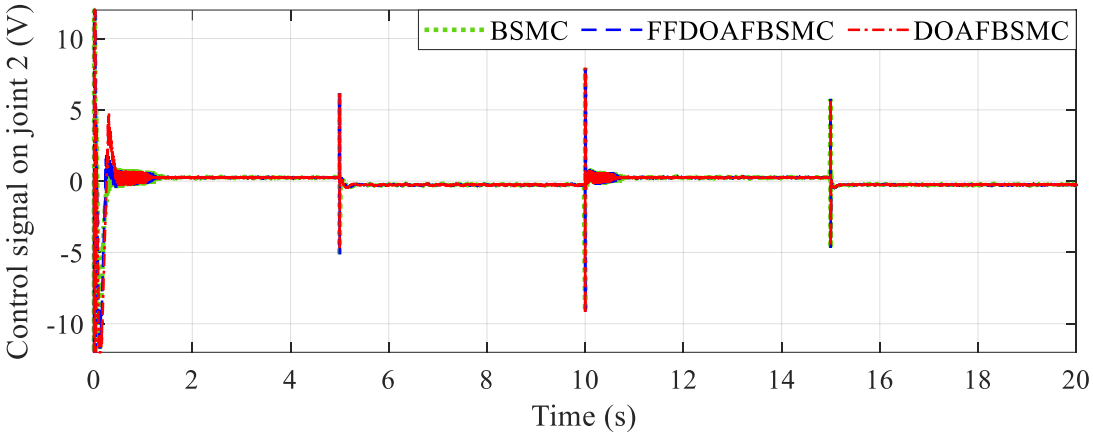

(b)

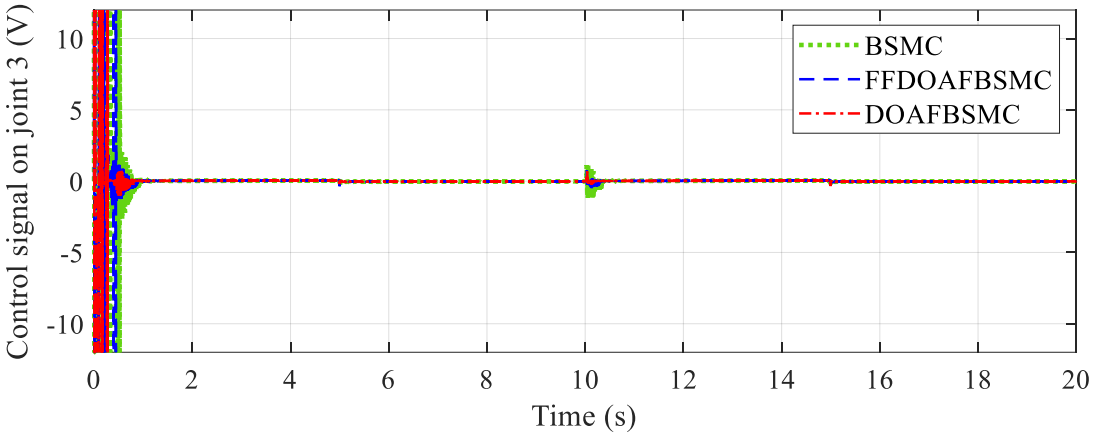

(c)

Figure 4-16 The control signal acting on the: (a) *first joint*, (b) *second joint, and* (c) *third joint.*

4.4.2 Case study 2

In this case, sine function signals are used as the desired performance. The three joints trajectory are designed as:

$$\mathbf{q}_d = \begin{pmatrix} q_{d1} \\ q_{d2} \\ q_{d3} \end{pmatrix} = \begin{pmatrix} 60\sin\left(\pi t/5 - \pi/2\right) \\ 40\sin\left(\pi t/5 - \pi/2\right) + 60 \\ 60\sin\left(\pi t/5 - \pi/2\right) + 90 \end{pmatrix} \text{(degree)} \tag{4.90}$$

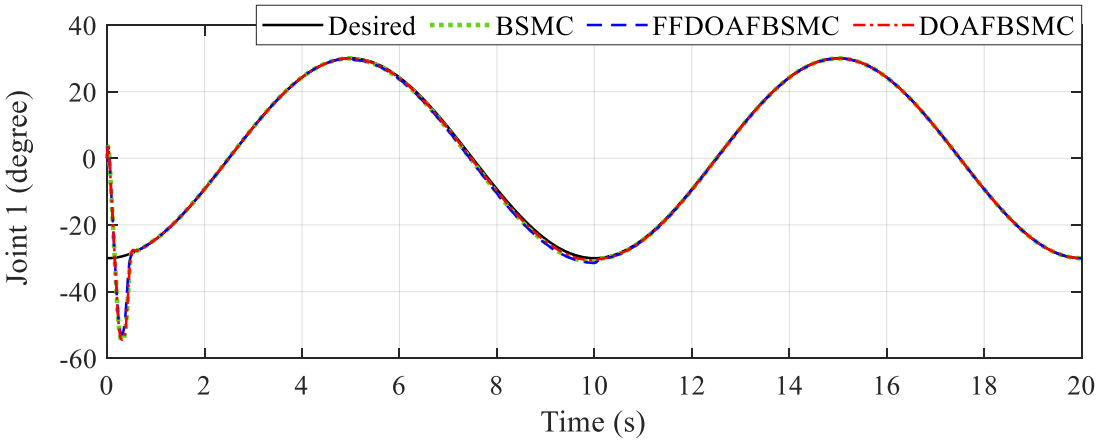

(a)

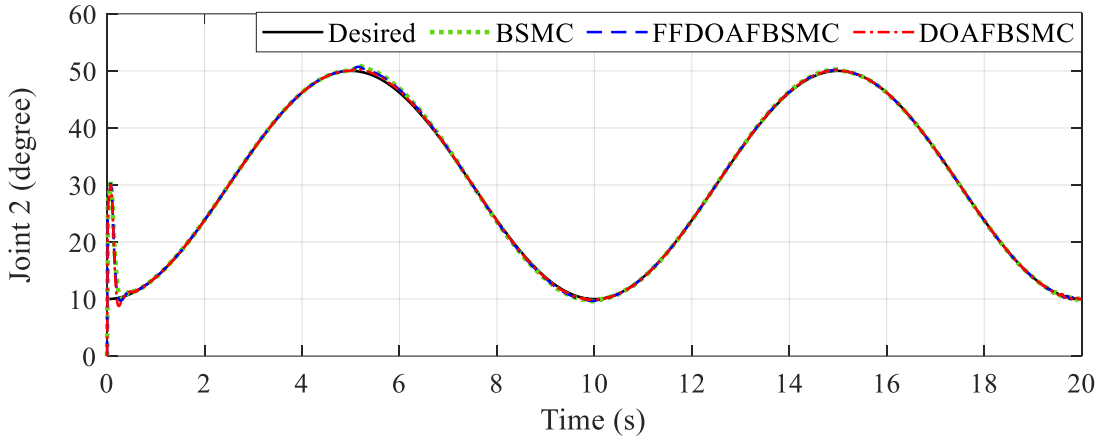

(b)

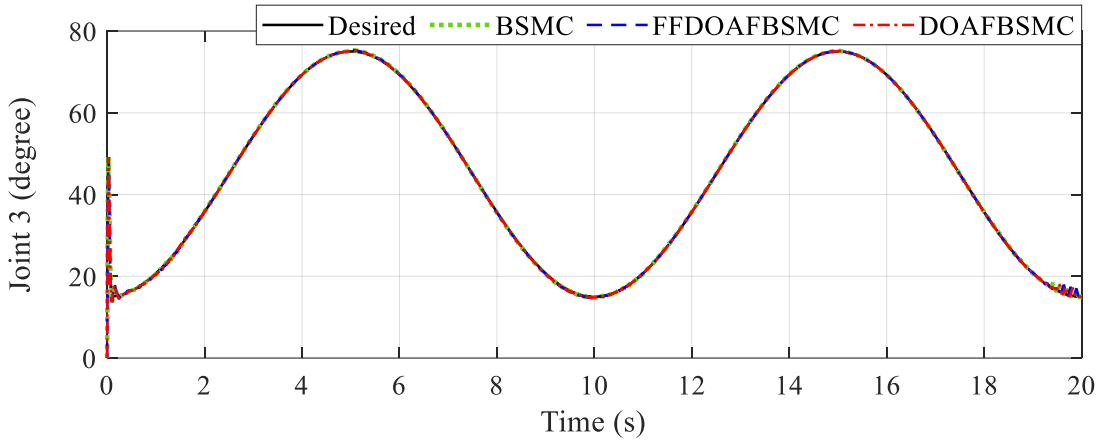

(c)

Figure 4-17 The tracking performance of the: (a) *first joint;* (b) *second joint;* (c) *third joint.*

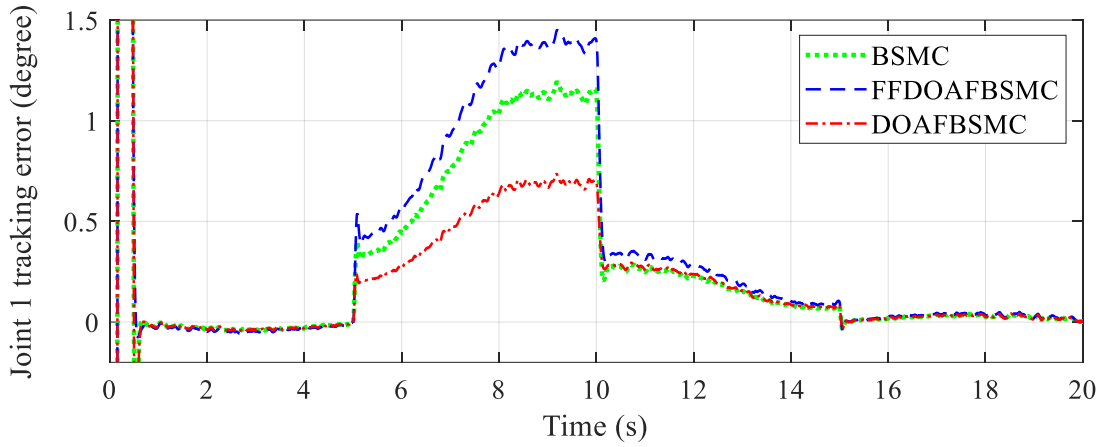

(a)

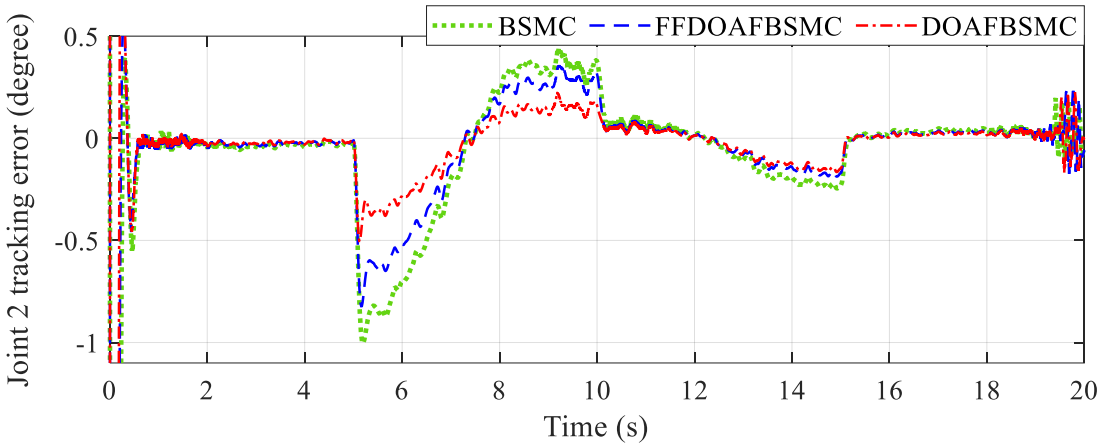

(b)

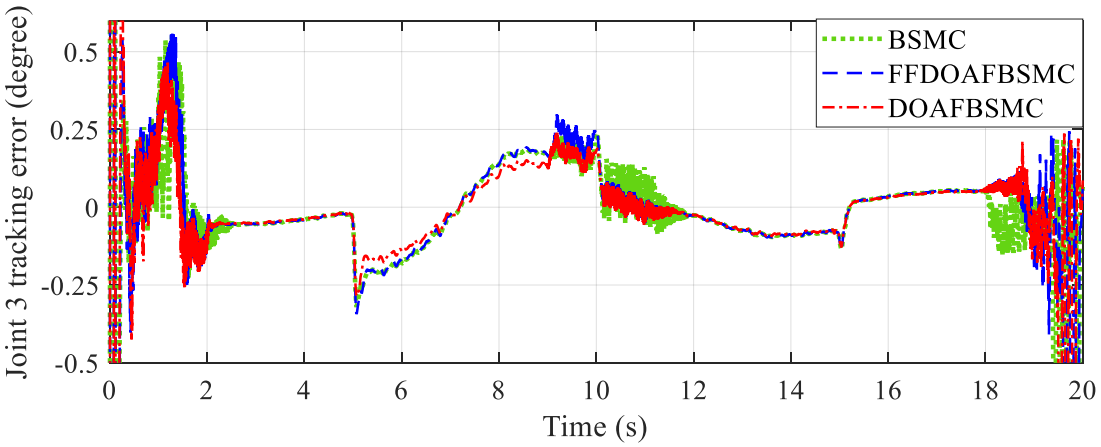

(c)

Figure 4-18 The tracking error of: (a) *The first joint,* (b) *the second joint, and* (c) *the third joint.*

In this case study, the sinusoidal signals are used as a smooth function to investigate the feedback states. The tracking performance and tracking error of the three joints are described in **Figure 4-17** and **Figure 4-18**, respectively. The load torques estimated are depicted in **Figure 4-19** and the control input

signals are depicted in **Figure 4-20**. As can be seen in Figure 14, no matter how changed the load torques is, the DO can estimate its change for the compensation.

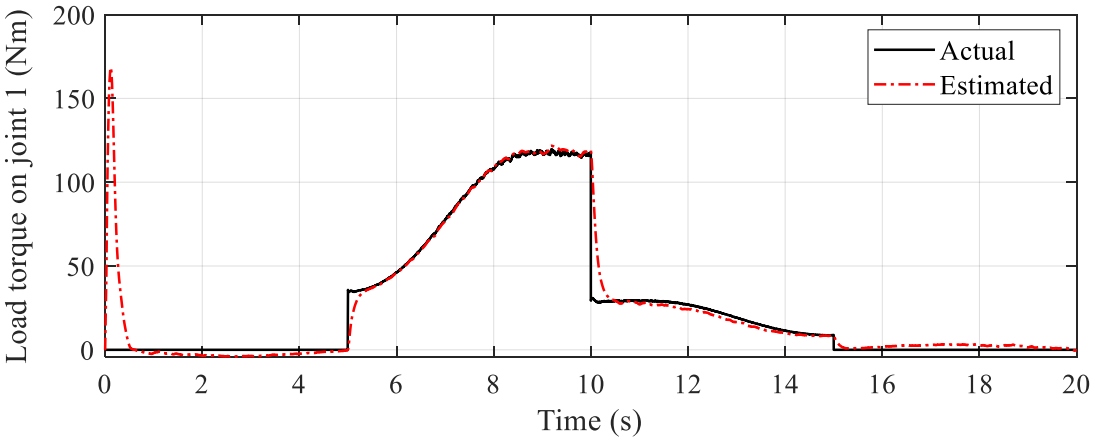

(a)

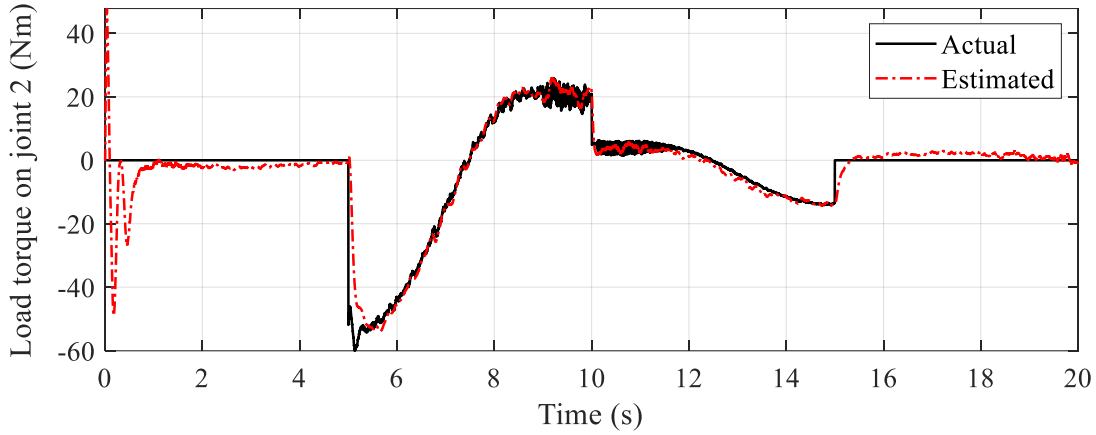

(b)

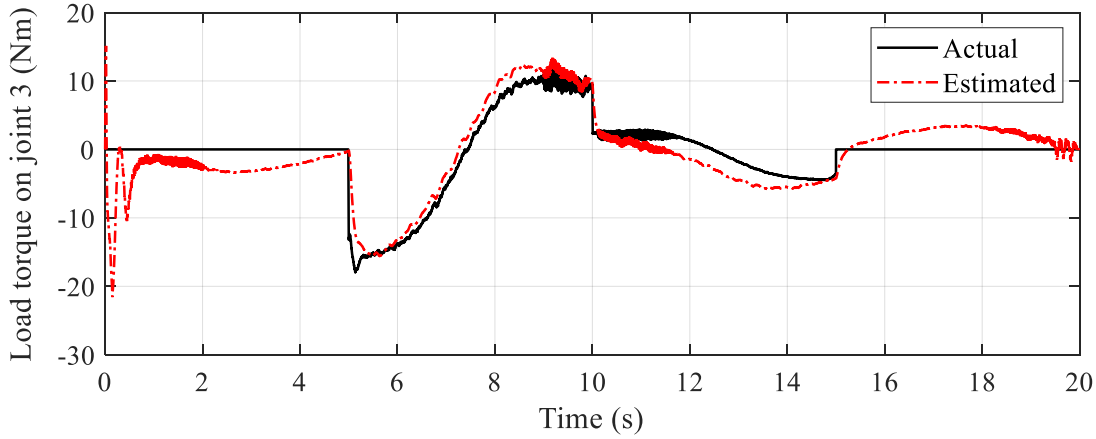

(c)

Figure 4-19 The load torque estimated of the: (a) *first joint,* (b) *second joint, and* (c) *third joint.*

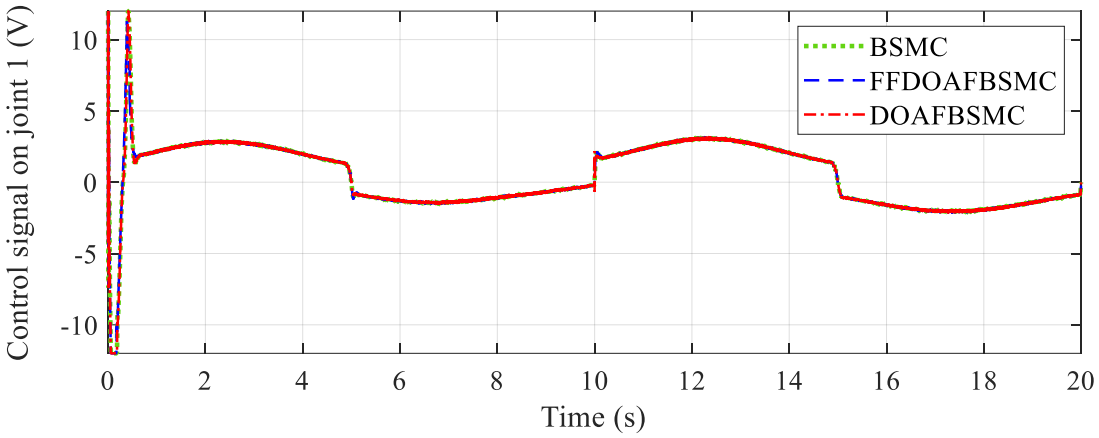

(a)

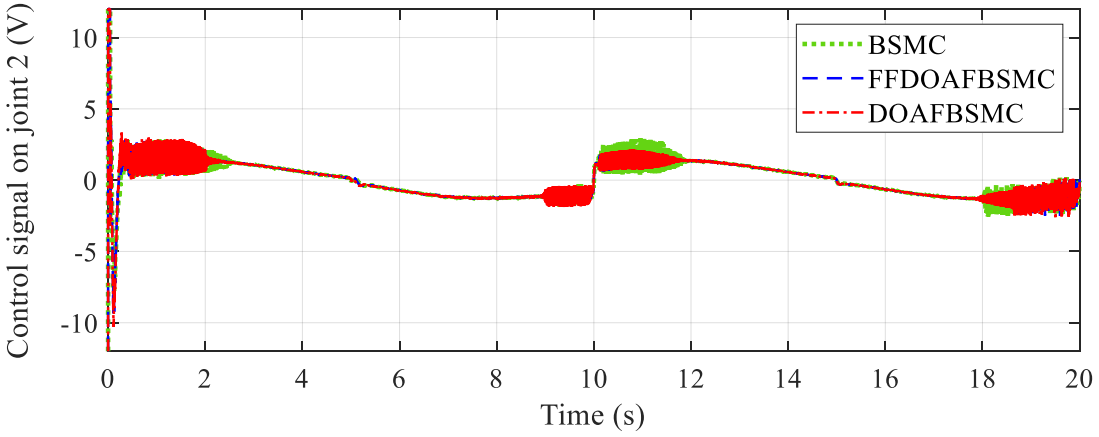

(b)

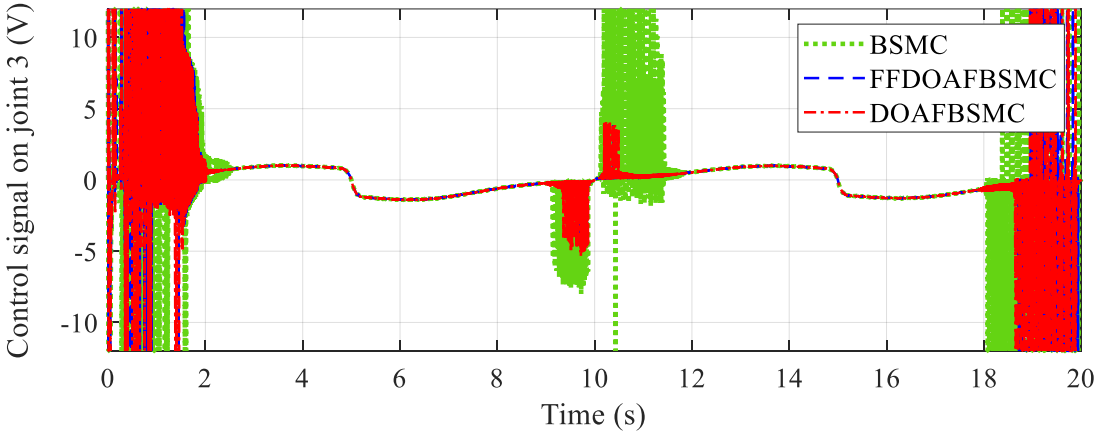

(c)

Figure 4-20 The control signal acting on the: (a) *first joint,* (b) *second joint, and* (c) *third joint.*

4.4.3 Case study 3

This last simulation is implemented in task space (Cartesian co-ordinate). The end-effector is controlled to track the ellipse curve. The desired trajectory based on the working space of the robot in 3D space is supposed to be:

$$\mathbf{P} = \begin{pmatrix} P_x \\ P_y \\ P_z \end{pmatrix} = \begin{pmatrix} 0.3 + 0.1\sin(\pi t / 5) \\ 0.2\sin(\pi t / 5) \\ -0.55 + 0.1(P_x + P_y) \end{pmatrix} (m) \tag{4.91}$$

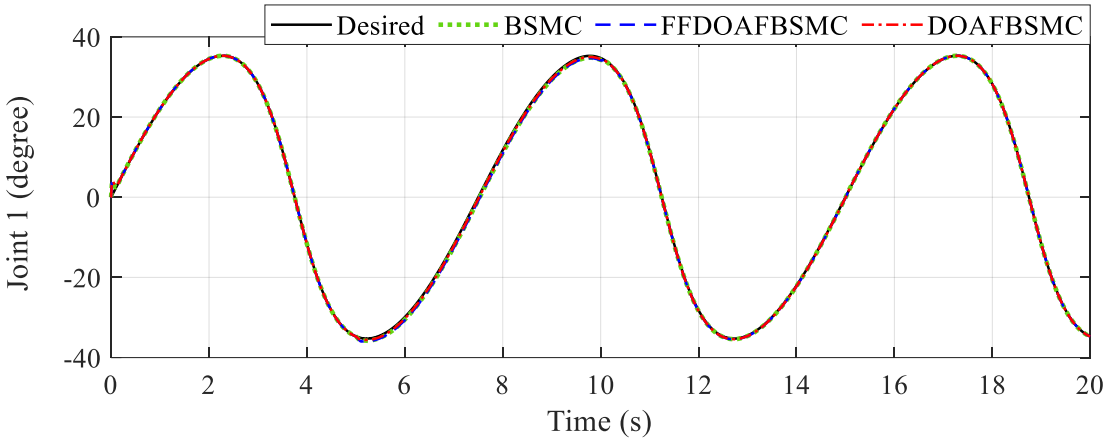

(a)

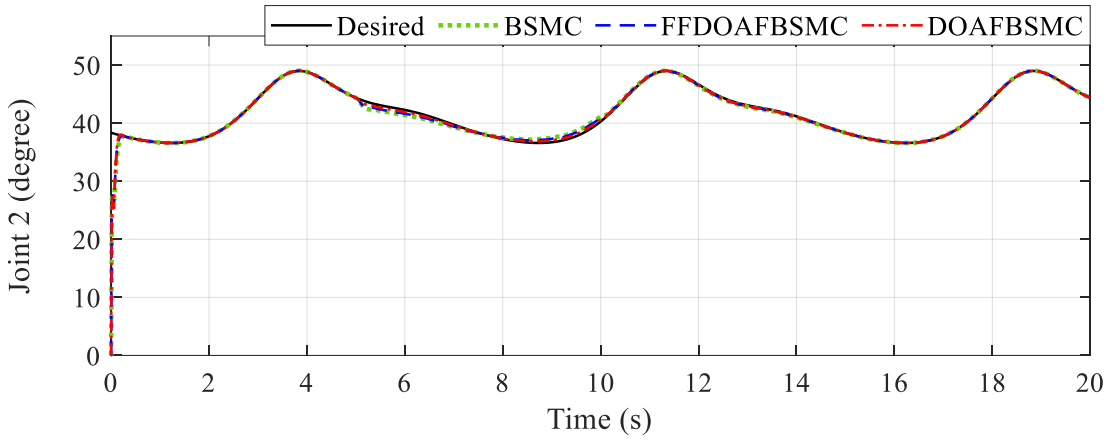

(b)

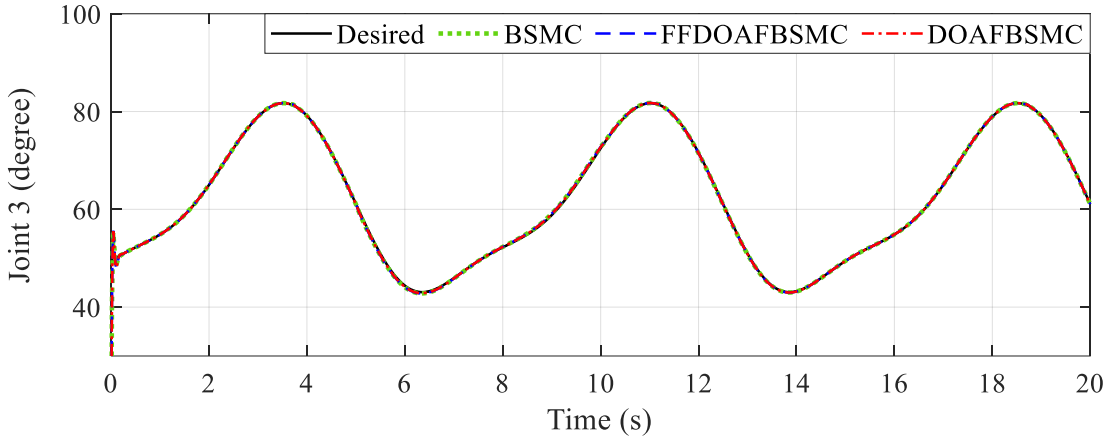

(c)

Figure 4-21 The tracking performance of the: (a) *first joint;* (b) *second joint;* (c) *third joint.*

The Jacobian matrix is expressed in Appendix A. The tracking performance and the tracking error of the three joints are described in **Figure 4-21** and **Figure 4-22**, respectively. The end-effector behavior in X, Y, Z directions and in 3D Cartesian space is depicted in **Figure 4-23** and **Figure 4-24**, respectively. The load torques estimated are depicted in **Figure 4-25** and **Figure 4-26** shows the control input signals of the three joints.

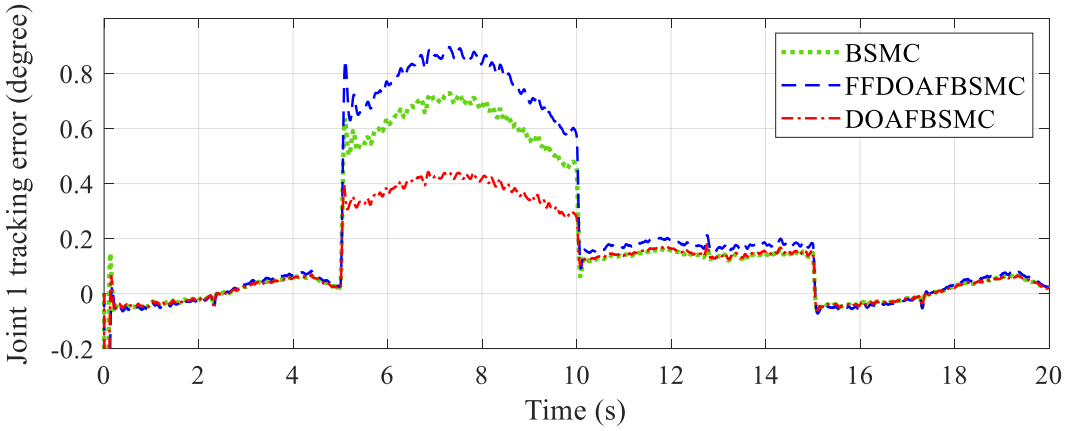

(a)

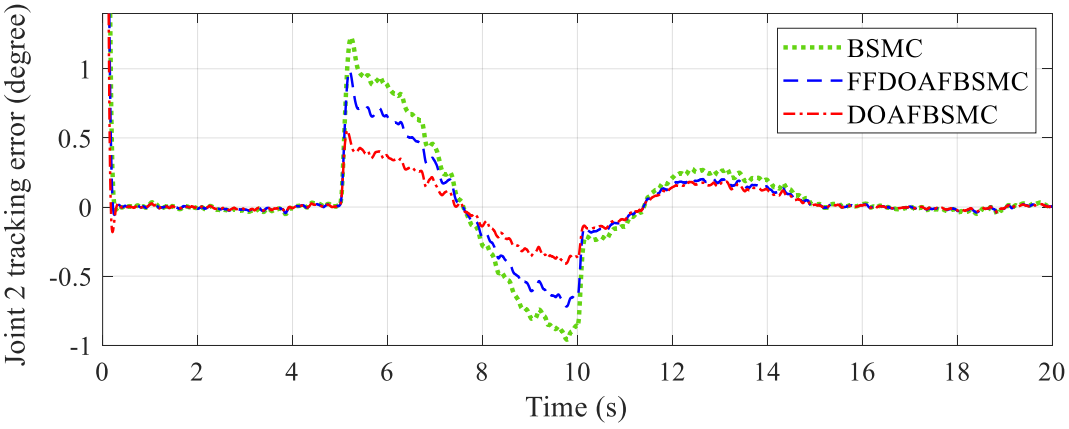

(b)

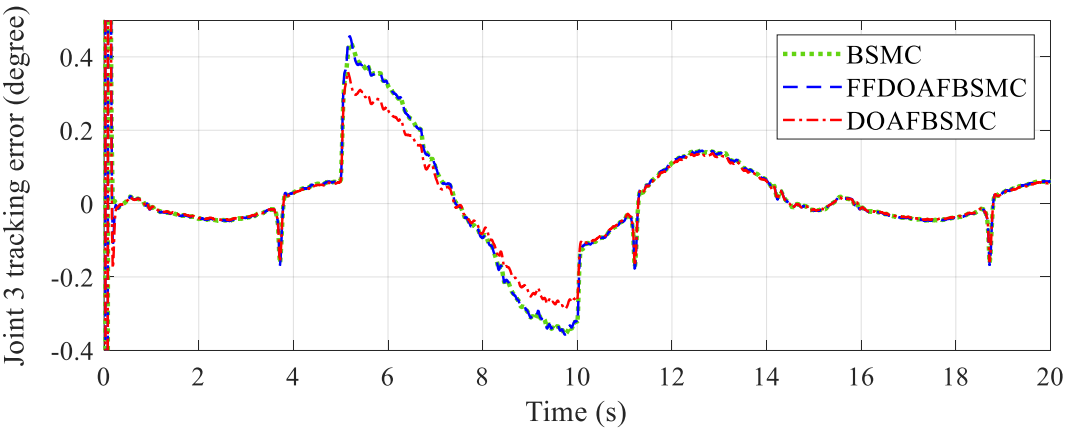

(c)

Figure 4-22 The tracking error of the: (a) *first joint*, (b) *second joint, and* (c) *third joint.*

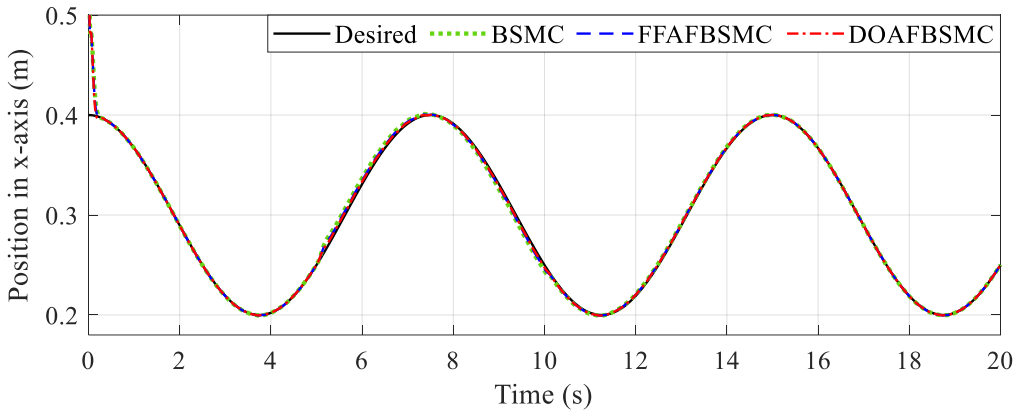

(a)

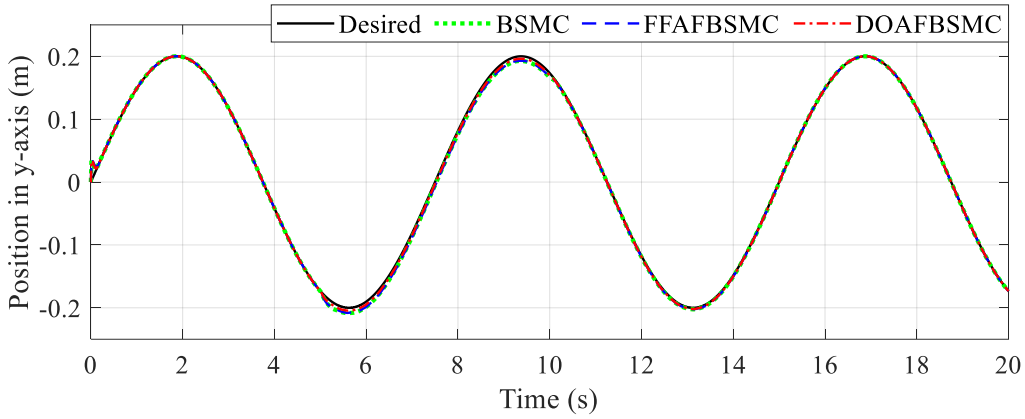

(b)

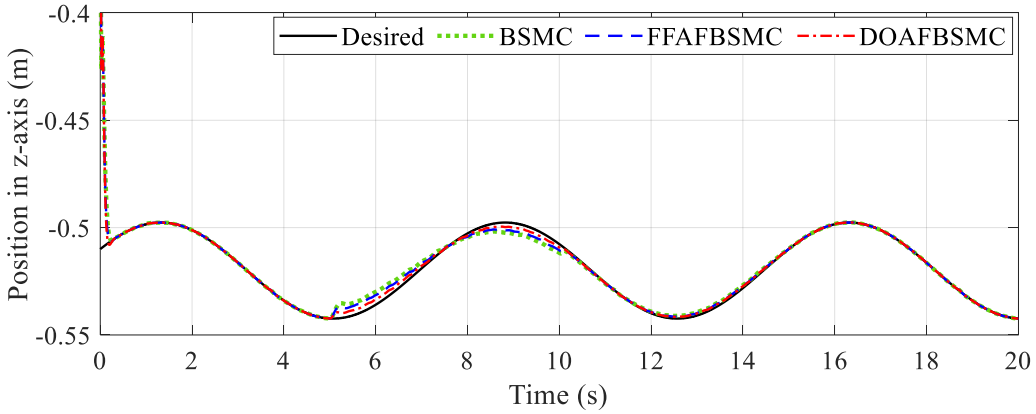

(c)

Figure 4-23 The tracking performance in: (a) *X direction,* (b) *Y direction, and* (c) *Z direction.*

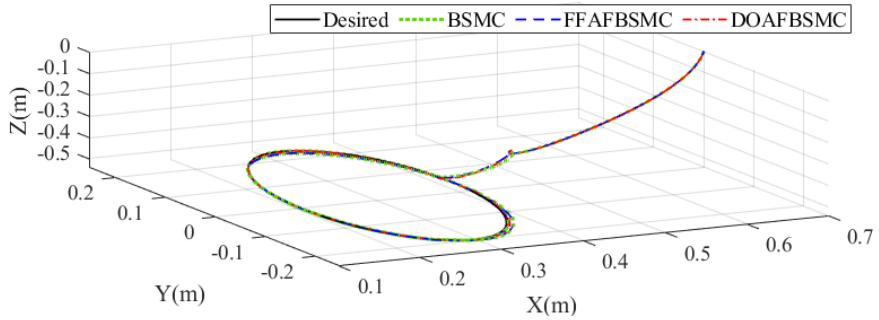

Figure 4-24 Response of the manipulator in 3D space.

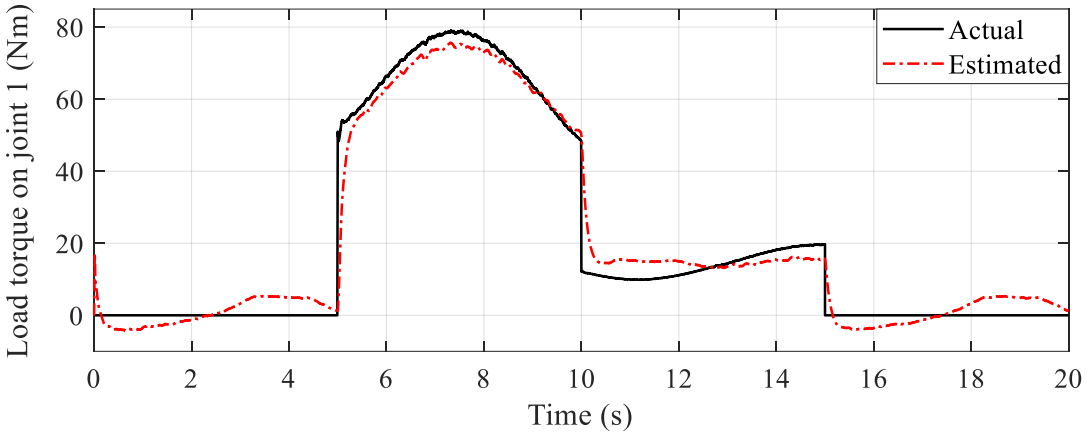

(a)

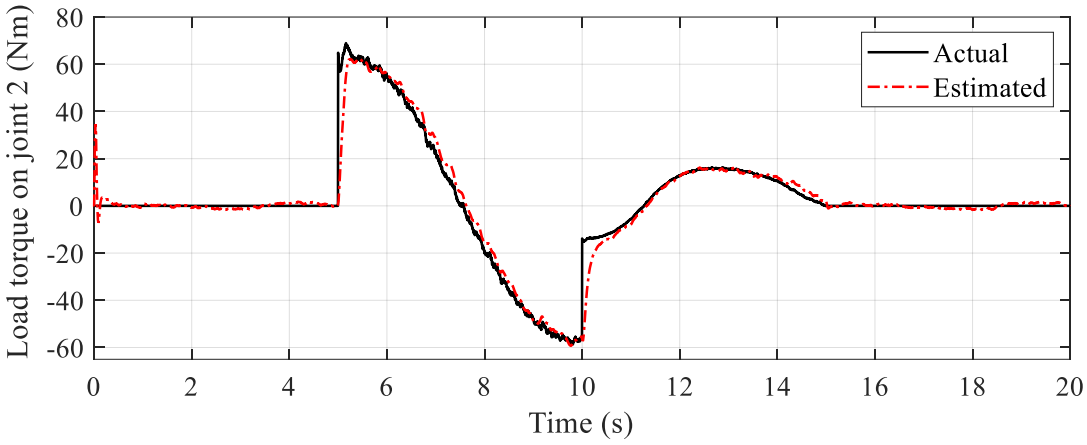

(b)

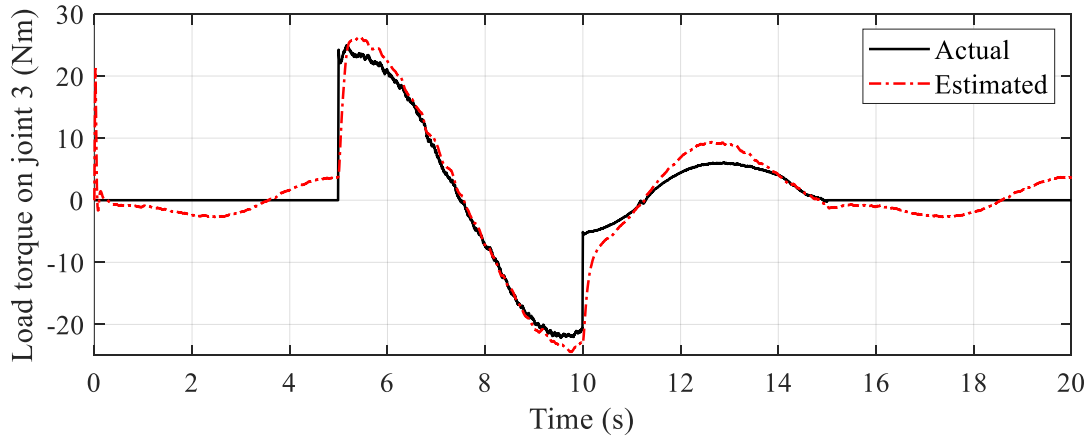

(c)

Figure 4-25 The load torque estimated on (a) *first joint,* (b) *second joint, and* (c) *third joint.*

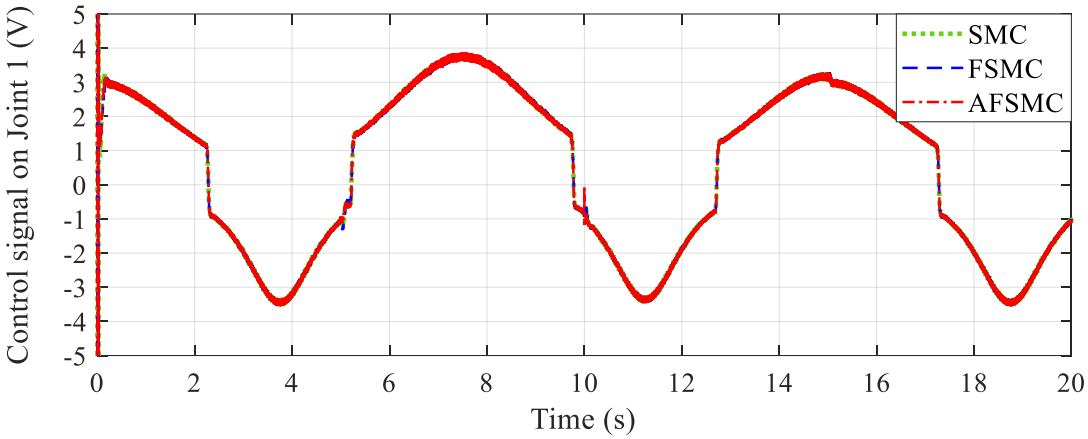

(a)

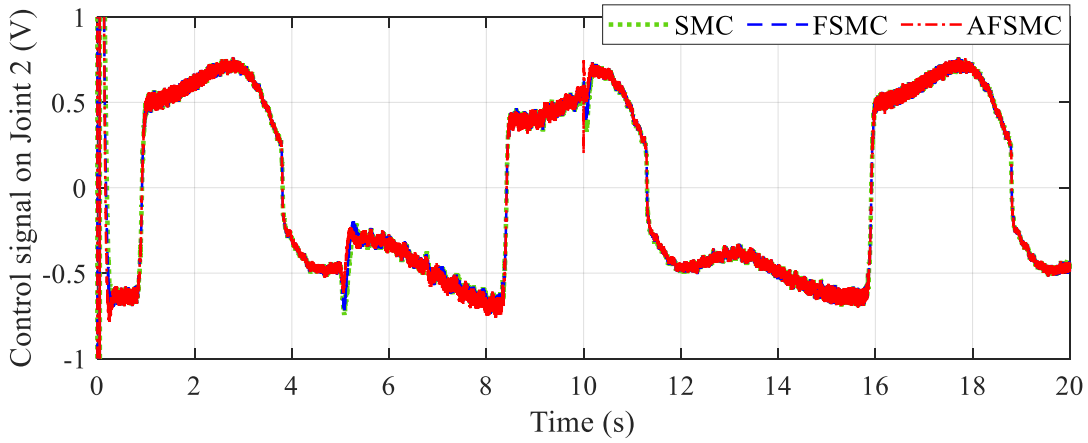

(b)

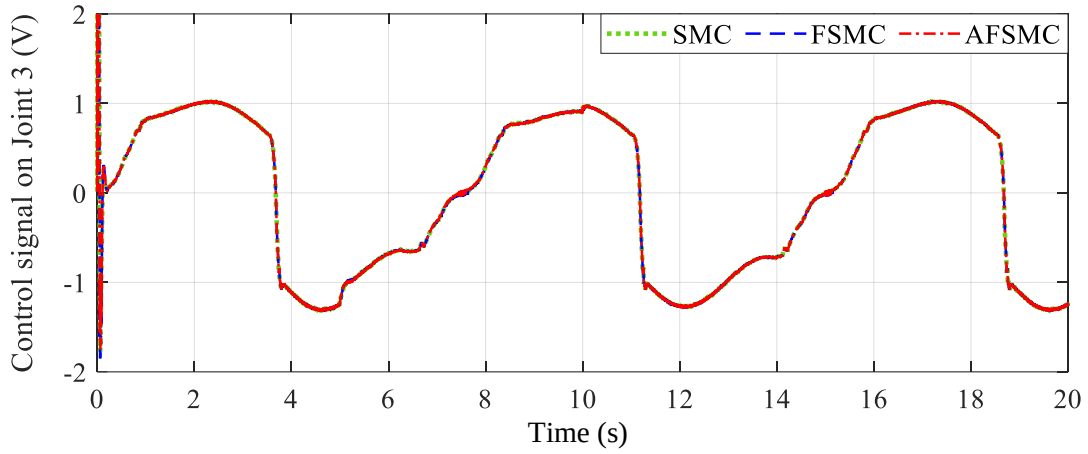

(c)

Figure 4-26 The control signal acting on the: (a) *first joint,* (b) *second joint, and* (c) *third joint.*

In the three case studies, the payload suddenly changes to 20 kg at the 5th second and drops to 5 kg and zero at the 10th and 15th second, respectively. The change of the payload results in changing in the external loads torque. As can be seen in **Figures 4-11**, **4-15**, and **4-19** corresponding to the three case studies, the torques load can be observed and its profile correspond to that of the payload. The

observed torques load of the second joint are similar to that of the third joint because of the same motion in the space. Owing to the fuzzy rules described in Table 2, the observed torques load can track the actual one, thus calculating and compensating the control signals. Herein only the magnitude of the torques load is considered because neither of the values of torques load are negative or positive, they all affect the tracking performance of the system. With the adaptive law for torques load compensation, the AFSMC can exhibit and achieve the best performance in comparison with conventional SMC and FSMC. The conventional sliding mode scheme can adopt the robustness; however, the trackability is degraded due to the changing parameters affecting indirectly the manipulator dynamics. When applying the fuzzy logic system, the control signals can be partially compensated, and with the use of compensator inherited from using disturbance observer (DO), the exerted torques load have been observed and the trackability is improved significantly.

4.5 Experiments

4.5.1 Experimental test bench setup

To verify and compare with the simulation, the proposed algorithm is applied on the real 3-DOF hydraulic manipulator. The hardware connection is depicted in **Figure 4-27**. The dash lines stand for the data derived from the system, and the solid lines stand for the command signal from the computer. The hardware setup includes the computer (PC) for data processing, the hydraulic supply for the manipulator, and the 3-DOF hydraulic manipulator communicating with the PC via terminal 68 LPR and the PCIE Card (PCIE-6363). The hydraulic manipulator supplied by the hydraulic system is driven by electro-hydraulic actuators equipped with incremental rotary encoders E40H6-5000-3-V-5 to measure the movement. The data read from encoders is then processed by the MATLAB program via PCIE card. After processing, the command signal from the computer is sent to the system to drive the servo valve amplifier SVA-R-1, thus generating the manipulator to follow the desired trajectory.

4.5.2 Experimental Results

In the experiments, we consider three case studies. The parameters of the system are same as defined in Tables 3 and 4. The initial of the three joints is set when the actuators reach the limited position (maximum extend for cylinder and maximum angular position for rotary actuators). The parameter of the sliding surface is $\boldsymbol{\lambda}_1$ = diag (35, 30, 25), and the parameters of the robust terms in Equation (4.49) are $\mathbf{K}_1 = diag(40, 40, 40)$ and $\boldsymbol{\eta}_1$ = *diag* (1.8, 1.8, 1). The values of $\mathbf{K}_1$ and $\boldsymbol{\eta}_1$ are different from the simulation because the real system has many uncertainties because of its structure and

the different drivers used to run the manipulator, the gain is scheduled such that the system can operate smoothly. All the controller gains are kept same in the three case studies.

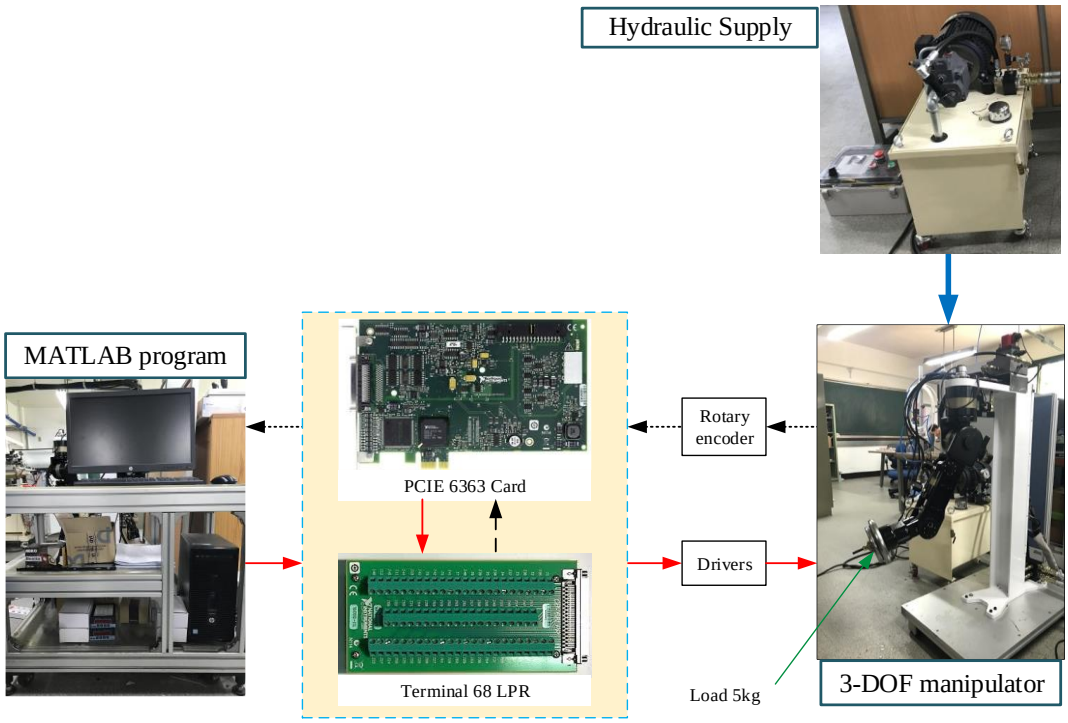

Figure 4-27 Setup test bend for experiments.

4.5.2.1 Case study 1

The sinusoidal signal desired trajectory is considered and set as:

$$\mathbf{q}_d = \begin{pmatrix} q_{d1} \\ q_{d2} \\ q_{d3} \end{pmatrix} = \begin{pmatrix} 30\sin\left(2\pi t/5\right) \\ 30+20\sin\left(2\pi t/5+\pi/2\right) \\ 40+20\sin\left(2\pi t/5\right) \end{pmatrix} (\text{degree}) \tag{4.92}$$

In this case study, no load is attached into the end-effector. Therefore, the comparison is implemented between the conventional back-stepping slide ding mode control (BSMC) and AFBSMC. The tracking performance and tracking error of the three joints is described in **Figure 4-28** and **Figure 4-29**, respectively.

4.5.2.2 Case study 2

The desired trajectory is set as same sinusoidal signal as the first case study, but 5 kg external payload is attached. The tracking performance and tracking error of the three joints is depicted in **Figure 4-30** and **Figure 4-31**, respectively.

4.5.2.3 Case study 3

Step signal is applied instead of using smooth signal like the two above case studies or tooth saw profile like in the simulation. The controller parameters are still kept same as the original value setup above. The tracking performance and tracking error of the system is shown in **Figure 4-32** and **Figure 4-33**, respectively.

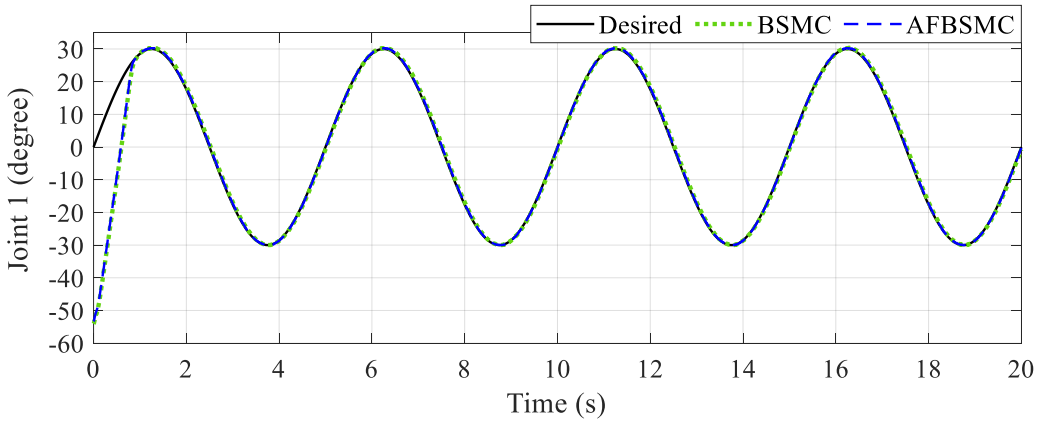

(a)

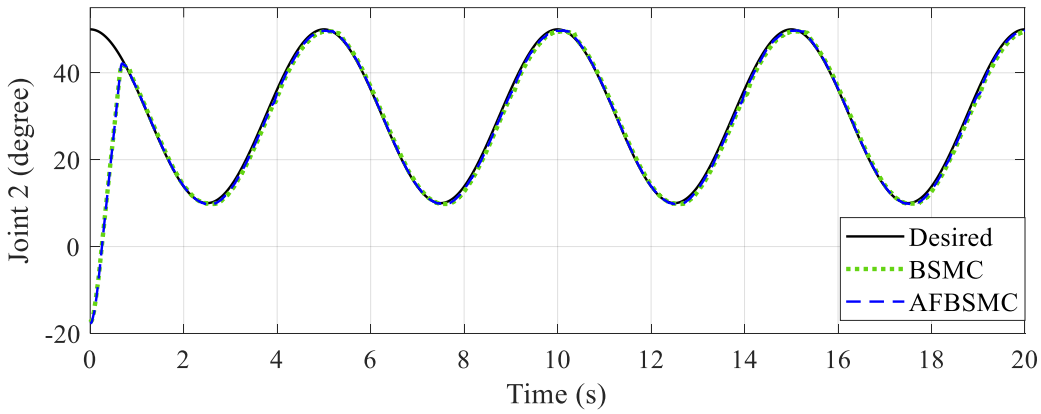

(b)

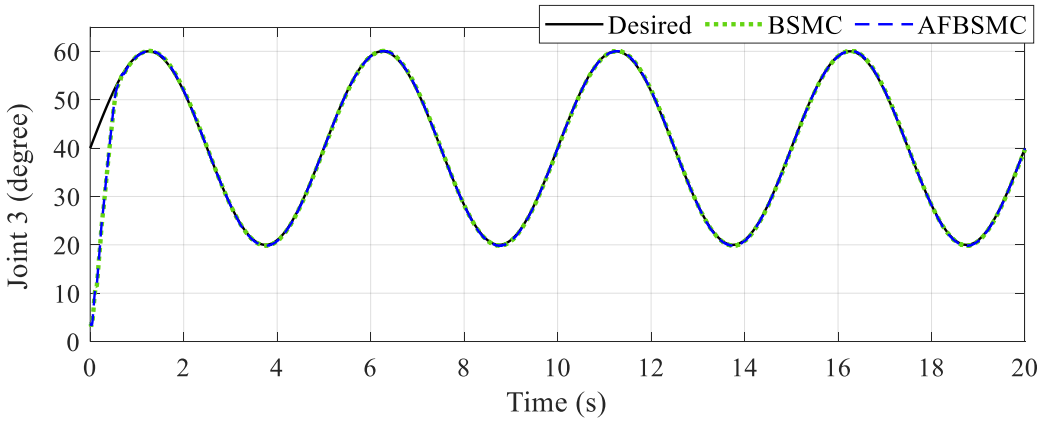

(c)

Figure 4-28 Case study 1: The tracking performance, in case of sinusoidal signal without load, of the: (a) first joint; (b) second joint; (c) third joint.

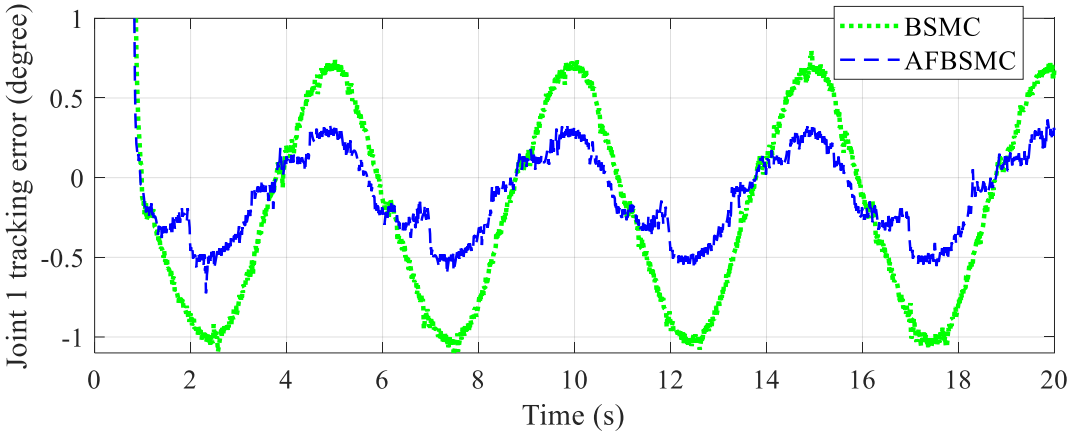

(a)

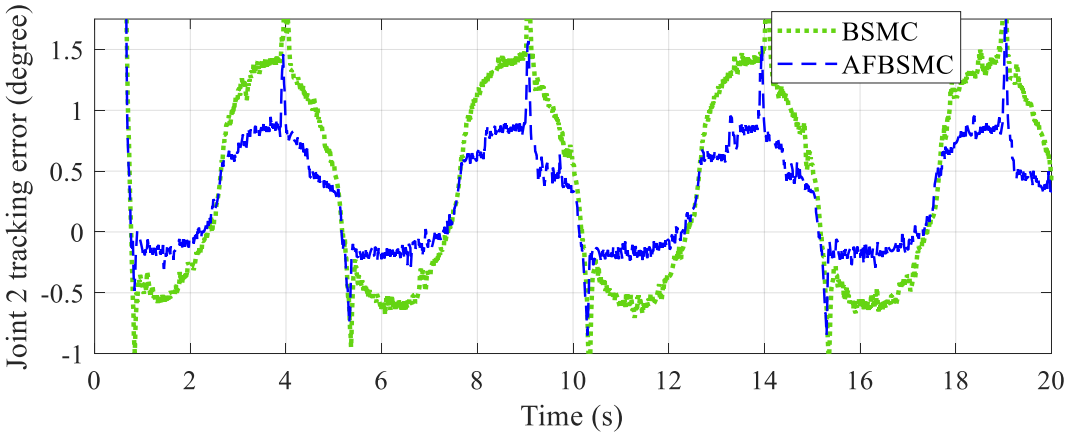

(b)

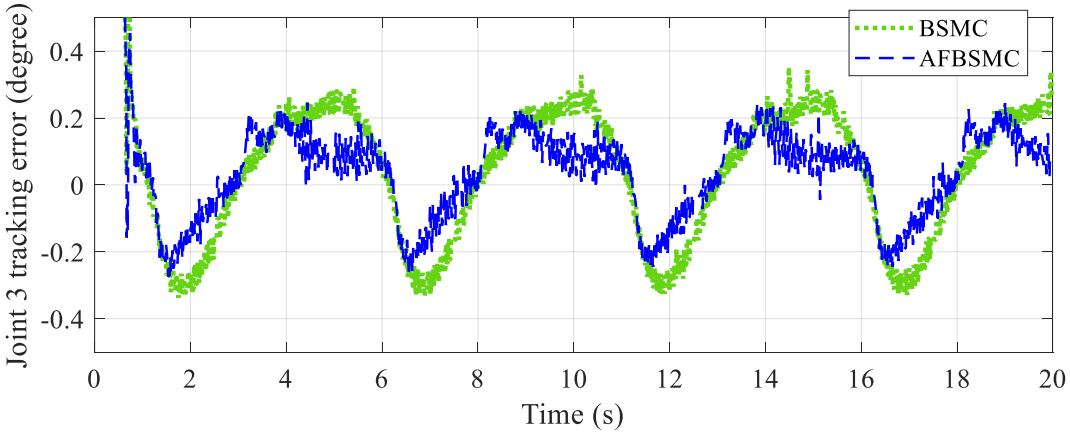

(c)

Figure 4-29 Case study 1: The tracking error, in case of sinusoidal signal without load, of the: (a) first joint; (b) second joint; (c) third joint.

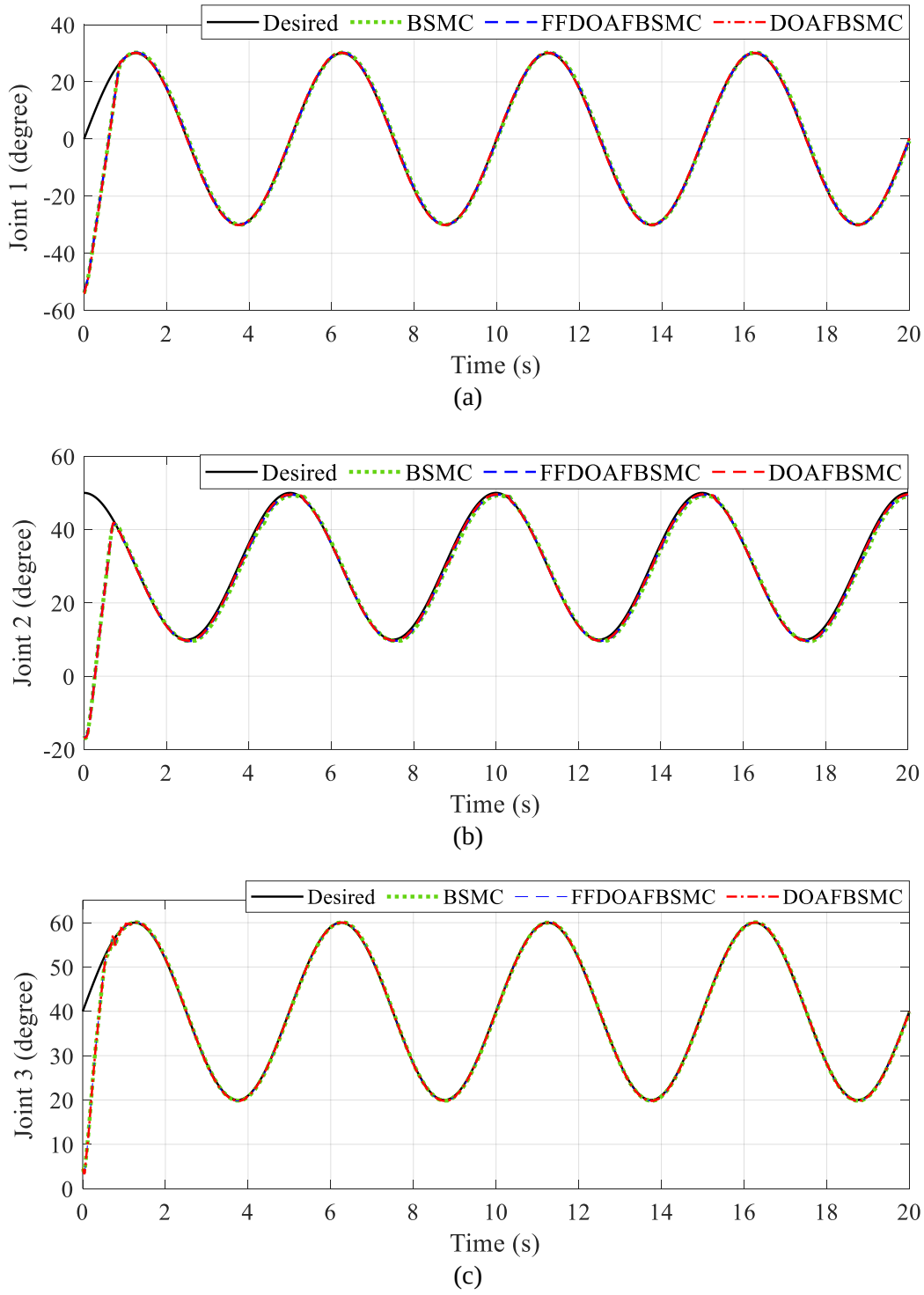

Figure 4-30 Case study 2: Tracking performance, in case of sinusoidal signal with load, of the: (a) first joint; (b) second joint; (c) third joint.

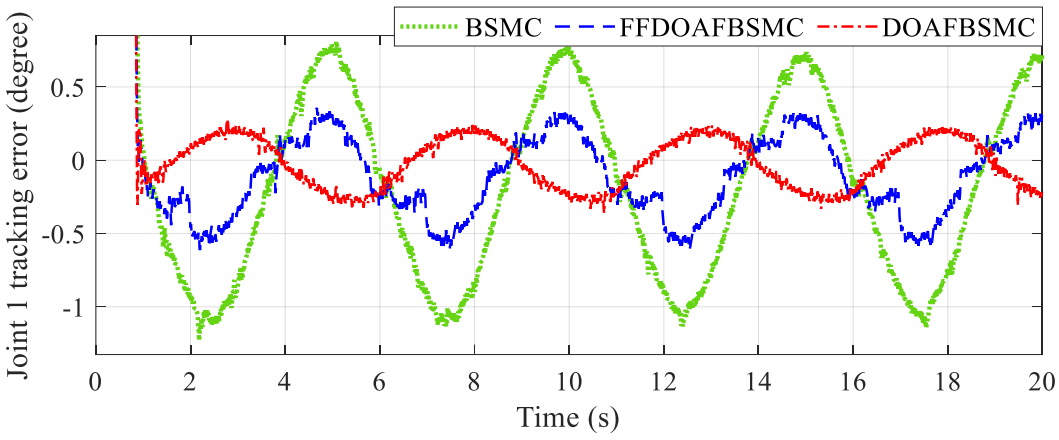

(a)

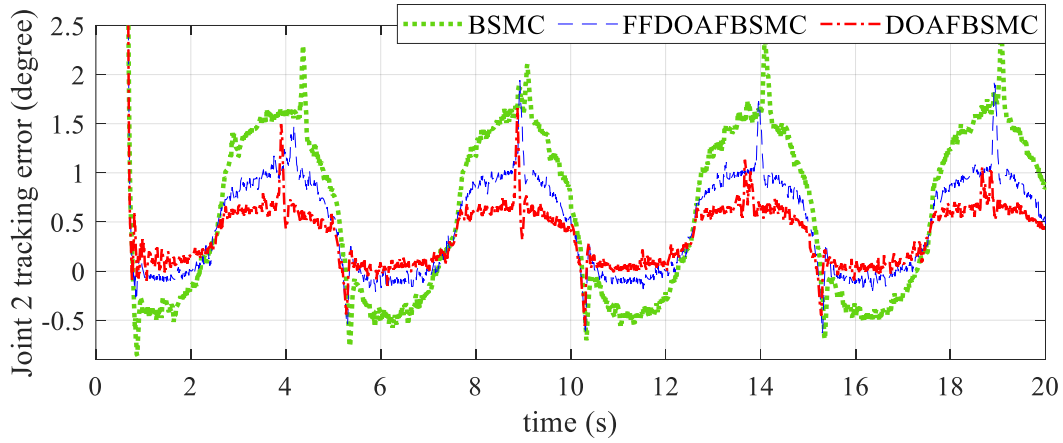

(b)

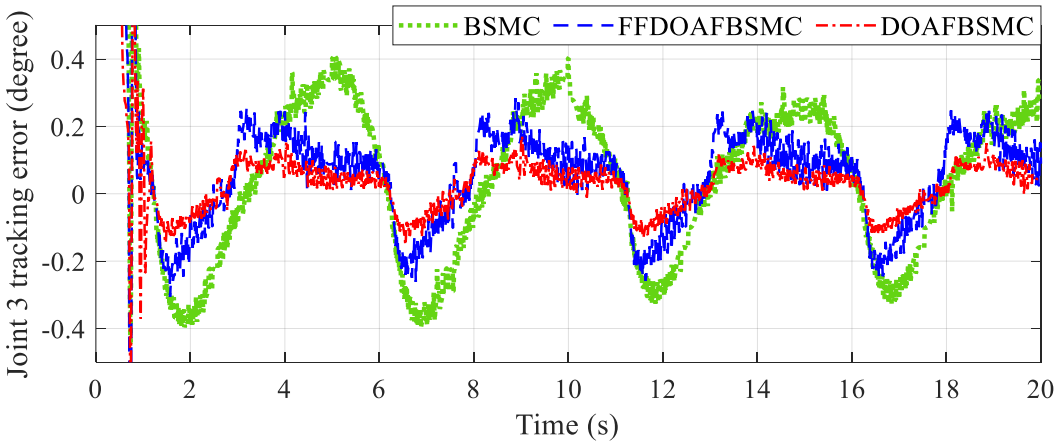

(c)

Figure 4-31 Case study 2: Tracking error, in case of sinusoidal signal with load, of the: (a) first joint; (b) second joint; (c) third joint.

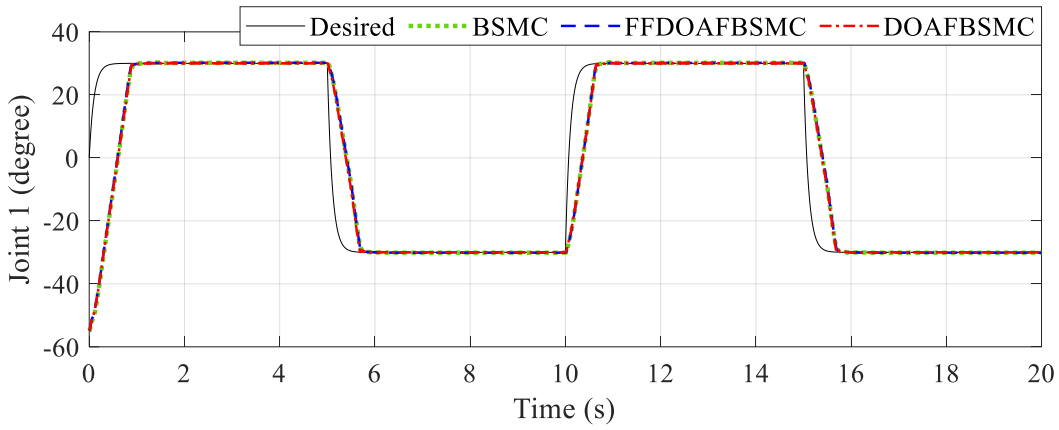

(a)

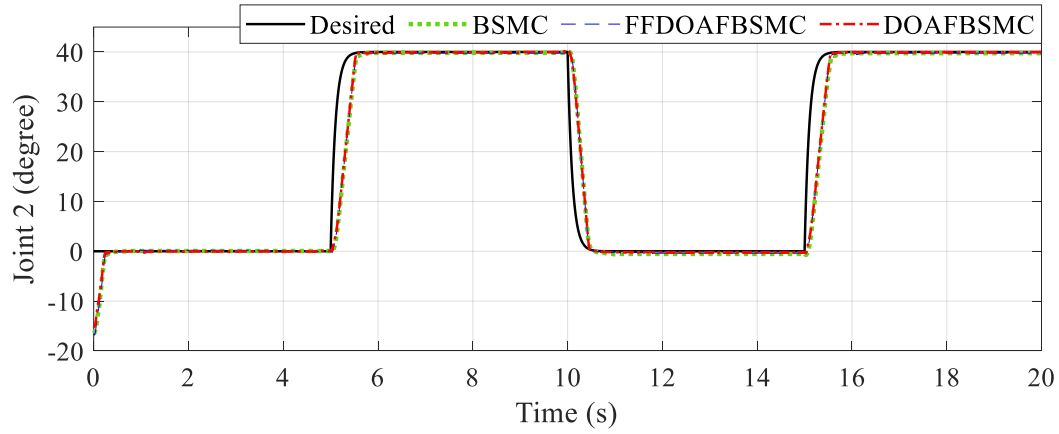

(b)

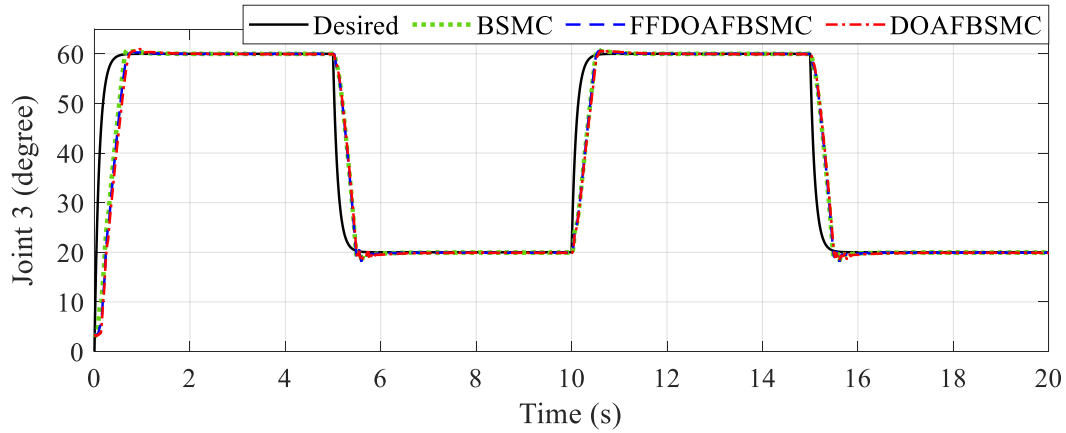

(c)

Figure 4-32 Case study 3: Tracking performance, in the case of step response, of the: (a) first joint; (b) second joint; (c) third joint.

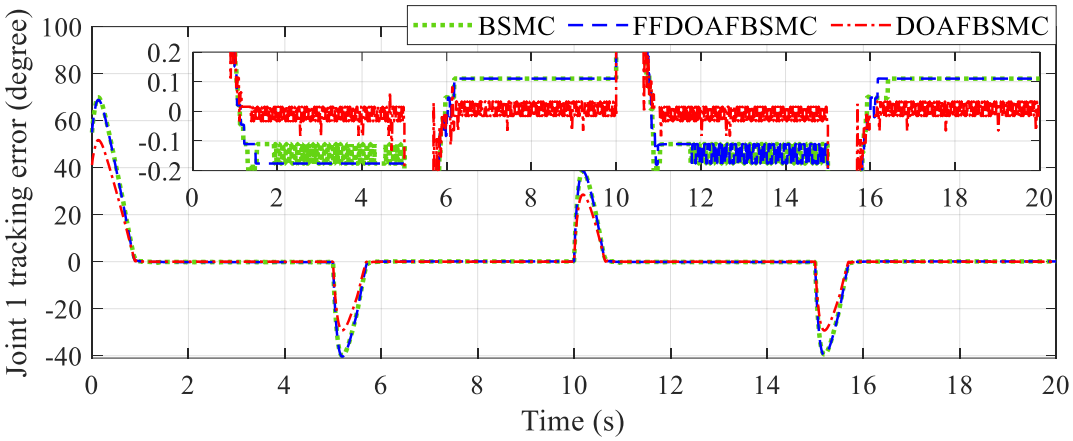

(a)

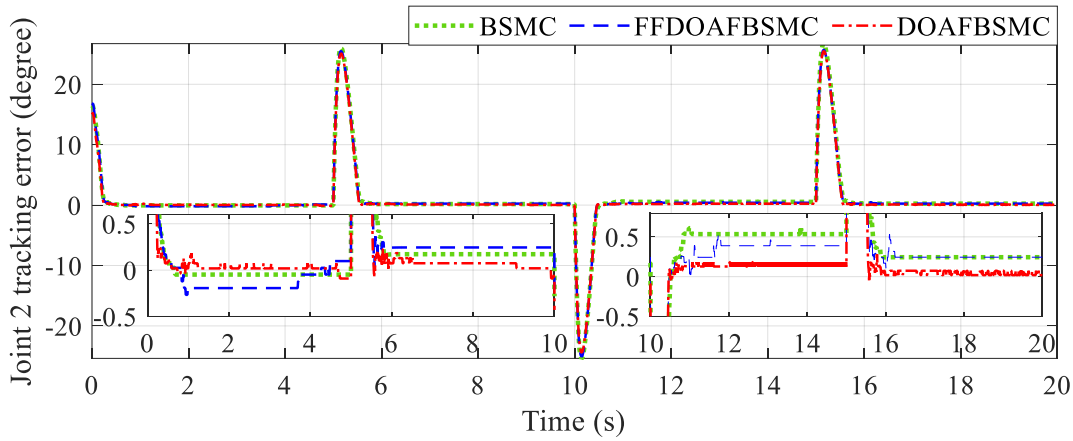

(b)

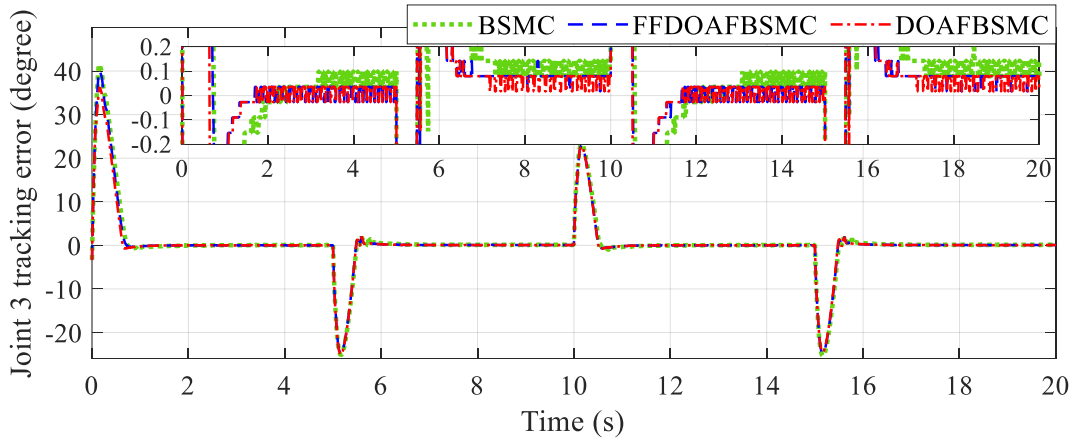

(c)

Figure 4-33 Case study 3: Tracking error, in the case of step response, of the: (a) first joint; (b) second joint; (c) third joint.

As can be seen in the three case studies, depicted from **Figure 4-28** to **Figure 4-33**, especially in the second and third case studies, the performance of the three joints is quite similar with the simulations,

in which the errors when employing the DOAFBSMC is the smallest compared with that of the FFDOAFBSMC) and conventional ABSMC. The error of the third joint in case of load and without load is quite similar. This can be explained as the short length of the third joint gets less affected from the load. But because of the length in the second link and dynamics coupling torque between the third and the second link, the error of the second joint is a little greater than that of when no load affected. When utilizing AFBSMC, the error decreased significantly. Same profile in the first joint in comparison between with and without load.

4.6 Discussions

In this study, the behavior of the 3-DOF hydraulic manipulator including actuator was analyzed. The tracking performance of the manipulator was investigated under the presence of the external payload. This main issue was addressed by using the proposed DOAFBSMC control scheme. It employed the advantages of the SMC in reducing the order system, strong robustness against perturbation, and BSP control in solving both the problem of stabilization and tracking trajectory. Besides, the GMO technique was employed to observe the change in the external torques induced by the variation of the external payload to adopt to the working condition. Comparative simulations and experiments were given, with the added noise and external payload, between the proposed algorithm with the conventional BSMC and FFDOAFBSMC to verify the effectiveness of the proposed methodology. The results proved that the proposed control methodology could improve the qualification of the 3-DOF hydraulic manipulator under the vastly changed payload, occurring during operation in practice. However, referring to the GMO design procedure, the accuracy of the external force estimation notably depended on the system dynamics. Therefore, this technique is restricted by the required well-known model to achieve an accurate estimation.

Chapter 5
Fault estimation and Fault-tolerant Control for n-DOF serial Hydraulic Manipulator in Constrained Motion

5.1 Introduction

Although the tracking performance could be achieved, all automatically controlled systems may be inevitably subjected to faults caused by system element, actuator or sensor in practice. The actuator and sensor faults are more popular due to the coupled association with the control algorithms design. As the highly coupled nonlinear characteristics, the actuator fault causes obvious effects on the system dynamics; therefore, they can be easily detected through monitoring abnormal system performances. Following the literature of actuator fault detection and isolation and estimation, such fault can be considered as matched or mismatched disturbances and observed by using observers such as ESO [26–28], DO [15], [29–31], uncertainty and disturbance estimator (UDE) [32,33], time-delayed estimation (TDE) [34–36], super-twisting algorithm [37], Kalman estimators [38], unknown input observer [39, 40], etc. Then, Fault-tolerant control (FTC) that combines these observers compensation with advanced control algorithms such as active disturbance rejection control (ADRC) [41,42], adaptive algorithms [43–45], or passive FTC with high robust gains can be employed to address the influence of the actuator fault.

Meanwhile, the sensor fault is generated from unknown constant or time-variant offset added to the measured signal and does not cause obvious influences. Due to the additive measurements, the system behavior is the same as the fault-free condition, but the measured feedback signal cannot present the true value of the system states. However, wrong feedback signal results in an unsuitable execution in terms of physical interactions; thus, being able to cause severe problems such as system performance deterioration and instability, loss of information fidelity unless promptly addressing [46]. Therefore, the main objective of the sensor fault detection is to critically achieve a fast and reliable sensor fault detection and estimation. Various methodologies for this topic were proposed. Nguyen et al. [47,48] employed a nonlinear UIO to detect the sensor fault on the mini motion package EHS. Nahian et al. [49] used an extended Kalman-Bucy unknown input observer to detect the sensor fault and estimate the system state and developed an FTC for the EHS. Brambilla et al [50] and Capisani et al [51] conducted a bank of observers based on the SMO for sensor fault detection and isolation on serial manipulators. Pang et al. constructed an active FTC with the SMO to address the influence of sensor fault on

automobile active suspension systems. Paviglianiti et al. [52] proposed a robust fault detection based on traditional Luenberger observer to detect and isolate the sensor faults on multi-output system. Various approaches can be referred from [53–55]. The UIO and SMO are usually employed for fault detection and isolation; however, the complicated calculation using LMI and requirement of coordinate transformation increase the difficulty for high-order nonlinear systems. The sensor faults, in another aspect, can be considered as extended states of the controlled system. Therefore, other methods, such as using extended state observer (ESO) or adaptive laws, can be constructed to effectively estimate the magnitude of the faulty signals. Sun et al. [84] proposed an adaptive observer to estimate the sensor fault for the active FTC design of linear multi-agent systems. By transferring to another form [85], the sensor fault was rearranged with the same channel as actuator fault. Khebbache et al. [86] derived an active FTC-based backstepping technique for a class of multi-input-multi-output nonlinear systems, in which adaptive laws for fault estimation were involved in each step of the recursive design. However, the approach supposed that all first measured outputs were fault-free. Moreover, by following the previous literature, most approaches just concerned the system sensor faults subjected to free motion. In other words, there is no achievement of sensor fault estimation algorithm in terms of constrained framework, in which force sensor used for interaction monitoring may be faulty.

Motivated from the above analyses of the favorable control methods, this study proposes an active FTC for an n-degree-of-freedom (n-DOF) serial hydraulic manipulator under the presence of sensor faults in constrained framework for the first time. To address the sensor faults effect, and furthermore for matched uncertainty, a robust fault estimation based on ESO is proposed to estimate the system state and faulty signal residual. Based on the estimated parameters, the active FTC is constructed so as to achieve the system output performance.

5.2 System modeling and Problem formulation

5.2.1 Structure of the impedance control

During interaction, the environment sets constraints on the geometric paths that can be followed by the end effector. This situation is generally referred to as constrained motion [87]. There are two paradigms named direct force control and indirect force control. The direct force control mainly refers to hybrid position/force. This technique is employed in the point of industrial applications in which a task space is partitioned into force sub-space and position sub-space determined by a switch matrix. However, low robustness and instability when operating in changeable or wavy surface are drawbacks of this strategy. Besides, information of constraint that is not always available is required to achieve

good accuracy. In this sense, the indirect force control, normally known as impedance control, is more preferable to construct the outer/inner force/position-based cascade control. The detail of constraint is not necessary since the methodology does not require the switch matrix to partition workspace like direct force method. Therefore, in this study, the position-based impedance control (PB-IC) is preferred to deal with a tradeoff between the force tracking and position tracking in constrained framework. The PB-IC structure is presented in **Figure 5-1**.

The concept of impedance control, in general definition, is first introduced by Hogan [88]. The concept for this approach is the position tracking performance is prior in free-motion. Conversely, in constrained-motion, the force interaction is prior to tracking the desired value; thus, the reference trajectory is consequently modified to satisfy the force regulation. The physical interaction between the end-effector of the robotic manipulator and environment is presented in **Figure 5-2**.

Assumption 5-1: *The environment is assumed to be rigid, with no damping during the interaction, and is presented by a stiff spring*.

From the deformation of the environment spring, the interactive force between the end-effector and environment is expressed by:

$$\mathbf{F}_{ext} = -K_e\left(\mathbf{X}_a - \mathbf{X}_e\right) \tag{5.1}$$

where $\mathbf{X}_a, \mathbf{X}_e \in R^3$ denote the end-effector position and environment location, respectively; K_e is the environment stiffness.

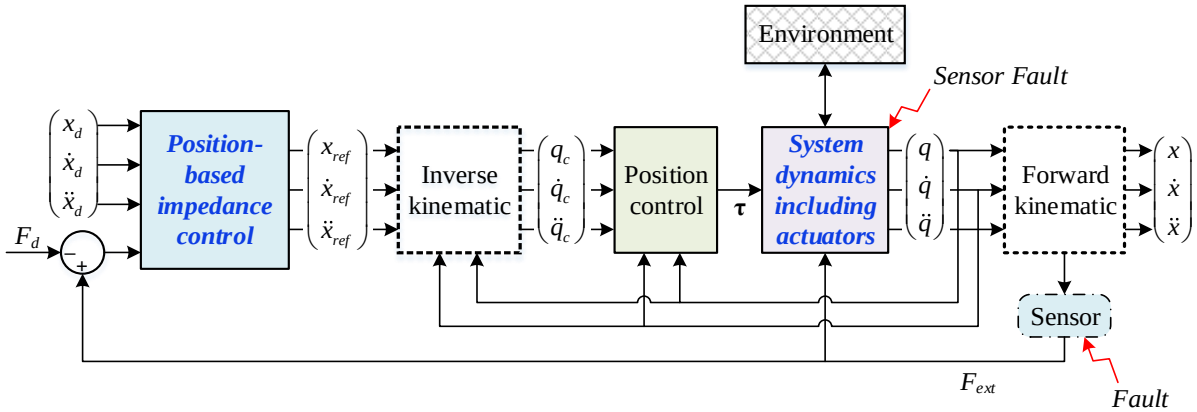

Figure 5-1 Structure of the position-based impedance control with sensor faults.

The conventional PB-IC, presenting the coupled interaction of the robot manipulator with environment, is redesigned from [89] by the second-order mass-spring-damper mechanisms as

$$\mathbf{D}_m\Delta\ddot{\mathbf{X}} + \mathbf{B}_m\Delta\dot{\mathbf{X}} + \mathbf{K}_m\Delta\mathbf{X} = \mathbf{u}_{imp} \tag{5.2}$$

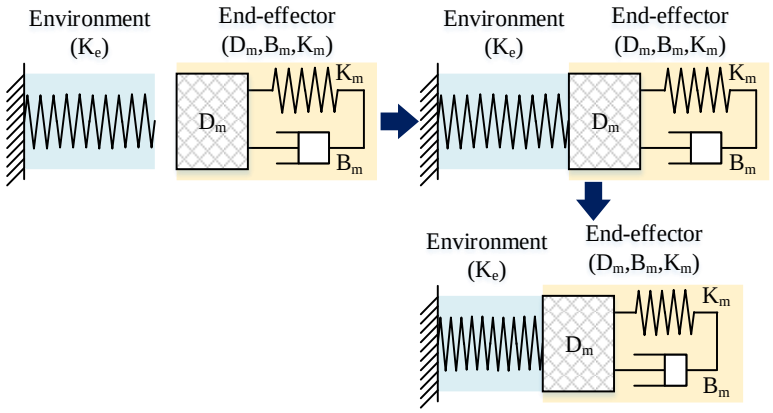

Figure 5-2 Illustration of physical interaction between the end-effector with environment.

where $\Delta\mathbf{X} = \mathbf{X}_d - \mathbf{X}_{ref}$; $\mathbf{X}_d$ and $\mathbf{X}_{ref}$ denote the desired and reference trajectories. $\mathbf{D}_m, \mathbf{B}_m, \mathbf{K}_m$ are matrices representing impedance behavior. $\mathbf{u}_{imp}$ is generated signal from force regulation and is defined as

$$\mathbf{u}_{imp} = \mathbf{K}_{Pf}\left(\mathbf{F}_{ext} - \mathbf{F}_d\right) + \mathbf{K}_{If}\int\left(\mathbf{F}_{ext} - \mathbf{F}_d\right) \tag{5.3}$$

with $\mathbf{F}_{ext}$ and $\mathbf{F}_d$ denote vectors of external force induced from interaction with the environment and desired force to be tracked, respectively; $\mathbf{K}_{Pf}$ and $\mathbf{K}_{If}$ are proportional and integrated controller gains.

5.2.2 System modeling with sensor faults

Consider the system behavior under the influence of sensor faults, the dynamics of the 3-DOF serial hydraulic manipulator including actuators in constrained framework is extended as

$$\begin{cases} \dot{\mathbf{x}}_1 = \mathbf{x}_2 \\ \dot{\mathbf{x}}_2 = \mathbf{M}^{-1}\left(\mathbf{x}_1\right)\left(\boldsymbol{\tau} - \mathbf{C}\left(\mathbf{x}_1, \mathbf{x}_2\right)\mathbf{x}_2 - \mathbf{G}\left(\mathbf{x}_1\right) - \boldsymbol{\Delta} - \mathbf{J}^T\left(\mathbf{q}\right)\mathbf{F}_{ext}\right) \\ \dot{\mathbf{x}}_3 = f\left(\mathbf{x}_1, \mathbf{x}_2\right) + \mathbf{g}\mathbf{u} - \boldsymbol{\psi}\mathbf{C}_{leak}\left(\mathbf{P}_{a1} - \mathbf{P}_{a2}\right) \\ \mathbf{y} = \mathbf{x}_1 + \mathbf{f}_{ss1} \\ \mathbf{F}_{ext,m} = \mathbf{F}_{ext} + \mathbf{f}_{ss2} \end{cases} \tag{5.4}$$

where $\mathbf{f}_{ss1}$ and $\mathbf{f}_{ss2}$ denote the vectors of sensor faults on encoder and force sensor, respectively; $\mathbf{F}_{ext,m}$ is a vector of measured interactive force.

Assumption 5-2: *The system outputs* $\mathbf{x}_1$, P_{ai1}, and P_{ai2} (i=1, …, n) *are measurable by sensors. Besides, all system states and their first derivative and all system dynamics are bounded*.

Assumption 5-3: *In this scope, to simplify the control algorithm design, the encoder and force sensors are supposed to be faulty. This implies the pressures are all correctly measured by pressure sensors*.

Assumption 5-4: *The fault signals are slow time-varying in comparison to the system dynamics*.

Assumption 5-5: *The sensor faults* $\mathbf{f}_{ss1}$ and $\mathbf{f}_{ss2}$, *and their time derivative are assumed to be bounded by positive constants, i.e.,* $0 \le \|\mathbf{f}_{ssi}\| \le \|\mathbf{f}_{ssi}\|_\infty \le \bar{f}_{ssi}$ *and* $0 \le \|\dot{\mathbf{f}}_{ssi}\| \le \|\dot{\mathbf{f}}_{ssi}\|_\infty \le \bar{\delta}_{f_{ssi}}$, *with i* = 1,2.

5.3 A novel robust fault estimation based extended state observer

Consider the sensor faults as state variables; first define $\mathbf{x}_{li} = \boldsymbol{\psi}\mathbf{C}_{leak}\left(\mathbf{P}_{a1} - \mathbf{P}_{a2}\right)$, $\mathbf{x}_{f_1} = \mathbf{f}_{ss1}$ and $\mathbf{x}_{f_2} = \mathbf{f}_{ss2}$, then the whole system is extended as

$$\begin{cases} \dot{\mathbf{x}}_1 = \mathbf{x}_2 \\ \dot{\mathbf{x}}_2 = \mathbf{M}^{-1}\left(\mathbf{x}_1\right)\left(\boldsymbol{\tau} - \mathbf{C}\left(\mathbf{x}_1, \mathbf{x}_2\right)\mathbf{x}_2 - \mathbf{G}\left(\mathbf{x}_1\right) - \boldsymbol{\Delta} - \mathbf{J}^T\left(\mathbf{q}\right)\mathbf{F}_{ext}\right) \\ \mathbf{y} = \mathbf{x}_1 + \mathbf{x}_{f_1} \\ \dot{\mathbf{x}}_{f_1} = \mathbf{h}_1\left(t\right) \\ \mathbf{F}_{ext,m} = \mathbf{F}_{ext} + \mathbf{x}_{f_2} \\ \dot{\mathbf{x}}_{f_2} = \mathbf{h}_2\left(t\right) \end{cases} \tag{5.5}$$

$$\begin{cases} \dot{\mathbf{x}}_3 = f\left(\mathbf{x}_1, \mathbf{x}_2\right) + \mathbf{g}\mathbf{u} - \mathbf{x}_{li} \\ \dot{\mathbf{x}}_{li} = \mathbf{h}\left(t\right) \end{cases} \tag{5.6}$$

where $\mathbf{h}\left(t\right), \mathbf{h}_1\left(t\right), \text{and}\, \mathbf{h}_2\left(t\right)$ are functions corresponding to derivative of the internal leakage and sensor faults, respectively.

Under the influence of the sensor faults, the robust observer based on extended state observer (ESO) is designed to estimate the system state as

$$\begin{cases} \dot{\hat{\mathbf{x}}}_1 = \hat{\mathbf{x}}_2 - \dfrac{\boldsymbol{\alpha}_1}{\sigma_1}\left(\hat{\mathbf{y}} - \mathbf{y}\right) \\ \dot{\hat{\mathbf{x}}}_2 = \mathbf{M}^{-1}\left(\mathbf{x}_1\right)\left(\boldsymbol{\tau} - \mathbf{C}\left(\mathbf{x}_1, \mathbf{x}_2\right)\mathbf{x}_2 - \mathbf{G}\left(\mathbf{x}_1\right) - \boldsymbol{\Delta}\right) \\ \qquad - \mathbf{M}^{-1}\left(\mathbf{x}_1\right)\mathbf{J}^T\left(\mathbf{q}\right)\hat{\mathbf{F}}_{ext} - \dfrac{\boldsymbol{\alpha}_2}{\sigma_1^2}\left(\hat{\mathbf{y}} - \mathbf{y}\right) \\ \hat{\mathbf{y}} = \hat{\mathbf{x}}_1 + \hat{\mathbf{x}}_{f_1} - \dfrac{\boldsymbol{\eta}_{f1}}{\sigma_1}\left(\hat{\mathbf{y}} - \mathbf{y}\right) \\ \dot{\hat{\mathbf{x}}}_{f_1} = -\dfrac{\boldsymbol{\eta}_{f1}}{\sigma_1^3}\left(\hat{\mathbf{y}} - \mathbf{y}\right) \\ \hat{\mathbf{F}}_{ext,m} = K_e\left(\hat{\mathbf{X}}_a - \mathbf{X}_e\right) + \hat{\mathbf{x}}_{f_2} \\ \dot{\hat{\mathbf{x}}}_{f_2} = -\dfrac{\boldsymbol{\eta}_{f2}}{\sigma_1^3}\left(\hat{\mathbf{F}}_{ext,m} - \mathbf{F}_{ext,m}\right) \end{cases} \tag{5.7}$$

$$\begin{cases} \dot{\hat{\mathbf{x}}}_3 = \mathbf{f}\left(\mathbf{x}_1, \mathbf{x}_2\right) + \mathbf{g}\mathbf{u} - \hat{\mathbf{x}}_{li} - \dfrac{2\boldsymbol{\alpha}_3}{\sigma_2}\left(\hat{\mathbf{x}}_3 - \mathbf{x}_3\right) \\ \dot{\hat{\mathbf{x}}}_{li} = -\dfrac{\boldsymbol{\alpha}_3^2}{\sigma_2^2}\left(\hat{\mathbf{x}}_3 - \mathbf{x}_3\right) \end{cases} \tag{5.8}$$

where $\mathbf{x}_i$ is the estimate of system state $\mathbf{x}_i$ (i=1,2,3); $\hat{\mathbf{F}}_{ext,m}$ is the estimate of measured interactive force $\mathbf{F}_{ext,m}$; and $\hat{\mathbf{x}}_{f_j}$, with (j=1,2), denotes the estimate of real sensor faulty $\mathbf{x}_{f_j}$; $\boldsymbol{\alpha}_1$, $\boldsymbol{\alpha}_2$, $\boldsymbol{\alpha}_3$, $\boldsymbol{\eta}_{f1}$, and $\boldsymbol{\eta}_{f2}$ are n-by-n tuned diagonal matrices gains of the ESO; σ_1 and σ_2 are arbitrarily small relating the bandwidth of the ESO.

The calculation of the end-effector estimation $\hat{\mathbf{X}}_a$ is calculated from the system state $\hat{\mathbf{x}}_1$ through forward kinematic as

$$\hat{\mathbf{X}}_a = f\left(\hat{\mathbf{x}}_1\right) \tag{5.9}$$

where $f\left(\hat{\mathbf{x}}_1\right)$ denotes the forward kinetic calculation.

Assumption 5-6: the function $f\left(\hat{\mathbf{x}}_1\right)$ is locally Lipchitz for $\mathbf{x}_1$, i.e., $\left\| f\left(\hat{\mathbf{x}}_1\right) - f\left(\mathbf{x}_1\right) \right\| \le \mathbf{f}_{fk}\tilde{\mathbf{x}}_1$.

From Equations (5.5) to (5.9), the dynamics of the state estimation errors is given by:

$$\begin{cases} \dot{\tilde{\mathbf{x}}}_1 = \tilde{\mathbf{x}}_2 - \dfrac{\boldsymbol{\alpha}_1}{\sigma_1}\tilde{\mathbf{y}} \\ \dot{\tilde{\mathbf{x}}}_2 = -\mathbf{M}^{-1}\left(\mathbf{x}_1\right)\left(\mathbf{J}^T\left(\mathbf{x}_1\right)K_e f\left(\tilde{\mathbf{x}}_1\right) - \tilde{\mathbf{x}}_{f2}\right) - \dfrac{\boldsymbol{\alpha}_2}{\sigma_1^2}\tilde{\mathbf{y}} \\ \tilde{\mathbf{y}} = \tilde{\mathbf{x}}_1 + \tilde{\mathbf{x}}_{f_1} - \dfrac{\boldsymbol{\eta}_{f1}}{\sigma_1}\tilde{\mathbf{y}} \\ \dot{\tilde{\mathbf{x}}}_{f_1} = -\dfrac{\boldsymbol{\eta}_{f1}}{\sigma_1^3}\tilde{\mathbf{y}} + \mathbf{h}_1 \\ \tilde{\mathbf{F}}_{ext,m} = K_e f\left(\tilde{\mathbf{x}}_1\right) + \tilde{\mathbf{x}}_{f_2} \\ \tilde{\mathbf{x}}_{f_2} = -\dfrac{\boldsymbol{\eta}_{f2}}{\sigma_1^3}\left(K_e \tilde{f}_{fw}\left(\tilde{\mathbf{x}}_1\right) + \tilde{\mathbf{x}}_{f_2}\right) + \mathbf{h}_2 \end{cases} \tag{5.10}$$

(5.11)

where $(\bullet) = (\bullet) - (\bullet)$.

Assumption 5-7: *It is noteworthy from* (5.10) *that the state estimation error of the end-effector position,* $f\left(\tilde{\mathbf{x}}_1\right) = f\left(\hat{\mathbf{x}}_1\right) - f\left(\mathbf{x}_1\right)$ *, depending on the estimation error of the joint angle, should be obtained from forward kinematic calculation. However, because it is the function of joint angle error and in order to facilitate the ESO design, the estimation error of the forward kinematic is linearized around the equilibrium zero and thus, by regarding Assumption 5-6, it is reasonably simplified by using an approximated gain* $\mathbf{f}_{fk}$ *. Moreover, neglecting the system dynamics error and identification process, it can be mathematically obtained without any other estimated error generated*.

Therefore, Equation (5.10) becomes:

$$\begin{cases} \dot{\tilde{\mathbf{x}}}_1 = \tilde{\mathbf{x}}_2 - \dfrac{\boldsymbol{\alpha}_1}{\sigma_1}\tilde{\mathbf{y}} \\ \dot{\tilde{\mathbf{x}}}_2 = -\mathbf{M}^{-1}(\mathbf{x}_1)\left(\mathbf{J}^T(\mathbf{x}_1)K_e f(\tilde{\mathbf{x}}_1) - \tilde{\mathbf{x}}_{f2}\right) - \dfrac{\boldsymbol{\alpha}_2}{\sigma_1^2}\tilde{\mathbf{y}} \\ \tilde{\mathbf{y}} = \tilde{\mathbf{x}}_1 + \tilde{\mathbf{x}}_{f_1} - \dfrac{\boldsymbol{\eta}_{f1}}{\sigma_1}\tilde{\mathbf{y}} \\ \dot{\tilde{\mathbf{x}}}_{f_1} = -\dfrac{\boldsymbol{\eta}_{f1}}{\sigma_1^3}\tilde{\mathbf{y}} + \mathbf{h}_1 \\ \tilde{\mathbf{F}}_{ext,m} = K_e \mathbf{f}_{fw}\tilde{\mathbf{x}}_1 + \tilde{\mathbf{x}}_{f_2} \\ \tilde{\mathbf{x}}_{f_2} = -\dfrac{\boldsymbol{\eta}_{f2}}{\sigma_1^3}\left(K_e \tilde{f}_{fw}(\tilde{\mathbf{x}}_1) + \tilde{\mathbf{x}}_{f_2}\right) + \mathbf{h}_2 \end{cases} \tag{5.12}$$

From the third Equation of (5.12), one obtains:

$$\tilde{\mathbf{y}} = \left(\mathbf{I}_n + \frac{1}{\sigma_1}\boldsymbol{\eta}_{f1}\right)^{-1}\left(\tilde{\mathbf{x}}_1 + \tilde{\mathbf{x}}_{f_1}\right) \tag{5.13}$$

Then, the dynamics of the state estimation error becomes:

$$\begin{cases} \dot{\tilde{\mathbf{x}}}_1 = \dfrac{1}{\sigma_1}\left(-\boldsymbol{\Xi}_{11}\tilde{\mathbf{x}}_1 + \tilde{\mathbf{x}}_2 - \boldsymbol{\Xi}_{13}\tilde{\mathbf{x}}_{f_1}\right) \\ \sigma_1\dot{\tilde{\mathbf{x}}}_2 = \dfrac{1}{\sigma_1}\left(-\boldsymbol{\Xi}_{21}\tilde{\mathbf{x}}_1 - \boldsymbol{\Xi}_{23}\tilde{\mathbf{x}}_{f_1} - \boldsymbol{\Xi}_{24}\tilde{\mathbf{x}}_{f_2}\right) \\ \sigma_1^2\dot{\tilde{\mathbf{x}}}_{f_1} = \dfrac{1}{\sigma_1}\left(-\boldsymbol{\Xi}_{31}\tilde{\mathbf{x}}_1 - \boldsymbol{\Xi}_{33}\tilde{\mathbf{x}}_{f_1}\right) + \varepsilon_1^2\mathbf{h}_1 \\ \sigma_1^2\dot{\tilde{\mathbf{x}}}_{f_2} = \dfrac{1}{\sigma_1}\left(-\boldsymbol{\Xi}_{41}\tilde{\mathbf{x}}_1 - \boldsymbol{\Xi}_{44}\tilde{\mathbf{x}}_{f_2}\right) + \varepsilon_1^2\mathbf{h}_2 \end{cases} \tag{5.14}$$

$$\begin{cases} \dot{\tilde{\mathbf{x}}}_3 = -\dfrac{2\boldsymbol{\alpha}_3}{\sigma_2}\tilde{\mathbf{x}}_3 + \tilde{\mathbf{x}}_{li} \\ \sigma_2\dot{\tilde{\mathbf{x}}}_{li} = -\dfrac{\boldsymbol{\alpha}_3^2}{\sigma_2}\tilde{\mathbf{x}}_3 + \sigma_2\mathbf{h} \end{cases} \tag{5.15}$$

where $\boldsymbol{\Xi}_{11} = \boldsymbol{\alpha}_2\left(\mathbf{I}_n + \dfrac{1}{\sigma_1}\boldsymbol{\eta}_{f1}\right) \in R^{n\times n}$, $\boldsymbol{\Xi}_{13} = \boldsymbol{\Xi}_{11} \in R^{n\times n}$, $\boldsymbol{\Xi}_{21} = \sigma_1^2\mathbf{M}^{-1}K_e f_{fk} + \boldsymbol{\alpha}_2\left(\mathbf{I}_n + \dfrac{1}{\sigma_1}\boldsymbol{\eta}_{f1}\right) \in R^{n\times n}$,

$\boldsymbol{\Xi}_{23} = \boldsymbol{\alpha}_2\left(\mathbf{I}_n + \dfrac{1}{\sigma_1}\boldsymbol{\eta}_{f1}\right) \in R^{n\times n}$, $\boldsymbol{\Xi}_{24} = \mathbf{M}^{-1} \in R^{n\times 3}$, $\boldsymbol{\Xi}_{31} = \boldsymbol{\eta}_{f1} \in R^{n\times n}$, $\boldsymbol{\Xi}_{33} = \boldsymbol{\Xi}_{31} \in R^{n\times n}$,

$\boldsymbol{\Xi}_{41} = \boldsymbol{\eta}_{f2}K_e f_{fk} \in R^{3\times n}$, $\boldsymbol{\Xi}_{44} = \boldsymbol{\eta}_{f2} \in R^{3\times 3}$.

Define auxiliary vectors of estimated error $\boldsymbol{\varepsilon}_1$ and $\boldsymbol{\varepsilon}_2$ as

$$\boldsymbol{\varepsilon}_1 = \left(\tilde{\mathbf{x}}_1, \sigma_1\tilde{\mathbf{x}}_2, \sigma_1^2\tilde{\mathbf{x}}_{f1}, \sigma_1^2\tilde{\mathbf{x}}_{f2}\right)^T \in R^{3n+3} \tag{5.16}$$

$$\boldsymbol{\varepsilon}_2 = \left(\tilde{\mathbf{x}}_3, \sigma_2\tilde{\mathbf{x}}_{li}\right)^T \in R^{2n} \tag{5.17}$$

Then, the dynamics state estimation errors take the form of:

$$\dot{\boldsymbol{\varepsilon}}_1 = \frac{1}{\sigma_1}\mathbf{A}_1\boldsymbol{\varepsilon}_1 + \sigma_1^2\mathbf{B}_1\mathbf{H}_1 \tag{5.18}$$

$$\dot{\boldsymbol{\varepsilon}}_2 = \frac{1}{\sigma_2}\mathbf{A}_2\boldsymbol{\varepsilon}_2 + \sigma_2\mathbf{B}_2\mathbf{H}_2 \tag{5.19}$$

with

$$\begin{gathered}\mathbf{A}_1 = \begin{bmatrix} -\boldsymbol{\Xi}_{11} & \mathbf{I}_n & -\boldsymbol{\Xi}_{13} & \mathbf{0}_{n\times 3} \\ -\boldsymbol{\Xi}_{21} & \mathbf{0}_{n\times n} & -\boldsymbol{\Xi}_{23} & -\boldsymbol{\Xi}_{24} \\ -\boldsymbol{\Xi}_{31} & \mathbf{0}_{n\times n} & -\boldsymbol{\Xi}_{33} & \mathbf{0}_{n\times 3} \\ -\boldsymbol{\Xi}_{41} & \mathbf{0}_{3\times n} & \mathbf{0}_{3\times n} & -\boldsymbol{\Xi}_{44} \end{bmatrix} \in R^{(3n+3)\times(3n+3)},\ \mathbf{A}_2 = \begin{bmatrix} -2\boldsymbol{\alpha}_3 & \mathbf{I}_n \\ -\boldsymbol{\alpha}_3^2 & \mathbf{0}_n \end{bmatrix} \in R^{2n\times 2n},\ \\ \mathbf{B}_1 = diag\begin{pmatrix}\mathbf{I}_n & \mathbf{I}_n & \mathbf{I}_n & \mathbf{I}_3\end{pmatrix} \in R^{(3n+3)\times(3n+3)},\ \mathbf{B}_2 = diag\begin{pmatrix}\mathbf{I}_n & \mathbf{I}_n\end{pmatrix} \in R^{2n\times 2n},\ \\ \mathbf{H}_1 = \begin{pmatrix}\mathbf{0}_{n\times 1} & \mathbf{0}_{n\times 1} & \mathbf{h}_1 & \mathbf{h}_2\end{pmatrix} \in R^{3n+3},\ \mathbf{H}_2 = \begin{pmatrix}\mathbf{0}_{n\times 1} & \mathbf{h}\end{pmatrix} \in R^{2n}\end{gathered} \tag{5.20}$$

where $\mathbf{I}_n$ denotes *n*-by-*n* identity matrix, $\mathbf{0}_{p\times q}$ denotes *p*-by-*q* zero matrix.

Since the matrices $\mathbf{A}_1$ and $\mathbf{A}_2$ are Hurwitz, then there exist matrices $\mathbf{P}_1$ and $\mathbf{P}_2$ that satisfy:

$$\begin{cases}\mathbf{A}_1^T\mathbf{P}_1 + \mathbf{P}_1\mathbf{A}_1 = -\mathbf{I}_{3n+3} \\ \mathbf{A}_2^T\mathbf{P}_2 + \mathbf{P}_2\mathbf{A}_2 = -\mathbf{I}_{2n}\end{cases} \tag{5.21}$$

Theorem 5-1: *Consider the faulty system* (5.5)*, and the proposed robust observer based on the ESO in Equation* (5.7)*, all signals of the system are uniformly ultimately bounded* (*UUB*) *and converges to the small neighborhood of the origin.*

Proof of Theorem 5-1:

Choosing the Lyapunov candidate $V_{ESO,1}$ as

$$V_{ESO,1} = \frac{1}{2}\boldsymbol{\varepsilon}_1^T\mathbf{P}_1\boldsymbol{\varepsilon}_1 \tag{5.22}$$

Taking derivative of the is $V_{ESO,1}$ yields:

$$\dot{V}_{ESO,1} = \frac{1}{2}\dot{\boldsymbol{\varepsilon}}_1^T\mathbf{P}_1\boldsymbol{\varepsilon}_1 + \frac{1}{2}\boldsymbol{\varepsilon}_1^T\mathbf{P}_1\dot{\boldsymbol{\varepsilon}}_1 \tag{5.23}$$

$$\begin{aligned}\Leftrightarrow \dot{V}_{ESO,1} &= \frac{1}{2}\left(\frac{1}{\sigma_1}\boldsymbol{\varepsilon}_1^T\mathbf{A}_1^T + \sigma_1^2\mathbf{H}_1^T\mathbf{B}_1^T\right)\mathbf{P}_1\boldsymbol{\varepsilon}_1 + \frac{1}{2}\boldsymbol{\varepsilon}_1^T\mathbf{P}_1\left(\frac{1}{\sigma_1}\mathbf{A}_1\boldsymbol{\varepsilon}_1 + \sigma_1^2\mathbf{B}_1\mathbf{H}_1\right) \\ &= \frac{1}{2\sigma_1}\boldsymbol{\varepsilon}_1^T\left(\mathbf{A}_1^T\mathbf{P}_1 + \mathbf{P}_1\mathbf{A}_1\right)\boldsymbol{\varepsilon}_1 + \sigma_1^2\boldsymbol{\varepsilon}_1^T\mathbf{P}_1\mathbf{B}_1\mathbf{H}_1\end{aligned} \tag{5.24}$$

$$\Leftrightarrow \dot{V}_{ESO,1} = -\frac{1}{2\sigma_1}\boldsymbol{\varepsilon}_1^T\mathbf{I}_{3n+3}\boldsymbol{\varepsilon}_1 + \sigma_1^2\boldsymbol{\varepsilon}_1^T\mathbf{P}_1\mathbf{B}_1\mathbf{H}_1 \tag{5.25}$$

Apply Young's inequality, Equation (5.25) becomes:

$$\begin{aligned}\dot{V}_{ESO,1} &\le -\frac{1}{2\sigma_1}\boldsymbol{\varepsilon}_1^T\mathbf{I}_{3n+3}\boldsymbol{\varepsilon}_1 + \frac{1}{2}\sigma_1^2\boldsymbol{\varepsilon}_1^T\mathbf{P}_1^T\mathbf{B}_1\mathbf{B}_1^T\mathbf{P}_1\boldsymbol{\varepsilon}_1 + \frac{1}{2}\sigma_1^2\mathbf{H}_1^T\mathbf{H}_1 \\ &\le -\frac{1}{2}\left(\frac{1}{\sigma_1} - \sigma_1^2\lambda_{\max}\left(\mathbf{P}_1^T\mathbf{B}_1\mathbf{B}_1^T\mathbf{P}_1\right)\right)\left\|\boldsymbol{\varepsilon}_1\right\|^2 + \frac{1}{2}\sigma_1^2\mathbf{H}_1^T\mathbf{H}_1\end{aligned} \tag{5.26}$$

$$\dot{V}_{ESO,1} \le -\gamma_{ESO,1}V_{ESO,1} + \Delta_{ESO,1} \tag{5.27}$$

Referring to the Lyapunov stability theorems and [24,90], the fault estimated based on the ESO is UUB and converges to the bound:

$$V_{ESO,1} \le V_{ESO,1}(0)e^{-\gamma_{ESO,1}t} + \frac{\Delta_{ESO,1}}{\gamma_{ESO,1}}\left(1 - e^{-\gamma_{ESO,1}t}\right) \tag{5.28}$$

where $\gamma_{ESO,1} = \min\left(\frac{1}{2}\left(\frac{1}{\sigma_1} - \sigma_1^2\lambda_{\max}\left(\mathbf{P}_1^T\mathbf{B}_1\mathbf{B}_1^T\mathbf{P}_1\right)\right)\right)$, $\Delta_{ESO,1} = \frac{1}{2}\sigma_1^2\mathbf{H}_1^T\mathbf{H}_1$.

Theorem 5-2: *Consider the system* (5.6)*, and the ESO in* (5.8)*, all signals of this system are UUB and converges to the small neighborhood of the origin*.

Proof of Theorem 5-2:

Choosing the Lyapunov candidate $V_{ESO,2}$ as

$$V_{ESO,2} = \frac{1}{2}\boldsymbol{\varepsilon}_2^T\mathbf{P}_2\boldsymbol{\varepsilon}_2 \tag{5.29}$$

Taking derivative of the is $V_{ESO,2}$ yields:

$$\dot{V}_{ESO,2} = \frac{1}{2}\dot{\boldsymbol{\varepsilon}}_2^T\mathbf{P}_2\boldsymbol{\varepsilon}_2 + \frac{1}{2}\boldsymbol{\varepsilon}_2^T\mathbf{P}_2\dot{\boldsymbol{\varepsilon}}_2 \tag{5.30}$$

$$\begin{aligned}\Leftrightarrow \dot{V}_{ESO,2} &= \frac{1}{2}\left(\frac{1}{\sigma_2}\boldsymbol{\varepsilon}_2^T\mathbf{A}_2^T + \sigma_2^2\mathbf{H}_2^T\mathbf{B}_2^T\right)\mathbf{P}_2\boldsymbol{\varepsilon}_2 + \frac{1}{2}\boldsymbol{\varepsilon}_2^T\mathbf{P}_2\left(\frac{1}{\sigma_2}\mathbf{A}_2\boldsymbol{\varepsilon}_2 + \sigma_2^2\mathbf{B}_2\mathbf{H}_2\right) \\ &= \frac{1}{2\sigma_2}\boldsymbol{\varepsilon}_2^T\left(\mathbf{A}_2^T\mathbf{P}_2 + \mathbf{P}_2\mathbf{A}_2\right)\boldsymbol{\varepsilon}_2 + \sigma_2^2\boldsymbol{\varepsilon}_2^T\mathbf{P}_2\mathbf{B}_2\mathbf{H}_2\end{aligned} \tag{5.31}$$

$$\Leftrightarrow \dot{V}_{ESO,2} = -\frac{1}{2\sigma_2}\boldsymbol{\varepsilon}_2^T\mathbf{I}_{2n}\boldsymbol{\varepsilon}_2 + \sigma_2^2\boldsymbol{\varepsilon}_2^T\mathbf{P}_2\mathbf{B}_2\mathbf{H}_2 \tag{5.32}$$

Apply Young's inequality, Equation (5.25) becomes:

$$\begin{aligned}\dot{V}_{ESO,2} &\le -\frac{1}{2\sigma_2}\boldsymbol{\varepsilon}_2^T\mathbf{I}_{2n}\boldsymbol{\varepsilon}_2 + \frac{1}{2}\sigma_2^2\boldsymbol{\varepsilon}_2^T\mathbf{P}_2^T\mathbf{B}_2\mathbf{B}_2^T\mathbf{P}_2\boldsymbol{\varepsilon}_2 + \frac{1}{2}\sigma_2\mathbf{H}_2^T\mathbf{H}_2 \\ &\le -\frac{1}{2}\left(\frac{1}{\sigma_2} - \sigma_2\lambda_{\max}\left(\mathbf{P}_2^T\mathbf{B}_2\mathbf{B}_2^T\mathbf{P}_2\right)\right)\left\|\boldsymbol{\varepsilon}_2\right\|^2 + \frac{1}{2}\sigma_2\mathbf{H}_2^T\mathbf{H}_2\end{aligned} \tag{5.33}$$

$$\dot{V}_{ESO,2} \le -\gamma_{ESO,2}V_{ESO,2} + \Delta_{ESO,2} \tag{5.34}$$

Also referring to the Lyapunov stability theorems and [24,90], the fault estimated based on the ESO is UUB and converges to the bound:

$$V_{ESO,2} \le V_{ESO,2}(0)e^{-\gamma_{ESO,2}t} + \frac{\Delta_{ESO,2}}{\gamma_{ESO,2}}\left(1-e^{-\gamma_{ESO,2}t}\right) \tag{5.35}$$

where $\gamma_{ESO,2} = \min\left(\frac{1}{2}\left(\frac{1}{\sigma_2} - \sigma_2^2\lambda_{\max}\left(\mathbf{P}_2^T\mathbf{B}_2\mathbf{B}_2^T\mathbf{P}_2\right)\right)\right)$, $\Delta_{ESO,2} = \frac{1}{2}\sigma_2\mathbf{H}_2^T\mathbf{H}_2$.

5.4 Development of adaptive fuzzy backstepping sliding mode control based on fault-tolerant control-based

In this section, the control laws of the AFBSMC, presented in Section 4.3, Chapter 4, are modified with the estimation of sensor fault signals and matched uncertainties. The overall AFBSMC algorithm with sensor faults is shown in **Figure 5-3**.

The virtual control law of the position tracking control loop is designed as

$$\mathbf{x}_{3d} = \mathbf{M}(\mathbf{x}_1)\dot{\mathbf{x}}_{2s} + \mathbf{C}(\mathbf{x}_1,\mathbf{x}_2)\mathbf{x}_{2s} + \mathbf{G}(\mathbf{x}_1) + \mathbf{J}^T\hat{\mathbf{F}}_{ext} + \hat{\boldsymbol{\Delta}} - \mathbf{K}_1\mathbf{s}_1 - \boldsymbol{\eta}_1\tanh\left(\frac{\mathbf{s}_1}{\sigma_s}\right) \tag{5.36}$$

where $\hat{\mathbf{F}}_{ext}$ represents for an estimated external force disturbance obtained from the ESO.

Choose a Lyapunov candidate V_1^{ESO} as

$$V_1^{ESO} = \frac{1}{2}\mathbf{s}_1^T\mathbf{M}\mathbf{s}_1 + \frac{1}{2}\tilde{\boldsymbol{\Delta}}^T\tilde{\boldsymbol{\Delta}} + \frac{1}{2}\boldsymbol{\varepsilon}_1^T\mathbf{P}_1\boldsymbol{\varepsilon}_1 \tag{5.37}$$

Taking derivative the Lyapunov candidate V_1^{ESO} with Property 3-1 and results obtained in Equations (3.29) and (5.25) yields:

$$\begin{aligned}\dot{V}_1^{ESO} = &-\mathbf{s}_1^T\left(\mathbf{x}_3 - \left(\tilde{\boldsymbol{\Delta}} + \hat{\boldsymbol{\Delta}}\right) - \mathbf{M}(\mathbf{x}_1)\dot{\mathbf{x}}_{2s} - \mathbf{C}(\mathbf{x}_1,\mathbf{x}_2)\mathbf{x}_{2s} - \mathbf{G}(\mathbf{x}_1)\right) - \mathbf{s}_1^T\mathbf{J}^T(\mathbf{x}_1)\hat{\mathbf{F}}_{ext} + \dot{\tilde{\boldsymbol{\Delta}}}^T\tilde{\boldsymbol{\Delta}} \\ &- \frac{1}{2\sigma_1}\boldsymbol{\varepsilon}_1^T\mathbf{I}_{3n+3}\boldsymbol{\varepsilon}_1 + \sigma_1^2\boldsymbol{\varepsilon}_1^T\mathbf{P}_1\mathbf{B}_1\mathbf{H}_1\end{aligned} \tag{5.38}$$

Substituting the virtual control signal in Equation (5.36) and adaptive law derived in Equation (3.27) into Equation (5.38) results in:

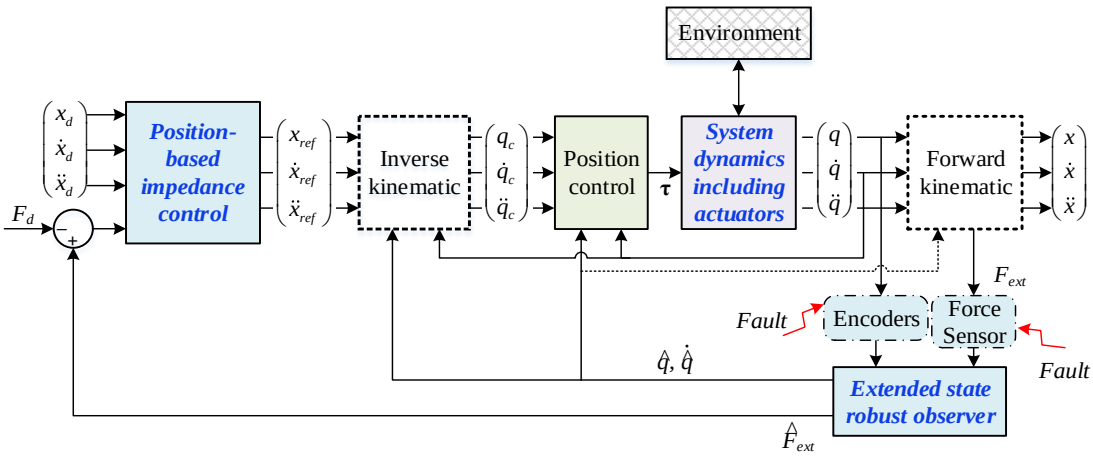

Figure 5-3 Proposed AFBSMC-based FTC with sensor faults.

$$\dot{V}_1^{ESO} = \mathbf{s}_1^T \left(\mathbf{J}_a^T \mathbf{e}_3 - \mathbf{K}_1 \mathbf{s}_1 - \boldsymbol{\eta}_1 \tanh\left(\frac{\mathbf{s}_1}{\sigma_s} \right) + \tilde{\mathbf{F}}_{ext} \right) - \frac{1}{2\sigma_1} \boldsymbol{\varepsilon}_1^T \mathbf{I}_{3n+3} \boldsymbol{\varepsilon}_1 + \sigma_1^2 \boldsymbol{\varepsilon}_1^T \mathbf{P}_1 \mathbf{B}_1 \mathbf{H}_1 \tag{5.39}$$

From Equation (5.39), the derivative of the Lyapunov function $\dot{V}_1^{ESO}$ is semi-negative if the error $\mathbf{e}_3$ converges to zero. Therefore, in order to regulate this error as small as possible, the sliding surface $\mathbf{s}_2 = \mathbf{e}_3$ is chosen and the Lyapunov candidate, presented in Equation (3.36), is modified by:

$$V_2^{ESO} = V_1^{ESO} + \frac{1}{2} \mathbf{s}_2^T \mathbf{s}_2 + \frac{1}{2} \boldsymbol{\varepsilon}_2^T \mathbf{P}_2 \boldsymbol{\varepsilon}_2 \tag{5.40}$$

Taking derivative V_2^{ESO} yields:

$$\begin{aligned} \dot{V}_2^{ESO} = {} & \mathbf{s}_1^T \left(\mathbf{J}_a^T \mathbf{e}_3 - \mathbf{K}_1 \mathbf{s}_1 - \boldsymbol{\eta}_1 \tanh\left(\frac{\mathbf{s}_1}{\sigma_s} \right) + \tilde{\mathbf{F}}_{ext} \right) - \frac{1}{2\sigma_1} \boldsymbol{\varepsilon}_1^T \mathbf{I}_{3n+3} \boldsymbol{\varepsilon}_1 + \sigma_1^2 \boldsymbol{\varepsilon}_1^T \mathbf{P}_1 \mathbf{B}_1 \mathbf{H}_1 \\ & + \mathbf{s}_2^T \left(\mathbf{f}\left(\mathbf{x}_1, \mathbf{x}_2 \right) + \mathbf{g}\mathbf{u} - \mathbf{x}_{li} - \dot{\mathbf{x}}_{3d} \right) - \frac{1}{2\sigma_2} \boldsymbol{\varepsilon}_2^T \mathbf{I}_{2n} \boldsymbol{\varepsilon}_2 + \sigma_2 \boldsymbol{\varepsilon}_2^T \mathbf{P}_2 \mathbf{B}_2 \mathbf{H}_2 \end{aligned} \tag{5.41}$$

Then, the control input signal is designed as

$$\mathbf{u} = \mathbf{g}^{-1} \left(-\mathbf{f}\left(\mathbf{x}_1, \mathbf{x}_2 \right) + \hat{\mathbf{x}}_{li} + \dot{\mathbf{x}}_{3d} - \mathbf{K}_2 \mathbf{s}_2 - \boldsymbol{\eta}_2 sign\left(\mathbf{s}_2 \right) - \mathbf{J}_a^T \mathbf{s}_1 \right) \tag{5.42}$$

Substituting the control law (5.42) into Equation (5.41), the influence of the lumped mismatched uncertainty is canceled out, then:

$$\begin{aligned} \dot{V}_2^{ESO} = {} & -\sum_{i=1}^{2} \mathbf{s}_i^T \mathbf{K}_i \mathbf{s}_i - \mathbf{s}_1^T \left(\boldsymbol{\eta}_1 \tanh\left(\frac{\mathbf{s}_1}{\delta} \right) - \tilde{\mathbf{F}}_{ext} \right) - \mathbf{s}_2^T \left(\boldsymbol{\eta}_2 sign\left(\mathbf{s}_2 \right) - \tilde{\mathbf{x}}_{li} \right) \\ & - \frac{1}{2\sigma_1} \boldsymbol{\varepsilon}_1^T \mathbf{I}_{3n+3} \boldsymbol{\varepsilon}_1 + \sigma_1^2 \boldsymbol{\varepsilon}_1^T \mathbf{P}_1 \mathbf{B}_1 \mathbf{H}_1 - \frac{1}{2\sigma_2} \boldsymbol{\varepsilon}_2^T \mathbf{I}_{2n} \boldsymbol{\varepsilon}_2 + \sigma_2 \boldsymbol{\varepsilon}_2^T \mathbf{P}_2 \mathbf{B}_2 \mathbf{H}_2 \end{aligned} \tag{5.43}$$

By applying Young's inequality and results in Equations (5.26) and (5.33), one obtains:

$$\begin{aligned} \dot{V}_2^{ESO} \le {} & -\mathbf{s}_1^T \mathbf{K}_1 \mathbf{s}_1 - \mathbf{s}_2^T \mathbf{K}_2 \mathbf{s}_2 - \mathbf{s}_1^T \left(\boldsymbol{\eta}_1 \tanh\left(\frac{\mathbf{s}_1}{\delta} \right) - \tilde{\mathbf{F}}_{ext} \right) - \mathbf{s}_2^T \left(\boldsymbol{\eta}_2 sign\left(\mathbf{s}_1 \right) - \tilde{\mathbf{x}}_{li} \right) \\ & - \frac{1}{2} \left(\frac{1}{\sigma_1} - \sigma_1^2 \lambda_{\max} \left(\mathbf{P}_1^T \mathbf{B}_1 \mathbf{B}_1^T \mathbf{P}_1 \right) \right) \left\| \boldsymbol{\varepsilon}_1 \right\|^2 + \frac{1}{2} \sigma_1^2 \mathbf{H}_1^T \mathbf{H}_1 \\ & - \frac{1}{2} \left(\frac{1}{\sigma_2} - \sigma_2 \lambda_{\max} \left(\mathbf{P}_2^T \mathbf{B}_2 \mathbf{B}_2^T \mathbf{P}_2 \right) \right) \left\| \boldsymbol{\varepsilon}_2 \right\|^2 + \frac{1}{2} \sigma_2 \mathbf{H}_2^T \mathbf{H}_2 \end{aligned} \tag{5.44}$$

$$\dot{V}_2^{ESO} \le -\gamma_{V_2^{ESO}} V_2^{ESO} + \zeta_{V_2^{ESO}} \tag{5.45}$$

According to [26,86], it can be concluded that the proposed algorithm is UUB in the presence of mismatched external force interaction, sensor faults and matched uncertainty (i.e. internal leakage). As a result, the Lyapunov candidate V_2^{ESO} is bounded by:

$$V_2^{ESO}(t) \le V_2^{ESO}(0) e^{-\gamma_{V_2^{ESO}} t} + \frac{\zeta_{V_2^{ESO}}}{\gamma_{V_2^{ESO}}} \left(1 - e^{-\gamma_{V_2^{ESO}} t} \right) \tag{5.46}$$

where $\gamma_{V_2^{ESO}} = \min\left(\begin{array}{l} \dfrac{1}{\sigma_1} - \sigma_1^2 \lambda_{\max}\left(\mathbf{P}_1^T \mathbf{B}_1 \mathbf{B}_1^T \mathbf{P}_1\right), \dfrac{1}{\sigma_2} - \sigma_2^2 \lambda_{\max}\left(\mathbf{P}_2^T \mathbf{B}_2 \mathbf{B}_2^T \mathbf{P}_2\right), \\ \lambda_{\min}\left(\mathbf{K}_1\right), \lambda_{\min}\left(\mathbf{K}_2\right), \lambda_{\min}\left(\boldsymbol{\eta}_1\right), \lambda_{\min}\left(\boldsymbol{\eta}_2\right) \end{array}\right) \geq 0$,

$\zeta_{V_2^{ESO}} = \mathbf{s}_1^T \tilde{\mathbf{F}}_{ext} + \mathbf{s}_2^T \tilde{\mathbf{x}}_{li} + \frac{1}{2}\sigma_1^2 \mathbf{H}_1^T \mathbf{H}_1 + \frac{1}{2}\sigma_2 \mathbf{H}_2^T \mathbf{H}_2$.

Remark 5-1: *Based on Assumption 5-5, the estimated errors of matched and mismatched uncertainties are bounded by assumedly predetermined upper bound, i.e.,* $\left\|\tilde{\bullet}\right\|^2 \leq \bar{\delta}_{bound}$ *. Hence, the robust terms* $\boldsymbol{\eta}_i$ *should be designed such that* $\eta_{ij(i=1,2;\, j=1,..,n)} \geq \bar{\delta}_{bound}$ *.*

Remark 5-2: *In order to enhance the force estimation, the estimation algorithm in Equation* (5.7) *is modified with adding signum function by*:

$$\begin{cases} \dot{\hat{\mathbf{x}}}_1 = \hat{\mathbf{x}}_2 - \dfrac{\boldsymbol{\alpha}_1}{\sigma_1}\left(\hat{\mathbf{y}} - \mathbf{y}\right) \\ \dot{\mathbf{x}}_2 = \mathbf{M}^{-1}\left(\mathbf{x}_1\right)\left(\boldsymbol{\tau} - \mathbf{C}\left(\mathbf{x}_1, \mathbf{x}_2\right)\mathbf{x}_2 - \mathbf{G}\left(\mathbf{x}_1\right) - \boldsymbol{\Delta}\right) \\ \qquad - \mathbf{M}^{-1}\left(\mathbf{x}_1\right)\mathbf{J}^T\left(\mathbf{q}\right)\hat{\mathbf{F}}_{ext} - \dfrac{\boldsymbol{\alpha}_2}{\sigma_1^2}\left(\hat{\mathbf{y}} - \mathbf{y}\right) \\ \hat{\mathbf{y}} = \hat{\mathbf{x}}_1 + \hat{\mathbf{x}}_{f_1} - \dfrac{\boldsymbol{\eta}_{f1}}{\sigma_1}\left(\hat{\mathbf{y}} - \mathbf{y}\right) \\ \dot{\mathbf{x}}_{f_1} = -\dfrac{\boldsymbol{\eta}_{f1}}{\sigma_1^3}\left(\hat{\mathbf{y}} - \mathbf{y}\right) \\ \hat{\mathbf{F}}_{ext,m} = K_e\left(\hat{\mathbf{X}}_a - \mathbf{X}_e\right) + \hat{\mathbf{x}}_{f_2} \\ \dot{\hat{\mathbf{x}}}_{f_2} = -\dfrac{\boldsymbol{\eta}_{f2}}{\sigma_1^3}\left(\hat{\mathbf{F}}_{ext,m} - \mathbf{F}_{ext,m}\right) - \dfrac{\boldsymbol{\eta}_{f3}}{\sigma_1^3} sign\left(\hat{\mathbf{F}}_{ext,m} - \mathbf{F}_{ext,m}\right) \end{cases} \tag{5.47}$$

5.5 Numerical simulation

5.5.1 Setup scenario

In this section, the scenario in which the influence of encoder and force sensor faults and effectiveness of the active FTC based on the integration of the FBSMC with ESO is verified through several comparative simulations on a 3-DOF serial hydraulic manipulator, as shown in figure 5-4 [12]. In order to simplify the calculation, the first joint of the 3-DOF serial hydraulic manipulator is fixed, i.e., $\mathbf{q}_1 = \dot{\mathbf{q}}_1 = 0$. Then, the objective is to investigate the behavior of the 2-DOF serial manipulator subject to encoder and force sensor faults. The constrained framework is located in the plane S_Z that is parallel to the plane (*XOY*). The system parameters, including mechanical part and hydraulic actuator part, are given in TABLE 1 and TABLE 2, respectively. The FBSMC controller gains are $\boldsymbol{\lambda} = 1000\mathbf{I}_2$, $\mathbf{K}_1 = 120\mathbf{I}_2$, $\boldsymbol{\eta}_1 = 0.5\mathbf{I}_2$, $\delta = 10^{-4}$, $\mathbf{K}_2 = 120\mathbf{I}_2$, $\boldsymbol{\eta}_2 = 0.5\mathbf{I}_2$.

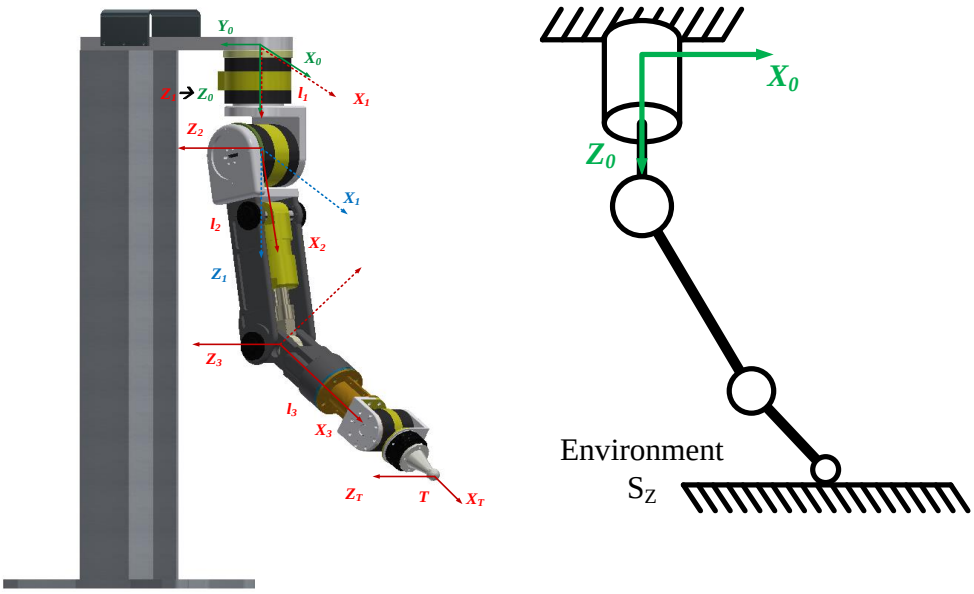

(a) (b)

Figure 5-4 3-DOF serial hydraulic manipulator: (a) Structure with link frame, and (b) working environment framework.

***Table 5-1**. Mechanical parameters.*

Symbol	Quantity	Value
m_1	Mass of the first link	2 [kg]
m_2	Mass of the second link	5.1 [kg]
m_3	Mass of the third link	4.7 [kg]
L_1	Length of the second link	0.5 [m]
L_2	Length of the third link	0.2 [m]

***Table 5-2**. Hydraulic parameters.*

Symbol	Quantity	Value [unit]
P_S	Supply pressure from the tank	100 [bar]
P_t	Return pressure to the tank	1 [bar]
K_v	Gain factor of the valve dynamics	$1.2\text{x}10^{-3}$ [m/V]
ω	Servo valve area gradient	0.024 [m^2]
ρ	Oil density	800 [kg/m^3]
β	Effective Bulk modulus	$1.25\text{x}10^{9}$ [pa]
A_{11}, A_{12}	Volumetric area of rotary actuator 2	$2\text{x}10^{-4}$ [m^3/rad]
A_{21}, A_{22}	Volumetric area of rotary actuator 3	$1.2\text{x}10^{-4}$ [m^3/rad]
A_{31}	Cylinder area of piston head part	$1.53\text{x}10^{-3}$ [m^2]
A_{32}	Cylinder area of piston rod part	$1.04\text{x}10^{-3}$ [m^2]

5.5.2 Simulation results

5.5.2.1 Case study 1: Occurrence of encoder sensor faults in free motion

In the first case study, we verify the effectiveness of the proposed fault estimation in the case of only signal faults occurrence on joint angle encoders in free motion. The desired joint trajectory and fault signals are given by:

$$\mathbf{q}_d = \mathbf{x}_{1d} = \begin{pmatrix} 0 \\ 45 + 30\sin\left(2\pi t/5\right) \\ 45 + 30\sin\left(2\pi t/5 + \pi/4\right) \end{pmatrix} (\text{degree}) \tag{5.48}$$

$$\mathbf{x}_{f1} = \begin{pmatrix} x_{f1,\text{joint}2} \\ x_{f1,\text{joint}3} \end{pmatrix}, x_{f1,\text{joint}2} = \begin{cases} 0 \ (\text{degree}) & \text{if } t < 10s \\ 10 \ (\text{degree}) & \text{if } t \geq 10s \end{cases}, x_{f1,\text{joint}3} = \begin{cases} 0 \ (\text{degree}) & \text{if } t < 20s \\ 10 \ (\text{degree}) & \text{if } t \geq 20s \end{cases} \tag{5.49}$$

The observer gains in (13) are $\sigma_1 = 0.1$, $\boldsymbol{\alpha}_1 = 2\mathbf{I}_2$, $\boldsymbol{\alpha}_2 = 2\mathbf{I}_2$, $\boldsymbol{\eta}_{f1} = 4\mathbf{I}_2$. The values of system performance and observers are all initialized as zero. The position tracking performance and state estimation of the two joints are depicted in **Figure 5-5**.

In these figures, the black continuous line denotes the desired joint angle trajectory $q_{i,ref}$, the blue dash line denotes the measured joint angles $q_{i,m}$, the red dot-dash line denotes the real joint angles $q_{i,r}$, the green dot-dot line denotes the estimated measured joint angles $q_{i,m,est}$, and the purple line denotes the estimated real joint angle $q_{i,r,est}$, with i = 2,3.

As can be seen in **Figure 5-5**, when faults occur, since the measured faulty signals are feedback to the controller, the actuator executes the faulty commanded signals; thus, the actual system performance is different from the desired trajectory.

Figure 5-6 shows the estimation of faulty signals. As the faults of the 2nd joint and 3rd joint occur at the time of 10 and 20 second, respectively, the robust observer can instantly respond to estimate their residual signals. The blue continuous line and red dot-dash line denote the sensor fault signals adding on the 2nd and 3rd joints, respectively; the green dot-dot line and purple dash line denote the estimated sensor fault signals with respect to the homologous real faults, respectively.

The idea of the robust observer is that the measured joint angle, including real and faulty signals, is estimated; thereby, the actual joint angle and faulty signal are then estimated and feedback to the controller.

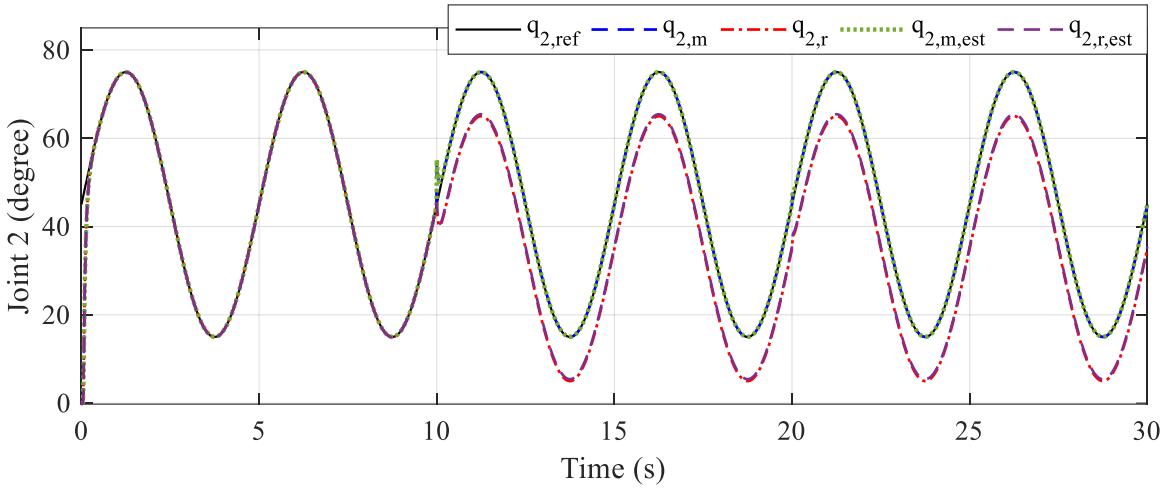

(a)

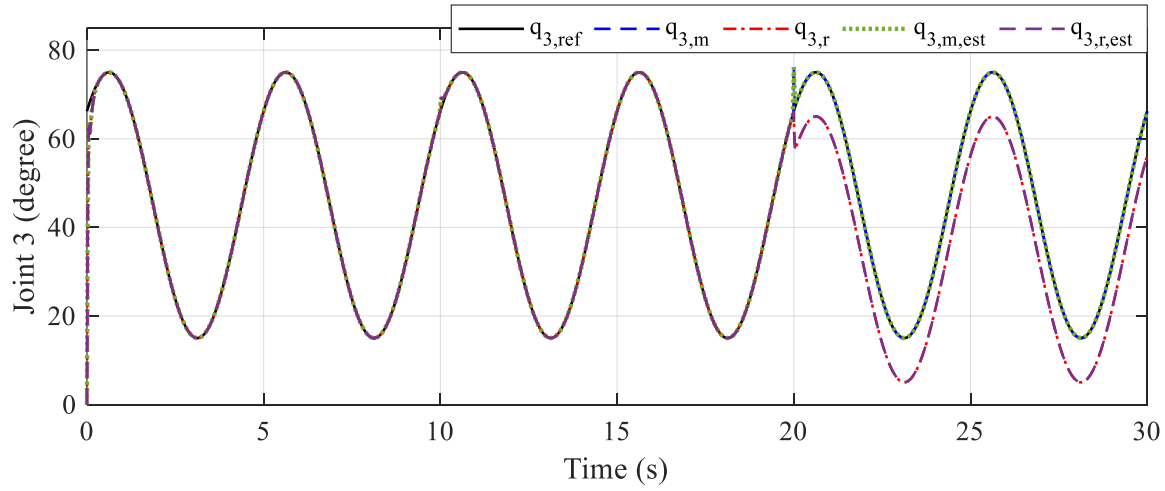

(b)

Figure 5-5 Position tracking performance and estimation without FTC under the presence of fault signals: (a) 2nd joint with measured joint angle feedback, (b) 3rd joint with measured joint angle feedback.

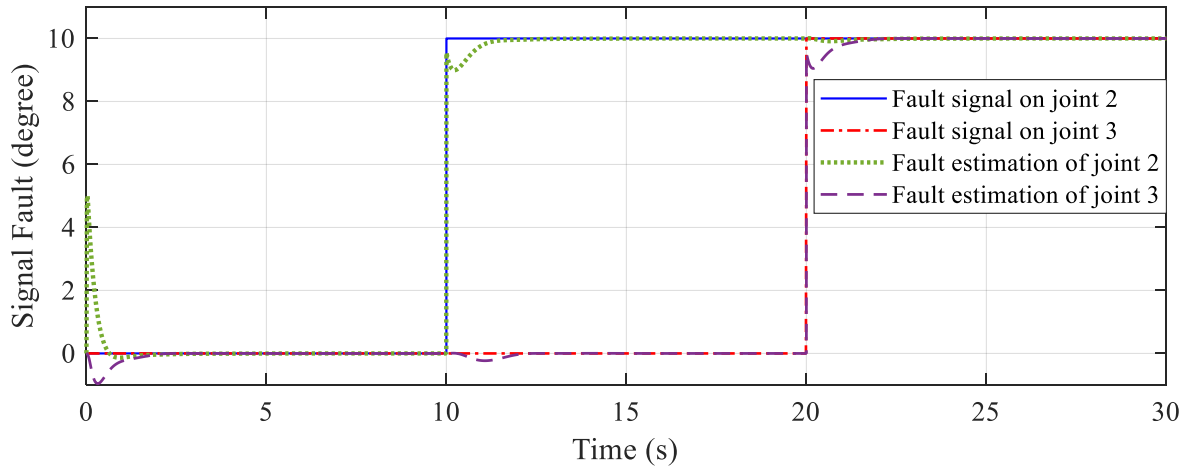

Figure 5-6 Real faults and faults estimation using robust observer.

Practically, signal faults are unknown; thus, the actual joint angles are not able to be monitored without fault estimation technique since only measured joint angle is available. With the fault estimation method, the actual joint angles and faulty signals are estimated. Then the estimated joint angles are assigned as feedback signals to the main active FTC. The effectiveness of this proposed control scheme is shown in **Figures 5-7** in which the actual joint angles are accurately estimated and follow the desired trajectory.

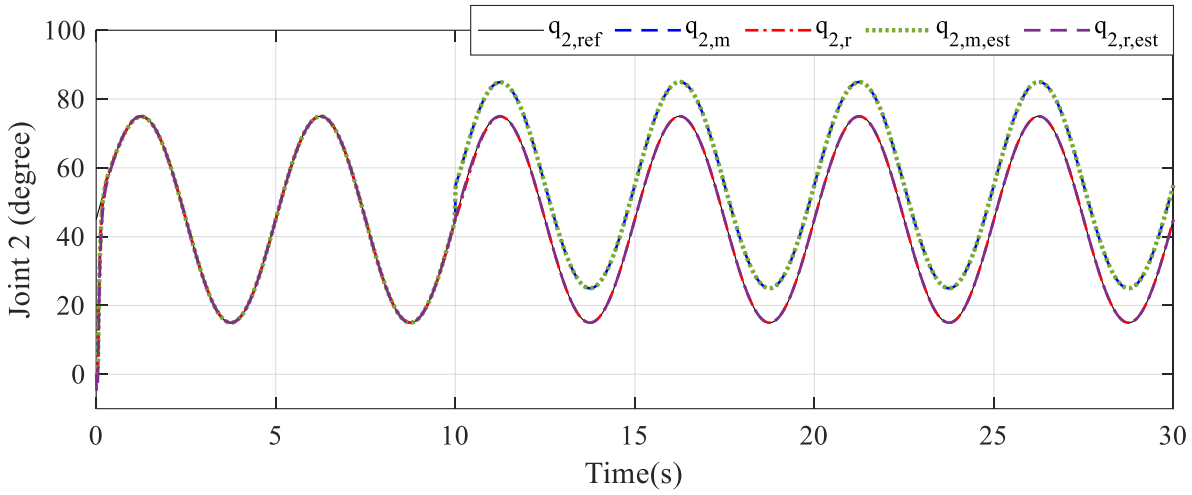

(a)

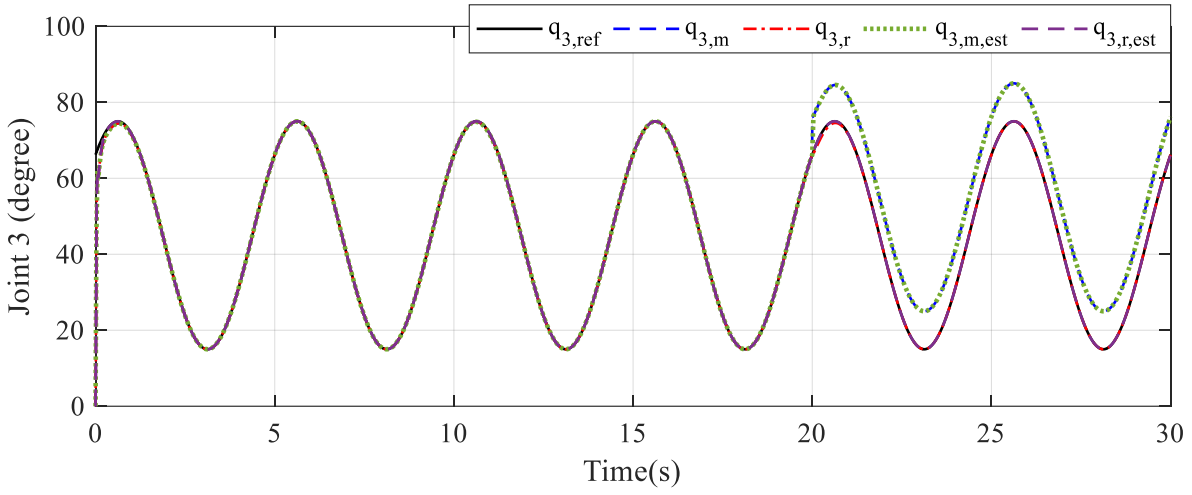

(b)

Figure 5-7 Position tracking performance under the FTC with ESO: (a) 2nd joint with the estimated joint angle feedback, (b) 3rd joint with the estimated joint angle feedback.

5.5.2.2 Case study 2: Occurrence of force sensor fault in constrained motion

In the second case study, the effectiveness of the active FTC is verified in the constrained framework. The desired trajectory and desired interactive force are given by:

$$\mathbf{X}_d = \begin{pmatrix} X_{d,X} \\ X_{d,Z} \end{pmatrix}(m)$$
$$= \begin{pmatrix} -\dfrac{2\left(X_{d,Xf} - X_{d,X0}\right)}{t_f^3}t^3 + \dfrac{3\left(X_{d,Xf} - X_{d,X0}\right)}{t_f^2}t^2 + X_{d,X0} \\ -\dfrac{2\left(X_{d,Zf} - X_{d,Z0}\right)}{t_f^3}t^3 + \dfrac{3\left(X_{d,Zf} - X_{d,Z0}\right)}{t_f^2}t^2 + X_{d,Z0} \end{pmatrix} \tag{5.50}$$

$$F_{d,Z}(N) = \begin{cases} 0 & \text{if } t < 4.5s \\ 30 & \text{if } 4.5 \le t < 9s \\ 0 & \text{if } 9 \le t < 13s \\ 15 & \text{if } 13 \le t \le 17s \\ 0 & \text{if } t > 17s \end{cases} \tag{5.51}$$

where $X_{d,X0} = 0.2(m)$ and $X_{d,Xf} = 0.85(m)$ denote the final and initial points of the desired trajectory along X-direction, respectively; $X_{d,Z0} = 0.5(m)$ and $X_{d,Zf} = -0.2(m)$ denote the final and initial points of the desired trajectory along Z-direction, respectively.

In this scenario, the manipulator is in interaction with the environment in the (S_Z) plane, only normal force in the Z-direction is considered; then, the environment location is given as

$$X_{env,Z} = 0.4(m) \tag{5.52}$$

In order to illustrate the sensor fault signals, the offset values are added to the feedback force and joint angles. The fault signals of encoder and force sensors are given by:

$$F_{d,Z,fault} = x_{f2,Z} \begin{cases} 0(N) & \text{if } t < 6s \\ -10(N) & \text{if } 6 \le t < 12s \\ -6(N) & \text{if } t > 12s \end{cases} \tag{5.53}$$

It is noteworthy that if the force sensor remains an offset value when the end-effector is not in contact with the environment, it is because of the calibration process. Therefore, the measured interactive force signal is only offset in the constrained motion when the desired force is not zero. Otherwise, the force sensor returns zero. The parameters of the impedance behaviors are $\mathbf{D}_m = 10\mathbf{I}_2$, $\mathbf{B}_m = 100\mathbf{I}_2$, $\mathbf{K}_m = 500\mathbf{I}_2$, $K_e = 5000$, force control gains are $\mathbf{K}_{Pf} = 4\mathbf{I}_2$, $\mathbf{K}_{If} = 60\mathbf{I}_2$, $\boldsymbol{\eta}_f = 0.5\mathbf{I}_2$; and force observer gains are $\boldsymbol{\eta}_{f2} = 200\mathbf{I}_2$, $\boldsymbol{\eta}_{f3} = 10\mathbf{I}_2$. The initial position of the end-effector is $X_{X0} = -0.2(m)$ and $X_{d,Z0} = 0.5(m)$.

Figure 5-8 shows the response of the measured force and actual force exerted on the end-effector. The negative value of force sensor fault signal in Equation (5.53) implies that the measured force is less than the actual interactive force. It means the control action attempts to generate more force than necessity without consideration of faulty signal. Practically, the actual interactive force cannot be obtained due to unknown signal fault. Only measured force, which includes the fault, is measured when

using force sensor. When employing the ESO, the measured force is estimated; thus, the actual force and signal fault are systematically estimated. The black continuous line denotes the desired force $F_{desired}$, the blue dash line denotes the measured interactive force $F_{ext,m}$, the red dot-dash line denotes the real interactive force $F_{ext,r}$, the green dot-dot line denotes the estimation of the measure interactive force $F_{ext,m,est}$, the purple line denotes the estimation of the real interactive force $F_{ext,r,est}$. With the estimation, the faulty signal is removed, and the estimated actual interactive force is feedback to the controller. Consequently, the actual force properly tracks the desired one whereas the measured force is offset by the exact faulty signal, as shown in **Figure 5-9**. The fault estimation and its estimated error are depicted in **Figures 5-10**(a) and **5-10**(b), respectively.

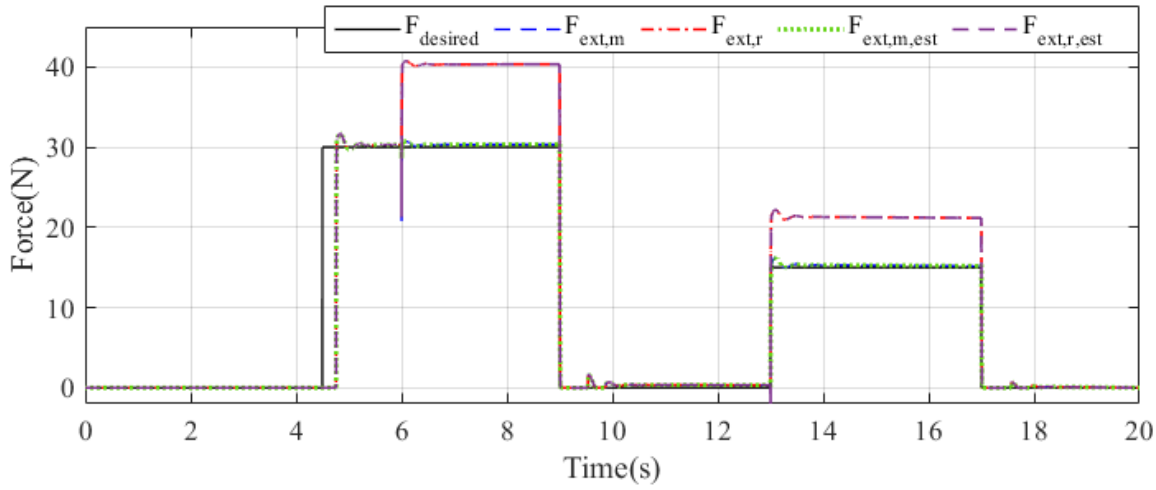

Figure 5-8 Force tracking performance and estimation results without FTC in the presence of sensor fault.

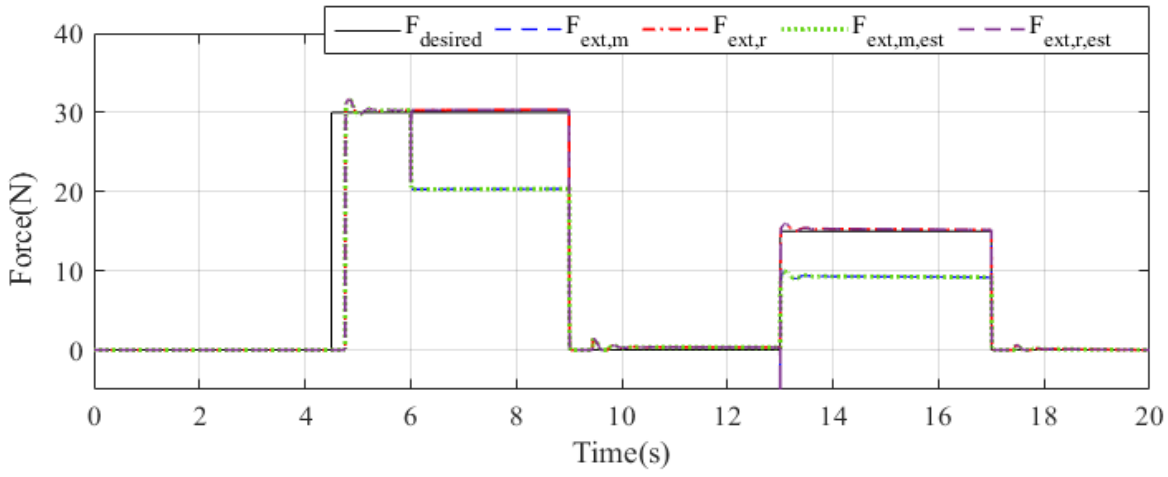

Figure 5-9 Force tracking performance under the FTC with ESO (i.e. estimated interactive force is feedback to the main controller).

Figure 5-11 shows the end-effector performance under the presence of force sensor fault in constrained framework conditions. The black continuous line denotes the originally desired trajectory,

the green continuous line denotes the environment, the blue dash line denotes the constrained behavior of the end-effector without FTC, and the red dot-dash line denotes the constrained behavior of the end-effector with the active FTC. As can be compared, the difference of real exerted interactive force results in the difference in the real end-effector behavior. With the force sensor fault estimation and active FTC, the end-effector performance is the same as the case of fault-free condition.

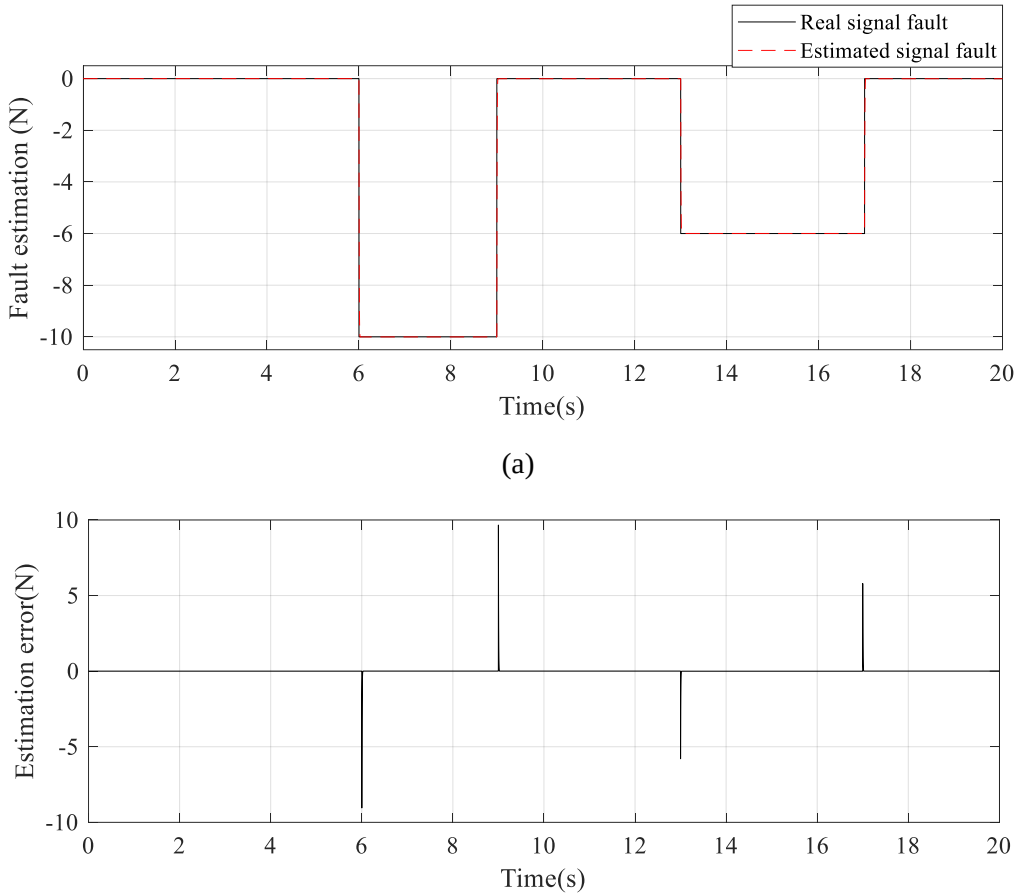

Figure 5-10 Signal fault estimation results: (a) magnitude of faulty signal, and (b) estimation error.

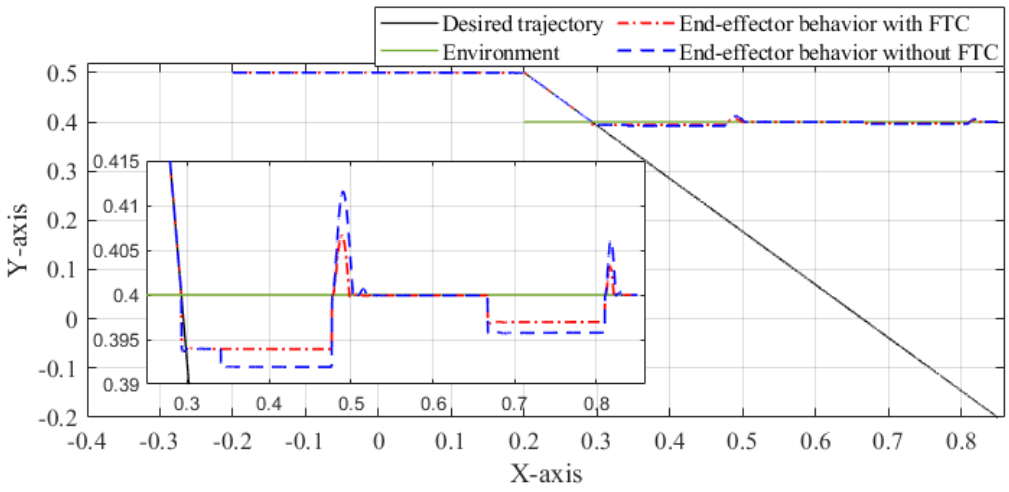

Figure 5-11 End-effector behavior under the presence of force sensor fault in constrained motion.

5.6 Conclusion

This paper proposed a novel fault estimation algorithm to detect and estimate both encoder and force sensor faults on the n-DOF serial hydraulic manipulator subjected to constrained framework conditions. These faults may originate from practical setup calibration or accommodation of measured signal offset due to long-term usage. To address the influence of the sensor faults, the fault estimation algorithm based on ESO was designed to detect and estimate the measured and actual joint angle and force faulty signals. In order to exhibit more fast convergence and estimation accuracy, some remarks with modified updating laws were introduced. Then, the estimated force was feedback to the impedance control block and the estimated actual joint angles were feedback to the main controller. Based on the feedback estimated variables, the active FTC-based FBSMC scheme was designed to execute the suitable action on the actuators. The stability of the proposed ESO and closed-loop system is mathematically proven by performing the Lyapunov theorems. The comparative simulations on the 3-DOF serial hydraulic manipulator verified the effectiveness of the proposed algorithm in instantly detecting and estimating the faulty residuals. With the advantage of the ESO, the real actual interactive force can be online estimated; thereby, force-sensorless-based ESO can be certainly implemented to replace the use of force sensors. This paper can be considered as a premise with some remaining limitations, which pertain to assumptions to facilitate the control methodology design such as consideration of forward kinematic in the ESO, the simultaneous joint angle and force sensor faults occurrences, fast time-variant signal faults, influences of friction and disturbances, or the hybrid observer may evoke interesting topics for further developments.

CHAPTER 6
Control strategy for Safety Operation with Contact-loss for n-DOF serial Hydraulic Manipulator in Constrained Motion

6.1 Introduction

The currently growing attractiveness in field of industrial applications such as polishing, welding, wiping, assembling, etc. reasonably results in requirements of workability in constrained framework. Generally, hybrid position/force control, impedance, and/or admittance controls which are directly involved in force regulation are frequently applied to deal with problems of physical interactions. Despite achieving good outcomes, safety operation of the manipulator in cases of sudden contact-loss due to moving out the constrained framework, step-change of environment, accidentally unloading or payload drop is rarely mentioned. Stability, robustness, and especially safety are mandatory requirements when the robot is in interacting with the environment. Therefore, to cope with and achieve human-like behaviors in those possible aforementioned issues, an energy-tank concept-based passivity control was proposed [91–93]. This concept is based on the fact that system potential energy is stored in springs or stiffness components (treated as virtual tanks) during the working processes. When the contact-loss or sudden change occurs, the end-effector is still being regulated such that force tracking is satisfied and the energy is released simultaneously; thereby, resulting in unexpected behaviors. Therefore, auxiliary variables are designed to passively detect and switch their states for deactivating force command signals and dissipating the energy when the contact-loss happens. Furthermore, a new trajectory reshaped for smooth and safe operation is also mentioned. This technique was expanded to several fields such as bilateral telemanipulation [94–96], surgical robotics [40–42], and industrial manipulator applications with variable stiffness [92,93,100]. In [92], Schindlbeck et al. utilized a unified passivity-based force/impedance control based-energy tank to not only deal with the contact-loss but also guarantee the stability and robustness of the KUKA/DLR LWR-III robot. In [93], Toedtheide et al. successfully investigated behaviors of a pneumatic actuator robotic system with unified torque/impedance control-based energy tank. Based on the literature overview, this chapter presents a virtual energy tank concept as a fault detection method to deal with a problem of accidental contact-loss on an n-degree-of-freedom (n-DOF) serial hydraulic manipulator in constrained frameworks.

Figure 6-1 3D design of the 6-DOF serial hydraulic KIRO robot.

The mechanical design of the 6-DOF serial hydraulic KIRO robot is shown in **Figure 6-1**. The KIRO robot is constructed with six revolute joints where the first five links are structured in closed-chain form and driven by hydraulic cylinders, and the last link is driven by hydraulic rotary actuator. The structure and working principle of all actuators follow the principle presented in Chapter 3. The simplified link frame of the KIRO robot is displayed in **Figure 6-2**.

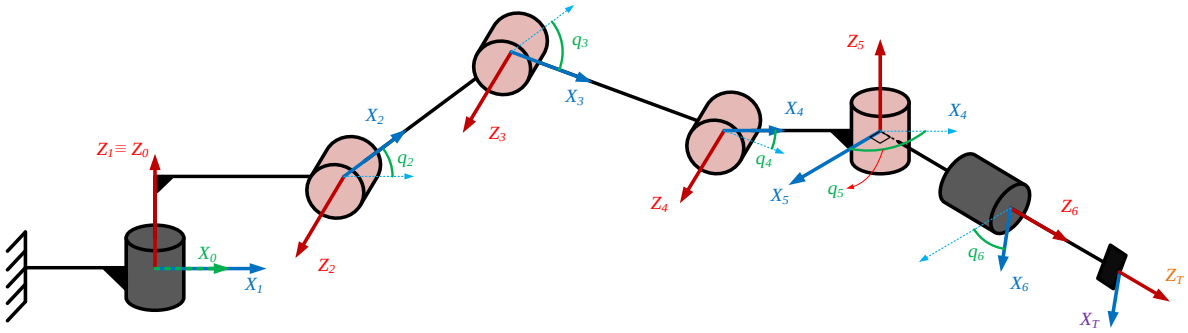

Figure 6-2 Schematic representation of the 6-DOF serial hydraulic KIRO robot.

The frame $\{i\}$ is attached rigidly to the link i^{th}, the basement is coincident with the link 0, and the frame {T} is referred to the end-effector frame. The axis Z_i of frame $\{i^{th}\}$ is coincident with the joint axis i^{th}. Different from conventional industrial manipulator where electric motors are utilized to directly generate rotational motion, the rotational motion of the first five links are generated from the homologous cylinders through closed-chain. Thereby, force produced by the cylinder is converted to torque that executes the rotational motion.

6.2 Modified position-based impedance control with virtual energy tank

6.2.1 Contact-loss consideration-based virtual energy tank and passivity control.

In this section, a virtual energy tank is employed with passivity control scheme to deal with sudden contact-loss situation. The schematic diagram for impedance control with virtual energy tank and passivity control algorithm is shown in **Figure 6-3**.

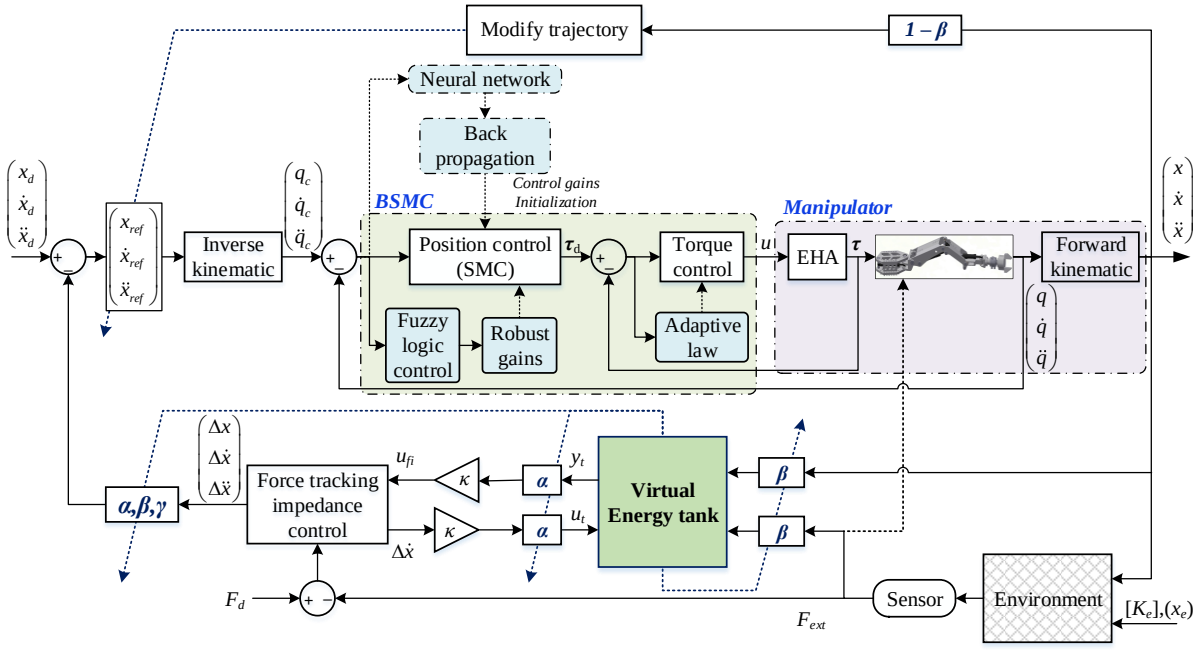

Figure 6-3 Schematic diagram of the impedance control with virtual energy tank and passivity control for contact lost consideration.

From the previous chapter, the position-based impedance control takes the form of:

$$\mathbf{D}_m\Delta\ddot{\mathbf{X}}+\mathbf{B}_m\Delta\dot{\mathbf{X}}+\mathbf{K}_m\Delta\mathbf{X}=\mathbf{u}_{imp} \tag{6.1}$$

$$\mathbf{u}_{imp}=\mathbf{K}_{Pf}\left(\mathbf{F}_{ext}-\mathbf{F}_d\right)+\mathbf{K}_{If}\int\left(\mathbf{F}_{ext}-\mathbf{F}_d\right)+\boldsymbol{\eta}_f\,sign\left(\mathbf{F}_{ext}-\mathbf{F}_d\right) \tag{6.2}$$

In this section, an accidental contact-loss due to the step-change of environment is considered as a fault. Hence, a fault-detection-based virtual energy tank is suggested to decouple force regulation as prior safety criterion. Define $\mathbf{x}_t$ is a state associated with the tank that stores energy. The dynamics of the virtual energy tank variable is expressed by [91]:

$$\dot{\mathbf{x}}_t=\beta\mathbf{x}_t^{-1}\left(\Delta\dot{\mathbf{x}}^T\mathbf{B}_m\Delta\dot{\mathbf{x}}-\gamma\Delta\dot{\mathbf{x}}^T\mathbf{u}_f\right)+\mathbf{u}_t \tag{6.3}$$

where $\mathbf{u}_t$ is the control input of the tank, and $\mathbf{u}_f$ is the additive control input signal of the force tracking impedance control scheme. $\mathbf{u}_t$ and $\mathbf{u}_f$ are calculated by:

$$\begin{pmatrix}\mathbf{u}_{fi}\\ \mathbf{u}_t\end{pmatrix}=\begin{bmatrix}0 & \boldsymbol{\kappa}\\ -\boldsymbol{\kappa}^T & 0\end{bmatrix}\begin{pmatrix}\Delta\dot{\mathbf{x}}\\ \mathbf{x}_t\end{pmatrix} \tag{6.4}$$

with $\boldsymbol{\kappa}$ is described as

$$\boldsymbol{\kappa}(\mathbf{F}_{ext},t)=\alpha\left(1-\gamma\right)\mathbf{x}_t^{-1}\mathbf{u}_{imp} \tag{6.5}$$

Three switching parameters α, β, γ are defined as the following:

$$\alpha=\begin{cases}1 & \text{if } T_t>T_l\\ 0 & \text{otherwise}\end{cases} \tag{6.6}$$

$$\beta = \begin{cases} 0 & \text{if } T_t \geq T^u \\ 1 & \text{otherwise} \end{cases} \tag{6.7}$$

$$\gamma = \begin{cases} 1 & \text{if } \Delta\dot{\mathbf{x}}^T \mathbf{u}_{imp} \leq 0 \\ 0 & \text{otherwise} \end{cases} \tag{6.8}$$

where T_t is energy stored in the virtual tank; α is a switched parameter when the energy tank reaches its lower bound T_l; β is a switched parameter in case the energy tank from the force/impedance controller exceeds an upper bound T^u; then this parameter is used to detect an occurrence of contact-loss; γ is presented to guarantee the stability of the overall system.

Remark 6-1: *The value of the lower bound T_l is set to be greater than 0 to avoid the singularity. In this work, the lower bound is set at 0.1, and the parameters α is consequently equal to 1.*

The energy stored in the virtual tank T_t is calculated as

$$T_t = \frac{1}{2}\mathbf{x}_t^T \mathbf{x}_t \tag{6.9}$$

Finally, extended dynamics of the impedance with contact-loss consideration is rewritten as the following:

$$\mathbf{D}_m \Delta\ddot{\mathbf{X}} + \mathbf{B}_m \Delta\dot{\mathbf{X}} + \mathbf{K}_m \Delta\mathbf{X} = \mathbf{u}_{imp-cl} \tag{6.10}$$

where $\mathbf{u}_{imp-cl}$ is a modified control input signal of impedance/contact-loss:

$$\mathbf{u}_{imp-cl} = \beta\gamma\mathbf{u}_{imp} + \beta\mathbf{u}_f \tag{6.11}$$

As can be seen in Equation (6.11), the additive term $\mathbf{u}_f$ and switching parameters β, and γ are supplemented to the force tracking control to decouple the signal from the force regulation when contact-loss happens. To demonstrate the stability of the closed-loop control system, the following candidate Lyapunov function is introduced [101]:

$$V_{imp} = \frac{1}{2}\Delta\dot{\mathbf{x}}^T \mathbf{D}_m(\mathbf{x})\Delta\dot{\mathbf{x}} + \frac{1}{2}\Delta\mathbf{x}^T \mathbf{K}_m(t)\Delta\mathbf{x} + \frac{1}{2}\mathbf{x}_t^T \mathbf{x}_t \tag{6.12}$$

Taking the derivative of the Lyapunov function, one obtains:

$$\dot{V}_{imp} = \Delta\dot{\mathbf{x}}^T \mathbf{D}_m \Delta\ddot{\mathbf{x}} + \Delta\mathbf{x}^T \mathbf{K}_m \Delta\dot{\mathbf{x}} + \mathbf{x}_t^T \dot{\mathbf{x}}_t \tag{6.13}$$

Substituting Equation (6.1) into Equation (6.13) yields:

$$\dot{V}_{imp} = \Delta\dot{\mathbf{x}}^T \mathbf{u}_{imp} - \Delta\dot{\mathbf{x}}^T \mathbf{B}_m \Delta\dot{\mathbf{x}} + \mathbf{x}_t^T \left(\beta\mathbf{x}_t^{-1}\left(\Delta\dot{\mathbf{x}}^T \mathbf{B}_m \Delta\dot{\mathbf{x}} - \gamma\Delta\dot{\mathbf{x}}^T \mathbf{u}_{imp}\right) - \boldsymbol{\kappa}\Delta\dot{\mathbf{x}}\right) \tag{6.14}$$

$$\dot{V}_{imp} = \Delta\dot{\mathbf{x}}^T \mathbf{u}_{imp} - \Delta\dot{\mathbf{x}}^T \mathbf{B}_m \Delta\dot{\mathbf{x}} + \left(\beta\left(\Delta\dot{\mathbf{x}}^T \mathbf{B}_m \Delta\dot{\mathbf{x}} - \gamma\Delta\dot{\mathbf{x}}^T \mathbf{u}_{imp}\right) - \Delta\dot{\mathbf{x}}^T \boldsymbol{\kappa}\mathbf{x}_t\right) \tag{6.15}$$

Substituting Equation (6.5) into Equation (6.15) results in:

$$\dot{V}_{imp} = \Delta\dot{\mathbf{x}}^T\mathbf{u}_{imp} - \Delta\dot{\mathbf{x}}^T\mathbf{B}_m\Delta\dot{\mathbf{x}} + \left(\beta\left(\Delta\dot{\mathbf{x}}^T\mathbf{B}_m\Delta\dot{\mathbf{x}} - \gamma\Delta\dot{\mathbf{x}}^T\mathbf{u}_f\right)\right) - \Delta\dot{\mathbf{x}}^T\alpha(1-\gamma)\mathbf{u}_{imp} \tag{6.16}$$

As introduced in Equation (6.6), to avoid the singularity, the lower limitation T_l should be set to be greater than zero and then, the switching α should be kept being 1 at all times. Therefore, the Equation (6.16) equivalents to:

$$\begin{aligned}\dot{V}_{imp} &= \Delta\dot{\mathbf{x}}^T\mathbf{u}_{imp} - \Delta\dot{\mathbf{x}}^T\mathbf{B}_m\Delta\dot{\mathbf{x}} + \left(\beta\left(\Delta\dot{\mathbf{x}}^T\mathbf{B}_m\Delta\dot{\mathbf{x}} - \gamma\Delta\dot{\mathbf{x}}^T\mathbf{u}_{imp}\right)\right) - \Delta\dot{\mathbf{x}}^T(1-\gamma)\mathbf{u}_{imp} \\ &= -(1-\beta)\left(\Delta\dot{\mathbf{x}}^T\mathbf{B}_m\Delta\dot{\mathbf{x}} - \gamma\Delta\dot{\mathbf{x}}^T\mathbf{u}_{imp}\right)\end{aligned} \tag{6.17}$$

Combining with the condition in Equation (6.8), then Equation (6.17) becomes:

$$\dot{V}_{imp} = \begin{cases} -(1-\beta)\left(\Delta\dot{\mathbf{x}}^T\mathbf{B}_m\Delta\dot{\mathbf{x}} - \gamma\Delta\dot{\mathbf{x}}^T\mathbf{u}_{imp}\right) \le 0, & if\ \Delta\dot{\mathbf{x}}^T\mathbf{u}_{imp} \le 0 \\ -(1-\beta)\Delta\dot{\mathbf{x}}^T\mathbf{B}_m\Delta\dot{\mathbf{x}} \le 0, & if\ \Delta\dot{\mathbf{x}}^T\mathbf{u}_{imp} > 0 \end{cases} \tag{6.18}$$

Thus, the closed-loop control system with energy tank is passive stable.

6.2.2 Modification of trajectory

The previous section presented the effectiveness and stability of using the energy tank for contact-loss detection. However, this action only helps to decouple the signal command from force control from the overall controller scheme. Thereby, the end-effector follows the setup desired trajectory. Moreover, due to reaching the upper bound of the energy tank, the end-effector may attempt to regulate force until draining all energy in the virtual tank in some cases. Consequently, unsafe motions may be executed. To completely exhibit safety motion when contact-loss happens, a new trajectory should be designed to smooth the motion of the end-effector. For this purpose, a controlled shaping function $\varphi(\zeta)$, where ζ is a shift variable, is introduced as [93]

$$\varphi_i = \begin{cases} 1 & \text{if } F_{di}^T\Delta p_i \ge 0 \\ \dfrac{1}{2}\left(1+\cos\left(\pi\dfrac{\zeta_i}{d_{i\max}}\right)\right) & \text{if } \left(F_{di}^T\Delta p_i < 0\right) \cap \left(0 < \zeta_i < d_{i\max}\right) \\ 0 & \text{otherwise} \end{cases} \tag{6.19}$$

$$\boldsymbol{\kappa}_\rho = \varphi\boldsymbol{\kappa} \tag{6.20}$$

where $\zeta_i = \Delta p_i - \Delta x_{si} sign(F_{di})$ (i = 1,2,3) is a shifted variable, Δp is the error between the modified trajectory and actual position, Δx_{si} is an arbitrary constant that describes a robust region which denotes the distance between the end-effector to the set-point for shaping motion, and $d_{i\max}$ is an arbitrary constant that denotes the width of the region for shaping. It follows that if the desired force F_{di} and the position error Δp encloses the robust region and passes the frontier, then the controller should be deactivated.

The role of designing the shaping function is to handle unexpected motion when contact-loss happens. A shaping function ρ is introduced to generate a smooth transition between the force and impedance control; thus, providing a smooth transition in position performance of the end-effector.

After generating a smooth transition between force and impedance control when contact loss occurs, the next important step is designing a suitable set-point such that the robot can follow without shock or unexpected motion. In order to avoid fast and unexpected motions in case of contact loss, which are caused by the impedance controller for large deflection from the set point, the set-point of the impedance control, called as commanded trajectory x_c, is set close to the contact point $\mathbf{x}_{contact}$ as $\mathbf{x}_c = \mathbf{x}_{fade} = \mathbf{x}_{contact} - \xi$, where $\mathbf{x}_{contact} = \mathbf{x}_{env}$ is the measured position of the end-effector at t_0 and ξ is a small number (Indeed, when contacting with the environment, the measured position of the end-effector is same as the environment. In the simulation, for illustration of impedance control, $\mathbf{x}_{contact}$ is the actual position of the end-effector and this variable is different from the location of environment). A possible fading function is applied to obtain a continuous transition to the new set point. The flowchart for the fading trajectory is illustrated in **Figure 6-4** in which the set-point is determined based on the switching parameter β and comparison between the current and last position based-time-delay than using pre-determined or knowledge of the location of environment as in [92,93].

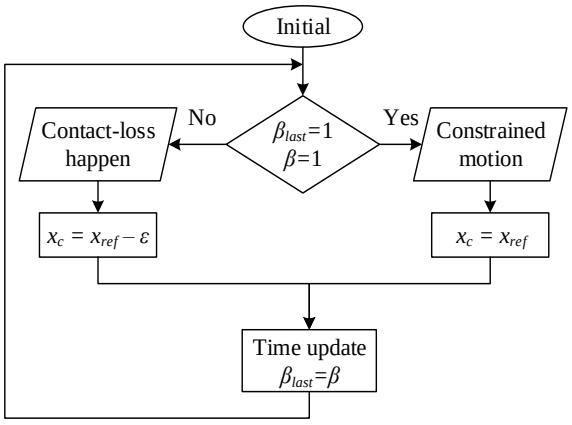

Figure 6-4 Strategy of fading function for smoothing trajectory.

6.3 Force sensorless-based extended state observer (ESO)

In this section, a force estimator is introduced to estimate the external torques at joint space, which reflect the external forces at the end-effector. The force estimator which is based on ESO estimates not only the unmeasured states but also the external moments. The overall control scheme of the proposed impedance control methodology is depicted in **Figure 6-5**.

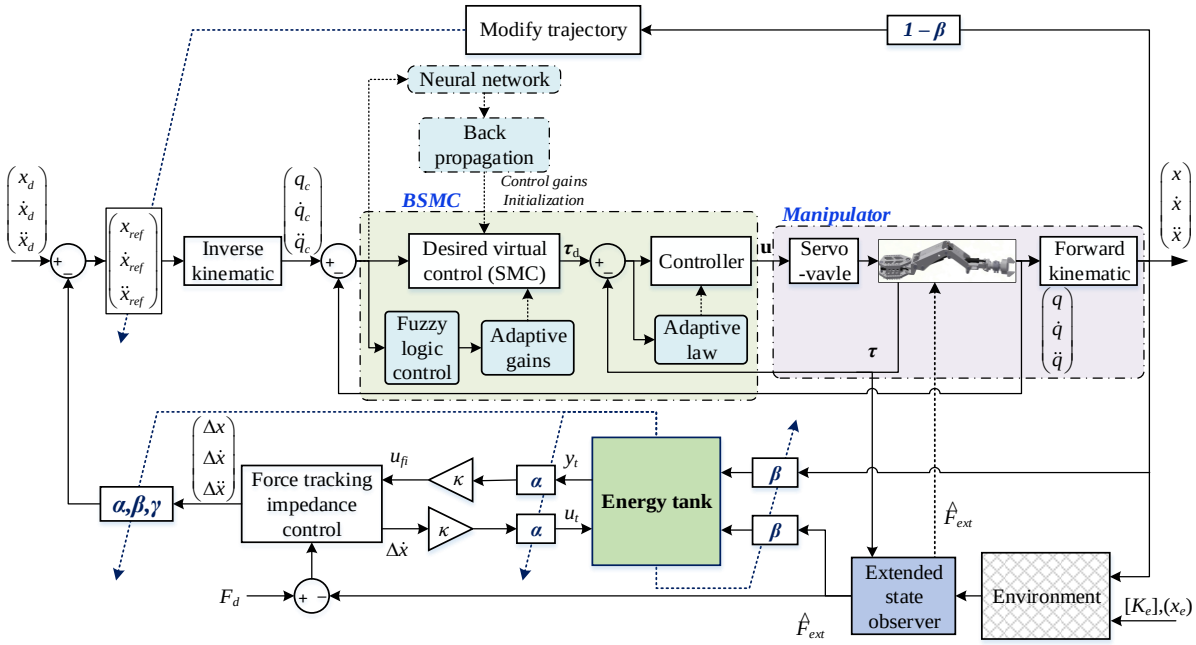

Figure 6-5 Impedance control-based energy tank with force observer for contact-loss problem.

In order to employ this estimator, an extra state $\mathbf{z}_3 \in R^6$ is added in the manipulator dynamics to present the external torque term, $\mathbf{M}^{-1}(\mathbf{z}_1)\boldsymbol{\tau}_{ext}$. Now, the system state is presented $\mathbf{z} = (\mathbf{z}_1 \quad \mathbf{z}_2 \quad \mathbf{z}_3)^T = (\mathbf{q}^T \quad \dot{\mathbf{q}}^T \quad \mathbf{M}^{-1}(\mathbf{z}_1)\boldsymbol{\tau}_{ext}) \in R^{18\times 1}$.

Assumption 6-1: *The difference of the state* $\mathbf{z}_3 \in R^6$ *is assumed to be bounded*, i.e., $\|\dot{\mathbf{z}}_3(t)\|_\infty \le \bar{\delta}_{z3}$, *where* $\bar{\delta}_{z3}$ *is a pre-determined positive constant*.

The manipulator dynamics is rewritten as follows:

$$\begin{cases} \dot{\mathbf{z}}_1 = \mathbf{z}_2 \\ \dot{\mathbf{z}}_2 = \mathbf{F}(\mathbf{z}_1, \mathbf{z}_2) + \mathbf{H}(\mathbf{z}_1)\mathbf{u} + \mathbf{z}_3 \\ \dot{\mathbf{z}}_3 = \boldsymbol{\chi}(t) \end{cases} \tag{6.21}$$

where $\boldsymbol{\chi}(t) \in R^6$ is the derivative of the state $\mathbf{z}_3$; $\mathbf{z}_3 = \mathbf{M}^{-1}(\mathbf{z}_1)\boldsymbol{\tau}_{ext}$; $\mathbf{H}(\mathbf{z}_1)$ derives $\mathbf{M}^{-1}(\mathbf{z}_1)$; and $\mathbf{F}(\mathbf{z}_1, \mathbf{z}_2)$ presents $-\mathbf{M}^{-1}(\mathbf{z}_1)\big(\mathbf{C}(\mathbf{z}_1, \mathbf{z}_2)\mathbf{z}_2 + \mathbf{G}(\mathbf{z}_1)\big)$.

Assumption 6-2: *We assume that the functions* $\mathbf{F}(\mathbf{z}_1, \mathbf{z}_2)$ *are locally Lipschitz for* $\mathbf{z}_2$.

Let $\hat{\mathbf{z}}$ express the estimated system state of $\mathbf{z}$ and $\tilde{\mathbf{z}}$ presents the estimation error $\tilde{\mathbf{z}} = \mathbf{z} - \hat{\mathbf{z}}$; then, the robotic dynamics in Equation (6.21) is represented as follows:

$$\dot{\mathbf{z}} = \mathbf{A}\mathbf{z} + \mathbf{B}\mathbf{u} + \phi(\mathbf{z}) + \mathbf{D}(\mathbf{z}) \tag{6.22}$$

where $\mathbf{A} = \begin{bmatrix} \mathbf{0}_6 & \mathbf{I}_6 & \mathbf{0}_6 \\ \mathbf{0}_6 & \mathbf{0}_6 & \mathbf{I}_6 \\ \mathbf{0}_6 & \mathbf{0}_6 & \mathbf{0}_6 \end{bmatrix} \in R^{18\times 18}$; $\mathbf{B} = \begin{bmatrix} \mathbf{0}_6 \\ \mathbf{H}(\mathbf{z}_1) \\ \mathbf{0}_6 \end{bmatrix} \in R^{18\times 6}$; $\phi(\mathbf{z}) = \begin{bmatrix} \mathbf{0}_{6\times 1} \\ \mathbf{F}(\mathbf{z}_1, \mathbf{z}_2) \\ \mathbf{0}_{6\times 1} \end{bmatrix} \in R^{18\times 1}$; $\mathbf{D} = \begin{bmatrix} \mathbf{0}_{6\times 1} \\ \mathbf{0}_{6\times 1} \\ \boldsymbol{\chi}(t) \end{bmatrix} \in R^{18\times 1}$.

The force estimator is presented as follows:

$$\dot{\hat{\mathbf{z}}} = \mathbf{A}\hat{\mathbf{z}} + \mathbf{B}\mathbf{u} + \phi(\hat{\mathbf{z}}) + \mathbf{\Pi}(\mathbf{z}_1 - \hat{\mathbf{z}}_1) \tag{6.23}$$

where $\phi(\hat{\mathbf{z}}) = \begin{pmatrix} \mathbf{0}_{6\times1} & \mathbf{F}^T(\mathbf{z}_1, \hat{\mathbf{z}}_2) & \mathbf{0}_{6\times1} \end{pmatrix}^T$, $\mathbf{\Pi} = \begin{pmatrix} 3\kappa_0\mathbf{I}_{6\times6} & 3\kappa_0^2\mathbf{I}_{6\times6} & \kappa_0^3\mathbf{I}_{6\times6} \end{pmatrix}^T \in R^{18\times6}$ presents the observer gain matrix; $\kappa_0 > 0$ is adjusted to enhance the observer performances.

From Equations (6.22) and (6.23), the estimation error dynamics is computed as

$$\dot{\tilde{\mathbf{z}}} = \mathbf{A}\tilde{\mathbf{z}} + \phi(\mathbf{z}) - \phi(\hat{\mathbf{z}}) - \mathbf{\Pi}\tilde{\mathbf{z}}_1 + \mathbf{D}(\mathbf{z}) \tag{6.24}$$

Let $\vartheta_i = \dfrac{\tilde{\mathbf{z}}_i}{\kappa_0^{\,i-1}} \in R^{6\times1}(i = 1,2,3)$, $\tilde{\phi} \triangleq \phi(\mathbf{z}) - \phi(\hat{\mathbf{z}})$. Then, the ESO in Equation (6.24) is represented as

$$\dot{\vartheta} = \kappa_0\mathbf{A}_n\vartheta + \frac{\tilde{\phi}}{\kappa_0} + \frac{\mathbf{D}(\mathbf{z})}{\kappa_0^2} \tag{6.25}$$

where $\mathbf{A}_n = \begin{bmatrix} -3\mathbf{I}_6 & \mathbf{I}_6 & \mathbf{0}_6 \\ -3\mathbf{I}_6 & \mathbf{0}_6 & \mathbf{I}_6 \\ -\mathbf{I}_6 & \mathbf{0}_6 & \mathbf{0}_6 \end{bmatrix} \in R^{18\times18}$ is a negative definite matrix.

From ***Assumption 6-2***, the below inequality can be obtained:

$$\left|\tilde{\phi}\right| = \left|\phi(\mathbf{z}_2) - \phi(\hat{\mathbf{z}}_2)\right| \le c\left|\vartheta_2\right| \tag{6.26}$$

Theorem 6-1: *When the force estimator in Equation* (6.23) *is used to estimate the external torques and the unmeasured states, and Inequality* (6.26) *is satisfied, then the estimation errors will be bounded by an appropriate region. The external force at the end-effector is computed from the external torques,* $\mathbf{z}_3$, by $\mathbf{F}_{load} = -\mathbf{J}^{-1}\mathbf{M}(\mathbf{z}_1)\hat{\mathbf{z}}_3$.

Proof of Theorem 6-1:

A Lyapunov function is chosen as follows:

$$V_{ESO} = \frac{1}{2}\vartheta^T\mathbf{P}\vartheta \tag{6.27}$$

where **P** is a positive definite matrix. It is selected how the below condition obtains

$$\mathbf{A}_n^T\mathbf{P} + \mathbf{P}\mathbf{A}_n = -2\mathbf{I}_{18\times18} \tag{6.28}$$

From (6.25), the differential Lyapunov function is expressed as

$$
\begin{aligned}
\dot{V}_{ESO} &= \frac{1}{2}\kappa_0 \vartheta^T \left(\mathbf{A}_n^T \mathbf{P} + \mathbf{P}\mathbf{A}_n\right)\vartheta + \frac{1}{2}\left(\frac{\tilde{\phi}}{\kappa_0} + \frac{\mathbf{D}(\mathbf{x})}{\kappa_0^2}\right)^T \mathbf{P}\vartheta + \frac{1}{2}\vartheta^T \mathbf{P}\left(\frac{\tilde{\phi}}{\kappa_0} + \frac{\mathbf{D}(\mathbf{x})}{\kappa_0^2}\right) \\
&= -\kappa_0 \vartheta^T \vartheta + \left(\frac{\tilde{\phi}}{\kappa_0} + \frac{\mathbf{D}(\mathbf{x})}{\kappa_0^2}\right)^T \mathbf{P}\vartheta \\
&\le -\left(\kappa_0 - \frac{c}{\kappa_0}\right)\|\vartheta\|_2^2 + \frac{\bar{\delta}}{\kappa_0^2}\lambda_{\max}(\mathbf{P})\|\vartheta\|_2 \\
&= \left(-\left(\kappa_0 - \frac{c}{\kappa_0}\right)\|\vartheta\|_2 + \frac{\bar{\delta}}{\kappa_0^2}\lambda_{\max}(\mathbf{P})\right)\|\vartheta\|_2
\end{aligned}
\tag{6.29}
$$

The differential Lyapunov function in Equation (6.29) is negative when $-\left(\kappa_0 - \frac{c}{\kappa_0}\right)\|\vartheta\|_2 + \frac{\bar{\delta}}{\kappa_0^2}\lambda_{\max}(\mathbf{P}) \le 0$. That means $\|\vartheta\|_2 \ge \frac{\bar{\delta}}{\kappa_0\left(\kappa_0^2 - c\right)}\lambda_{\max}(\mathbf{P})$. The accuracy of the force estimator is improved and the stability of the ESO is guaranteed when the bandwidth, κ_0, increases.

6.4 Whole system stability analysis

Similarly, the virtual control signal obtained in Equation (3.30) is modified as

$$
\mathbf{x}_{3d} = \mathbf{M}(\mathbf{x}_1)\dot{\mathbf{x}}_{2s} + \mathbf{C}(\mathbf{x}_1, \mathbf{x}_2)\mathbf{x}_{2s} + \mathbf{G}(\mathbf{x}_1) + \mathbf{J}^T \hat{\mathbf{F}}_{ext} + \hat{\mathbf{\Delta}} - \mathbf{K}_1^f \mathbf{s}_1 - \boldsymbol{\eta}_1^f \tanh\left(\frac{\mathbf{s}_1}{\sigma_s}\right) \tag{6.30}
$$

where $\hat{\mathbf{F}}_{ext}$ represents for an estimated external force disturbance obtained from the ESO.

Choose a Lyapunov candidate V_1^{ESO} as

$$
V_1^{ESO} = \frac{1}{2}\mathbf{s}_1^T \mathbf{M}\mathbf{s}_1 + \frac{1}{2}\tilde{\mathbf{\Delta}}^T \tilde{\mathbf{\Delta}} + \frac{1}{2}V_{ESO} \tag{6.31}
$$

Taking derivative the Lyapunov candidate V_1^{ESO} with Property 4-1 and results obtained in Equations (3.29) yields:

$$
\dot{V}_1^{ESO} = -\mathbf{s}_1^T\left(\mathbf{x}_3 - \left(\tilde{\mathbf{\Delta}} + \hat{\mathbf{\Delta}}\right) - \mathbf{M}(\mathbf{x}_1)\dot{\mathbf{x}}_{2s} - \mathbf{C}(\mathbf{x}_1, \mathbf{x}_2)\mathbf{x}_{2s} - \mathbf{G}(\mathbf{x}_1)\right) - \mathbf{s}_1^T \mathbf{J}^T(\mathbf{x}_1)\mathbf{F}_{ext} + \dot{\tilde{\mathbf{\Delta}}}^T \tilde{\mathbf{\Delta}} + \dot{V}_{ESO} \tag{6.32}
$$

Substituting the virtual control signal in Equation (6.30) and adaptive law derived in Equation (3.27) into Equation (6.32) results in:

$$
\dot{V}_1^{ESO} = \mathbf{s}_1^T\left(\mathbf{J}_a^T \mathbf{e}_3 - \mathbf{K}_1 \mathbf{s}_1 - \boldsymbol{\eta}_1 \tanh\left(\frac{\mathbf{s}_1}{\sigma_s}\right) + \tilde{\mathbf{F}}_{ext}\right) - \kappa_0 \vartheta^T \vartheta + \left(\frac{\tilde{\phi}}{\kappa_0} + \frac{\mathbf{D}(\mathbf{x})}{\kappa_0^2}\right)^T \mathbf{P}\vartheta \tag{6.33}
$$

$$
\dot{V}_1^{ESO} \le \mathbf{s}_1^T\left(\mathbf{J}_a^T \mathbf{e}_3 - \mathbf{K}_1^f \mathbf{s}_1 - \boldsymbol{\eta}_1^f \tanh\left(\frac{\mathbf{s}_1}{\sigma_s}\right) + \tilde{\mathbf{F}}_{ext}\right) - \left(\kappa_0 - \frac{c}{\kappa_0}\right)\|\vartheta\|_2^2 + \frac{\bar{\delta}}{\kappa_0^2}\lambda_{\max}(\mathbf{P})\|\vartheta\|_2 \tag{6.34}
$$

According to Theorem 6-1, result in Equations (3.42) and (6.29), conditions of designing $\mathbf{K}_1^f$ and $\boldsymbol{\eta}_1^f$, and result obtain in (3.44) the derivative of the Lyapunov candidate is semi-negative and bounded in the influence of external force disturbance; thus, the whole closed-loop system stability is guaranteed.

6.5 Numerical simulation results

6.5.1 Scenario for verification and setting parameters

In this simulation, we verify the proposed methodology on a 6-DOF serial hydraulic KIRO robot. The robot designed is structured with the five first links driven by cylinders and the last link driven by the rotary actuator as shown in Figure 3-1, Chapter 3. The parameters of the 6-DOF KIRO robot are described in Appendix B.

The manipulator behavior in case of treating impedance-contact-loss based on the virtual energy tank concept is compared with that of conventional impedance control. We suppose that the end-effector is commanded to work along the X-direction, as shown in **Figure 6-6**.

The simulation is constructed using MATLAB/Simulink program. The parameters of the hydraulic specification and hydraulic actuators are described in **Table 6-1** and **Table 6-2**, respectively. The controller parameters for contact-loss impedance control are described in **Table 6-3**. For the position control, the sliding surface is designed with $\mathbf{K}_1 = 100\mathbf{I}_6$, $\boldsymbol{\lambda}_1 = diag(1,1,1,1,1,2)$, and $\boldsymbol{\eta}_1 = 0.1\mathbf{I}_6$. For the torque control, the controller gains are utilized with $\mathbf{K}_2 = 100\mathbf{I}_6$, $\boldsymbol{\eta}_2 = 0.1\mathbf{I}_6$, and $\sigma_s = 10^{-4}$. The sampling time for simulation is set as $t_s = 0.001(s)$, and the simulation is implemented in the period of $T_{period} = 12(s)$.

Table 6-1. *Parameters of the hydraulic specification.*

Symbol	Description	Value
β	Bulk modulus	1.5 (Gpa)
C_d	Drag coefficient	0.62
ρ	Fluid density	861 (kg/m^3)
P_s	Supply pressure	200 (bar)
P_t	Tank pressure	3 (bar)
ω	Valve orifice area gradient	0.0024
K_{vi}	Valve gain	0.333×10^{-3}

Table 6-2. *Parameters of hydraulic actuators.*

Actuator ith		Bore Diameter	Rod Diameter	Stroke
Cylinder	1	70 (mm)	45 (mm)	192 (mm)
	2	80 (mm)	50 (mm)	180 (mm)
	3	80 (mm)	50 (mm)	200 (mm)
	4	70 (mm)	45 (mm)	175 (mm)
	5	63 (mm)	40 (mm)	100 (mm)
Rotary actuator	6	1.023×10^{-4} (m^3/rad)	1.023×10^{-4} (m^3/rad)	$280\times\frac{2\pi}{360}$ (rad)

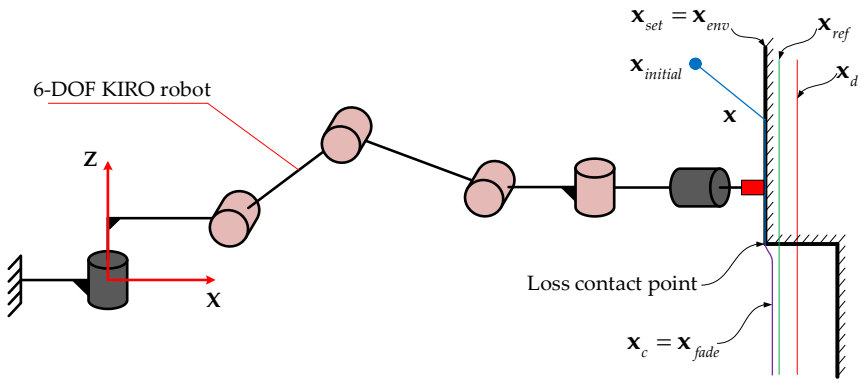

Figure 6-6 Scenario for algorithm of contact-loss validation.

Table 6-3. *Parameters of the contact-loss impedance control.*

Symbols	Value	Symbols	Value
K_e	2000 (N/m)	$\mathbf{K}_{If}$	$2\mathbf{I}_3$
$\mathbf{D}_m$	$0.001\times\mathbf{I}_3$	T^u	32 (J)
$\mathbf{B}_m$	$0.1\times\mathbf{I}_3$	T_l	0.1 (J)
$\mathbf{K}_m$	$0.2\times\mathbf{I}_3$	$d_{\max}$	0.1 (mm)
$\mathbf{K}_{Pf}$	$2\mathbf{I}_3$	Δx_s	0.01 (mm)

Remark 6-2: *In our simulation, the environment stiffness and impedance behavior matrix* $\mathbf{D}_m, \mathbf{B}_m, \mathbf{K}_m$ *are supposed to be known and set with fixed constants. We aim to demonstrate the response of the system when applying the impedance contact-loss algorithm. Practically, the impedance dynamics directly relates to the design of impedance control gains. Therefore, adaptive gains can be further investigated in future work.*

Remark 6-3*: The gains* $\mathbf{K}_{Pf}, \mathbf{K}_{If}$ *are firstly initialized based on system characteristic and trial-and-error method. The technique for identifying the initial value and adaptive laws to adopt with working operation will be developed in future works.*

Remark 6-4: *The value of upper bound* T^u *is chosen based on system characteristics and designer knowledge. Different systems and working conditions may result in different values. Therefore, the choice of a suitable value for the upper bound will be discussed in future works.*

6.5.2 Simulated results

To mimic the contact-loss, the environment profile is set as a step function as

$$x_{set} = \begin{cases} 2200(mm) \text{ if } t \le 7.62s \\ 2530(mm) \text{ if } t > 7.62s \end{cases} \tag{6.35}$$

As can be seen in Equation (6.35), we suppose that the contact loss happens at the time of t = 7.62 s. Indeed, the contact-loss can suddenly occur if the position along the X-direction suddenly changes.

Besides, the end-effector of the KIRO robot must apply a constant force of 100 N to the wall. The desired force induced from contacting command with the environment and moments induced from the command motions such as twisting, bending, etc., at the end-effector. Then, the desired force is set as

$$\mathbf{F}_d = \begin{pmatrix} F_{dx} & F_{dy} & F_{dz} & M_{dx} & M_{dy} & M_{dz} \end{pmatrix}^T = \begin{pmatrix} 100 & 0 & 0 & 0 & 0 & 0 \end{pmatrix}^T \tag{6.36}$$

6.5.2.1 Case study 1

In the first case study, we consider the smooth constraint and desired trajectory for the end-effector as described in **Figure 6-6**. Position tracking performances of conventional impedance and impedance contact-loss in X, Y, and Z directions are displayed in **Figure 6-7** to **Figure 7-9**, respectively. The continuous black line represents desired trajectory $(\bullet)_{desired}$, the black dot-line represents the arbitrary environment $(\bullet)_{env}$, the blue dot-dash line represents the end-effector position of conventional impedance response $(\bullet)_{imp}$, and the dash red line represents the end-effector trajectory of impedance contact-loss $(\bullet)_{imp-cl}$. For the shake of simplicity in the case of force responses, the desired force $\left(F_{desired}\right)$, external impedance force $\left(F_{ext-imp}\right)$, and external impedance contact-loss $\left(F_{ext-imp-cl}\right)$ are presented by italic symbols hereafter since these values are investigated in only X-direction.

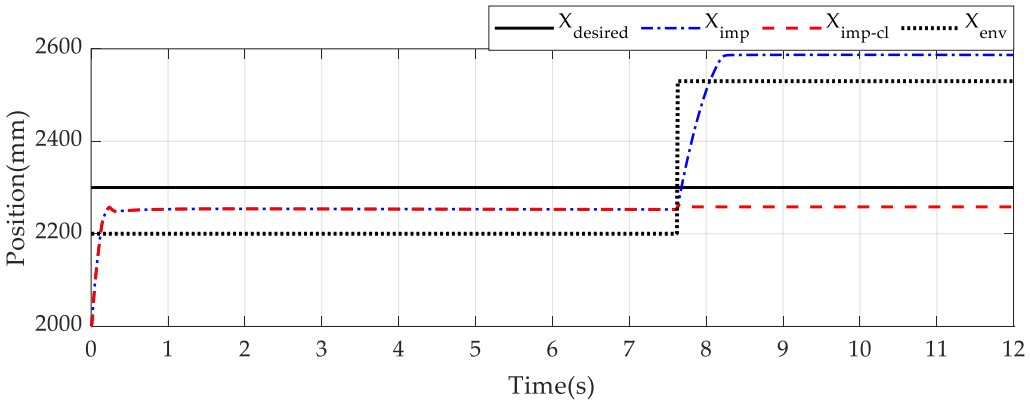

Figure 6-7 Position tracking of the end-effector in X-direction.

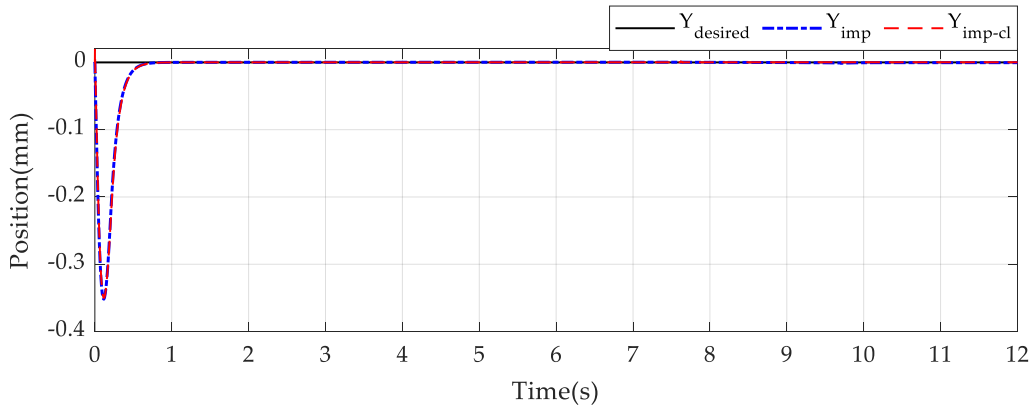

Figure 6-8 Position tracking of the end-effector in Y-direction.

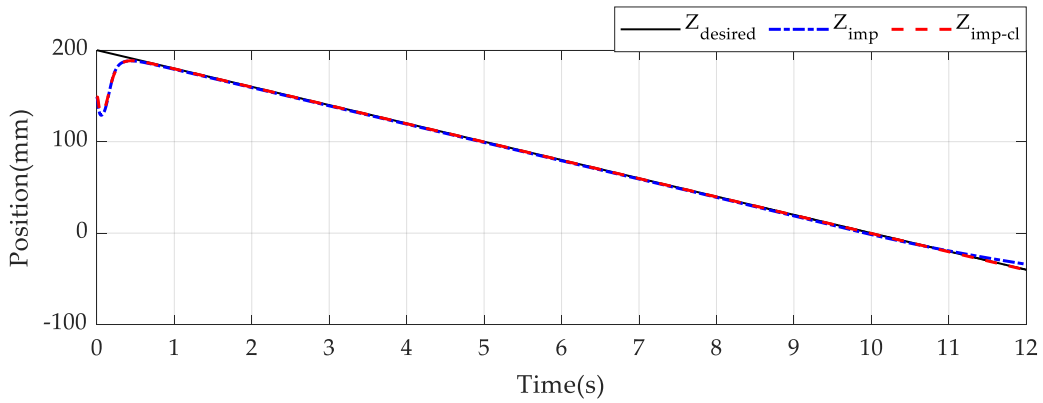

Figure 6-9 Position tracking of the end-effector in X-direction.

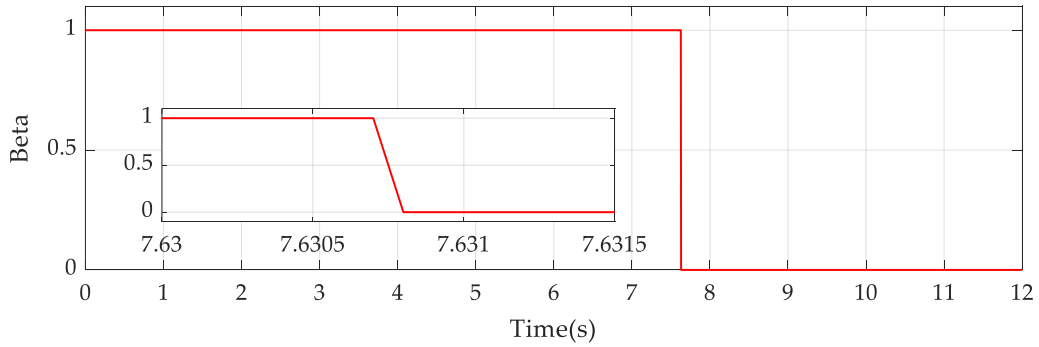

Figure 6-10 Response of the switched parameter β when contact-loss happens.

At the time of approximately 7.62 s, the sudden change in the environment framework causes contact-loss. At that time, the interacting force immediately decreases to zero, and the tank variable increases until its energy reaches the upper limit T^u at the time of approximately 7.63 s. Then, the parameters β and φ simultaneously switch their values, as shown in Figure 6-10. The time for switching value of both parameter β is slightly delayed from the time of contact-loss. The reason for this phenomenon is that when contact-loss happens at the time of 7.62 s, the value of the tank variable x_t increases; thus, increasing the value of energy tank T_t until reaching the upper limitation T^u. When the value of T_t equals T^u, parameter β is automatically passively switched from 1 to 0, and the trajectory is then faded. The switching of parameter φ occurs when satisfying both two conditions: after contact-loss is detected and condition in Equation (6.19). It is noticed that the problem of overshoot at the beginning of contact motion is not considered in this study. This problem will be considered as the next step of improvements for safety interactions.

Due to using the energy tank, the end-effector can generally maintain the same level with a very small position shifted. This is because the force control signal is deactivated, and the energy stored in a virtual spring-damper of each joint is dissipated. In the case of conventional impedance control, the end-effector moves until it reaches the constrained framework again at the time of 8.2 s as the requirement of force tracking effort. The force performances in two situations are depicted in **Figure 6-11**, in which

the black continuous line represents desired force $F_{desired}$, the green dot line and blue dot-dash line represent the measured and estimated external interactive forces in the conventional impedance algorithm, respectively; and the purple continuous line and red dash line represent the measured and estimated external interactive forces of impedance-contact-loss in X-direction, respectively. **Figure 6-12** shows the estimation error of the measured and estimated interactive forces in the case of impedance-contact-loss. This concludes that the ESO can totally take place the use of force sensor to obtain the interactive force for impedance control design.

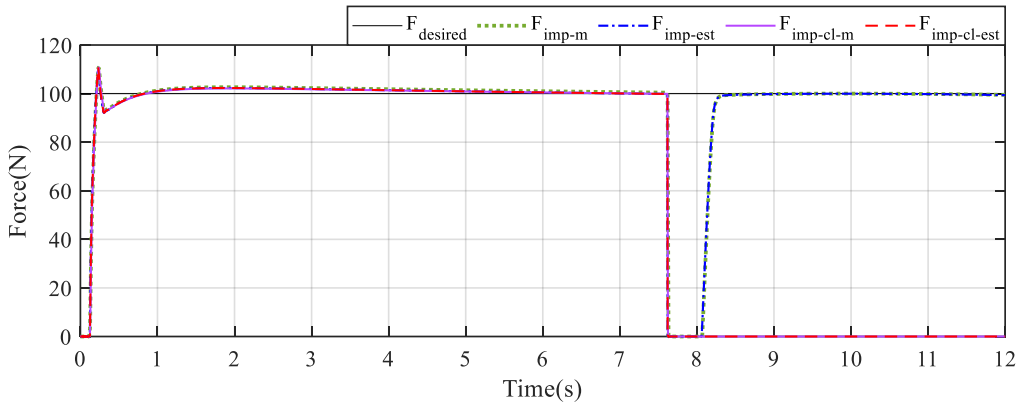

Figure 6-11 Force tracking performance subjected to contact-loss situation.

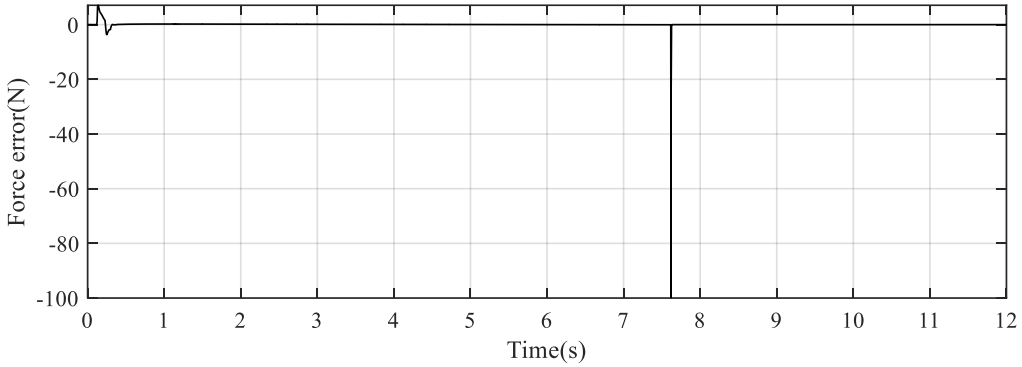

Figure 6-12 Estimation error between the actual and the estimated interactive forces.

6.5.2.2 Case study 2

In this second simulation, we consider the case of a rippled surface of the constrained framework to evaluate responses of the energy tank variable under several different values of force control gains. The constrained framework is presented as

$$x_{env} = \begin{cases} 2200 + 20\sin\left(2\pi t / 1.75\right)(mm) & if\ t < 7s \\ 2200(mm) & if\ 7 \le t \le 7.62s \\ 2535(mm) & \text{otherwise} \end{cases} \quad (6.37)$$

Similar to the first case study, we suppose that the contact-loss happens at the time of 7.62s. In this case study, only tracking evaluation along the X-direction and response of the virtual energy tank variable are discussed due to similar responses of tracking performances in Y and Z-directions and other switching parameters. Furthermore, we investigate the end-effector and energy variable behaviors under several different control gains. Herein, we consider six different control gains and display by different types of lines. The tracking effort and response of the energy variable are displayed in **Figure 6-13** and **Figure 7-14**.

Particularly, green lines, blue lines, and red lines denote tracking efforts when the force proportional gain is set as $K_{Pf}=1, K_{Pf}=1.75, K_{Pf}=2$, respectively. Among that, dashed lines, dashed-dot lines, and continuous lines present system behaviors when the force integral gains are $K_{If}=1, K_{If}=2, K_{If}=3$, respectively. It is noteworthy that since the force control is only regulated in X-direction, then in this case, we consider force control gains as a scalar, not matrix as defined above.

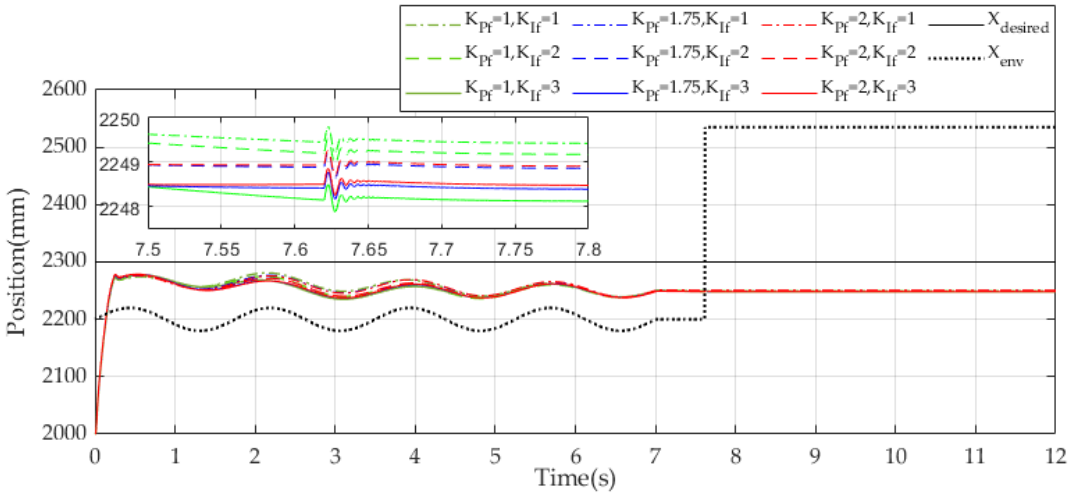

Figure 6-13 Response of the end-effector in X-direction under different force control gains.

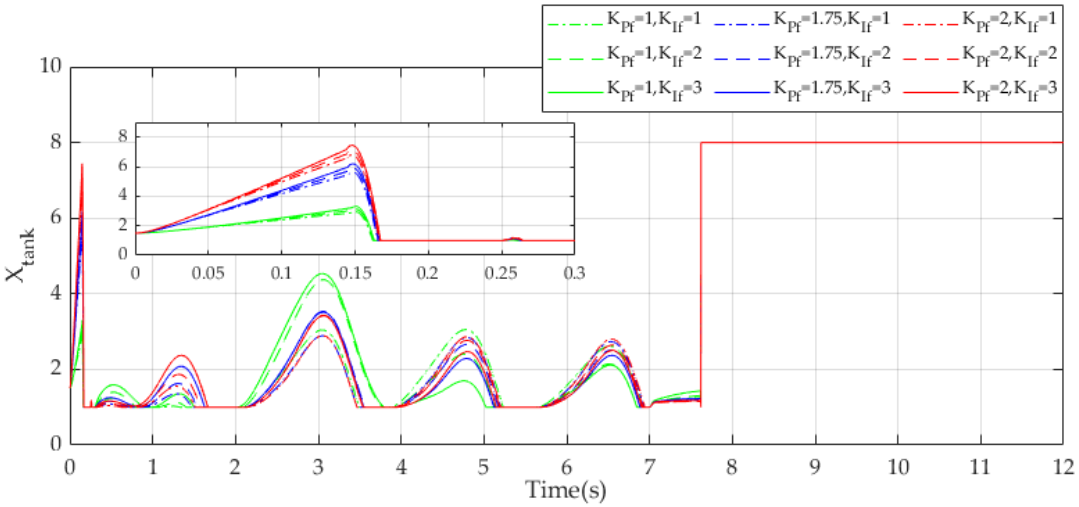

Figure 6-14 Response of the energy variable under different force control gains.

As can be seen in **Figures 6-13** and **6-14**, the tracking performance of the end-effector changes under rippled framework no matter how different values of force control gains are. Due to consideration of the rippled surface, the force tracking effort varies around the desired value of 100 (N). The force tracking effort directly affects position tracking performance. Generally, larger values of the force control gains generate more accurate, faster and smoother response of the end-effector when contact-loss happens. However, too-large values of control gains (in this case is when the values of K_{Pf} is greater than 2) may degrade tracking efforts and execute unexpected motions as a trade-off. As revealed in **Figure 6-14**, large gains may result in more overshoot phenomenon at the beginning. Besides, since all lines reach the upper bound at the same time, the switching parameter β changes its state at the time of approximately 7.63s, same as the first case study despite different force control gains.

6.5.2.3 Case study 3

In the third case study, we consider friction exerting on Z-direction. This friction force is supposed to be proportional to external force exerting at the end-effector on X-direction as

$$F_{fr3} = \mu F_{ext-imp} \tag{6.38}$$

where μ = 0.001 is a ratio parameter.

Similar to the second case study, green lines, blue lines, and red lines denote tracking efforts when the force proportional gain is set as $K_{Pf} = 1, K_{Pf} = 1.75, K_{Pf} = 2$, respectively. Among that, dashed line, dashed-dot lines, and continuous lines present the system behaviors when the force integral gains are $K_{If} = 1, K_{If} = 2, K_{If} = 3$, respectively.

As can be seen in **Figure 6-15**, at the time of contact-loss happens, different values of force control gains result in different responses of the end-effector. In this scenario, we consider different values of proportional and integral gains. The derivative gain is maintained at the same value as the first case study because this gain is only used to eliminate the overshoot of the control effort. Among the two control gains, the proportional gain K_{Pf} dominates the tracking performance. Small gains result in slow response but less overshoot at the beginning. On the contrary, large values of proportional gain generally lead to fast response and smoother movement when contact-loss happens. The integral gains can help to enhance tracking performance; however, these gains cannot be arbitrarily set to large values. **Figure 6-16** shows that responses of the energy variable also vary under the rippled framework and different values of the force control gains. Thereby, one can easily deduce that different times for switching the parameter β are obtained due to different time for reaching the upper bound of the energy variable as shown in **Figure 6-17** (the parameter β switches if and only if the energy variable reaches the upper bound). Therefore, the control gains should be carefully designed in the case of friction as one considerable factor to achieve better performance.

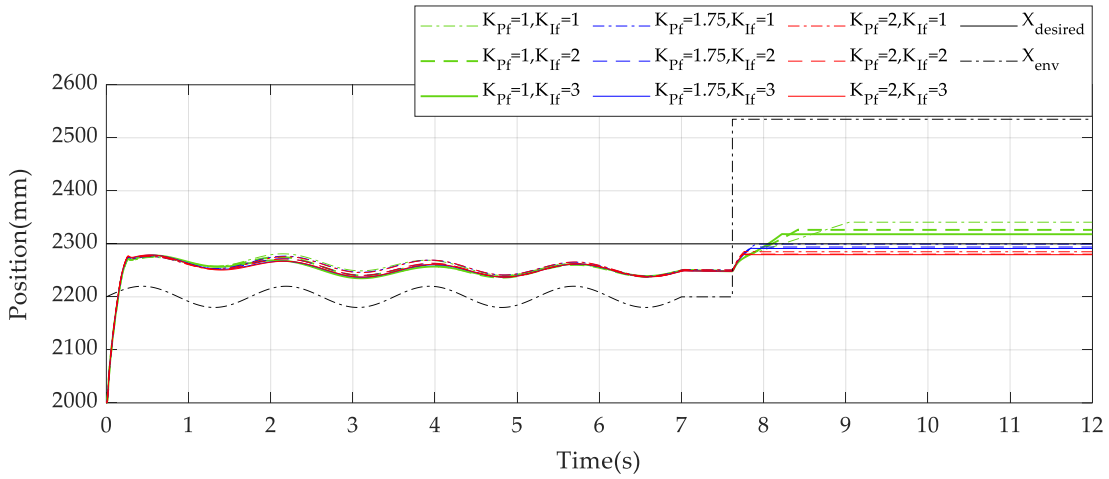

Figure 6-15 Response of the end-effector in X-direction in case of friction under different force control gains.

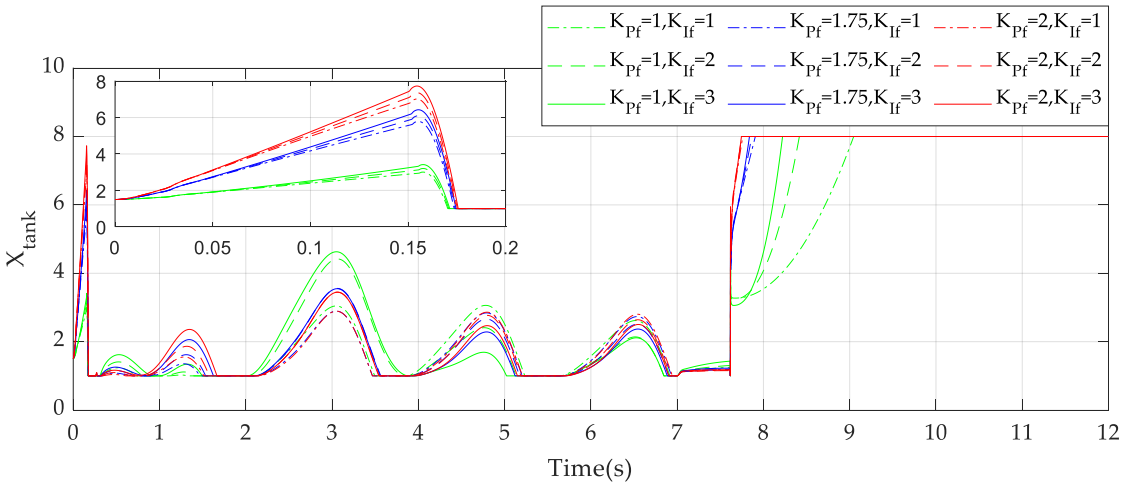

Figure 6-16 Response of the energy variable in case of friction under different force control gains.

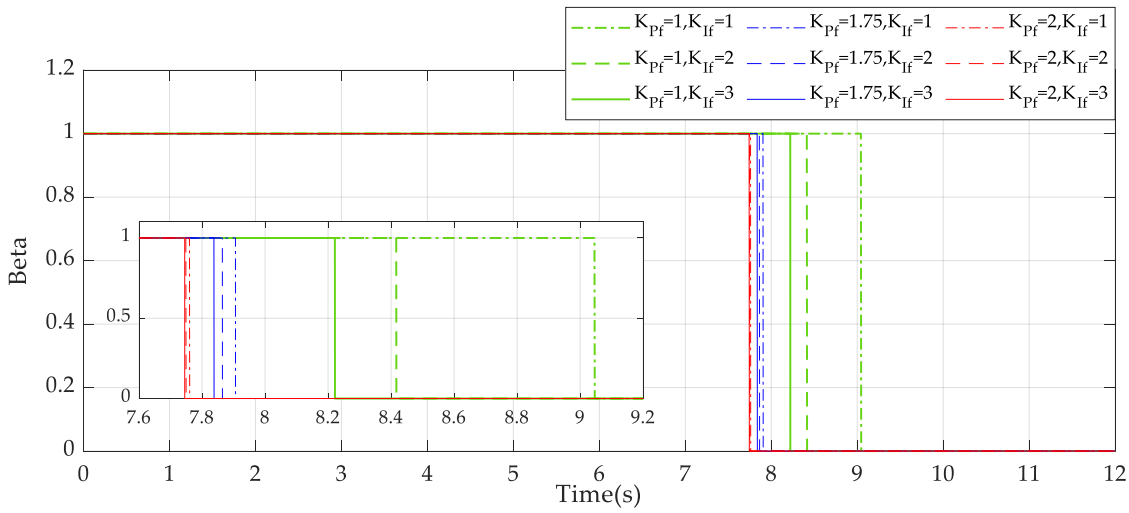

Figure 6-17 State of the switching parameter β under different force control gains.

Furthermore, it is noteworthy that at the beginning, when the motion of the manipulator is switched from free-motion to constrained-motion, the free motion of the end-effector is also considered as contact-loss. If the initial point is too far from the constrained framework, more energy is required to drive the end-effector to the target and thus, the energy may reach the limitation before the system is in constrained-framework and execute undesirable motions. Thereby, the initial point should be set as not far from the contact point. This problem can also be solved by increasing a large value of the upper bound T^u; however, smooth movement may not be executed because more time is required for the energy variable to reach the upper bound. Hence, one should refer step by step to solve this problem by designing adaptive laws to decouple the force control in free motion, or adaptive upper boundary to satisfy different working conditions.

6.6 Conclusion

In this paper, we intensively presented the method for solving the problem of contact-loss based on using the energy tank for the n-degree-of-freedom serial manipulator. The contact-loss probably occurs in the case of constrained motion when the end-effector of the manipulator moves out of the constrained framework. In this scenario, the end-effector follows the virtual commanded trajectory resulting from the force tracking effort. When the contact-loss happens, the potential energy stored in the virtual spring/damper mechanism in each joint has instantaneously released. According to this behavior, the fault detection based on the energy tank was designed with several passive switched parameters to decouple the force action. This helped to prevent the system from getting damaged or unexpected motions. Furthermore, to avoid shock at the point of contact-loss, the command trajectory was modified based on time-delay instead of using the location of environment as presented in previous works. This method compared the end-effector positions between the recent step and previous step along with passive switched parameters to smooth the output performance. Additionally, the adaptive laws for the inner position control loop were derived to enhance system performance and facilitate further development of advanced methodology such as force sensor-less using observer or optimization. From the simulations, the end-effector movement after contact-loss happened was maintained moving in same level as in constrained framework and the smooth movement was executed thanks to utilizing the fading trajectory algorithm to generate the new commanded trajectory in comparison with those under conventional impedance control. Consequently, the control methodology showed its ability in both tracking performance and contact-loss reaction. Additionally, to comprehensively investigate the force-controlled system behaviors, we discussed the influence of force regulation loop to system response and the end-effector dynamics in which different values of force control gains were examined. Generally,

gains of the force control loop, and also boundary parameters of the energy tank, directly decided the smooth motion and stability of the whole system in not only free motion but also constrained framework, and after contact-loss happened. Therefore, depending on working characteristic and requirements, the boundary limitation of the energy tank and controller gains should be dedicatedly designed to obtain optimal performance. Besides, remaining problems such as influences of friction, initial condition, or adaptive boundary evoke interesting topics for further study and development. This algorithm can be expanded to other practical applications for safety such as at the end of mechanical turning, milling, or planning process, manufacture in automation fields, or reaction of the end-effector when suddenly dropping a payload.

Chapter 7
Conclusion and future work

7.1 Conclusions

This dissertation presented the problems of n-DOF serial robotic manipulators subjecting to real industrial applications. In order to address these existing problems, the system behavior including actuator dynamics was first mathematically derived. Then the control strategy based on the core of ABSMC, which takes the advantages of the SMC in robustness against matched perturbations and BSP in step-by-step recursive process of control design for system state stabilization, was dedicatedly designed with adaptive laws to address influence of matched and mismatched uncertainties. Nevertheless, the adaptive laws, directly designed based on the system state error, in some senses, cannot completely deal with influences arising from mismatched uncertainties and unmeasured variables. Therefore, disturbance observers were employed to estimate and compensate for these influences. The DO-based GMO was considered due to its property of efficiently detecting and estimating mismatched uncertainty such as external force disturbance or payload variation without requiring the measurement of system acceleration. The ability of the GMO to address the slow and fast time-varying disturbance was also analyzed. Besides, to cancel out the effect of estimated error, the FLC was exploited to flexibly adjust the robust terms of the ABSMC. Moreover, the initial control gains for verification were also discussed based on performing the neural network. With the use of this technique, the controller parameters were systematically initialized, at which an ideal model with no influence of the matched and mismatched uncertainties was considered, instead of heuristically using trial-and-error method. The closed-loop system stability was mathematically proven by performing Lyapunov theorems. The effectiveness and workability of the proposed methodology was verified and compared with conventional SMC and FFDOAFBSMC in both simulations and experiments on the 3-DOF serial hydraulic manipulator under the presence of external payload.

Although the effectiveness of the proposed algorithm was verified, the verification was implemented on the n-DOF serial hydraulic manipulator in free motion. The GMO can estimate and compensate for the influence of mismatched disturbance; nevertheless, the estimation accuracy depended on the system model. As a result, the well-known model is preferred to achieve the more accurate estimation. Additionally, all system state was assumed to be well monitored without occurrence of sensor faulty signals. The occurrence of the sensor faults generates the incorrect control action executing on the actuators. In order to overcome this problem, the robust fault estimation and fault-

tolerant control algorithms were proposed to address the problem of the system faults. Unlikely to previous works, which proposed the fault estimation and fault-tolerant control focusing on the position sensor fault in free motion, this work considered the influence of sensor faults in both encoder and force sensor faults subject to impedance control in constrained framework. The PB-IC was first conducted, with the sensor faults being initialized by offset the measured joint angle and force signals. Then, the robust fault estimation was constructed based on ESO to estimate both faulty signals, actual signals and unmeasured variables. Moreover, both mismatched and matched disturbances were also able to be estimated with the ESO. With the estimated system state being feedback to the impedance AFBSMC, the active FTC was designed to generate the proper control action to the actuators was designed. The Lyapunov theorems were used to prove closed-loop system stability. The simulation results, obtained from simulations on 3-DOF hydraulic manipulator, indicated that the active FTC could accurately estimate the signals fault of the measured joint angle and force and matched and mismatched uncertainties.

The proposed control scheme demonstrated its effectiveness; however, besides the sensor faults occurrence, the safety operation of the system subjects to shock or sudden contact-loss in constrained framework should be considered. Therefore, the modified impedance was constructed with virtual energy tank and passivity control algorithm concepts. By employing auxiliary variables with suitable constraints, the force control action was decoupled from the closed-loop system when the sudden contact-loss happened due to step-change in the working framework environment. The passive stability of the methodology was evidently proven using another Lyapunov theorem that considered the virtual energy tank variable and passive variables. Besides, the fading trajectory was integrated to modify the reference trajectory and smooth the end-effector performance after the contact-loss happened. Comparative simulations were carefully implemented on the 6-DOF KIRO robot to evaluate the superior effectiveness of the proposed control scheme with conventional PB-IC. Moreover, the influence of the force control gains, and environment characteristics were also investigated.

In summary, the contributions of this thesis are

- Generalized the typically highly nonlinear system and dedicatedly derived the system dynamics with the influence of mismatched and matched disturbances
- Designed disturbance observers to estimate the unmeasured variables and uncertainties, and adaptive laws to enhance the system stability and robustness
- Considered the control gains initialization based on the gradient descent method
- Proposed the robust fault estimation based on ESO to address the problem of sensor faults in constrained motion

- Applied the ESO as a force-sensorless method to replace the use of force sensor
- Considered the contact-loss for safety operation based on the virtual energy tank and passivity control concepts.

7.2 Future works and developments

Although most existing problems were covered in this dissertation, the control methodology was constructed based on several assumptions which are difficult to manage in the point of practical applications. For the proposed control scheme, the control robust terms were adjusted by employing the FLC with the simple use of triangle membership functions, which was heuristically designed based on the knowledge of designers; therefore, it is difficult to generalize for any nonlinear systems. Besides, the system dynamics was supposed to be well-known with some assumedly pre-determined parameters. Indeed, system identification process should be considered to obtain the system dynamics including internal parameters of the hydraulic circuit. In terms of the impedance control, the control methodology just focused on dealing with the problem of sensor fault as high level of applications. The sensor faults were assumed to not be occurred simultaneously to facilitate the fault estimation design. Additionally, the impedance behavior and influence of the force control gains were not clearly discussed, and the environment stiffness was supposed to be well-known. Similarly, in the algorithm of the contact-loss, the choice of the upper energy tank should be flexibly adapted regarding the system behavior.

Regarding the presented contents and the outlined shortcomings, this current work can be considered as a premise for further algorithm development. In term of the control strategy design, non-singular fast terminal SMC and super twisting algorithm can be applied for chattering free and fast convergence with adaptive laws. Besides, optimization can also be integrated to achieve the optimal parameters. The influence of matched and mismatched uncertainties and system dynamics can be addressed with the use of time-delayed estimation or radial basis function neural network. More and simultaneous faults type should be clarified in the industrial point of view. For the force regulation in constrained frameworks, adaptive variable impedance control, input saturation and adaptive output constraints, or online estimation of the environment stiffness can be extended to deal with the existing and other challenges.

Appendixes

Appendix A

A.1 3-DOF hydraulic manipulator dynamics

According to the manipulator structure in Figure 1, following the inward and outward iteration method, the manipulator dynamic is derived by equations:

$$\mathbf{M}(\mathbf{q})=\begin{pmatrix} m_{11} & 0 & 0 \\ 0 & m_{22} & m_{23} \\ 0 & m_{32} & m_{33} \end{pmatrix}, \mathbf{C}(\mathbf{q},\dot{\mathbf{q}})=\begin{pmatrix} C_{11} & C_{12} & C_{13} \\ C_{21} & C_{22} & C_{23} \\ C_{31} & C_{32} & C_{33} \end{pmatrix}, \mathbf{G}(\mathbf{q})=\begin{pmatrix} g_1 \\ g_2 \\ g_3 \end{pmatrix} \tag{A.1}$$

where

$$\begin{cases} m_{11}=m_3 l_3^2 c_{23}^2+2m_3 l_2 l_3 c_2 c_{23}+(m_2+m_3) l_2^2 c_2^2. \\ m_{22}=(m_2+m_3) l_2^2+2m_3 l_2 l_3 c_3+m_3 l_3^2. \\ m_{23}=m_{32}=m_3 l_3^2+m_3 l_2 l_3 c_3. \\ m_{33}=m_3 l_3^2. \end{cases}$$

$$\begin{cases} C_{11}=-m_3 l_3^2 c_{23} s_{23}(\dot{\theta}_2+\dot{\theta}_3)-(m_2+m_3) l_2^2 c_2 s_2 \dot{\theta}_2-m_3 l_2 l_3\left[s_2 c_{23}\dot{\theta}_2+c_2 s_{23}(\dot{\theta}_2+\dot{\theta}_3)\right] \\ C_{12}=-m_3 l_3^2 s_{23} c_{23}\dot{\theta}_1-m_3 l_2 l_3 s_2 c_{23}\dot{\theta}_1-(m_2+m_3) l_2^2 s_2 c_2 \dot{\theta}_1-m_3 l_2 l_3 c_2 s_{23}\dot{\theta}_1 \\ C_{13}=-c_{31}=-m_3 l_3^2 s_{23} c_{23}\dot{\theta}_1-m_3 l_2 l_3 c_2 s_{23}\dot{\theta}_1 \end{cases}$$

$$\begin{cases} C_{23}=-m_3 l_2 l_3 s_3 \dot{\theta}_3-m_3 l_2 l_3 s_3 \dot{\theta}_2 \\ C_{22}=-m_3 l_2 l_3 s_3 \dot{\theta}_3 \\ C_{21}=\ m_3 l_3^2 s_{23} c_{23}\dot{\theta}_1+m_3 l_2 l_3 s_2 c_{23}\dot{\theta}_1+(m_2+m_3) l_2^2 s_2 c_2 \dot{\theta}_1+m_3 l_2 l_3 c_2 s_{23}\dot{\theta}_1 \end{cases}$$

$$\begin{cases} C_{33}=\ 0 \\ C_{32}=\ m_3 l_2 l_3 s_3 \dot{\theta}_2 \\ C_{31}=\ m_3 l_3^2 s_{23} c_{23}\dot{\theta}_1+m_3 l_2 l_3 c_2 s_{23}\dot{\theta}_1 \end{cases}$$

$$\begin{cases} g_1=0 \\ g_2=-m_3 g l_3 s_{23}-(m_2+m_3) g l_2 s_2 \\ g_3=-m_3 g l_3 s_{23} \end{cases}$$

$c_i=\cos(q_i), \mathrm{s}_i=\sin(q_i),$

$c_{ij}=\cos(\mathrm{i}+\mathrm{j})=\mathrm{c}_i\,\mathrm{c}_j-\mathrm{s}_i\,\mathrm{s}_j, s_{ij}=\sin(i+j)=\mathrm{c}_i\,\mathrm{s}_j+\mathrm{s}_i\,\mathrm{c}_j, (i=1,2,3;\ j=1,2,3)$

The general form of transformation matrix is calculated as

$${}_{i}^{i-1}T=\begin{bmatrix} cq_i & -sq_i & 0 & a_{i-1} \\ sq_i c\alpha_{i-1} & cq_i c\alpha_{i-1} & -s\alpha_{i-1} & -s\alpha_{i-1} d_i \\ sq_i s\alpha_{i-1} & cq_i s\alpha_{i-1} & c\alpha_{i-1} & c\alpha_{i-1} d_i \\ 0 & 0 & 0 & 1 \end{bmatrix} \tag{A.2}$$

A.2 Forward kinetic and Jacobian matrix

According to the manipulator structure in Figure 4-1, follow the Denavit-Hartenberg [1], the parameters and its dynamics are defined, and the kinematic equation of the end-effector is calculated as:

$$\begin{pmatrix} X_P \\ Y_P \\ Z_P \end{pmatrix} = \begin{pmatrix} (l_2 s_2 + l_3 s_{23}) c_1 \\ (l_2 s_2 + l_3 s_{23}) s_1 \\ l_2 c_2 + l_3 c_{23} \end{pmatrix} (m) \tag{A.3}$$

Then taking derivative respect to time, the velocity and Jacobian matrix can be obtained as

$$\begin{pmatrix} \dot{X}_P \\ \dot{Y}_P \\ \dot{Z}_P \end{pmatrix} = J \begin{pmatrix} \dot{q}_1 \\ \dot{q}_2 \\ \dot{q}_3 \end{pmatrix}, J = \begin{pmatrix} -s_1 (l_2 s_2 + l_3 s_{23}) & c_1 (l_2 c_2 + l_3 c_{2+3}) & l_3 c_1 c_{23} \\ c_1 (l_2 s_2 + l_3 s_{23}) & s_1 (l_2 c_2 + l_3 c_{2+3}) & l_3 s_1 c_{23} \\ 0 & -l_2 s_2 - l_3 s_{23} & -l_3 s_{23} \end{pmatrix} \tag{A.4}$$

Appendix B

According to [44], Denavit-Hartenberg parameters of the 6-dof hydraulic manipulator are specified as shown in Table 4.

Table B-1 *The link parameters of the 6-DOF KIRO robot.*

i^{th}	α_{i-1} (degree)	a_{i-1} (mm)	d_i (mm)	q_i
1	0	0	0	q_1
2	–90	200	0	q_2
3	0	765	0	q_3
4	0	582	0	q_4
5	90	340	0	q_5
6	90	0	400	q_6
T	0	0	300	0

The Jacobian matrix and other matrices of inertia, Coriolis, and Gravity in Cartesian space are calculated from MATLAB program based on the those one in joint space that follows the procedure in [1] and [102].

Published papers and patents

List of International SCI(E) Papers

[1] H. T. Do, T. D. Dang, **H. V. A. Truong** and K. K. Ahn. "Maximum Power Point Tracking and Output Power Control on Pressure Coupling Wind Energy Conversion System," IEEE Transactions on Industrial Electronics, vol. 65, no. 2, pp. 1316-1324, 2018. Doi: 10.1109/TIE.2017.2733424.

[2] T. X. Dinh, T. D. Thien, **T. H. V. Anh,** and K. K. Ahn. "Disturbance Observer Based Finite Time Trajectory Tracking Control for a 3 DOF Hydraulic Manipulator Including Actuator Dynamics,". IEEE Access, vol. 6, pp. 36798-36809, 2018.

[3] Duc-Thien Tran, **Hoai-Vu-Anh Truong**, and Kyoung Kwan Ahn, "Adaptive Backstepping Sliding Mode Control Based RBFNN for a Hydraulic Manipulator Including Actuator Dynamics," Applied Sciences, vol. 9, no. 6, 2018.

[4] **Hoai-Vu-Anh Truong**, Duc-Thien Tran, Kyoung Kwan Ahn, "A Neural Network Based Sliding Mode Control for Tracking Performance with Parameters Variation of a 3-DOF Manipulator," Applied Sciences, vol. 9, no. 10, 2019.

[5] **Hoai-Vu-Anh Truong**, Duc-Thien Tran, Xuan Dinh To, and Kyoung Kwan Ahn, "Adaptive Fuzzy Backstepping Sliding Mode Control for a 3-DOF Hydraulic Manipulator with Nonlinear Disturbance Observer for Large Payload Variation," Applied Sciences, vol. 9, no. 16, 2019.

[6] T. C. Do, **H. V. A**. **Truong,** H. V. Dao, C. M. Ho, X. D. To, T. D. Dang, and K. K. Ahn, "Energy Management Strategy of a PEM Fuel Cell Excavator with a Supercapacitor/Battery Hybrid Power Source," Energies, vol. 12, 2019.

[7] **Truong, H.V.A.**; Dao, H.V.; Do, T.C.; Ho, C.M.; To, X.D.; Dang, T.D.; Ahn, K.K. "Mapping Fuzzy Energy Management Strategy for PEM Fuel Cell–Battery–Supercapacitor Hybrid Excavator," Energies, vol. 13, 2020.

[8] Dao, H.V., To, X.D., **Truong, H.V.A.** et al. "Optimization-Based Fuzzy Energy Management Strategy for PEM Fuel Cell/Battery/Supercapacitor Hybrid Construction Excavator," Int. J. of Precis. Eng. and Manuf.-Green Tech. 2020. (Accepted)

https://doi.org/10.1007/s40684-020-00262-y

[9] Ha, K., **Truong, H.V.A.**, Dang, T.D. et al." Recent Control Technologies for Floating Offshore Wind Energy System: A Review,". Int. J. of Precis. Eng. and Manuf.-Green Tech., vol. 8, pp. 281-301, 2021. https://doi.org/10.1007/s40684-020-00269-5

[10] **Truong, H.V.A.**; Trinh, H.A.; Ahn, K.K. "Safety Operation of n-DOF Serial Hydraulic Manipulator in Constrained Motion with Consideration of Contact-Loss Fault," Appl. Sci., vol. 10, 2020.

[11] Trinh, H.-A.; **Truong, H.V.A.**; Ahn, K.K. "Fault Estimation and Fault-Tolerant Control for the Pump-Controlled Electrohydraulic System," Actuators, vol. 9, 2020.

[12] Duc Thien Tran, Hoai Vu Anh Truong, Kyoung Kwan Ahn. "Adaptive Nonsingular Fast Terminal Sliding Mode Control of Robotic Manipulator Based Neural Network Approach," Int. J. of Precis. Eng. and Manuf., vol. 22, pp. 417-429, 2021.

https://doi.org/10.1007/s12541-020-00427-4

[13] Hoai Vu Anh Truong, Hoai An Trinh, Duc Thien Tran, and Kyoung Kwan Ahn, "A Robust Observer for Sensor Faults Estimation on n-DOF Manipulator in Constrained Framework Environment," IEEE Access, vol. 9, 2021.

[14] Hoai Vu Anh Truong, Xuan Dinh To, Duc Thien Tran, Quoc Hung Hoang, Hoang Vu Dao, Kyoung Kwan Ahn, "A Study of Impedance Control and Contact-loss for The 6-DOF Serial Hydraulic Manipulator," Mechanical Systems and Signal Processing (Submitted)

[15] Hoai Vu Anh Truong, Tri Dung Dang, Cong Phat Vo, Kyoung Kwan Ahn, "Feasibility of Active Control Strategies for Load Mitigation and System Enhancement of Floating Offshore Wind Turbines: A Review," Renewable & Sustainable Energy Reviews (Submitted)

List of domestic KCI papers

[1] Tri Dung Dang, Tri Cuong Do, **Hoai Vu Anh Truong**, Cong Minh Ho, Hoang Vu Dao, Yu Ying Xiao, EunJin Jeong and Kyoung Kwan Ahn. Design, Modeling and Analysis of a PEM Fuel Cell Excavator with Supercapacitor/Battery Hybrid Power Source. Journal of Drive and Control, Vol.16 No.1 pp.45-53 Mar. 2019

[2] To Xuan Dinh, Le Khac Thuy, Nguyen Thanh Tien, Tri Dung Dang, Cong Minh Ho, **Hoai Vu Anh Truong**, Hoang Vu Dao, Tri Cuong Do and Kyoung Kwan Ahn. Modeling and Energy Management Strategy in Energetic Macroscopic Representation for a Fuel Cell Hybrid Electric Vehicle. Journal of Drive and Control, Vol.16 No.2 pp.80-90 Jun. 2019.

List of conference papers

[1] Tri Dung Dang, Cong Binh Phan, **Hoai Vu Anh Truong**, Chau Duy Le, Minh Tri Nguyen and Kyoung-Kwan Ahn. A study on modeling of a hybrid wind wave energy converter system. 2016 16th International Conference on Control, Automation and Systems (ICCAS 2016). Oct. 16-19, 2016 in HICO, Gyeongju, Korea.

[2] Duc Thien Tran, Minh Nhat Nguyen, Xuan Dinh To, **Hoai Vu Anh Truong**, Keunhui Jeong, Giho Jun and Kyoung Kwan Ahn, Indirect adaptive backstepping control via Radial Basis Function Neural Network for Electro-Hydraulic Actuator, The 21st International Conference on Mechatronics Technology, HCM, Vietnam, Oct. 2017.

[3] Duc Thien Tran, Xuan Dinh To, **Hoai Vu Anh Truong**, Keunhui Jeong, Giho Jun and Kyoung Kwan Ahn, RBFNN approximation based backstepping sliding mode control of Electro-hydraulic Actuator, the 13th Korea Robotics Society Annual Conference, South of Korea, Jan. 2018.

[4] **Hoai Vu Anh Truong**, Duc Thien Tran, Kyoung Kwan Ahn, Neural Network Sliding mode control for 3-DOF manipulator, The 22nd International Conference on Mechatronics Technology, Jeju, Korea, Oct. 2018.

[5] Duc Thien Tran, **Hoai Vu Anh Truong**, Xuan Dinh To, Bomoon Seo, Kyoung Kwan Ahn, Adaptive sliding mode control with backstepping technique for hydraulic manipulator the 33rd Institute of Control robotics and Systems 2018, Buan, South of Korea, May 2018.

[6] **H. V. A. Truong**, T.D. Dang, E.J. Jeong, Y.S. Park, J.S. Yun and K.K. Ahn. A Fundamental Study on a PEM Fuel Cell Excavator. 드라이브·컨트롤 2019 춘계학술대회논문집 2019. 06. 26~28 KSFC Conference S4-6.

List of registered patents

[1] Nguyen Minh Tri, Phan Cong Binh, Dang Tri Dung, **Truong Hoai Vu Anh**,이현수, Ahn Kyoung Kwan. 가변 블레이드 구조를 가진 풍력 발전 터빈 (Wind Turbine With Adjustable Blades Structure). 등록번호 10-1754863. 공고일자 2017 년 07 월 06 일.

[2] **Truong Hoai Vu Anh**, Phan Cong Binh, Nguyen Minh Tri, 이현수, Dang Tri Dung, Ahn Kyoung Kwan. 기계 유압 동력인출방식의 하이브리드 파력발전시스템 (Hybrid wave energy converter system with mechanical hydraulic power take-off system). 등록번호 10-1763803. 공고일자 2017 년 08 월 01 일.

[3] Dang Tri Dung, Phan Cong Binh, **Truong Hoai Vu Anh**, Nguyen Minh Tri, 이현수, Ahn Kyoung Kwan. 파력발전기 (Wave energy converter). 등록번호 10-1754862. 공고일자 2017 년 07 월 19 일.

[4] Phan Cong Binh, Dang Tri Dung, **Truong Hoai Vu Anh**, Nguyen Minh Tri, 이현수. 하이브리드 풍력-파력 발전기 9Hybrid wind wave power plant). 등록번호 10-1763802. 등록일자 2017 년 07 월 26 일.

[5] **Truong Hoai Vu Anh**, Do Tri Cuong, Dang Tri Dung, Dao Hoang Vu. 다중 동력원을 갖는 차량의 동력제어방법 (Power Management Control Method Of Vehicle Having Multi Power Source). Application number: 10-2019-0039550. 등록번호 10-2153626. 공고일자 2020 년 09 월 08 일.

[6] **Truong Hoai Vu Anh**, Dang Tri Dung, Do Tri Cuong. 해수 및 신재생 에너지를 이용한 수소발생 시스템 (Hydrogen Generation System Using Seawater And Renewable Energy). Application number: 10-2019-0053138. 공개번호 10-2020-0129235. 공개일자 2020 년 11 월 18 일

[7] **Truong Hoai Vu Anh**, Dang Tri Dung, Dao Hoang Vu. 수소생산 기능을 가지는 하이브리드 발전 시스템 (Hybrid Power Generation System Having Hydrogen Generation Function). Application number: 10-2019-0051400. 공개번호 10-2020-0127384. 공개일자 2020 년 11 월 11 일.

[8] **Other 9 patents submitted**

References

[1] J. C. John, Introduction to Robotics Mechanics and Control, 3rd ed.; Addison-Wisley: Reading, MA, USA; Pearson Education Inc.: Upper Saddle River, NJ, USA, 1989.

[2] Spong, M.W.; Seth, H.; Vidyasagar, M. Robot Dynamics and Control, 1st ed.; John Wiley & Sons, Inc.: New York, NY, USA, 2005.

[3] J. Yuan, "Adaptive control of robotic manipulators including motor dynamics," IEEE Trans. Robot. Autom., vol. 11, pp. 612–617, 1995.

[4] T. J. Tarn, A. K. Bejczy, X. Yun, and Z. Li, "Effect of motor dynamics on nonlinear feedback robot arm control," IEEE Trans. Robot. Autom., vol. 7, pp. 114–122, 1991.

[5] B. S. Chen, H. J. Uang, and C. S. Tseng, "Robust tracking enhancement of robot systems including motor dynamics: A fuzzy-based dynamic game approach," IEEE Trans. Fuzzy Syst., vol. 6, pp. 538–552, 1998.

[6] D. G. Caldwell, G. A. Medrano-Cerda, and M. Goodwin, "Control of pneumatic muscle actuators," IEEE Control Syst. Mag., vol. 15, pp. 40–48, 1995.

[7] M. Papoutsidakis, A. Chatzopoulos, and D. Tseles, "Hydraulics and Pneumatics: A Brief Summary of their Operational Characteristics," J. Multidiscip. Eng. Sci. Technol., vol. 5, pp. 8973–8977, 2018.

[8] C. J. Chiag and Y. C. Chen, "Neural network fuzzy sliding mode control of pneumatic muscle actuators," Eng. Appl. Artif. Intell., vol. 65, pp. 68–86, 2017.

[9] D. C. T. Tu and K. K. Ahn, "Intelligent phase plane switching control of pneumatic artificial muscle manipulators with magneto-rheological brake," Mechatronics, vol. 16, pp. 85–95, 2006.

[10] D. C. T. Tu and K. K. Ahn, "Nonlinear PID control to improve the control performance of 2 axes pneumatic artificial muscle manipulator using neural network," Mechatronics, vol. 16, pp. 577–587, 2006.

[11] M. Papoutsidakis, A. Xatzopoulos, G. P. Smyraiou, and D. Tseles, "PLC Programming Case Study for Hydraulic Positioning Systems Implementations," Int. J. Comput. Appl., vol. 167, pp. 49–53, 2017.

[12] T. Mostafa and M. J. Yarmohammadi, "Development of a Self-tuning PID Controller on Hydraulically Actuated Stewart Platform Stabilizer with Base Excitation," Int. J. Control Autom. Syst., vol. 16, pp. 2990–2999, 2018.

[13] Miroslav, K.; Ioannis, K.; Petar, K. Nonlinear and Adaptive Control Design; John Wiley & Sons. Inc.: New York, NY, USA, 1995; pp. 490–492.

[14] D. T. Tran, H. V. A. Truong, and K. K. Ahn, "Adaptive Backstepping Sliding Mode Control Based RBFNN for a Hydraulic Manipulator Including Actuator Dynamics," Appl. Sci., vol. 9, 2019.

[15] H. V. A. Truong, D. T. Tran, X. D. To, K. K. Ahn, and M. Jin, "Adaptive Fuzzy Backstepping Sliding Mode Control for a 3-DOF Hydraulic Manipulator with Nonlinear Disturbance Observer for Large Payload Variation," Appl. Sci., vol. 9, 2019.

[16] S. L. Shi, J. X. Li, and Y. M. Fang, "Extended-State-Observer-Based Chattering Free Sliding Mode Control for Nonlinear Systems With Mismatched Disturbance," IEEE Access, vol. 6, pp. 22952-22957, 2018.

[17] Wilfrid, P. Sliding Mode Control in Engineering; Marcel Dekker, Inc.: New York, NY, USA, 2002.

[18] W. H. Chen, J. Yang, L. Guo, and S. Li, "Disturbance-Observer-Based Control and Related Methods—An Overview," IEEE Trans. Ind. Electron., vol. 63, no. 2, pp. 1083-1095, Feb. 2016.

[19] Wen-Hua Chen, D. J. Ballance, P. J. Gawthrop, and J. O'Reilly, "A nonlinear disturbance observer for robotic manipulators," IEEE Trans. Ind. Electron., vol. 47, no. 4, pp. 932-938, Aug. 2000.

[20] W. Kim, D. Shin, D. Won, and C. C. Chung, "Disturbance-Observer-Based Position Tracking Controller in the Presence of Biased Sinusoidal Disturbance for Electrohydraulic Actuators," IEEE Trans. Control. Syst. Technol., vol. 21, pp. 2290–2298, 2013.

[21] C. Sun, J. Fang, J. Wei, and B. Hu, "Nonlinear Motion Control of a Hydraulic Press Based on an Extended Disturbance Observer," IEEE Access, vol. 6, pp. 18502–18510, 2018.

[22] Z. Has, M. F. Rahmat, A. R. Husain, and M. N. Ahmad, "Robust Precision Control for a Class of Electro-Hydraulic Actuator System based on Disturbance Observer," Int. J. Precis. Eng. Manuf., vol. 16, pp. 1753–1760, 2015.

[23] Q. Guo, Y. Zhang, B. Celler, and S. Su, "Backstepping Control of Electro-Hydraulic System Based on Extended-State-Observer with Plant Dynamics Largely Unknown." IEEE Trans. Ind. Electron., vol. 63, no. 11, pp. 6909-6920, Nov. 2016.

[24] J. Yao and W. Deng, "Active Disturbance Rejection Adaptive Control of Hydraulic Servo Systems," IEEE Trans. Ind. Electron., vol. 64, no. 10, pp. 8023-8032, Oct. 2017.

[25] C. Wang, Z. Zhang, H. Wang, B. Zhao, and L. Quan, "Disturbance observer-based output feedback control of hydraulic servo system considering mismatched uncertainties and internal pressure dynamics stability," IET Control. Theory Appl., vol. 14, pp. 1046–1056, 2020.

[26] H. A. Trinh, H. V. A. Truong, and K. K. Ahn, "Fault Estimation and Fault-Tolerant Control for the Pump-Controlled Electrohydraulic System," Actuators, vol. 9, 2020.

[27] D. T. Tran, M. Jin, and K. K. Ahn, "Nonlinear Extended State Observer Based on Output Feedback Control for a Manipulator With Time-Varying Output Constraints and External Disturbance," IEEE Access, vol. 7, pp. 156860-156870, 2019.

[28] H. V. Dao, D. T. Tran, and K. K. Ahn, "Active Fault Tolerant Control System Design for Hydraulic Manipulator with Internal Leakage Faults based on Disturbance Observer and Online Adaptive Identification," IEEE Access, to be published. DOI: 10.1109/ACCESS.2021.3053596.

[29] X. D. To, D. T. Tran, H. V. A. Truong, and K. K. Ahn, "Disturbance Observer Based Finite Time Trajectory Tracking Control for a 3 DOF Hydraulic Manipulator Including Actuator Dynamics," IEEE Access, vol. 6, pp. 36798-36809, 2018.

[30] X. B. Dang, Q. T. Dinh, J. Bae, and K. K. Ahn, "An Effective Disturbance-Observer-Based Nonlinear Controller for a Pump-Controlled Hydraulic System," IEEE Trans. Mech., vol. 25, no. 1, pp. 32-43, Feb. 2020.

[31] M. Homayounzade and A. Khademhosseini, "Disturbance Observer-based Trajectory Following Control of Robot Manipulators," Int. J. Control Autom. Syst., vol. 17, pp. 203-211, 2019.

[32] Y. Xin, X. Rong, Y. Li, B. Li, and H. Chai, "Movements and Balance Control of a Wheel-Leg Robot Based on Uncertainty and Disturbance Estimation Method," IEEE Access, vol. 7, pp. 133265-133273, 2019.

[33] B. Ren, Q. C. Zhong, and J. Chen, "Robust Control for a Class of Nonaffine Nonlinear Systems Based on the Uncertainty and Disturbance Estimator," IEEE Trans. Ind. Electron., vol. 62, no. 9, Sep. 2015.

[34] J. Choi, J. Baek, W. Lee, Y. S. Lee, and S. Han, "Adaptive Model-Free Control With Nonsingular Terminal Sliding-Mode for Application to Robot Manipulators," IEEE Access, vol. 8, pp. 169897-169907, 2020.

[35] J. Lee, P. H. Chang, and M. Jin, “An Adaptive Gain Dynamics for Time Delay Control Improves Accuracy and Robustness to Significant Payload Changes for Robots,” IEEE Trans. Ind. Electron., vol. 67, no. 4, pp. 3076-3085, Apr. 2020.

[36] Y. Wang, S. Meng, F. Ju, B. Chen, and H. Wu, “A Novel Model-Free Robust Control of Cable-Driven Manipulators,” IEEE Access, vol. 7, pp. 125532-125541, 2019.

[37] M. Bahrami, M. Naraghi, and M. Zareinejad, “Adaptive Super-twisting Observer for Fault reconstruction in Electro-hydraulic Systems,” ISA Transactions, vol. 76, pp. 235-245, 2018.

[38] M. H. Amoozgar, A. Chamseddine, and Y. Zhang, “Experimental Test of a Two-Stage Kalman Filter for Actuator Fault Detection and Diagnosis of an Unmanned Quadrotor Helicopter,” J. Intell. Robot Syst., vol. 70, pp.107-117, 2013.

[39] S. A. Nahian, T. Q. Dinh, H. V. Dao, and K. K. Ahn, “An Unknown Input Observer–EFIR Combined Estimator for Electrohydraulic Actuator in Sensor Fault-Tolerant Control Application,” IEEE/ASME Trans. Mech., vol. 25, no. 5, pp. 2208-2219, Oct. 2020.

[40] V. D. Phan, C. P. Vo, H. V. Dao, and K. K. Ahn, “Robust fault-tolerant control of an electro-hydraulic actuator with a novel nonlinear unknown input observer,” IEEE Access, to be published. DOI: 10.1109/ACCESS.2020.Doi.

[41] M. H. Nguyen, H. V. Dao, and K. K. Ahn, “Active Disturbance Rejection Control for Position Tracking of Electro-Hydraulic Servo Systems under Modeling Uncertainty and External Load,” Actuators, vol. 10, no. 2, 2021.

[42] Y. Huang and W. Xue, “Active disturbance rejection control: Methodology and theoretical analysis,” ISA Transactions, vol. 53, pp. 963-976, 2014.

[43] M. Van, S. S. Ge, and H. Ren, “Robust Fault-tolerant Control for a Class Second-order Nonlinear Systems Using an Adaptive Third-order Sliding Mode Control,” IEEE Trans. Syst. Man Cyber: System, vol. 47, no. 2, pp. 221-228, Feb. 2017.

[44] M. Van, X. P. Do, and M. Mavrovouniotis, “Self-tuning fuzzy PID-nonsingular fast terminal sliding mode control for robust fault tolerant control of robot manipulators,” ISA Transactions, vol. 96, pp. 60-68, 2020.

[45] A. T. Vo and H. Kang, “A Novel Fault-Tolerant Control Method for Robot Manipulators Based on Non-Singular Fast Terminal Sliding Mode Control and Disturbance Observer,” IEEE Access, vol. 8, pp. 109388-109400, 2020.

[46] V. Reppa, M. M. Polycarpou and C. G. Panayiotou, “Adaptive Approximation for Multiple Sensor Fault Detection and Isolation of Nonlinear Uncertain Systems,” IEEE Trans. Neu. Net. Learn. Syst., vol. 25, no. 1, pp. 137-153, Jan. 2014.

[47] V. T. Nguyen and C. Ha, “Experimental Study of Sensor Fault-Tolerant Control for an Electro-Hydraulic Actuator Based on a Robust Nonlinear Observer,” Energies, vol. 12, no. 22, 2019.

[48] V. T. Nguyen and C. Ha, “Sensor Fault-Tolerant Control Design for Mini Motion Package Electro-Hydraulic Actuator,” Processes, vol. 7, no. 2, 2019.

[49] S. A. Nahian, Q. T. Dinh, P. Chowdhury, D. Das, and K. K. Ahn, “Modeling and Fault Tolerant Control of an Electro-Hydraulic Actuator,” Int. J. Precis. Eng. Manuf., vol 17, pp. 1285-1297, 2016.

[50] D. Brambilla, L. M. Capisani, A. Ferrara, and P. Pisu, “Fault Detection for Robot Manipulators via Second-Order Sliding Modes,” IEEE Trans. Ind. Electron., vol. 55, no. 11, pp. 3954-3963, Nov. 2008.

[51] L. M. Capisani, A. Ferrara, A. Ferreira de Loza, and L. M. Fridman, “Manipulator Fault Diagnosis via Higher Order Sliding-Mode Observers,” IEEE Trans. Ind. Electron., vol. 59, no. 10, pp. 3979-3986, Oct. 2012.

[52] G. Paviglianiti, F. Poerri, F. Caccavale, M. Mattei, “Robust fault detection and isolation for proprioceptive sensors of robot manipulators,” Mechatronics, vol. 20, no. 1, pp. 162-170, Feb. 2010.

[53] H. Pang, Y. Shang, and P. Wang, “Design of a Sliding Mode Observer-Based Fault Tolerant Controller for Automobile Active Suspensions With Parameter Uncertainties and Sensor Faults,” IEEE Access, vol. 8, pp. 186963-186975, 2020.

[54] J. Wang, F. Fang, X. Yi, and Y. Liu, “Dynamic event-triggered fault estimation and sliding mode fault-tolerant control for networked control systems with sensor faults,” Appl. Math. Comput., vol. 389, 2021.

[55] D. Li, Y. Wang, J. Wang, C. Wang, and Y. Duan, “Recent advances in sensor fault diagnosis: A review,” Sens. Actuators, A, vol. 309, 2020.

[56] J. Hu and R. Xiong, "Contact Force Estimation for Robot Manipulator Using Semiparametric Model and Disturbance Kalman Filter," in IEEE Transactions on Industrial Electronics, vol. 65, no. 4, pp. 3365-3375, April 2018.

[57] L. Chan, F, Naghdy, and D. Stirling, “Extended active observer for force estimation and disturbance rejection of robotic manipulators,” Robot. Auton. Syst., vol. 61, no. 12, pp. 1277-1287, Dec. 2013.

[58] Y. Lin, H. Zhao, and H. Ding, “External Force Estimation for Industrial Robots With Flexible Joints,” IEEE Robot. Automation Letters, vol. 5, no. 2, pp. 1311-1318, April 2020.

[59] W. He, Y. Dong, and C. Sun, "Adaptive Neural Impedance Control of a Robotic Manipulator With Input Saturation," in IEEE Transactions on Systems, Man, and Cybernetics: Systems, vol. 46, no. 3, pp. 334-344, March 2016.

[60] A. K. Ravandi, E. Khanmirza, and K. Daneshjou, “Hybrid force/position control of robotic arms manipulating in uncertain environments based on adaptive fuzzy sliding mode control,” Appl. Soft Comput., vol. 70, pp. 864–874, 2018.

[61] Z. Yang, J. Z. Peng, and Y. H. Liu, “Adaptive neural network force tracking impedance control for uncertain robotic manipulator based on nonlinear velocity observer,” Neurocomputing, vol. 331, pp. 263–280, 2019.

[62] F. Coutinho and R. Cortesão, “Online stiffness estimation for robotic tasks with force observers,” Control Eng. Pract., vol. 24, pp. 92–105, 2014.

[63] E. Sariyildiz and K. Ohnishi, “On the Explicit Robust Force Control via Disturbance Observer,” IEEE Trans. Ind. Electron., vol. 62, no. 3, pp. 1581-1589, March 2015.

[64] A. Wahrburg, J. Bös, K. D. Listmann, F. Dai, B. Matthias and H. Ding, “Motor-Current-Based Estimation of Cartesian Contact Forces and Torques for Robotic Manipulators and Its Application to Force Control,” IEEE Trans. Automation Sci. Eng., vol. 15, no. 2, pp. 879-886, April 2018.

[65] Y. Ohba, M. Sazawa, K. Ohishi, T. Asai, K. Majima, Y. Yoshizawa et al., “Sensorless Force Control for Injection Molding Machine Using Reaction Torque Observer Considering Torsion Phenomenon,” IEEE Trans. Ind. Electron., vol. 56, no. 8, pp. 2955-2960, Aug. 2009.

[66] Seul Jung and T. C. Hsia, “Neural network impedance force control of robot manipulator,” IEEE Trans. Ind. Electron., vol. 45, no. 3, pp. 451-461, June 1998.

[67] K. Kronander and A. Billard, “Stability Considerations for Variable Impedance Control,” IEEE Trans. Robot., vol. 32, no. 5, pp. 1298-1305, Oct. 2016.

[68] A. C. Huang and M. C. Chien, “Adaptive control of robot manipulators: a unified regressor-free approach,” World Scientific, 2010.

[69] Slotine, J. E.; Li, W. Applied Nonlinear Control. Prentice Hall, Englewood Cliffs, New Jersey 07632.

[70] E. Ilyas, “Sliding mode control with PID sliding surface and experimental application to an electromechanical plant,” ISA Trans., vol. 45, pp. 109–118, 2006.

[71] M. Van, M. Mavrovouniotis, and S. S. Ge, “An Adaptive Backstepping Nonsingular Fast Terminal Sliding Mode Control for Robust Fault Tolerant Control of Robot Manipulators,” IEEE Trans. Syst. Man Cyber.: System, vol. 49, no. 7, pp. 1448-1458, July 2019.

[72] Singh, S.; Qureshi, M.S.; Swarnkar, P. Comparison of Conventional PID Controller with Sliding Mode Controller for a 2-Link Robotic Manipulator. In Proceedings of the International Conference on Electrical Power and Energy Systems (ICEPES), Bhopal, India, 14–16 December 2016.

[73] N. Nikdel, M. A. Badamchizadeh, V. Azimirad, and M. A. Nazari, “Adaptive backstepping control for an n-degree of freedom robotic manipulator based on combined state augmentation,” Robot. Comput. Integr. Manuf., vol. 44, pp. 129–143, 2017.

[74] J. W. Rong and M. Rajkumar, “Design of Fuzzy-Neural-Network-Inherited Backstepping Control for Robot Manipulator Including Actuator Dynamics,” IEEE Trans. Fuzzy Syst., vol. 22, pp. 709–722, 2014.

[75] K. K. Ahn, D. N. C. Nam, and M. Jin, “Adaptive Backstepping Control of an Electrohydraulic Actuator,” IEEE/ASME Trans. Mechatronics, vol. 19, no. 3, pp. 987-995, June 2014.

[76] M. T. Nguyen, N. C. N. Doan, H. G. Park, and K. K. Ahn, “Trajectory control of an electro-hydraulic actuator using an iterative backstepping control scheme,” Mechatronics, vol. 29, pp. 96–102, 2015.

[77] H. V. A. Truong, H. A. Trinh, and K. K. Ahn, “Safety Operation of n-DOF Serial Hydraulic Manipulator in Constrained Motion with Consideration of Contact-Loss Fault,” Appl. Sci., vol.10, no. 22, 2020.

[78] A. Levant, “Robust exact differentiation via sliding mode technique,” Automatica, vol. 34, pp. 379–384, 1998.

[79] A. Levant, “Higher-order sliding modes, differentiation and output feedback control,” Int. J. Control, vol. 76, pp. 924-941, 2003.

[80] M. Van, S. S. Ge, and H. Ren, “Finite Time Fault Tolerant Control for Robot Manipulators Using Time Delay Estimation and Continuous Nonsingular Fast Terminal Sliding Mode Control,” IEEE Trans. Cyber., vol. 47, no. 7, pp. 1681-1693, July 2017.

[81] A. Mohammadi, M. Tavakoli, H. J. Marquez, and F. Hashemzadeh, “Nonlinear disturbance observer design for robotic manipulators,” Control Eng. Pract., vol. 21, p. 253–267, 2013.

[82] Marquez, H. J. (2003). Nonlinear control systems. Hoboken, NJ: John Wiley & Sons Inc.

[83] Yuri, S.; Christopher, E.; Leonid, F.; Arie, L. Sliding Mode Control and Observation, Control Engineering; Springer: New York, NY, USA, 2014.

[84] Y. Sun, Y. Xia, J. Zhang, and D. W. Ding, “Adaptive Fault-Tolerant Output Regulation of Linear Multi-Agent Systems With Sensor Faults,” IEEE Access, vol.8, pp. 159440-159448.

[85] K. Zhang, B. Jiang, and V. Cocquempot, “Adaptive observer-based fast fault estimation,” Int. J. Control Autom. Syst., vol. 6, no. 3, pp. 320-326, 2008.

[86] H. Khebbache, S. Labiod, and M. Tadjine, “Adaprive sensor fault-tolerant control for a class of multi-input-multi-output nonlinear systems: Adaptive first-order filter-based dynamics surface control approach,” ISA Transaction, vol. 80, pp. 89-98, 2018.

[87] B. Siciliano and L. Villani, “Introduction” in Robot Force Control, 1st ed. New York, USA: Springer, 1999, ch. 1, pp. 1-6.

[88] Hogan

[89] J. Duan, Y. Gan, M. Chen, and X. Dai, “Adaptive variable impedance control for dynamic contact force tracking in uncertain environment,” Robot. Auton. Syst., vol. 102, pp. 54-65, 2018.

[90] J. Yao, Zong. Jiao, and D. Ma, “Extended-State-Observer-Based Output Feedback Nonlinear Robust Control of Hydraulic Systems With Backstepping,” IEEE Trans. Ind. Electron., vol. 61, no. 11, pp. 6285-6293, Nov. 2014.

[91] F. Ferraguti, C. Secchi and C. Fantuzzi, “A tank-based approach to impedance control with variable stiffness,” in 2013 IEEE International Conference on Robotics and Automation, Karlsruhe, Germany, 2013, pp. 4948-4953.

[92] C. Schindlbeck and S. Haddadin, “Unified passivity-based Cartesian force/impedance control for rigid and flexible joint robots via task-energy tanks,” in 2015 IEEE International Conference on Robotics and Automation (ICRA), Seattle, WA, USA, 2015, pp. 440-447.

[93] A. Toedtheide, E. Shahriari and S. Haddadin, “Tank based unified torque/impedance control for a pneumatically actuated antagonistic robot joint,” in 2017 IEEE International Conference on Robotics and Automation (ICRA), Singapore, 2017, pp. 1255-1262.

[94] D. J. Lee, and K. Huang, “Passive-set-point modulation framework for interactive robotic systems,” IEEE Trans. Robot., vol. 26, pp. 354–369, 2010.

[95] M. Franken, S. Stramigioli, S. Misra, C. Secchi and A. Macchelli, “Bilateral Telemanipulation With Time Delays: A Two-Layer Approach Combining Passivity and Transparency,” IEEE Trans. Robot., vol. 27, no. 4, pp. 741-756, Aug. 2011.

[96] A. Franchi, C. Secchi, H. I. Son, H. H. Bulthoff and P. R. Giordano, “Bilateral Teleoperation of Groups of Mobile Robots With Time-Varying Topology,” IEEE Trans. Robot., vol. 28, no. 5, pp. 1019-1033, Oct. 2012.

[97] Feio, J.; Martins, J.M.; Sá da Costa, J. Variable Impedance Control of Manipulator Robots Applied to Orthopedic Surgery. In Proceedings of the 7th Workshop on Advanced Control and Diagnosis, Zielona Gra, Poland, 17–18 November 2009.

[98] Kordasz, M.; Kuczkowski, K.; Sauer, P. Study on Possible Control Algorithms for Lower Limb Rehabilitation System. In Proceedings of the 2011 IEEE International Conference on Rehabilitation Robotics, Zurich, Switzerland, 29 June–1 July 2011.

[99] F. Ferraguti et al., “An Energy Tank-Based Interactive Control Architecture for Autonomous and Teleoperated Robotic Surgery,” IEEE Trans. Robot., vol. 31, no. 5, pp. 1073-1088, Oct. 2015.

[100] Tadele, T.S.; de Vries, T.J.A.; Stramigioli, S. Combining energy and power based safety metrics in controller design for domestic robots. In Proceedings of the 2014 IEEE International Conference on Robotics and Automation (ICRA), Hong Kong, China, 31 May–7 June 2014; pp. 1209–1214.

[101] A. Albu-Schaffer, C. Ott, and G. Hirzinger, “A unified passivity-based control framework for position, torque and impedance control of flexible joint robots,” Int. J. Robot. Res., vol. 26, pp. 23–39, 2007.

[102] E. J. Jung, J. H. Kim, and M. Jin, “Kinematic Analysis of Hydraulic Manipulators for a Disaster Response Robot,” In Proceedings of the 14th International Conference on Ubiquitous Robots and Ambient Intelligence (URAI), Jeju, Korea, 28 June–1 July 2017; pp. 208–209.